

**INFLUENCE OF VARIOUS WELDING SEQUENCE SCHEMES ON  
THE LOAD BEARING CAPACITY OF SQUARE HOLLOW SECTION  
T-JOINT**

Von der Fakultät für Architektur, Bauingenieurwesen und Stadtplanung der  
Brandenburgischen Technischen Universität Cottbus-Senftenberg zur Erlangung des  
akademischen Grades eines Doktor-Ingenieurs genehmigte Dissertation

vorgelegt von

M.Sc.-Ing. Milad Moradi Eshkafti

Aus Eizeh, Iran

Gutachter: Prof. Dr.- Ing. habil. Hartmut Pasternak  
Gutachter: Prof. Dr.- Ing. Ben van Rensburg  
Gutachter: Prof. Dr.- Ing. habil. Marian Gizejowski

Tag der Disputation: October 25, 2017

### ACKNOWLEDGEMENT

Undertaking this PhD has been a truly life-changing experience for me and it would not have been possible to do without the support and guidance that I received from many people.

I would like to first say a very big thank you to my supervisor Prof. Hartmut Pasternak for all support he gave me during my research. I would like to thank him for believing in me and giving me the opportunity to do my research. I appreciate all his contributions of time, ideas, and funding to make my PhD. Thank you Professor Rensburg and Professor Gizejowski for coming a long way. It has been my pleasure having you in the defense.

My appreciation also goes to the members of FMPA (Research and Material Testing at Brandenburg University of Technology) for their friendly collaboration, especially Micha and Mike with their great advices and ideas.

I gratefully acknowledge the funding received towards my PhD from Brandenburg State (GradV) and Prof. Christiane Hipp.

I am indebted to a family in Germany who have opened their home to me. My words are unable to express how much I love this family. Thanks Robin, Rico, Iris and Juli for all you have done. You have helped me finding myself a new place to call home. You have left me speechless with your kindness and love.

I would also like to say a heartfelt thank you to my mom and dad, Pari and Keyvan for always believing in me and encouraging me to follow my dreams. My lovely sisters and brothers, Maryam, Fati, Mamal and Reza. It was not possible chasing my dreams without their support.

Also my mom and brother from London Louise and Oli. They taught me distance means nothing when love is there. I have an amazing family, unique in many ways. Their support has been always unconditional. My family have given up many things for me to reach my goals. This work could not be done without unconditional support and love from my family, they have been always there and cheering me up during the long working days through the whole way. The best of appreciation and love goes to them.

## ABSTRACT

From modelling point of view, it will be very useful if the parameters of interest which contribute to the residual stresses and distortions in various types of welded joint and structure application can be simulated numerically so that welding performance with respect to the various aspects could be assessed and evaluated in an efficient manner.

The present study extends the previous work of [1], [2], [3], [4], [5], [6] and focuses on numerical simulation of welding sequence effects on temperature distribution, residual stresses and distortions and load bearing capacity of a T-joint made by square hollow sections. The aim of this work is to investigate the influence of various welding sequence patterns and welding imperfections on the load bearing capacity of a S355 steel square hollow section (SHS) T-Joint. Two different FE-based programs are used to simulate the welding process: the ABAQUS Welding Interface (AWI) and SYSWELD v2014. The type of welding process used is metal active gas (MAG) welding. A fillet weld with a throat thickness of 5mm is performed. Temperature distribution has been measured at different distance with respect to the weld bead for better validation of results from the simulation. Due to the geometrical characteristics of this type of joint, a compressive test is performed. A displacement with a magnitude of -110 mm is applied on the upper surface of the vertical member (brace). The displacement of several points while the loading process has been measured by inductive displacement transducers. Total number of six specimens were tested. Three joints were welded the same for checking the test set-up (statically checks). The ratio of the width of the branch member to the chord member  $\beta=0.5$  was kept the same for all specimens. So, the influence of welding schemes could be investigated clearer.

The failure and the joint behaviour under loading condition are analysed. For better evaluation of results apart from the main cases, two extra numerical simulations are performed which help making a sufficient conclusion. The results for stresses in the x, y and z directions, after and before loading, are plotted and discussed. Furthermore it has been clearly explained if lower magnitude of residual stresses could lead to a positive gain in strength or not. The differences and influencing parameters on the load bearing capacity are identified. Additionally, some recommendations for AWI users are given. Stress concentration and how the number of start and end points could influence the overall behaviour of the joints are recognized.

**KEYWORDS:** T-joint; ABAQUS AWI; SYSWELD; MAG welding; SHS; stress; distortion.

## ZUSAMMENFASSUNG

Von der Modellierung her ist es nötig, die beitragenden Parameter der verbleibenden Spannungen und Verzerrungen in verschiedenen Schweißverbindungen und deren Strukturen so numerisch zu simulieren, dass die Schweißleistung in einer effizienten Vorgehensweise bewertet wird.

Die vorgelegte Studie baut auf den vergangenen Arbeiten von [1], [2], [3], [4], [5], [6] auf und konzentriert sich auf die numerischen Folgen des Schweißens infolge Temperaturverteilung, Eigenspannungen, Verzüge und Tragfähigkeit an T-Knoten, die aus quadratischen Hohlprofilen bestehen. Ziel dieser Arbeit ist, die Konsequenzen verschiedener Schweiß-Verfahrensmuster auf Tragfähigkeit von Hohlprofilen (SHS) an T-Knoten aus S355 zu untersuchen. Die Schweißsimulation erfolgte mit zwei Programmen: the ABAQUS Welding Interface (AWI) und SYSWELD v2014. Als Schweißtechnik wurde das metal active gas (MAG-Verfahren) verwendet, wobei die Kehlnahtdicke 5mm beträgt. Für eine bessere Validierung der Ergebnisse wurde die Temperaturverteilung in unterschiedlichen Abständen, vom der Schmelzbad, gemessen. Aufgrund der geometrischen Abmessungen dieses Knotens wurde zuletzt ein Druckversuch durchgeführt. Auf den vertikalen Stab (Pfosten) wurde eine Imperfektionen (Verzug) von -110mm aufgebracht. Die Verformung während dem Belastungsprozess wurde dabei von Wegaufnehmer gemessen. Es wurden insgesamt sechs Knoten getestet. Drei Knoten wurden in gleicher Weise geschweißt, um den Aufbau zu überprüfen (statische Prüfung). Das Verhältnis der Dicken von Strebe und Gurt wurden für alle Knoten mit  $\beta=0.5$  angenommen. Auf diese Weise konnte der Einfluss des Schweißens klarer untersucht werden.

Unter der Belastung wurde das Knotenverhalten analysiert. Für eine bessere Bewertung der Ergebnisse wurden zwei Extrasimulationen durchgeführt, um eine effektivere Zusammenfassung zu gewährleisten. Die Ergebnisse für die Spannungen in X, Y und Z Richtungen wurden, vor und nach dem Druckversuch, analysiert und verglichen. Außerdem wurde untersucht, ob sich geringere Eigenspannungen positiv auf die Tragfähigkeit [Widerstand] des Knotens auswirken. Zudem wurden die unterschiedlichen Parameter, welche Auswirkungen auf die Tragfähigkeiten haben, gekennzeichnet. Zusätzlich wurden Vorschläge für AWI-Nutzer gemacht. Zum Schluss wurde angegeben, inwieweit die Spannungskonzentration und die Anzahl der Anfangs- und Endpunkte das allgemeine Verhalten der Knoten beeinflussen.

**SCHLAGWORTE:** T-Knoten; ABAQUS AWI; SYSWELD; MAG-Schweißen; SHS; Spannungen; Verzüge



TABLE OF CONTENTS

ABSTRACT .....	I
TABLE OF CONTENTS .....	II
LIST OF FIGURES .....	VI
LIST OF TABLES .....	XIII
NOMENCLATURE .....	XIV
1 INTRODUCTION .....	1
1.1 Relevance of This Research .....	1
1.1.1 Scientific Relevance .....	1
1.1.2 Industrial Relevance .....	2
1.2 Research Approach.....	3
1.3 Selected Case Studies .....	4
1.4 Structure of the Thesis.....	5
1.4.1 Coordinate System.....	5
1.5 Thesis Outline.....	5
2 BACKGROUND.....	7
2.1 Hollow Structural Sections - Introduction.....	7
2.2 Literature Review on T-joint .....	8
2.2.1 Resistance of the SHS Loaded Face.....	12
2.2.2 Initial Stiffness of the SHS Loaded Face.....	12
2.2.3 Membrane Stiffness of the RHS Loaded Face .....	13
2.3 Eurocode 3 Approach.....	13
2.4 Modes of Failure .....	15
2.5 Analytical Models .....	17
2.5.1 Yield Line Model .....	17
2.5.2 Chord Side Wall Bearing or Buckling Model .....	20
2.6 Classification of Connections.....	21
2.7 Welding Sequencing.....	21
2.7.1 Progressive Welding.....	29
2.7.2 Back-step Welding .....	30
2.7.3 Skip Welding.....	30
3 NUMERICAL MODELLING OF WELDING.....	32
3.1 Background .....	32

## TABLE OF CONTENTS

3.2	Numerical Modelling of a Technological Problem .....	32
3.3	Numerical Modelling of Welding in a Historical Perspective.....	33
3.4	The Coupled Problem.....	35
3.5	Residual Stresses .....	37
3.5.1	Description of Welding Residual Stresses.....	38
3.6	Thermo-Mechanical Analysis of Welding .....	43
3.7	Heat Source Modelling with ABAQUS .....	45
3.8	Geometrical Consideration in the Modelling of Welding .....	45
3.9	The Moving Heat Source Principle in ABAQUS AWI (ABAQUS Welding Interface).....	46
3.9.1	Material Properties .....	47
3.10	Governing Equations .....	54
3.10.1	Thermal Analysis.....	54
3.10.2	Mechanical Analysis .....	55
3.10.3	Strain Decomposition .....	55
3.11	Boundary Conditions.....	56
3.11.1	Thermal Boundary Conditions .....	56
3.11.2	Mechanical Boundary Conditions .....	57
3.12	Microstructural Transformation .....	58
3.12.1	Welding Effects .....	58
4	EXPERIMENTS .....	62
4.1	Chapter Synopsis .....	62
4.2	Material Model .....	62
4.3	Specimen Geometry .....	63
4.4	Fabrication of Joints .....	65
4.4.1	Cutting of the Members.....	65
4.4.2	Tack Welding .....	66
4.4.3	Welding Procedure .....	66
4.4.4	Welding Conditions.....	67
4.5	Temperature Measurement.....	68
4.6	Test Set-up.....	72
4.6.1	Boundary Conditions.....	73
4.6.2	Strain Gauges .....	74
4.6.3	Inductive Displacement Transducer .....	76
4.7	Load Application.....	77

## TABLE OF CONTENTS

4.7.1	Load-Deflection Behaviour .....	78
4.7.2	Load-Strain Behaviour .....	82
4.8	Failure Modes.....	84
4.9	Conclusion.....	86
5	NUMERICAL MODELLING.....	88
5.1	Chapter Synopsis .....	88
5.2	Finite Element Modelling.....	89
5.3	Boundary Conditions.....	90
5.4	Material Definition .....	92
5.5	Models Validation .....	92
5.6	Welding Simulation.....	93
5.7	Temperature Field .....	94
5.8	Numerical Load-Deflection Behaviour .....	97
5.9	Distortions .....	102
5.10	Residual Stresses .....	103
5.10.1	Progressive Welding.....	105
5.10.2	Double-Phase Progressive Welding .....	111
5.10.3	Skip Welding.....	115
5.10.4	Back-Step and Skip Welding (8 welds).....	120
5.11	Conclusion.....	123
6	GENERAL CONCLUSIONS .....	125
7	FUTURE WORKS .....	128
8	REFERENCES .....	129
9	APPENDICES.....	139

## LIST OF FIGURES

Figure 1.1: Welding residual stress and distortion correlation [21].	2
Figure 1.2: Flow chart of the activities reported in the presented thesis.	3
Figure 1.3: T-joint which has been studied in this thesis.	4
Figure 1.4: Weld sequences studied in this thesis. From left to right progressive welding, double-phase progressive welding, skip welding and reverse skip welding.	5
Figure 1.5: Definition of the joint geometry and coordinate system used for all spatial results in the present thesis.	5
Figure 2.1: Application of SHS T-joints in buildings [24] and [25].	8
Figure 2.2: Reinforced and unreinforced joints, a) equal width, b) unequal width and hunch connections studied by [30] and [32].	10
Figure 2.3: Welded T-joint.	10
Figure 2.4: Typical force-displacement or moment-rotation curves for the RHS loaded face.	12
Figure 2.5: Failure modes of hollow section joints T- and K- [47].	14
Figure 2.6: Specimen during test (left), joint failure (right) [53].	16
Figure 2.7: Weld failure in Vierendeel truss, T-joint CHS [52].	16
Figure 2.8: Failure modes of T-joint under concentrated force.	17
Figure 2.9: Yield line model for a T joint [66].	18
Figure 2.10: Yield line pattern for SHS T-joint [67].	19
Figure 2.11: Hinge yield line model [67].	21
Figure 2.12: Comparison of resulting distortion for two different welding sequences [70].	22
Figure 2.13: Welding sequences for thin-wall butt-welds employed in [73], from left to right: progressive welding, backstep welding, symmetric welding.	22
Figure 2.14: Calculated longitudinal stresses for the welding sequences shown in Figure 2.13. In seam direction (left) and transverse to the weld seam (right) in the centre of the weld ( $Y=150\text{mm}$ ), [73].	23
Figure 2.15: Welding sequences for based-on-plates employed in [75]. From left to right: end-centre, centre-end and end-centre-centre-end.	23
Figure 2.16: Calculated longitudinal (left) and transversal (right) stresses at the weld centre line for the welding sequences shown in Figure 2.15 [75].	23
Figure 2.17: Welding sequences for progressive welding (left), welding sequences for block welding (right).	24
Figure 2.18: Vertical deflection under different welding sequences [83].	26
Figure 2.19: Misses stress distribution under different welding sequences [83].	27

Figure 2.20: Geometry, finite element mesh and welding sequences [84].....	28
Figure 2.21: Comparison of longitudinal residual stresses of nine sequences [84]. .....	29
Figure 2.22: Comparison of transverse stresses of nine sequences [84]. .....	29
Figure 2.23: A sample of skip welding [86].....	30
Figure 2.24: A sample of skip welding adopted by [85]. .....	30
Figure 3.1: The sequence of steps in the solution of a technological problem [89].....	33
Figure 3.2 The major interactions, decoupling and mutual influencing of temperature field, stress, deformation and microstructural field after [98]. .....	36
Figure 3.3: Stress level, discipline, dependent effects and variables. ....	37
Figure 3.4: First, second and third order residual stresses ( $\sigma I$ , $\sigma II$ , $\sigma III$ ) in crystallite, structure, acting in y-direction, plotted over coordinate x, $\sigma II$ recorded as crystallite mean value; after [98]. .....	38
Figure 3.5: Temperature field iso-surfaces around welding heat source moving uniformly and linearly on a plate. ....	38
Figure 3.6: Illustration of a fusion zone [103].....	39
Figure 3.7: Metal-active gas welding (MAG) [104]. ....	39
Figure 3.8: Location and position of an only one pass weld for welding two pieces of plates with the same geometry 200*100*8 millimetre. ....	41
Figure 3.9: Residual longitudinal stress field at the end time of welding. ....	41
Figure 3.10: Residual longitudinal stress field after cooling time of 550 seconds.....	42
Figure 3.11: Residual transverse stress field at the end of welding. ....	43
Figure 3.12: Residual transverse stress field after cooling time of 550 seconds.....	43
Figure 3.13: Moving double ellipsoid heat source model. Normal distribution of volumetric heat source density in front and rear of the weld [105].....	44
Figure 3.14: Principle of the moving heat source with successive activation of elements serving as filler material [107]. ....	46
Figure 3.15: Cross section of mesh to model the weld preparation. Illustrating the temperature distribution [108]......	47
Figure 3.16: Thermal conductivity as a function of temperature [106]. ....	48
Figure 3.17: Density as a function of temperature [106].....	49
Figure 3.18: Specific heat as a function of temperature [106]. ....	50
Figure 3.19: Yield stress as a function of temperature [108]. ....	51
Figure 3.20: Young's modulus as function of temperature [106]. ....	52
Figure 3.21: Thermal expansion coefficient as function of temperature [106]......	53
Figure 3.22: Schematic representation of isotropic hardening in principle stress space.....	54

Figure 3.23: Isotropic hardening stress curves for selected temperatures [106].	54
Figure 3.24: Metallurgical zones in a single-pass weld categorized by maximum temperature at each region [116].	59
Figure 3.25: Zones of the HAZ [117].	59
Figure 3.26: CCT diagram and phase composition of S355 steel.	60
Figure 4.1: Universal testing machine UTM (left) and material testing specimen (right).	63
Figure 4.2: Yielding (left), necking (middle) and failure (right).	64
Figure 4.3: True stress-strain (left), engineering stress-strain (right).	65
Figure 4.4: Horizontal Metal Cutting Band Saw Machine.	66
Figure 4.5: preparation of the members (left), tack welding (middle) and tack welded joint (right).	66
Figure 4.6: Welding procedure and the welding machine.	67
Figure 4.7: Sequences of welding, welding start and stop locations.	68
Figure 4.8: Location of thermocouples used for measurement of strain.	69
Figure 4.9: Progressive welding, thermocouples on SHS chord member.	69
Figure 4.10: Progressive welding, thermocouples on SHS brace member.	70
Figure 4.11 Double-phase progressive welding, thermocouples on SHS Chord member	71
Figure 4.12: Double-phase progressive welding, thermocouples on SHS brace member.	71
Figure 4.13: Skip welding, thermocouples on SHS chord member.	72
Figure 4.14: Skip welding, thermocouples on SHS brace member.	72
Figure 4.15: Load application machine and test set-up.	73
Figure 4.16: Boundary condition and clamping.	74
Figure 4.17: Strain gauges on chord and brace members.	76
Figure 4.18: Inductive displacement transducer [119].	76
Figure 4.19: Inductive displacement transducer locations.	77
Figure 4.20: Test set-up arrangements.	78
Figure 4.21: Load-displacement behaviour at top of the brace member.	79
Figure 4.22: First test, failure in the displacement transducers.	79
Figure 4.23: Load-displacement behaviour of chord top face.	80
Figure 4.24: Load-displacement behaviour at chord side walls.	80
Figure 4.25: Load-displacement behaviour at chord bottom face.	81
Figure 4.26: Strain gauge 1 (left) and strain gauge 2 (right).	82
Figure 4.27: Strain gauge 3 (left) and strain gauge 4 (right).	83
Figure 4.28: Strain gauge 5 (left) and strain gauge 6 (right).	83
Figure 4.29: Strain gauge 7 (left) and strain gauge 8 (right).	84

Figure 4.30: Strain gauge 9 (left) and stain gauge 10 (right). .....	84
Figure 4.31: Failure modes joint 1 to 6. ....	85
Figure 5.1: Extra adopted cases in the numerical analysis. ....	88
Figure 5.2: Geometry with the finite element mesh for the three-dimensional analysis. ....	89
Figure 5.3: Adopted boundary conditions during welding. ....	90
Figure 5.4: Nodal and side supports adopted for the loading analysis. ....	91
Figure 5.5: The geometry and applied load. ....	92
Figure 5.6: Temperature distribution, Fusion zone and heat affected areas (SYSWELD). ....	95
Figure 5.7: Temperature distribution on the chord – welding simulation vs experiment for progressive welding. ....	95
Figure 5.8: Temperature distribution on the brace – welding simulation vs experiment for progressive welding. ....	96
Figure 5.9: Temperature distribution on the chord – welding simulation of skip welding. ....	96
Figure 5.10: Temperature distribution on the brace – welding simulation of skip welding. ....	97
Figure 5.11: Measured tolerance in the wall thickness of the chord member in mm. ....	97
Figure 5.12: Progressive welding - load deflection behaviour of the T-joint, SYSWELD (left) and ABAQUS (right). ....	98
Figure 5.13: Deformed T-joint, test (left) and numerical simulation (right). ....	98
Figure 5.14: Numerical load vs displacement for all investigated cases. ....	99
Figure 5.15: Load vs Displacement from ABAQUS and SYSWELD. ....	100
Figure 5.16: Load-deflection behaviour for points 3 and 4. ....	101
Figure 5.17: Load-deflection behaviour for points 5 and 6. ....	102
Figure 5.18: Load-deflection behaviour for point 7. ....	102
Figure 5.19: Welding induced deformation, SYSWELD (left) and ABAQUS (right). ....	103
Figure 5.20: Influence of welding imperfections on the load bearing capacity of the T-joint. ....	104
Figure 5.21: Von Mises stresses before the loading process, SYSWELD (left) and ABAQUS AWI (right). ....	104
Figure 5.22: Von Mises stresses after the loading process, SYSWELD (left) and ABAQUS AWI (right). ....	104
Figure 5.23: Line along which the stress is plotted. ....	105
Figure 5.24: Progressive welding - stress distribution in x direction before the loading process, SYSWELD (left) and ABAQUS AWI (right). ....	105
Figure 5.25: Progressive welding - stress distribution in x direction before the loading process. ....	106
Figure 5.26: Progressive welding - stress distribution in x direction after the loading process, SYSWELD (left) and ABAQUS AWI (right). ....	106

Figure 5.27: Progressive welding - stress distribution in x direction after the loading process...	107
Figure 5.28: Stress distribution in y direction before the loading process, SYSWELD (left) and ABAQUS AWI (right). .....	107
Figure 5.29: Stress distribution in y direction before the loading process. ....	108
Figure 5.30: Stress distribution in y direction after the loading process, SYSWELD (left) and ABAQUSD AWI (right). ....	108
Figure 5.31: Stress distribution in y direction after the loading process. ....	109
Figure 5.32: Stress distribution in z direction after the welding process, SYSWELD (left) and ABAQUS AWI (right). ....	109
Figure 5.33: Stress distribution in z direction after the welding process. ....	110
Figure 5.34: Stress distribution in z direction after the loading process, SYSWELD (left) and ABAQUS AWI (right). ....	110
Figure 5.35: Stress distribution in z direction after the loading process. ....	111
Figure 5.36: Double-phase progressive welding - stress distribution in x direction before the loading process. ....	111
Figure 5.37: Double-phase progressive welding - stress distribution in x direction after the loading process. ....	112
Figure 5.38: Double-phase progressive welding - stress distribution in y direction before the loading process. ....	113
Figure 5.39: Double-phase progressive welding - stress distribution in y direction after the loading process. ....	113
Figure 5.40: Double-phase progressive welding - stress distribution in y direction before the loading process. ....	114
Figure 5.41: Double-phase progressive welding - stress distribution in y direction after the loading process. ....	115
Figure 5.42: Skip welding - stress distribution in x direction before the loading process. ....	115
Figure 5.43: Skip welding - stress distribution in x direction after the loading process. ....	116
Figure 5.44: Skip welding - stress distribution in y direction before the loading process. ....	116
Figure 5.45: Skip welding - stress distribution in y direction after the loading process. ....	117
Figure 5.46: Skip welding - stress distribution in z direction before the loading process. ....	117
Figure 5.47: Skip welding - stress distribution in z direction after the loading process. ....	118
Figure 5.48: Stress distribution for both software in x direction before the loading process. ....	119
Figure 5.49: Stress distribution for both software in Z direction before the loading process. ....	120
Figure 5.50: Load-deflection behaviour of the numerically investigated cases. ....	121



Figure 5.51: Mean stress distribution before the loading process (a=N1, b=N2, c=N3, d=N4 and e=N5).....	122
Figure 5.52: Temperature iso-surfaces, SYSWELD (left) and ABAQUS AWI (right).....	123
Figure 9.1: Measuring the initial geometry by using surveying camera. ....	139
Figure 9.2: Lines along which the initial and after welding geometry was measured. ....	140
Figure 9.3: Initial and after welding geometry for chord top surface at middle line.....	140
Figure 9.4: Initial and after welding geometry for the brace member midline in z direction. ....	141
Figure 9.5: Initial and after welding geometry for the chord top surface edge. ....	141
Figure 9.6: Initial and after welding geometry for the chord top surface edge in z direction. ....	141
Figure 9.7: Initial and after welding geometry for the brace midline in x direction. ....	142
Figure 9.8: Initial and after welding geometry for chord top surface at middle line.....	142
Figure 9.9: Initial and after welding geometry for the brace member midline in z direction. ....	142
Figure 9.10: Initial and after welding geometry for the chord top surface edge. ....	143
Figure 9.11: Initial and after welding geometry for the chord top surface edge in z direction. ...	143
Figure 9.12: Initial and after welding geometry for the brace midline in x direction. ....	143
Figure 9.13: Initial and after welding geometry for chord top surface at middle line.....	144
Figure 9.14: Initial and after welding geometry for the brace member midline in z direction. ...	144
Figure 9.15: Initial and after welding geometry for the chord top surface edge. ....	144
Figure 9.16: Initial and after welding geometry for the chord top surface edge in z direction ...	145
Figure 9.17: Initial and after welding geometry for the brace midline in x direction. ....	145
Figure 9.18: Weld throat thickness measurement. ....	146
Figure 9.19: Temperature distribution from the thermo-couples on the chord member. ....	147
Figure 9.20: Temperature distribution from the thermo-couples on the brace member.....	147
Figure 9.21: Longitudinal stress - single phase material.....	148
Figure 9.22: Longitudinal stress – multi-phase material.....	148
Figure 9.23: Welding induced distortion for the midline on the chord top surface- progressive welding. ....	149
Figure 9.24: Welding induced distortion for the midline on the chord top surface- two phases progressive welding.....	149
Figure 9.25: Welding induced distortion for the midline on the chord top surface- skip welding. ....	149
Figure 9.26: Welding induced distortion for the midline on the brace in x direction- progressive welding. ....	150
Figure 9.27: Welding induced distortion for the midline on the brace in x direction- two phases progressive welding.....	150

## LIST OF FIGURES

Figure 9.28: Welding induced distortion for the midline on the brace in x direction- skip welding. .....	150
Figure 9.29: Welding induced distortion for the midline on the brace in z direction- progressive welding. ....	151
Figure 9.30: Welding induced distortion for the midline on the brace in z direction- two phases progressive welding.....	151
Figure 9.31: Welding induced distortion for the midline on the brace in z direction- skip welding. .....	151
Figure 9.32: Distribution of longitudinal residual stresses in thickness of the chord member. ...	152
Figure 9.33: Load-displacement behaviour of points located 60 mm away from the brace on both sides on the chord.....	152
Figure 9.34: Load-displacement curves for the point on the bottom of the chord. ....	153
Figure 9.35: Load-displacement curves for the points on chord side walls. ....	153
Figure 9.36: Plastic strain distribution. ....	154

## LIST OF TABLES

Table 1-1: Chemical composition of the structural steel S355 [22].....	5
Table 2-1: Methodolgy for the strength calculation of T-joints between RHS [47]. .....	15
Table 2-2: Parameters for plastic hinges and plastic work for the general mechanism [68].....	20
Table 3-1: Welding parameters. ....	40
Table 3-2: Heat source parameters. ....	40
Table 3-3: Heat source parameters after [106]. ....	45
Table 4-1: Detailed information on material specimens. ....	63
Table 4-2: Stress and elongation results for eight specimen made of S355.....	64
Table 4-3: Welding conditions for the case studies.....	67
Table 4-4: Strain gauge dimensions and resistance.....	75
Table 4-5: Test matrix. ....	81
Table 5-1: cases investigated in numerical simulation.....	88
Table 5-2: First order element types used for thermal and mechanical analyses.....	90
Table 5-3: Welding and heat source parameters. ....	93
Table 5-4: Points at which the temperature have been measured.....	94
Table 5-5: Maximum load reached for the investigated numerical and experimental cases.....	100

NOMENCLATURE

$h_0$	The height of the chord member;
$h_1$	The height of the brace member;
$b_0$	The width of the chord member;
$b_1$	The width of the brace member;
$t_0$	The wall thickness of the chord member;
$t_1$	The wall thickness of the brace member;
$\theta$	The included angle between brace member and the chord;
$\beta$	The ratio $b_1/b_0$ ;
$\mu_1$	The ratio $b_1/t_1$ ;
$\mu_0$	The ratio $b_0/t_0$ ;
$\gamma$	The ratio of the chord width or diameter to twice its wall thickness $b_0/(2t_0)$ ;
$S_j$	The rotational stiffness of a joint;
$S_{j,ini}$	The initial rotational stiffness of a joint ;
$\phi$	The rotation of a joint;
$M_{j,Rd}$	The design moment resistance of a joint;
$N_{1,Rd}$	The design value of the resistance of the joint, expressed in terms of internal axial force in member;
$f_{y0}$	The yield strength of a chord member;
$f_b$	The buckling strength of the chord side wall;
$l_i$	The yield lines length;
$\varphi_i$	The rotation angel;
$f_{yi}$	The yield strength of member;
$\eta$	The ratio of the brace member depth to the chord diameter or width $\frac{h_i}{d_0}$ and the arc efficiency
$k_n$	A factor defined where it occurs;
$b_{eff}$	The effective width for a brace member to chord connection;
$b_{e,p}$	The effective width for punching shear;
$E$	The elastic modulus;
$n$	The ratio $(\frac{\sigma_{0,Ed}}{f_{y0}})/\gamma_{M5}$ (used for RHS chords);
$\delta$	The height of the brace member displacement;

$m_p$	The ratio $(\frac{f_{y0} * t_0^2}{4})$ ;
$N_1$ or $P$	The force applied on the brace member;
$\sigma^I$	The first order residual stresses;
$\sigma^{II}$	The second order residual stresses;
$\sigma^{III}$	The third order residual stresses;
<i>GMAW</i>	Gas metal arc welding;
<i>MAG</i>	Metal arc gas welding;
<i>HAZ</i>	The heat affected zone;
<i>Fz</i>	The fusion zone;
$v$	The velocity of welding;
$I$	The current of welding (A);
$U$	The voltage of welding (V);
$a_1$	The front length of the heat source;
$a_2$	The rear length of the heat source;
$b$	The width of the heat source;
$c$	The depth of the heat source;
$Q$ or $q$	The heat flux per unit area;
$q_f$	The power density in front ellipsoid;
$q_r$	The power density in rear ellipsoid;
$f_f$	Fraction of heat deposited in front ellipsoid;
$f_r$	Fraction of heat deposited in rear ellipsoid;
$a$	The throat thickness of the weld bead;
$C_p$	The heat capacity of a material (specific heat);
$\rho c_p$	The heat capacity as a combined property;
$h$	The specific enthalpy of $dH = mdh$ ;
$\rho$	The density of the material;
$\Delta T$	Temperature change $T_1$ to $T_2$ ;
$m$	The mass of the material;
$Q_L$	The latent heat;
$k$	The heat conductivity;
$Q_V$	The heat supplied externally into the body per unit volume from the welding process;
$V$	The volume of solid material;
$S$	The Surface area;

$p_j$	The body force at any point within the volume;
$\partial_{ij,i}$	The stress tensor;
$\delta\bar{\epsilon}$	The virtual strain (corresponding to the virtual deformation);
$\delta\bar{u}$	A virtual displacement field;
$T$	The surface traction at any point on S;
$\epsilon_{ij}^{total}$	The total strain;
$\epsilon_{ij}^e$	The strain in parts caused by elasticity;
$\epsilon_{ij}^p$	The strain in parts caused by plasticity;
$\epsilon_{ij}^{tp}$	The strain in parts caused by transformation plasticity;
$\epsilon_{ij}^{vp}$	The strain in parts caused by viscoplasticity;
$\epsilon_{ij}^c$	The strain in parts caused by creep;
$\epsilon_{ij}^{th}$	The strain in parts caused by temperature;
$h_{con}$	The Film coefficient;
$T_0$	The Sink temperature;
$\epsilon$	The Emissivity constant;
$\sigma$	The Stefan-Boltzmann constant;
$T_z$	The Absolute zero on the actual temperature considered;
$T_{amb}$	The ambient temperature;
$F_f$	The frictional force;
$\mu$	The static or kinetic frictional coefficient;
$N$	The Normal force;
$\bar{h}$	The combined heat transfer coefficient;
$\bar{u}$	The virtual displacement field;
$\alpha$	The linear thermal expansion coefficient;
$TL$	The materials liquids temperature;
$TS$	The materials solidus temperature;

## Computer Modelling

“This is a process by means of providing the computer with mathematical equations, clear and unequivocal description of the system under study, by including the relations in between inputs and outputs and also getting advantages of using this description to simulate or model the described system.”

(Academic Press Dictionary of Science Technology)

## Welding

“Welding is used for joining separate parts of metal in a continuous metallic bond. In cold-pressure welding, high pressure is applied at room temperature. Forge welding (or forging) is done by means of hammering, with the addition of heat. In many process, the points to be joined are melted, additional molten metal is added as a filler, and the bond is allowed to cool. The Thomson process, melting is caused by resistance to an applied electric current. Another process is that of the atomic hydrogen flame, in which hydrogen molecules passing through an electric arc are broken into atoms by absorbing energy. Outside the arc the molecules reunite yielding heat to weld the material in the process.”

(The Columbia Electronic Encyclopedia)

## Simulation

“The technique of imitating the behaviour of some situation or process (whether economic, military, mechanical, etc.) by means of suitably analogous situation or apparatus, especially for the purpose of study or personal training.”

(The Oxford English Dictionary)

**Author’s own words:** It is done to present an image or behaviour of a physical system. This process may be done by a computer or also a physical model. This model is built to represent some aspects (behaviour) of the system which can be due to any purposes.

(M. Moradi)

# 1 INTRODUCTION

## 1.1 Relevance of This Research

### 1.1.1 Scientific Relevance

Nowadays, welding is used widely for connecting the members made of metal. Welding as other techniques for joining of components has its own consequences and disadvantages. Residual stresses and distortions can occur near the weld bead due to localized heating by the welding process and subsequent rapid cooling. High residual stresses in regions near the weld may promote brittle fractures, fatigue, or stress corrosion cracking. Meanwhile, residual stresses in the base plate may reduce the buckling strength of the structure members and overall load bearing capacity. Therefore, welding residual stresses must be minimized to control them according to the respective requirements [7].

Previous investigators have developed several methods, including heat treatment, hammering, preheating, vibration stress relieving, and weld sequencing to reduce the residual stresses attributed to welding. In these methods, to choose an available welding sequence is simpler and efficient for reduction of welding residual stresses. Because many welded structures which cannot be post-weld manufacturing measures after welding contain residual stresses of varying degree. Therefore, developing an available welding sequence and accurately predicting welding residual stresses for welds system are necessary for achieving the safest design. For an investigation of reducing weld residual stress, Jonassen [8] described the effect of welding procedures on reducing the residual stresses for butt-welded steel plates. Rybicki [9] and [10] developed a method for reducing tensile stresses on the inner surfaces of the girth welded pipes. The process entails inductively heating the outside of a welded pipe while cooling the inner surface with flowing water. Josefson [11] and [12] calculated the welding residual stresses that were numerically analysed for a girth-butt welded thin-walled pipe during different post-weld treatments. Brust and Rybicki [13] developed a method called backlay welding that can be effective in producing compressive residual stresses on the pipes inner surface. Ueda [14] investigated the effectiveness of the heat-sink welding to improve the residual stresses of a pipes circumferential joint. Chou and Lin [15] Reduced residual stresses by parallel heat welding type 304 stainless steel specimens. For the effect of welding sequence, Weck [16] and Watanabe [17] have studied how welding sequence affect residual stress build-up. Kihara [18] investigated how welding sequence affects residual stress and shrinkage in slit-type welds and circular-path welds. Jonassen [8] describes the effects of certain block and other special welding procedures on the magnitude of residual stresses in butt-welded steel plates of 1-in thickness. T.



Schenk [19] studied the influence of clamping and sequencing on a T-joint made by plates and has reported that this technique could be highly used in automobile, ship, railway and in general steel structures as it has great results in terms of stresses and deformation.

Regarding welding distortion a very strong relation is governed as shown in Figure 1.1. Apart from sequencing and its effects, boundary condition has also a great influence on stress and distortion distribution. Distortion is closely related to the amount of residual stress and the degree of joint restraint during welding process. As rule of thumb, the welded joint with lower degree of restraint has an advantage due to less residual stress but it tends to get higher distortion. Conversely, the welded joint with higher degree of restraint has less distortion but it will further result in higher residual stress [20].

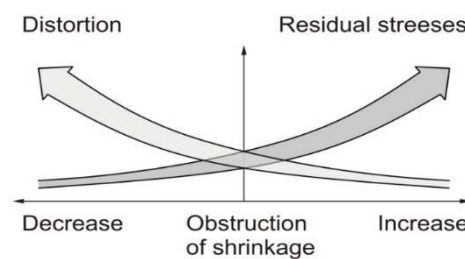


Figure 1.1: Welding residual stress and distortion correlation [21].

Apart from all these mentioned neuromas studies, this research aims to expand the pervious works. A great attention is paid, first on how welding sequencing influences the residual stresses and distortion, on the other hand the influence of sequencing on load bearing capacity is studied. Until today the attention in terms of sequencing was mostly paid to small specimens but the influence of sequencing on closed sections has never been studied. It has never been studied how the sequencing influences the durability and strength of joints in steel structures. This research has been done in order to answer the questions regarding to this issue and cover the missing parts.

### 1.1.2 Industrial Relevance

Nowadays, cost and time both play important roles in industry and are the factors to be considered highly. Apart from the scientific point of view, sequencing brings cost, material and time saving for the industry. This technique improves productivity and quality. This technique could be used in automotive, ship, building industry the most. In ship industry where a big side wall of a ship is considered which is the face to bear the pressure, welding of pieces of plates together, brings to attention the sequencing and welding in a way which led to less distortions and residual stresses and at the end good quality and load bearing. The same is considered in building industry when dealing with hollow sections and other steel members. Whether the joints are under compressive/tensile or bending forces, welding imperfections can be lowered by this technique which led to better bearing capacity.

This work aims to investigate the influence of welding sequencing on the load bearing capacity. Previous works as mentioned in scientific relevance verified that welding sequencing has influence on welding imperfections but further investigation and the influence of sequencing on the load bearing capacity of structures made by hollow sections is missing.

## 1.2 Research Approach

This research aim is to investigate the influence of sequencing on residual stresses, distortions and load bearing capacity. In this research 6 joints made by square hollow sections are considered. For this work a combined experimental and modelling approach is performed. This includes thermal and the mechanical fields during welding, for instance temperatures, distortions, residual stresses are measured. Figure 1.2 shows the working flow of this research and the aspects which are considered.

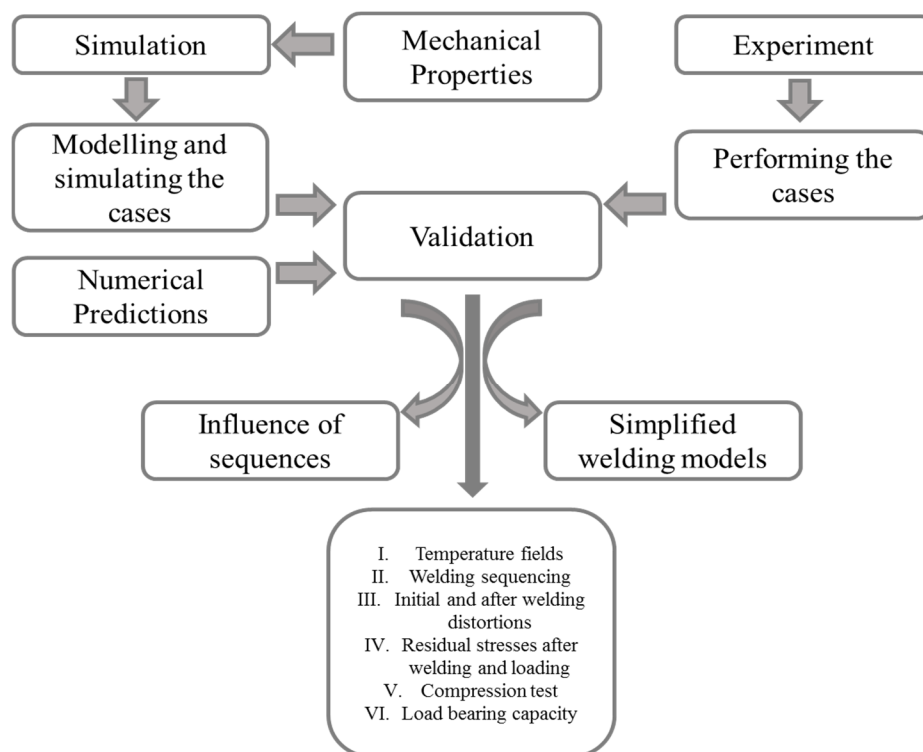


Figure 1.2: Flow chart of the activities reported in the presented thesis.

In order to investigate the influence of sequencing on distortions, residual stresses and load bearing capacity the facilities have been prepared for both modelling and experiments. A model was developed in ABAQUS 6.14-2 in order to predict the behaviour of the joint for welding and loading tests. For the mentioned model the thermal and mechanical properties for S355 were gathered from literatures and material libraries such as Simufact.Material. Later the mechanical properties were scaled by the true stress and strain achieved by material tensile testing.

Welding simulation for the six joints has been done by programs such as SYSWELD and ABAQUS AWI. The results from the simulations are compared with the results from experiments. After

validation the welding sequences has been investigated, the influence of each single welding sequence on the load bearing capacity has been clarified numerically and experimentally. For understanding the phenomena some extra cases have been considered in the numerical simulations and later some conclusions and recommendation have been given.

### 1.3 Selected Case Studies

In the present research work, four case studies have been chosen to provide experimental data for the model validation and comparisons. The case studies all include a T-joint made by square hollow sections as shown in Figure 1.3. The branch or the brace has been chosen to be smaller than the chord member as in most of cases in practice. The brace has a height of 600 mm, width of 100 mm and thickness of 4 mm. the chord is 1200 mm long, width of 200 mm and wall thickness of 6.3 mm. The members are welded using MAG (gas metal arc welding). The brace is located vertically on the face centre of the chord. Both members are from the same material S355. The material properties are explained in details in chapter 3.

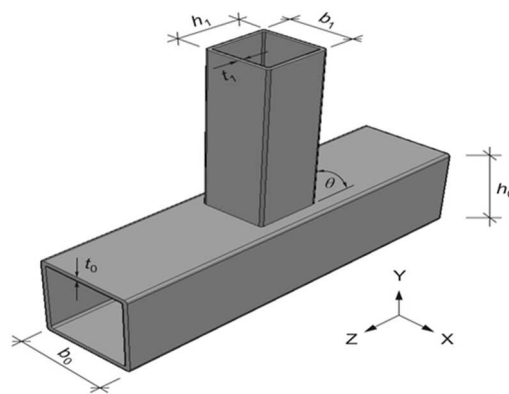


Figure 1.3: T-joint which has been studied in this thesis.

Figure 1.4 presents the case studies in this thesis. Four different cases are studied experimentally. However, more cases are involved in the numerical investigations for delivering a better conclusion. All joints are welded with the same machine, same parameters at the same welding centre. Welding has been done by hand. According to the size of the welds and members, it is difficult to perform welding with automatic welding machines so called robots. Great effort has been put on weld thickness in order to keep the weld throat thickness more or less the same along the weld ( $a = 5$  mm). From the first case three joints are prepared for statistical analysis, hence they have been welded and undergone loading sooner. Arrows in Figure 1.4 present the welding direction and the circle filled elements present the start and end points of welding.

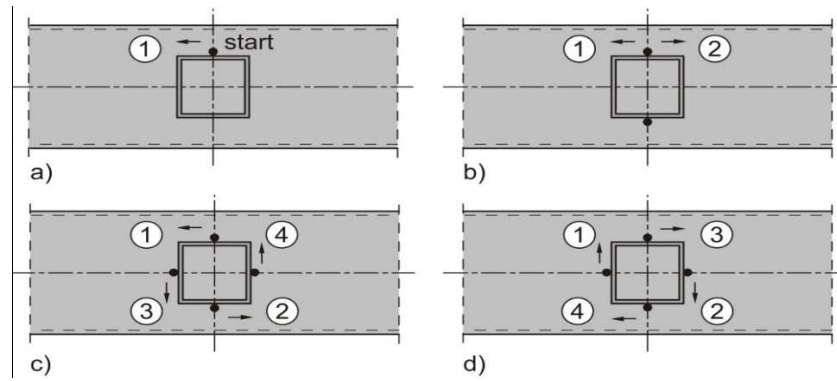


Figure 1.4: Weld sequences studied in this thesis. From left to right progressive welding, double-phase progressive welding, skip welding and reverse skip welding.

Table 1-1 lists the chemical composition of steel S355 which has been used in both numerical and experimental investigations in the presented thesis.

Table 1-1: Chemical composition of the structural steel S355 [22].

Element	C	Fe	Mn	N	P	S	Si
%	0.17	98.127	1.6	0.005	0.017	0.011	0.02

## 1.4 Structure of the Thesis

### 1.4.1 Coordinate System

Figure 1.5 shows the coordinate system used within the present thesis. The geometry is defined as in section 1.3,  $h_1, b_1$  and  $t_1$  are respectively the brace height, width and wall thickness.  $h_0, b_0$  and  $t_0$  are the height, width and wall thickness of the chord.

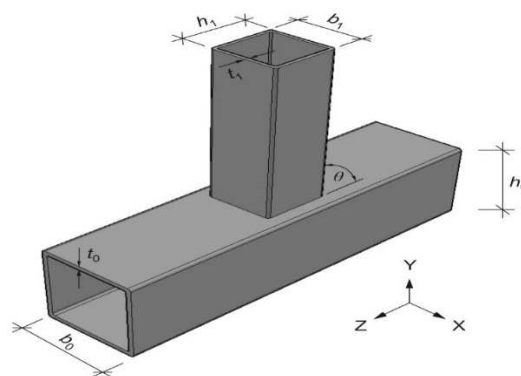


Figure 1.5: Definition of the joint geometry and coordinate system used for all spatial results in the present thesis.

## 1.5 Thesis Outline

The thesis is structured presenting in the next chapter, chapter 2, a literature review of the recent researches conducted about structural hollow sections (SHS) and their applications in various fields, especially in the structural field. This chapter goes through the design equations, methods for

determining the load bearing capacity and how Eurocode approach is made. Modes of failures due to various loading conditions are shown and furthermore the classification of different connections. Chapter 3 gives an overall background of numerical modelling of welding. Welding imperfections are explained in detail. The coupling of various analyses are introduced. A special attention in this chapter is paid to welding simulation by ABAQUS AWI and the material used for such an extension.

The experimental investigations in the fourth chapter, focus on the influence of various welding sequences on the overall behaviour and load bearing capacity of the T-joints. The material properties from the tensile tests are presented. A good measurement of temperature distribution while welding is offered for various welding sequences. This chapter also goes through loading of T-joints after welding. How different parts behave while loading are measured by use of inductive displacement transducers and strain gauges. At the end of this chapter the results are compared and the differences are highlighted.

The fifth chapter offers numerical welding simulation and finite element analysis of each single test that has been done in the experiment. Two different software (SYSWELD and ABAQUS AWI) are used for modelling of welding and also load application. The validation of results started from matching the temperature distribution and further load bearing of each joint. The results of this part are compared with the results from the experiments. The differences between both programs are summarized. At the end of this chapter a conclusion is made which presents the influencing parameters on the load bearing capacity of the T-joint and how each single welding sequence affects the overall behaviour of the joint.

The main conclusions from the results obtained in the previous two chapters are summarized in chapter 6.

Chapter 7 gives some recommendations for the future research activities and further related information. Chapter 8 includes the valuable literatures used for each single part of this work respectively and details are placed in the ninth chapter.

## 2 BACKGROUND

### 2.1 Hollow Structural Sections - Introduction

Hollow structural sections (HSS) have played an increasingly important role in steel structural applications during the last twenty years in the whole world. One cannot examine the behaviour of square hollow sections (SHS) joints and members without considering their historical development. The use of SHS as well as RHS arose after circular hollow sections (CHS) had been around for many years [23]. The increasing use of CHS highlighted the special techniques needed for end profiling when connecting CHS members together in order to get a good fit needed for welding. These skills were often only available to big fabricators and producers of circular hollow sections and limited the application to a wider market. The recognition that SHS with its flat surfaces provided significant advantages such as:

- Their geometrical shape effectively resists torsion and out-of-plane forces; the exposed surface area is less than that of conventional wide flange shapes, thus facilitating the application of protective coatings; their clean lines and smooth surfaces permit architects to satisfy the required aesthetic objectives.
- Maintenance of SHS members is easier and cheaper than that of the more traditional sections.
- Simple end cuts of square and rectangular HSS are sufficient for weld connecting members together.

HSS are used in buildings, bridges, piles, tunnel supports and electrical transmission towers, etc. one of the most common types of construction is the Vierendeel truss. The Vierendeel truss was first developed by Arthur Vierendeel in 1896. Unlike conventional trusses with triangular voids and pin connections designed to take axial forces, this system was developed to resist bending forces at the joints, along with axial forces for the members. The Vierendeel truss is designed with chord members connected to bracing members, typically at  $90^\circ$  to one another (Figure 1.1). This type of connection is also known as a T-joint. For a Vierendeel truss with an even number of cells, which has the applied load at every joint, the middle brace does not exhibit bending moments, only axial forces. As expected the top chord is in compression while the bottom chord is in tension. In many cases, Vierendeel truss members are made of steel Rectangular and Square Hollow Sections (RHS and SHS). The high concentration force of the brace can cause the top chord RHS and SHS sidewalls to buckle near the joint. Since T-joints are commonly used in beam to column connections the load

capacity of the structure may be governed by the strength of its joint including the weld strength, especially when thin-walled sections are used.

The main purpose of this study is the analysis of welded T-type joints fabricated from square hollow sections. Figure 2.1 shows some application of SHS T-joints in various structures.



Figure 2.1: Application of SHS T-joints in buildings [24] and [25].

## 2.2 Literature Review on T-joint

A considerable amount of research work has been conducted on single chord RHS and SHS T-joints in order to study the behaviour of this type of joint. The material, load application, section geometry and boundary conditions can be counted as variable in between all these works. However, still these great works point out the importance of this type of joint.

It should be mentioned aims differ in each study done and due to the aims the geometry differs. For example, experimental results have been reported by [26], [27], [28], [29] and [30]. They have undertaken analytical and numerical modelling investigations.

Jubb and Redwood [26] have indicated that, from experimental tests, an unreinforced equal width joint would behave in an approximately rigid manner. They also stated that for unequal width connections, there is a considerable reduction in joint stiffness and hence the assumption of using rigid joints in the design of Vierendeel trusses is inappropriate. Redwood, analysed the unreinforced joint with  $\lambda < 1$  by considering the top flange plate of the chord and a thin plate loaded through a symmetrically located inclusion. The plate problem was solved numerically in the elastic range, using the finite difference method, and gave reasonable agreement with the results obtained from the unreinforced joint tests.

Blockley and Eastwood [31] used the same basic analysis for this type of joint taking into account the rounded corners of the chord member. Consequently, the longitudinal edges of the top chord plate were presumed to deflect as well as rotate during the loading process. They established an empirical formula to calculate the stiffness of the plate edge vertical support, while Jubb [26] estimated the rotational stiffness.

Mansour and Carol [32], [30] did a similar analysis considering the plate resting on elastic springs along its longitudinal edges for both unreinforced and haunch joints as shown in Figure 2.2. Their results compared best with experimental results of [27], [28], [31] when the vertical spring constant  $\rightarrow \infty$ , with the rotational spring constant  $> 0$ . They concluded that the unreinforced unequal width joints were very weak.

Their theoretical results and El- Zanaty's experimental results [33] indicated that the haunch type connection is an excellent strengthening method. Brady [34] also undertook to study the effect of using different reinforcing devices of unequal width connections under applied moment.

Mouty [35] worked out theoretical formulas for the calculation of the strength of welded joints. His tests were carried out up to the point of plastic failure. Based on certain experimental results, he proposed a simple yield line model. He assumed that the area under the inclusion is infinitely rigid and is subjected to either translation (axial rigidity) or rotation only (rotational rigidity).

Using the upper bound limit theorem, he obtained a failure mechanism for both cases and calculated the ultimate load and moment as a function of the dimensions of the chord and the inclusion for a prescribed yield stress.



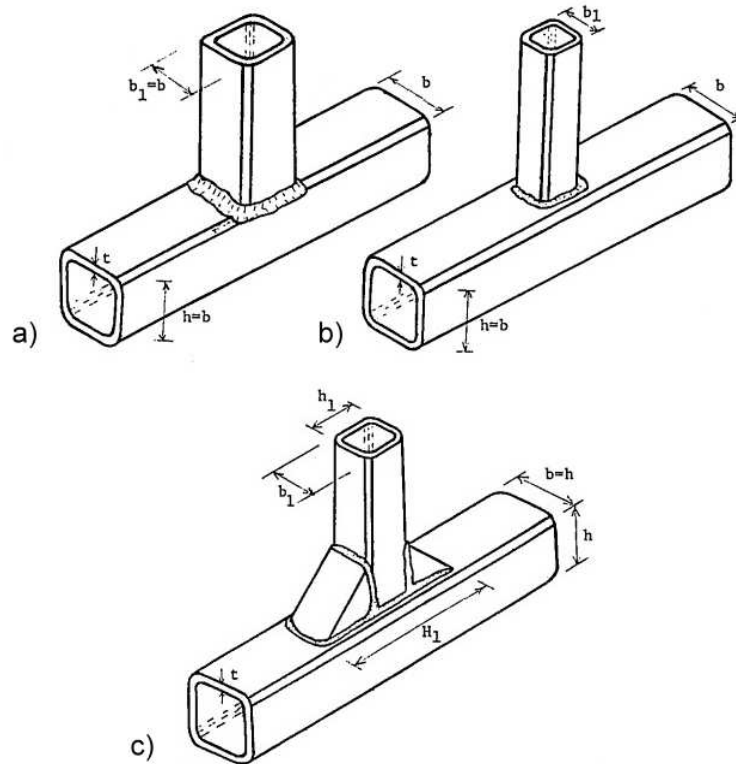


Figure 2.2: Reinforced and unreinforced joints, a) equal width, b) unequal width and hunch connections studied by [30] and [32].

Figure 2.3 shows the geometry adopted in this study, known as "T- Joint", where the horizontal element is the chord, to which the vertical element, the brace, is fully welded. In this work, the brace is submitted to axial compression loading, incremented up to joint failure.

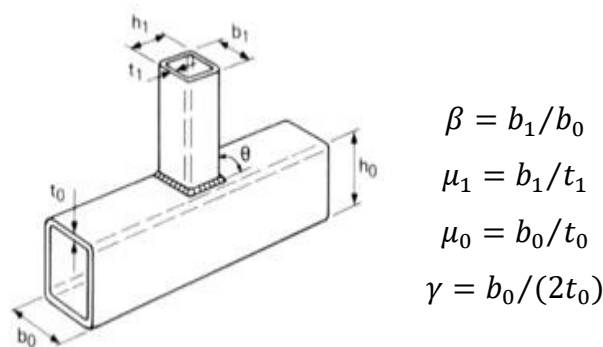


Figure 2.3: Welded T-joint and design equations [36].

Three approaches have been adopted in the past to study joints between hollow section members: experimental, numerical, and analytical. [29] Refers the study of Stewarts and Loyds in 1965 where some tests aiming at studying the resistance of such joints were carried out, and the first consistent study was performed by [26]. However, the big boost in this field occurred only in the eighties of the 20th century, when a large number of studies were registered. [30] Performed a numerical study with shell elements to evaluate the joints resistance; [29] studied the strength of multiple geometries

of connections between rectangular hollow sections; [37], [38] presented significant advances for predicting the plastic load of joints with the aid of yield lines mechanisms.

The geometrical parameters usually used to characterize the joint behaviour are illustrated in Figure 2.3, and dictate the response in terms of resistance and stiffness. [39], [40] obtained force-displacement or moment-rotation curves for a wide range of T-joints and have correlated the variation of those parameters with the joint's main features. They also proposed a deformation limit as a way to estimate the ultimate load of the joints [29], [41] carried out numerical and experimental studies on RHS joints with welded steel plates and concluded that the joint resistance increases as  $\beta$  increases and as  $\mu$  or  $\gamma$  decrease. Similar conclusions were published by [42], [43], [44], [37], [38], [45] that deal with the manufacturing, design and assembly of hollow sections, joints and structures. [46] Performed experimental and numerical studies on this joint geometry with similar conclusions.

[47], [27] experimentally studied the behaviour of joints between I-beams and RHS columns connected by endplates and welded bolts, and evaluated the accuracy of existing methods for predicting their resistance. They also proposed a model to evaluate the joints stiffness accounting for the column loaded face contribution.

In T-joint, the brace or beam transmits axial loading to the chord or column loaded face that is mobilized in bending and shear and is very frequently the critical component for the joint deformability and resistance, as accepted by most authors, e.g., [38], [43], [44], [27]. This is also reflected in design codes/standards, e.g. [36], [48], and justifies a special attention to this component.

The typical force-displacement curve (or moment-rotation curve) of the chord face is illustrated in Figure 2.4, as observed by many authors, namely [47], [28], [49], [50], and may be characterized by three different domains and by three major features: the elastic domain characterized by the initial stiffness,  $S_{j,ini}$ ; a second domain revealing a drop in stiffness as yielding begins and formation of a bending mechanism with a corresponding force  $F_{pl}$  when yielding is generalized; and the third domain reflecting the component behaviour after complete yielding and presenting a positive slope characterized by the membrane stiffness  $S_{j,m}$ . This membrane stiffness is revealed for slender RHS faces (i.e. for a large values of the  $\mu_0$  parameter), as stated by [47].

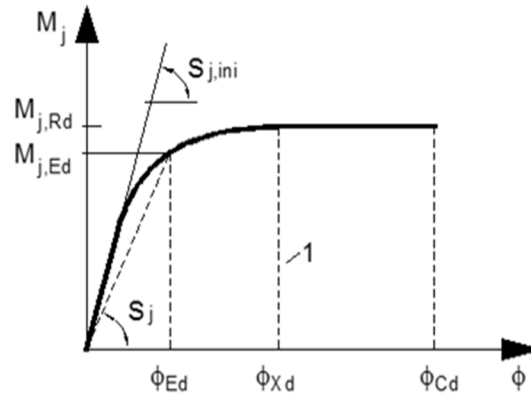


Figure 2.4: Typical force-displacement or moment-rotation curves for the RHS loaded face [36].

### 2.2.1 Resistance of the SHS Loaded Face

As a consequence of the behaviour shown in Figure 2.4, it may be quite hard to identify in a force-displacement curve or in a moment-rotation curve (obtained experimentally or numerically) the failure load  $F_{pl}$  or the failure moment  $M_{pl}$ . In fact, the membrane effect masks the onset of the yielding mechanism, except for thick faces where membrane action is negligible, as stated by [47]. The awareness of this fact made some authors to develop alternative criteria to the plastic analysis or to the identification of a knee in a known force-resistance or moment-rotation curve.

### 2.2.2 Initial Stiffness of the SHS Loaded Face

A quite limited number of authors studied in the past the initial or elastic stiffness ( $S_{j,ini}$ ) when the loaded face of a hollow section is involved. They have concluded that this feature strongly increases with the increase of the chord face thickness  $t_{wc}$ : [30], [37], [47], [49], [50]. It increases also with the increase of the parameter  $\beta$  (related to the loaded area width) and more intensively for larger values of  $\beta$ , but decreasing with increasing bending flexibility at the borders of the plate [51], [47]. As far as the stiffness prediction is concerned, [37], [52] state that this component's elastic stiffness should be evaluated experimentally or by finite element simulations. Other authors established empirical equations to predict the initial stiffness of this component based on experimental or numerical results for specific cases: [30] published abacuses to derive the initial stiffness of a particular RHS joint geometry based on the finite differences method; [53] proposed a similar expression for the initial stiffness of RHS faces with directly welded I-beams based on the results of 72 experimental tests; [54] proposed numerical expressions to derive non-linear moment-rotation curves including the initial and membrane stiffness as a combination of the joint geometrical parameters and [49] proposed an expression to predict the initial stiffness of a particular minor axis joint (where the web behaviour is quite similar to the RHS loaded face) based on experimental tests and numerical simulations results.

A prediction of the initial stiffness as a function of the parameters showed in Figure 2.4 by more general analytical proposals based on physical models adjusted by numerical or experimental results were proposed by [51], [47]. Again, a common feature of all these observations and models is the fact that the elastic stiffness increases for larger values of  $\beta$  and for smaller values of  $\mu$  and  $\gamma$ .

### 2.2.3 Membrane Stiffness of the RHS Loaded Face

The third domain in Figure 2.4 reflects the component behaviour after the formation of a complete yielding mechanism and is characterized by the membrane stiffness  $S_{j;m}$ . This membrane stiffness leads to an over strength of the SHS face but may vanish in some circumstances, such as compression of the member containing the loaded face, or cyclic loading [47]. This justifies the fact that the membrane over strength should not be considered as a strength reserve but as a higher load level that may overstress other components of the joint such as bolts or welds, and should therefore be considered. This effect was observed experimentally and numerically by various authors, such as [55], [29], [56], [39], [47], [28], [50]. The major conclusion from these studies is that membrane effect is more relevant for slender SHS faces (for large  $\mu_0$  parameter) [47].

In the authors knowledge, the only existing analytical models to predict the membrane stiffness (and therefore the over strength of the component chord face) based on the joint geometry and the parameters in Figure 2.3 were proposed by [57], [47].

## 2.3 Eurocode 3 Approach

Eurocode 3, EN 1993-1-8 (2005) presents a design methodology for joints between hollow sections where only the resistance is accounted for. This methodology imposes the analysis of the relevant failure modes in Figure 2.5, and in Table 2-1 the relevant analytical equations to predict the resistance of the joint geometry in Figure 2.3 are indicated.

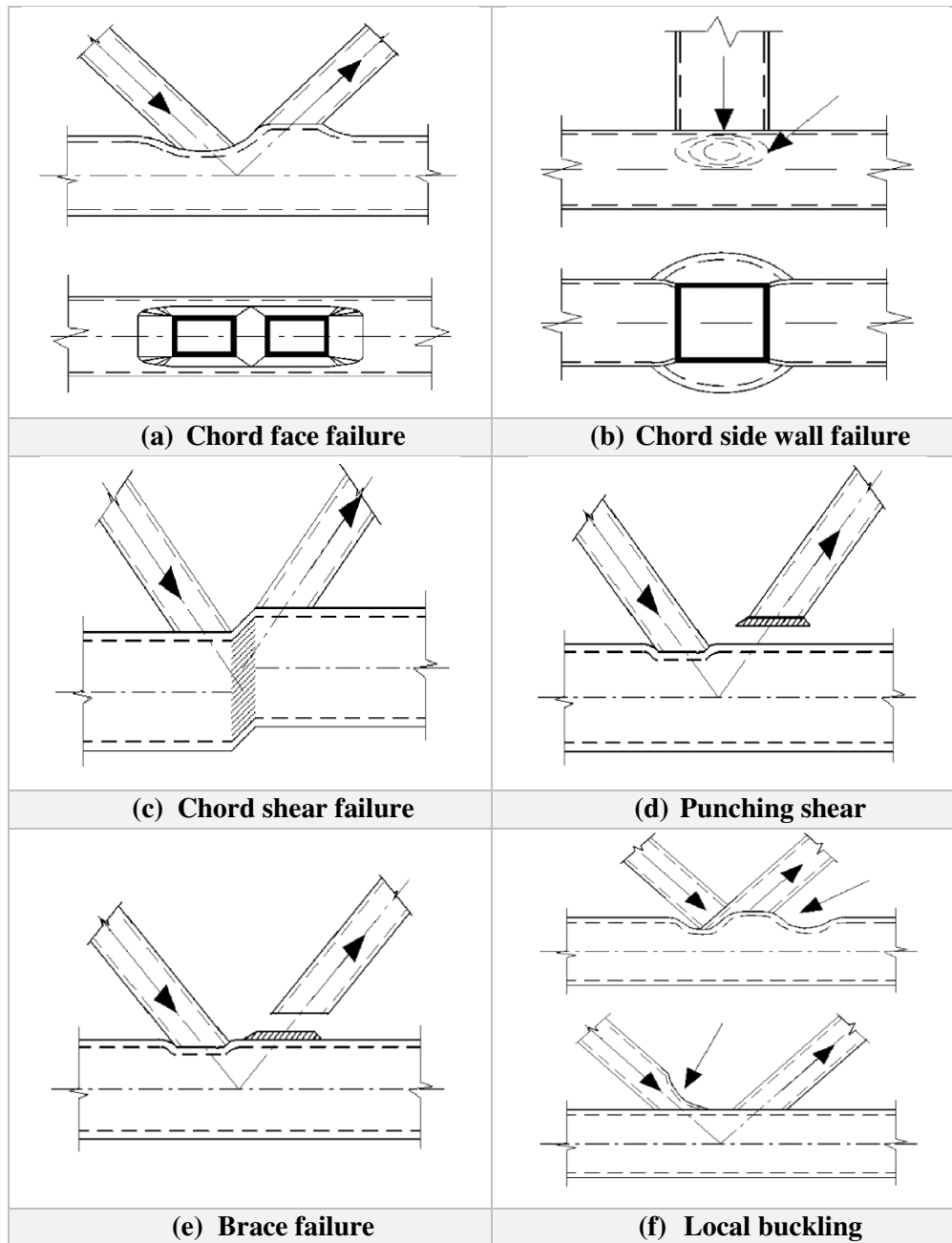
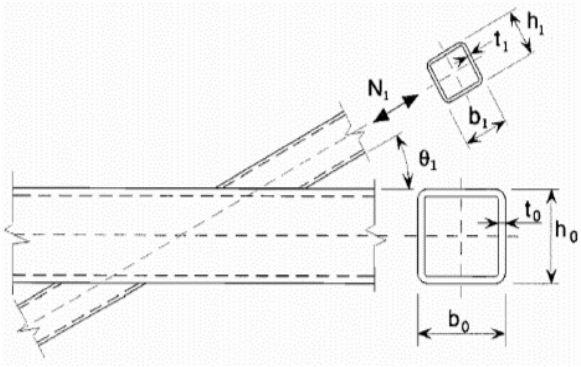


Figure 2.5: Failure modes of hollow section joints T- and K- [36].

Table 2-1: Methodolgy for the strength calculation of T-joints between RHS [36].

Type of joint	Design resistance
	<p>Chord face failure <math>\beta \leq 0.85</math></p> $N_{1,Rd} = \frac{k_n f_{y0} t_0^2}{(1 - \beta) \sin \theta_1} \left( \frac{2\eta}{\sin \theta_1} + 4\sqrt{1 - \beta} \right) / \gamma_{M5}$ <p>Chord side wall buckling <math>\beta = 1.0</math></p> $N_{1,Rd} = \frac{k_n f_b t_0}{\sin \theta_1} \left( \frac{2h_1}{\sin \theta_1} + 10t_0 \right) / \gamma_{M5}$ <p>Brace failure <math>\beta \geq 0.85</math></p> $N_{1,Rd} = f_{yi} t_1 (2h_1 - 4t_1 + 2b_{eff}) / \gamma_{M5}$ <p>Punching shear <math>0.85 \leq \beta \leq (1 - \frac{1}{\gamma})</math></p> $N_{1,Rd} = \frac{f_{y0} t_0}{\sqrt{3} \sin \theta_1} \left( \frac{2h_1}{\sin \theta_1} + 2b_{e,p} \right) / \gamma_{M5}$
For $0.85 \leq \beta \leq 1.0$ use linear interpolation between the values for chord face failure at $\beta \leq 0.85$ and the governing value for the chord side failure at $\beta = 1.0$ (side wall buckling or chord shear).	
<p>For tension: <math>f_b = f_{y0}</math></p> <p>For compression:</p> $f_b = \alpha f_{y0} \text{ (for T and Y joints)}$ $f_b = 0.8 \alpha f_{y0} \sin \theta_1 \text{ (for X joints)}$ <p>Where <math>\alpha</math> is the reduction factor for flexural buckling obtained from EN 1993-1-1 using the relevant buckling curve and a normalized slenderness <math>\bar{\lambda}</math> determined from:</p> $\bar{\lambda} = 3.46 \frac{(\frac{h_0}{t_0} - 2) \sqrt{\frac{1}{\sin \theta_1}}}{\pi \sqrt{\frac{E}{f_{y0}}}}$	$b_{eff} = \frac{10}{b_0/t_0} \frac{f_{y0} t_0}{f_{yi} t_1} b_1 \text{ but } b_{eff} \leq b_1$ $b_{e,p} = \frac{10}{b_0/t_0} b_1 \text{ but } b_{e,p} \leq b_1$ <p>For <math>n &gt; 0</math> (compression):</p> $k_n = 1.3 - \frac{0.4n}{\beta}$ <p>But <math>k_n \leq 1.0</math></p> <p>For <math>n \leq 0</math> (tension):</p> $k_n = 1.0$

## 2.4 Modes of Failure

Welding is the most common joining method in Vierendeel trusses. This joining method leaves a high stress concentration near the weld toe and the failure mostly happens in that area on the hollow section surface [52] and [58]. In the recent years a lot of research work on improving the static strength of axially loaded CHS and SHS T-joints were performed, [59], [60], [61], [62]. However, only few works exist for this type of joint loaded by considering welding and its imperfections. Depending on the loading condition various failures can happen. However, weld and its imperfection has been always an influencing factor on the load bearing capacity and in general the overall behaviour of the joint. In some loading conditions such as in-plane, out-of-plane as well as

axial compressive load on T-joint, the weld failure is presumed not to be critical in design guides [52], [63] and [64]. However, this kind of failure is proven to be critical and more likely to happen as well as chord face failure as illustrated in Figure 2.6 where a T-joint made by square hollow section is loaded by in-plane moment.

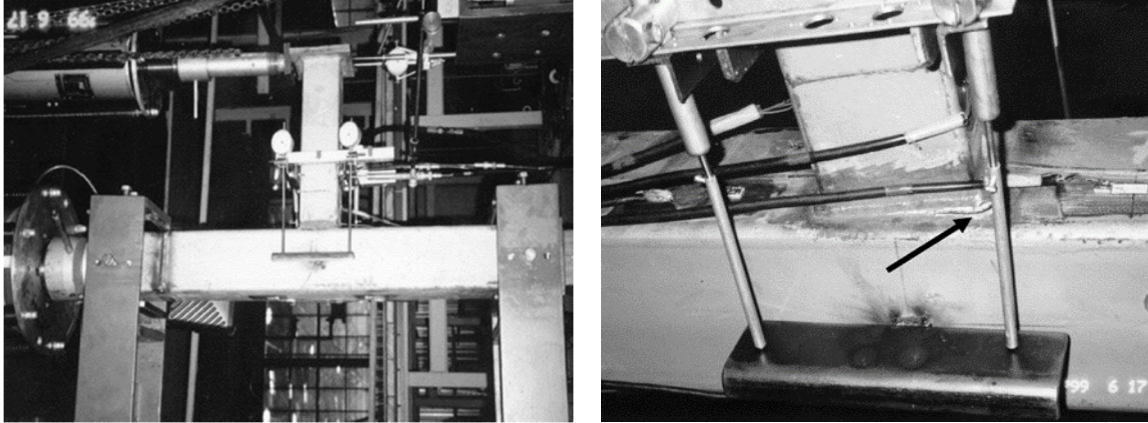


Figure 2.6: Specimen during test (left), joint failure (right) [53].

Another valuable work on a T-joint is done by [52], where the brace member was in tension. The T-joint was made by circular hollow sections. This experimentally and numerically performed work pointed out the importance of weld and its consideration. The failure that the joint experienced is shown in Figure 2.7.



Figure 2.7: Weld failure in Vierendeel truss, T-joint CHS [52].

Same as circular hollow section joints, the ultimate load capacity is based on the maximum load deformation diagram (if the chord deformation is less than  $0.03b_o$ ) or the load at a deformation of  $0.03b_o$  of the chord. Similar to the connections between circular hollow sections to avoid weld failure, the welds should be stronger than the connected members and the throat thickness should satisfy the same requirements. Prequalified full penetration welds can always be considered to be stronger than the connected members. Similar to connections for circular hollow sections, the width to wall thickness ratios  $b/t$  have been limited in the current design recommendations to avoid local

buckling and/or to limit deformations. As a result still the failure modes listed here should be checked for the joint made by square hollow section.

- Brace failure (effective width)
- Chord face
- Chord punching shear
- Chord side wall failure
- Chord shear failure

Due to the fact that square hollow sections can be connected with various orientations and in various combinations, several failure modes have to be considered, which makes the checking procedure more complicated. Figure 2.8 shows the common failure modes for a T-joint compressively loaded.

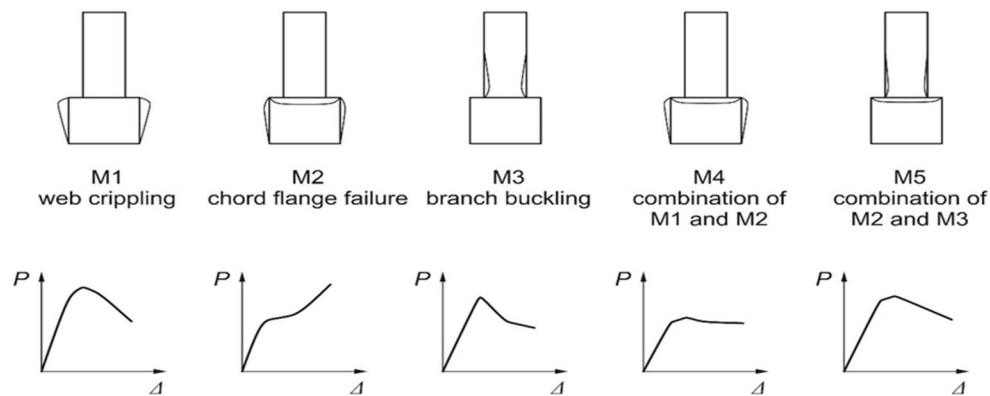


Figure 2.8: Failure modes of T-joint under concentrated force [65].

## 2.5 Analytical Models

The load bearing capacity equations for SHS joints which are given in design recommendations are based on the yield line theory which are based on experimental findings. These equations are only valid for certain failure modes. For square hollow section T-joints the failure can happen in the chord or brace or partly in both.

### 2.5.1 Yield Line Model

The yield line model, originally developed by Johansen [66] for plates, is widely used for joints between square and rectangular hollow sections. For joints with medium  $\beta$  ratios the yield line model gives a good estimate of the chord face plastification capacity [67], [68]. For very small  $\beta$  ratios the deformation to realise the yield line pattern may be too high. For high  $\beta$  ratios the model predicts infinite strengths and other failure modes will be governing, e.g. punching shear or side wall failure. In principle, the yield line method is an upper bound approach; therefore, various yield line patterns have to be examined in order to obtain the lowest capacity. However, the difference in capacity between the various yield line patterns is relatively small. Furthermore, local strain hardening effects and membrane action is ignored. Therefore, the simplified yield line pattern



shown in Figure 2.9 (model a) is generally used for T, Y and X joints instead of the more complicated pattern.

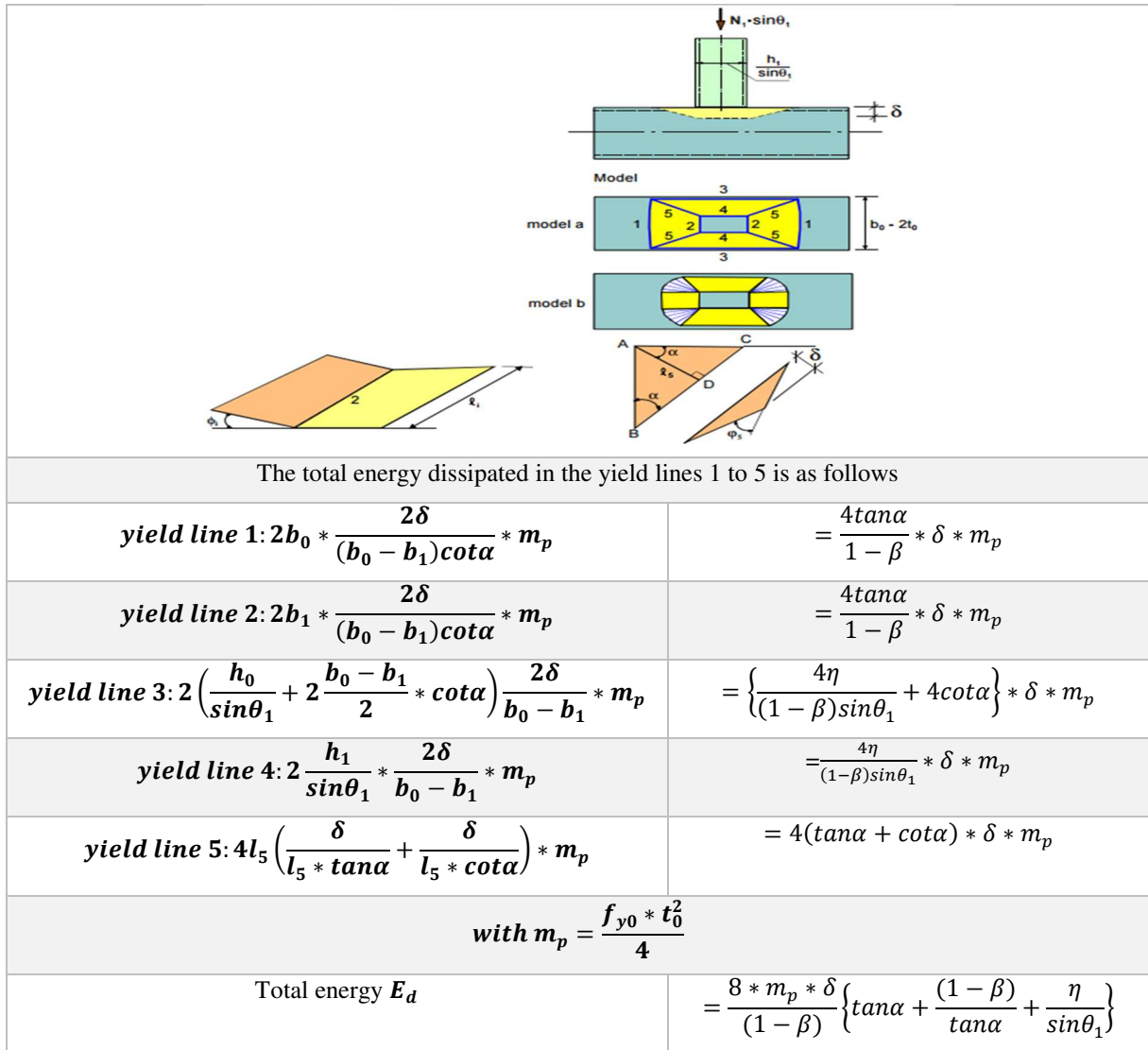


Figure 2.9: Yield line model for a T-joint [68].

The model b was used by Wardenier [69] which is more complicated than model one and shown in Figure 2.10. In this model the secondary angel  $\theta_2$  was taken into account which is not included in the equations mentioned above.

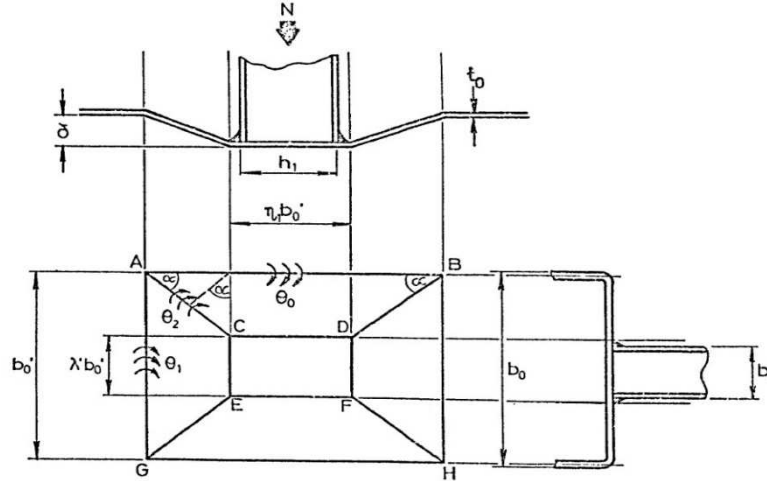


Figure 2.10: Yield line pattern for SHS T-joint [69].

The principle of the yield line method is based on equating the external energy by the external force  $N_1$  over a deflection  $\delta$  and the internal energy by the plastic hinge system with yield lines length  $l_i$  and rotation angles  $\varphi_i$ .

$$N_1 * \sin\theta_1 * \delta = \sum l_i * \varphi_i * m_p \quad (2.1)$$

The energy dissipated in the various yield lines is also indicated in Fig. 9.3. Equating the sum to the external work gives:

$$N_1 * \sin\theta = \frac{2f_{y0} * t_0^2}{1 - \beta} \left( \tan\alpha + \frac{(1 - \beta)}{\tan\alpha} + \frac{\eta}{\sin\theta_1} \right) \quad (2.2)$$

This is a minimum for:

$$\frac{dN_1}{d\alpha} = 0 \text{ or} \quad (2.3)$$

$$\tan\alpha - \sqrt{1 - \beta} \quad (2.4)$$

Substitution of eq. (9.5) in (9.3) gives the capacity:

$$N_1 = \frac{f_{y0} * t_0^2}{(1 - \beta)} \left( \frac{2\eta}{\sin\theta_1} + 4\sqrt{1 - \beta} \right) \frac{1}{\sin\theta_1} \quad (2.5)$$

In this model some simplifications have been incorporated, i.e. the thickness of the sections has been neglected ( $b_0 - 2t_0 \approx b_0$ ). The same applies to the weld sizes, which have not been incorporated. For K-joints, also yield line models can be used. However, the load transfer becomes more complicated since in the gap area the stress situation in the yield hinge is largely influenced by membrane stresses, shear stresses and work hardening. These effects complicate the models in such a way that semi-empirical formulae are used for design.

According to the expected failure modes due to loading three analytical models (brace effective width, punching shear model and chord shear model) have been not been check and kept out of the analysis. The yield line theory could be calculated numerically and experimentally. If the results from non-linear numerical simulation are in a good agreement with experimental analysis and the failure modes are as predicted in EN1993-2005, hence there is no need for checking the equations listed above (see Figure 1.7).

This method could be used for both the brace member and the chord member. Björk and Marquis [70] calculated the ultimate capacity of 15 welded RHS X-joints numerically. Based on their findings this method could deliver good results for the brace member in tension. However, they stated that this method could be also used for the brace member in compression. The equations for the length of the yield lines, as well as force unit length, plastic deformation and plastic work are plotted in Table 2-2.

Table 2-2: Parameters for plastic hinges and plastic work for the general mechanism [70].

#	Number of yield zones	Length of yield zone	Force unit length	Plastic deformation	Plastic work $W_{in,i}$
1	2	$b_0 - t_0$	$\frac{t_0^2}{4} f_y$	$\frac{\delta_p}{x}$	$\frac{t_0^2}{2} f_y \frac{b_0 - t_0}{x} \delta_p$
2	2	$b_0 - t_0 - 2y$	$\frac{t_0^2}{4} f_y$	$\frac{\delta_p}{x}$	$\frac{t_0^2}{2} f_y \frac{b_0 - t_0 - 2y}{x} \delta_p$
3	2	$h_1 + 2a + 2x$	$\frac{t_0^2}{4} f_y$	$\frac{\delta_p}{y}$	$\frac{t_0^2}{2} f_y \frac{h_1 - 2a - 2x}{y} \delta_p$
4	2	$h_1 + 2a$	$\frac{t_0^2}{4} f_y$	$\frac{\delta_p}{y}$	$\frac{t_0^2}{2} f_y \frac{h_1 + 2a}{y} \delta_p$
5	4	$\sqrt{x^2 + y^2}$	$\frac{t_0^2}{4} f_y$	$\sqrt{x^2 + y^2} xy$	$t_0^2 f_y \left[ \frac{x}{y} + \frac{y}{x} \right] \delta_p$

### 2.5.2 Chord Side Wall Bearing or Buckling Model

T, Y and X joints with a high  $\beta$  ratio generally fail by yielding or buckling of the chord side walls, shown in Figure 2.11. The model used is similar to that used for beam to column connections between I-sections [69]. For joints with  $\beta=1.0$  the capacity can be easily determined by:

$$N_1 = 2f_{y0} * t_0 \left( \frac{h_1}{\sin\theta_1} + 5t_0 \right) * \frac{1}{\sin\theta_1} \quad (2.6)$$

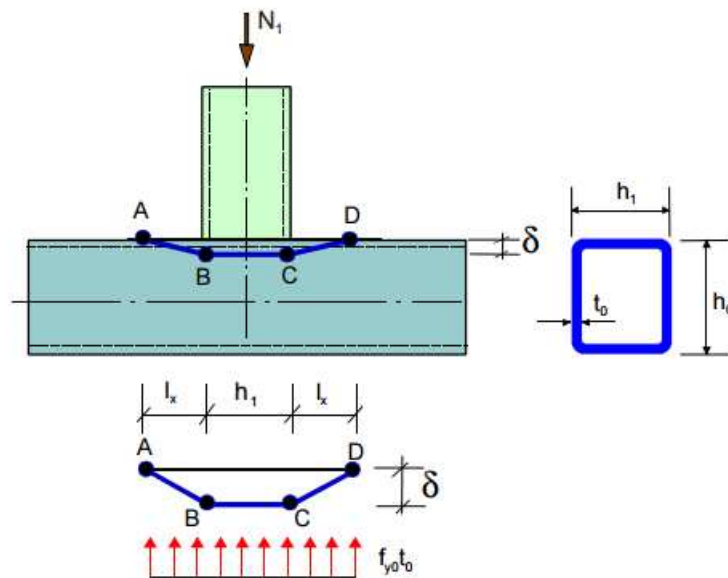


Figure 2.11: Hinge yield line model [69].

## 2.6 Classification of Connections

The joints investigated in this work could be divided into four groups. The joints are unreinforced and unequal width joints. In terms of unequal width member in T-connection, such as the one which is studied here under axial loading, most of the load is transferred from the branch member which is the brace to the face of the chord as they are connected in the same plane by weldment. The value of  $\theta$  is kept as 90 in all joints. In order to study the influence of welding sequencing on the behaviour of the joints, welding has been done in various sequences. From the first sequence which would just involve a single weld, three joints are made for statistical analysis. In total 4 different sequences are compared, which are as follows.

## 2.7 Welding Sequencing

Research on finding optimum welding sequences dates back to the 1940s [8] and 1950s [71] and considerable research has been reported on the reduction of residual stresses due to optimised sequencing. Welding is technique which is done differently in terms of sequencing around the world. In most of cases welders are not really aware of the differences. However, some researchers have tried to point out the differences by performing various welding sequences as mentioned below. Distortion reduction has been studied by [72] who reported welding simulations of ¼ inch thick aluminium sheets. The results are shown in Figure 2.12 and agree well with experiments performed in order to verify the simulations. Apparently, the welding imperfections can be reduced significantly if the welding sequence is chosen appropriately. The reduction achieved by the optimised welding sequence (A) is approximately a factor of two compared to sequence (B).

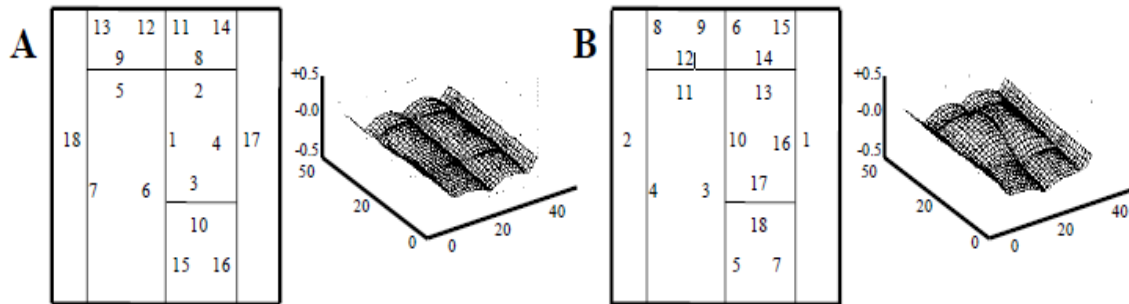


Figure 2.12: Comparison of resulting distortion for two different welding sequences [72].

Not only is the distortion dependent on the welding sequence but also the residual stresses, as shown by [73]. Here, the stresses have been calculated elastically and superposed for all welding passes on multi-pass butt-welded pipe joints. The superposed result is in fair agreement for the real distribution of the residual stresses and has been applied to find a welding sequence to minimise the distortion. This optimised sequence has been found by manual comparison of different sequences; i.e., a trial and error approach.

It is also possible to perform numerical analysis in order to find an optimum welding sequence as shown by [74]. Welding simulation has been performed on a circular weld where only the radial distortion is of concern. The welding sequence has been optimised using a genetic algorithm and is a more or less arbitrary combination of eight subwelds. Using this optimal sequence, welding distortion is reduced by 80 %. For continuous welding; i.e., welding in one run without stopping, the radial displacement is significantly higher compared to the optimum welding sequence. However, there is still homogeneous radial shrinkage which cannot be avoided. Unfortunately, no explanation is given concerning why the optimum sequence yields better results.

The influence of welding sequence for GMA welding of butt-welds and the effects on residual stresses has been investigated by [75]. The dimensions of the plate and the three welding sequences employed are shown in Figure 2.13. The thickness of the plate is 5 mm, the material is SAE 1020. Figure 2.14 shows the resulting longitudinal residual stresses. Symmetric welding caused the lowest residual stresses while back-step and progressive welding show the same results. However, the stresses oscillate in the direction of the weld seam due the welding sequence.

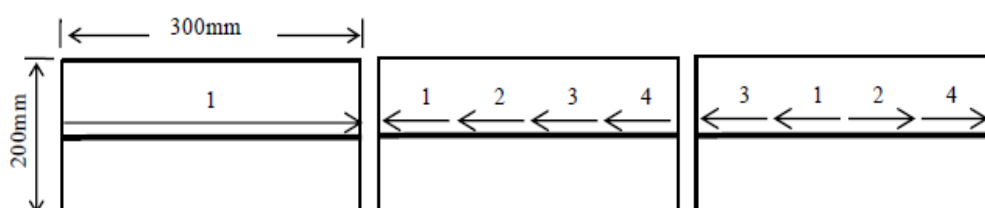


Figure 2.13: Welding sequences for thin-wall butt-welds employed in [75], from left to right: progressive welding, back-step welding, symmetric welding.

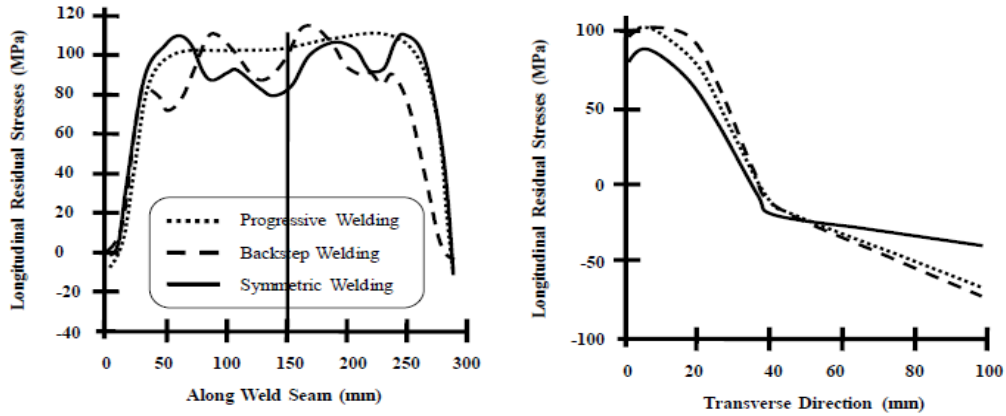


Figure 2.14: Calculated longitudinal stresses for the welding sequences shown in Figure 2.13. In seam direction (left) and transverse to the weld seam (right) in the centre of the weld (Y=150mm), [75].

Similar studies have been performed by [76] for 5 mm thick bead-on-plate welds. However, in this study, two parallel welding torches were used to weld the sample. The dimensions of the plate and the welding sequences employed are shown in Figure 2.15. Figure 2.16 shows the predicted longitudinal and transverse stresses. The welding process from centre to end yields the lowest residual stresses. This result is similar to the results found by [75]. Unfortunately, in neither publication are validations given, or a model described to explain the mechanism leading to lower residual stresses.

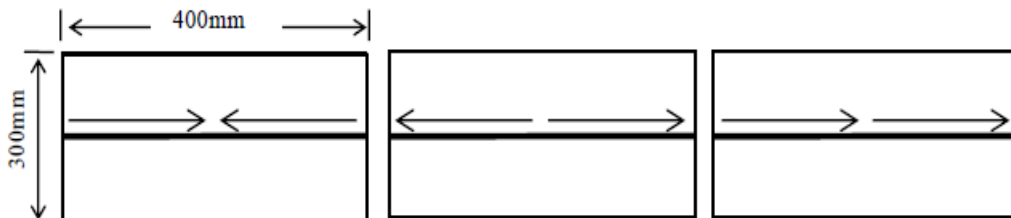


Figure 2.15: Welding sequences for based-on-plates employed in [77]. From left to right: end-centre, centre-end and end-centre-centre-end.

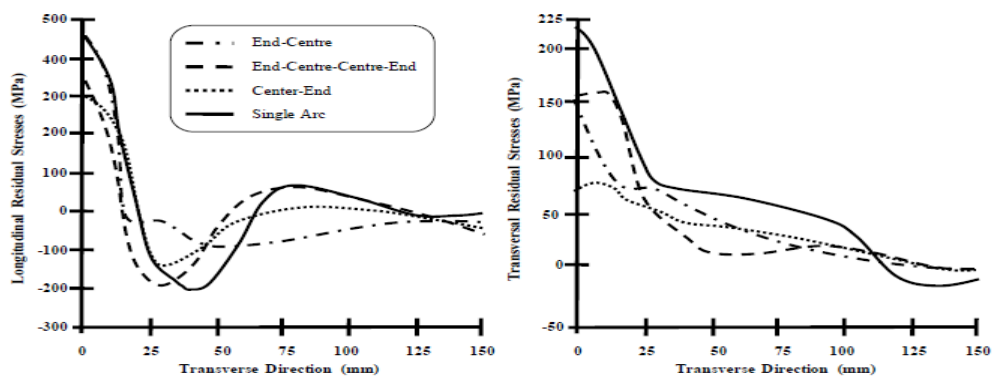


Figure 2.16: Calculated longitudinal (left) and transversal (right) stresses at the weld centre line for the welding sequences shown in Figure 2.15 [77].

Zhang [78] reported numerical simulations of GMA welded T-Joints. It has been concluded that the welding sequence can reduce the amount of bending distortion by approximately 25 %. However, neither the material model is explained, nor is it clear how the welding sequences are employed. Schenk [79] reported a reduction of 37 % of the welding distortion of an electron beam welded (circular) gear wheel using multiple beams in parallel. Lin [80] employed different welding sequences for the packaging of butterfly laser diodes. The welding distortion was reduced by a factor of five using the optimum sequence.

Optimised welding sequences are not only applied in order to minimise distortion and residual stress, but also to minimise the total time required to weld a component. Neural network algorithms, which like genetic algorithms are also a stochastic optimisation method, have been presented by [81], [82], and [83] for minimizations of the welding time by optimisation of robot movement. A genetic algorithm has been presented by [84] in order to find a distortion and cycle time minimising welding and clamping sequence for resistance spot welding of an automotive vehicle body assembly.

Influence of various welding sequence on residual stress and distortion was studied by [85]. In this study the numerical models were successfully validated by experimental tests. The results shows the welding sequences have significant effects on the residual stresses and distortions, both in magnitude and distribution mode. As a recommendation of this study, the optimization of welding sequences should be investigated numerically or experimentally before the construction welded structure. Figure 2.17 shows the welding sequences adopted in this study.

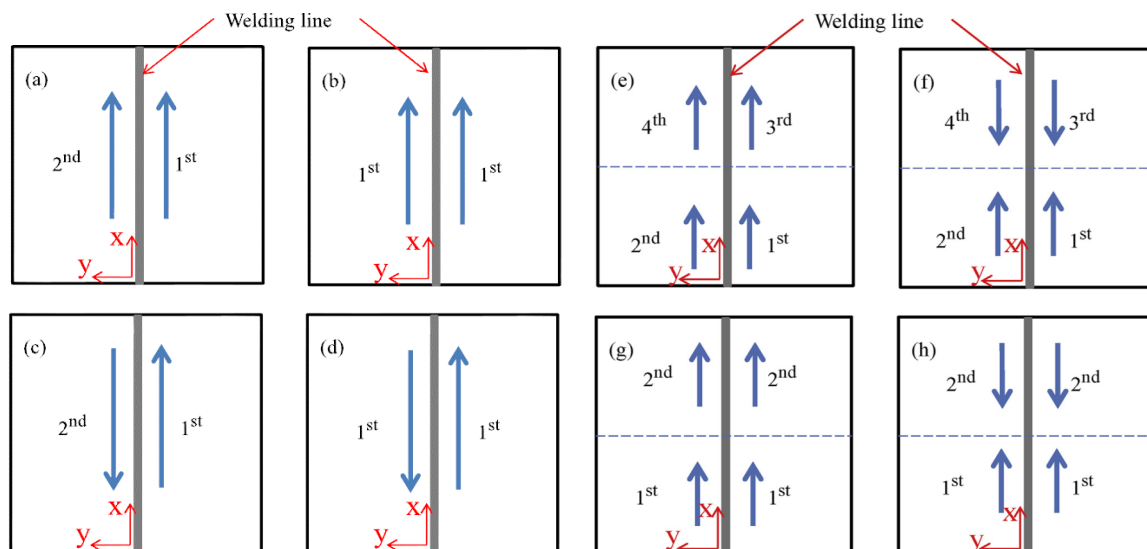


Figure 2.17: Welding sequences for progressive welding (left), welding sequences for block welding (right).

According to the outcome of this study, the welding deposition sequence significantly influences the magnitude and deformation mode of the deflections shown in Figure 2.18. The magnitude of the deflection in the double-side welds is smaller than that in the single side welds both in

progressive and block welds. The single-side weld sequence causes more distortion than double-side weld sequence in the T-joint weld.

Welding along the same direction of the previous weld will induce the maximum vertical deflection in both single- and double-side welding procedures. The double-side welding procedure which induces minimum vertical distortion and relatively smaller residual stress is recommended for the practise. Moreover, the progressive welding must be considered firstly in order to avoid the stress concentration at the weld start/end location. In case the block welding cannot be avoided, the second step welding along the opposite direction is recommended. The residual stress distribution near the weld start/end in block weld in the middle of the plate are influenced by the welding sequence, especially for the transverse residual stress. The stress is concentrated near the weld start/end locations. In other regions the welding deposition sequence has no significant influence on the welding induced residual stresses. Vertical deflection and stress distribution under different welding sequences are respectively shown in Figure 2.18 and Figure 2.19.



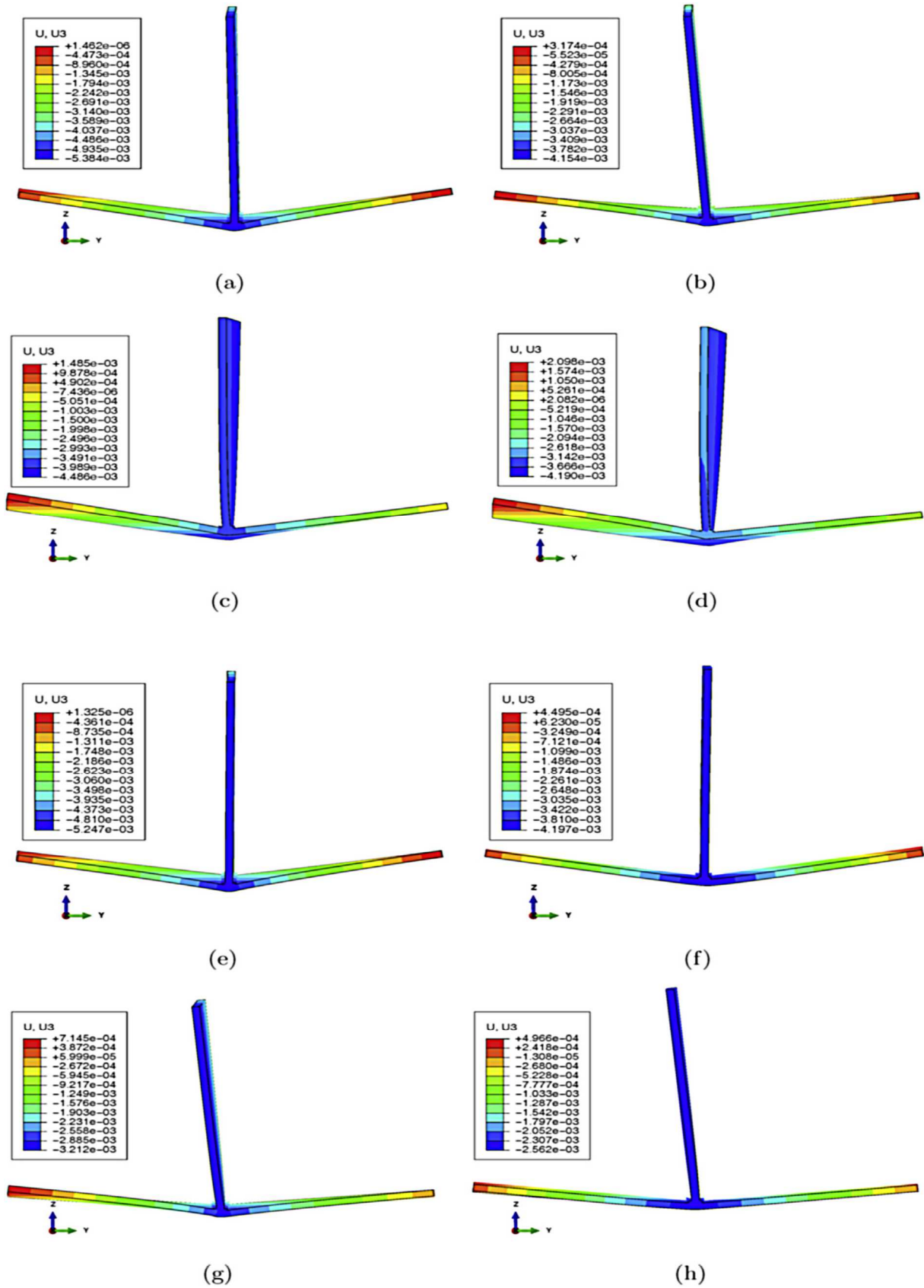


Figure 2.18: Vertical deflection (m) under different welding sequences [85].

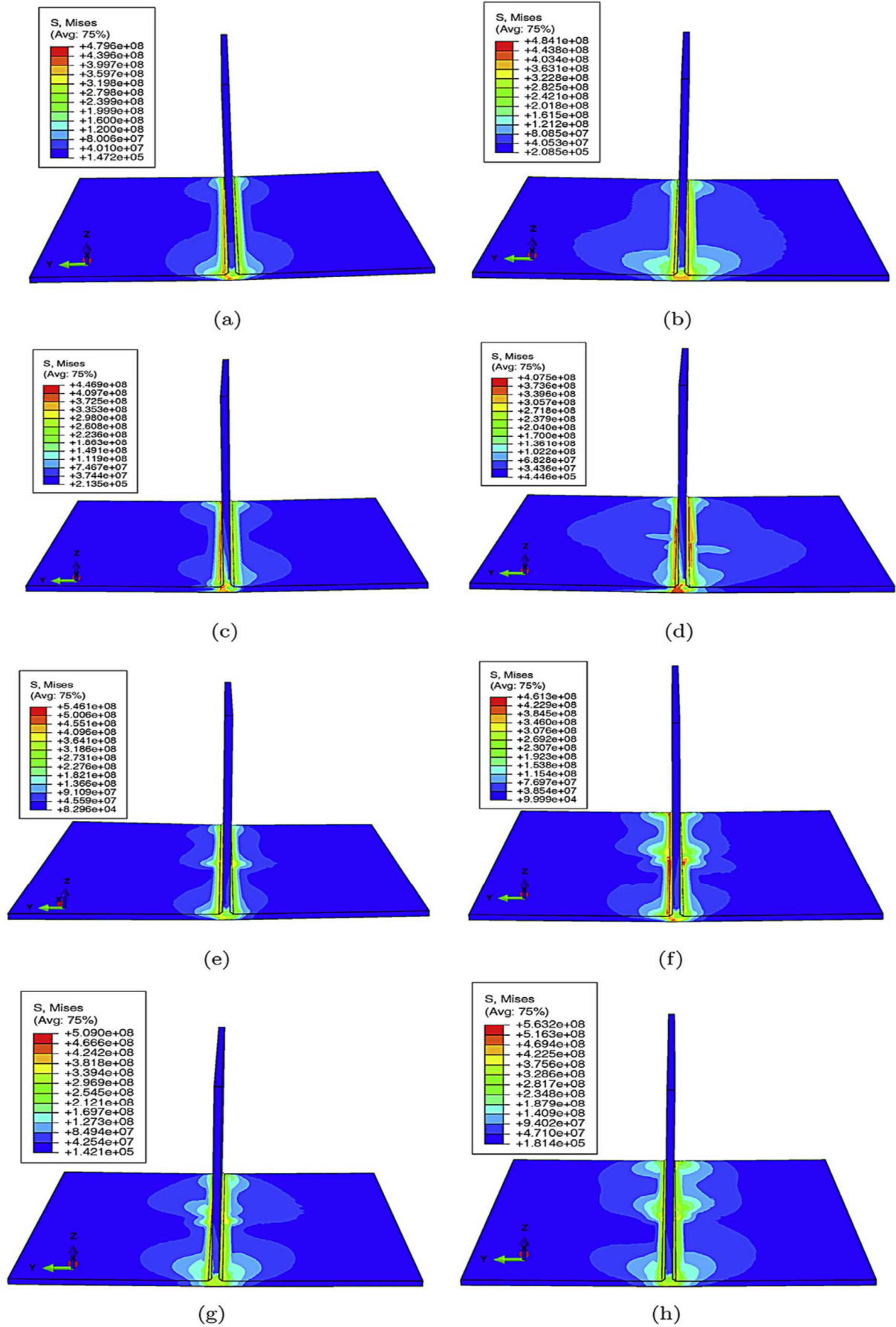


Figure 2.19: Mises stress distribution (Pa) under different welding sequences [85].

In another study by [86] a three-dimensional finite element approach based on ABAQUS code was developed to investigate the effect of welding sequence on welding residual stress distribution in a thin-walled aluminium alloy structure. Figure 2.20 shows the geometry, mesh and the welding sequences adopted.

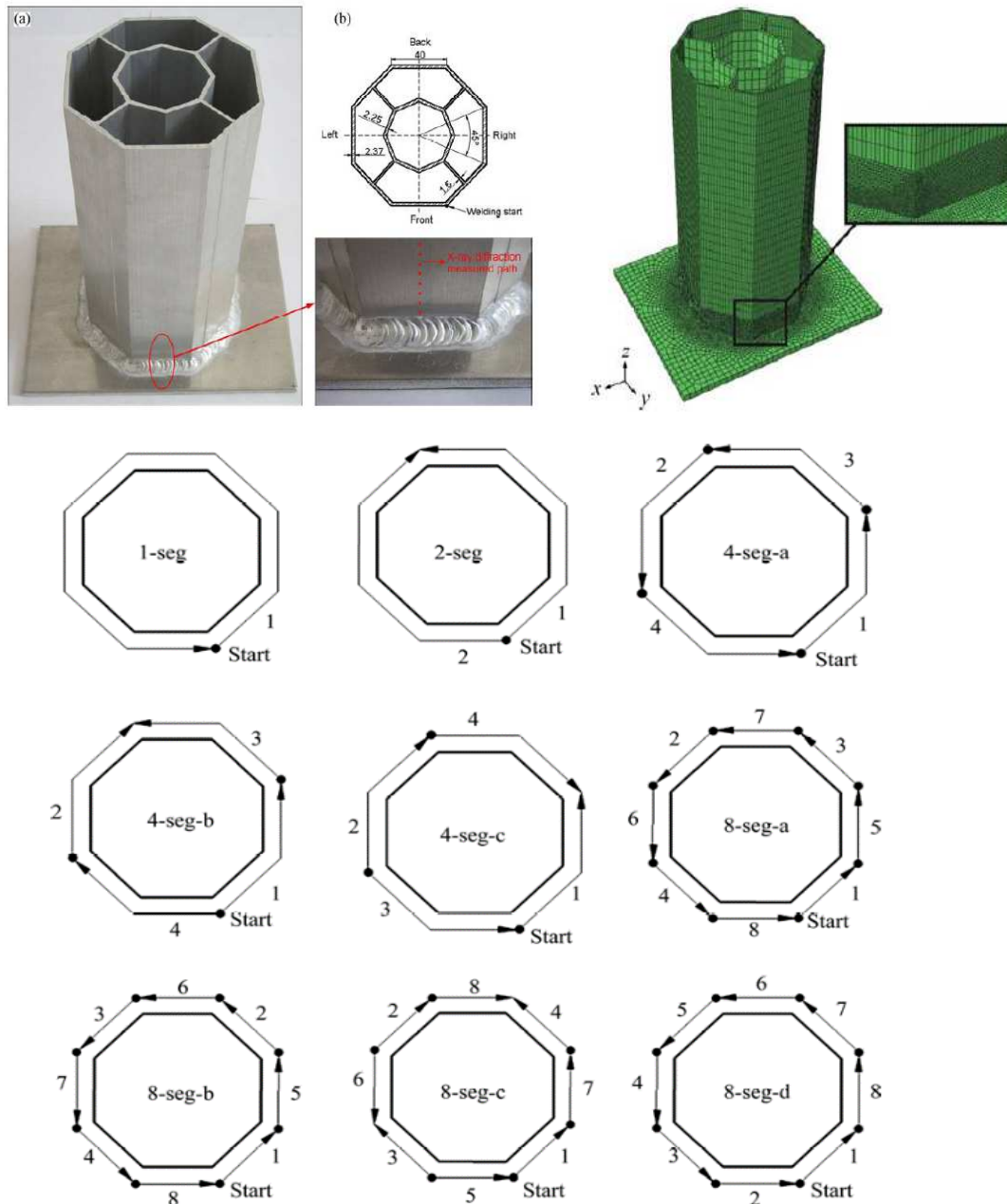


Figure 2.20: Geometry, finite element mesh and welding sequences [86].

According to the outcome of this study the distribution of residual stresses is affected by welding sequence and reasonable welding sequences can effectively reduce the residual stresses. As recommended by the author, back-step welding is the optimal welding sequence and symmetric welding is also an available welding sequence. Figure 2.21 and Figure 2.22 shows how residual stresses are distributed in each welding sequence.

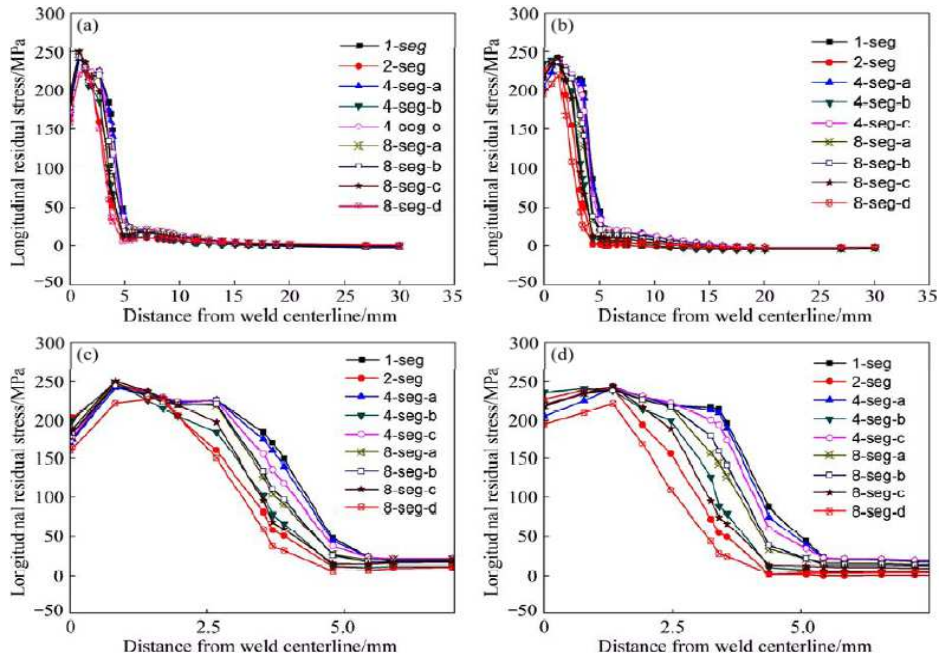


Figure 2.21: Comparison of longitudinal residual stresses of nine sequences [86].

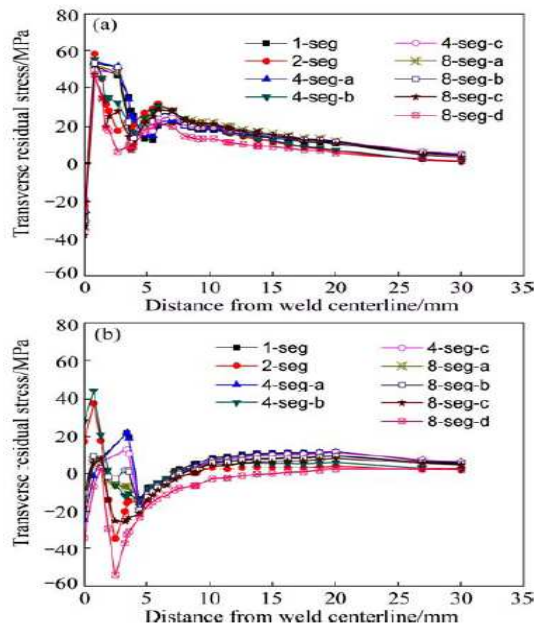


Figure 2.22: Comparison of transverse stresses of nine sequences [86].

Here some of the most common welding sequences adopted in some experimental and numerical investigation are plotted and shortly explained.

### 2.7.1 Progressive Welding

This is the most typical weld used widely around the world. Depending on the joint this weld can be done by hand or automatic machines so called robots. In most of cases, this welding technique leads to high heat input, large thermal expansion and weld pool which results in great stresses and

distortions while cooling. There are valuable works in which it is stated that progressive welding leads to the highest magnitude of stresses [1], [19], [75]. This welding technique can be done in various phases such as two phases and three phases progressive welding.

### 2.7.2 Back-step Welding

In back-step welding technique the welding pass is divided into several parts depending on the length and geometry for instance Figure 2.23. The welding direction is kept the same. However the start point and end points would differ by giving enough time to the end points to cool down. Thus, the next welding portion does not begin at the end of the previous section. Thereby, a cooling of the individual segments allows and reduces the heating of the weld bead. In this way, the weld is not heated too much, whereby the shrinkage is kept small and low-pressure and tensile stresses form which change at short distances. This method is mainly used in shipbuilding, in the joining of workpieces with small thicknesses, are used [72] and [87].

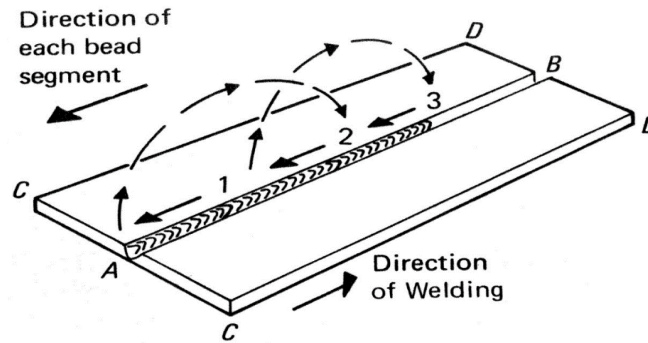


Figure 2.23: A sample of skip welding [88].

### 2.7.3 Skip Welding

This welding technique in some cases so called jump welding differs from the back step welding. Here a welding portion is skipped and welded only after completing the following section as shown in Figure 2.24. In this way, each section has more time to cool down depending on the length of each weld. In this welding technique the heat input is interrupted several time depending on the number of welds. Thus strains and stresses are reduced.

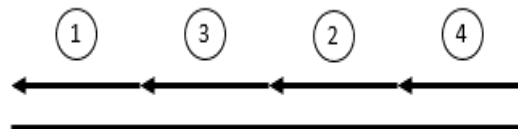


Figure 2.24: A sample of skip welding adopted by [87].

Day by day the influence of welding and its imperfections is becoming more like a concern on which so much money is being investigated. For instance in Germany, and the Brandenburg University of Technology Cottbus-Senftenberg and all the Projects being funded by various

institutes and being deeply investigated numerically and experimentally at the Department of Civil Engineering and Urban Planning. In the welded structures, the stability of the structures can't be discussed without taking into account the welding imperfections. As mentioned earlier in this chapter, so much attention has been paid to the stiffness and the ultimate load that a joint made by SHS could stand, also some influencing parameters have been found. How much and in which extent each parameter could have an influence on the strength of a joint can differ also differ depending on some other parameters such as the material, boundary conditions, loading conditions as well as welding process. The investigation area can even get more complicated by taking into account the variables of the welding process and also various possible welding sequencing schemes. In this work it has been tried to develop the ideas and works of [79], [80], [81], [82], [83] and fill the gap by taking into account, the influence of various welding sequencing schemes on the load bearing capacity. So many numerical and experimental investigations have been done with a focus on the welding imperfections by keeping geometry, material, welding process and loading direction and magnitude as constant. This work will help understanding how important it is to investigate residual stresses and deformation induced by welding when the joint or the structure is being considered as in practise. The idea have been developed more in the numerical investigations and the joints have been studied in terms of residual stresses and deformation in two different phases, before and after the loading process with focus on finding, if an increase in the number of welds could be critical for the joint and the structure.



# 3 NUMERICAL MODELLING OF WELDING

## 3.1 Background

The origin of welding can be sought as long ago as the Bronze Age when pressure welding was used to make small items. Such items are estimated more 2000 years old. In the middle Ages people made so many tools and other things of iron by forging or welding by hammering. 200 years ago in 1800, Sir Humphry Davy managed to produce an arc between two carbon electrodes using a battery. This became a practical process in the mid-nineteenth century and by the end of the century gas welding and cutting, metal arc welding and resistance welding were developed and became common used joining processes, [89].

Since then welding has become one of the most important industrial processes if not the most important. It is often said that over 50% of the gross national product of the U.S.A. is related to welding in one way or another. This is also governed in countries such as Germany, China, India and etc., [89]. Nowadays, nearly all products in everyday life are welded or made by equipment that is welded. Despite the significance of welding and the fact that it is the most important way of joining pieces of metal in order to make them act as a single piece, computer simulations of welding processes are rather limited compared to other industrial processes. This problem is not shocking as welding involves more sciences and variable parameters than those involved in most of the industrial processes.

Here the author tries to clarify various issues in numerical modelling of welding. starting from the a general overview of numerical welding simulation, the history, influencing parameters, welding of T-nodes, welding imperfections, the coupling effects and geometrical aspects which need to be considered.

## 3.2 Numerical Modelling of a Technological Problem

Numerical modelling is the best way to solve technical issues, otherwise it is impossible. Numerical modelling gives the possibility to the users to see what is happening in reality with taking into account some assumptions. Also, competence about the quantities such as temperatures, microstructures and stresses developing during the process can be obtained.

Generally the definition above does not mean that experiments are pointless. Actually experiments provide engineers with some important parameters such as material properties and various

behaviours from the pieces to be tested. That is so important for validation of the model and approaching the realistic process description. Experiments help engineering by providing them with appropriate input for the numerical models. The experiments are important, in order to be used for the verification and validation of the numerical modelling which would lead to solve the technical problems. When first the numerical model has been validated, it is often generalised to more or less similar technical and geometrical problems and can be used for optimisation of designs [90].

Whether the user design for usability or optimisation, the work requires the sequence of steps which is plotted in the Figure 3.1, from technological problem to the solution. The analytical solution is normally an exact solution of a simple model whereas the numerical solution always is an approximation of a more complex model. In all cases the solution has to be interpreted in relation to the physical problem, an essential part of the mathematical modelling task with risk for misinterpretation leading to wrong conclusions of otherwise correct mathematical results. Since all the steps in the solution sequence to degree imply assumptions, the technological solution will be an approximation of the original problem no matter the solution model [91].

Actually, the sequence of steps in the solution of a technological problem is an approximation of the original problem no matter the solution method, is important to stand in mind when assumptions are made for conditions the numerical model is built on upon and hence the results depend on.

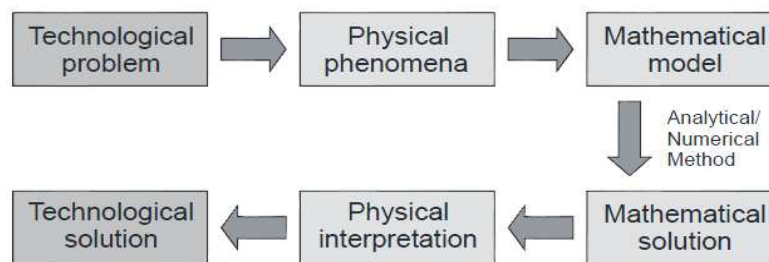


Figure 3.1: The sequence of steps in the solution of a technological problem [91].

### 3.3 Numerical Modelling of Welding in a Historical Perspective

The analytic theory of heat transfer under conditions applicable to welding was established in 1930s by [92]. During the 1940s and 1950s, the theory was extended and refined. Probably among the most referenced from this time are [93]. Also for the heat conduction in general [94]. A great and the first presentation on the thermal stresses theory by taking into account the non-linear phenomena is given in the valuable work of [95]. Before the mid-1980s, limited computing power forced the numerical analysis to two-dimensional models though most welding situations result in fully three-dimensional states of stresses and deformations.

About 20 years was what the phrase “the nearest future” in the remark by [96], “For economic reasons, plane models seem to be necessary at least for the nearest future” had to cover before fairly



complex three-dimensional models could be analysed within reasonably computing time. The first three-dimensional transient heat transfer analyses were published in the mid-1980s. A few years later, the coupling to thermal stress analyses on quite simple models were feasible from a computer hardware point of view.

One of the quantitative goals for computational weld mechanics that was stated at this time was, that by means of numerical modelling of welding it must be possible to analyse three-dimensional temperatures, microstructures, displacements, stresses, strain and defects all together 100 or more times faster than actual welding time [97]. That required an increase in analysis speed of 100.000 times from then 0.1 mm welding per CPU minute for three-dimensional thermal stress analyses with low cost computers<sup>1</sup>. It was stated that considerable gain immediately could be provided by moving to state of the art workstations with multiple concurrent processing. The rest of the speed-up, approximately a factor of 100, was expected to come from algorithm developments. This goal was believed to be achieved within a couple of years and furthermore to be “quite mature within five years” [97]. That the developments did not exactly go that fast is no secret. In the next five years from 1988 or so, judging from the majority of the literature published, much attention was given the coupling effects, microstructure formation and temperature distribution in the melt pool. The detailed three-dimensional geometrical modelling of these local welding aspects was now possible from a computational point of view compared to thermal stress analysis of the complete structure being welded. As addressed in [98], “There are many reasons why thermal stress analysis of welds is a much more challenging problem than thermal-microstructure analysis”.

Among the reasons is the fact that thermal stresses generated by the welding process travel over the complete structure while the thermal-microstructure analysis only involve material a short distance from the weld path and therefore a smaller geometrical model need only be analysed. This is the result of the fact that the thermal field is governed by parabolic partial differential equations whereas the mechanical field is governed by elliptic partial differential equations. To this comes that the mesh used for thermal-stress analysis must be finer than the mesh used for the thermal analysis and even this relation gives no serious difficulties for the thermal solver with large temperature increments whereas temperature increments that generates stresses larger than the yield strength make it difficult to do an accurate thermal-stress analysis.

In the mid-1990s, an increasing number of work has been published considering calculations of welding induced transient and residual stresses. Mostly standard joints as e.g. butt welds, pipe girth

---

<sup>1</sup> For the perspective it should be noted that in 1987 IBM introduced its PS/2 machines, which made the 3½-inch floppy disk drive and video graphics array (VGA) standard for IBM computers. It was the first IBMs to include Intel's 80386 chip and the year when IBM released a new operating system, OS/2, which allowed the use of a mouse with IBMs for the first time. In 1989 Intel released the 80486 microprocessor with an optimised instruction set and an enhanced bus interface doubling the performance of the 386 without increasing the clock rate [97].

welds, T-joints etc. has been analysed and only rarely with multi-pass welds or several passes in each weld. Adaptive meshing techniques have been used in some cases also in combination with solid-to-shell solutions in order to reduce the problem, still very dedicated for the purpose and far from the desired general tool for the engineer. In this context it should be noted that considerable commercial efforts have been put into making software packages for numerical simulation of general welding applications, probably the most comprehensive being the French product SYSWELD<sup>2</sup>.

### 3.4 The Coupled Problem

The objectives of computational weld mechanics are various, e.g. strength of weld, defects, fatigue and corrosion properties or the purpose can be development of welding processes or procedures. Numerical modelling of welding involves in the general case solution of the governing equations for heat flow, fluid dynamics, microstructures, deformations and diffusion of chemical elements. To this come special considerations as e.g. electromagnetism, plasma physics, droplet dynamics (generation/formation and transfer), etc. All these phenomena are strongly coupled though not equally important or relevant at all for all welding processes. Depending on the point of view, the evolution of certain variables such as temperature, microstructure, displacement, strain and stress are in focus.

Many authors have discussed and presented figures illustrating the different interactions and coupling effects one has to consider in relation to welding, among these authors are e.g. [99], [100], [101], [102]. The handling of specific fundamental phenomena in modelling of welds is addressed in [103]. Mainly based on these references, some of the interactions and coupling effects are described and methodically shown in Figure 3.2.

---

<sup>2</sup> Since the purpose of this project has been to gain experience and knowledge of different modelling approaches, material models etc. a general-purpose tool as ABAQUS has been used beside SYSWELD.

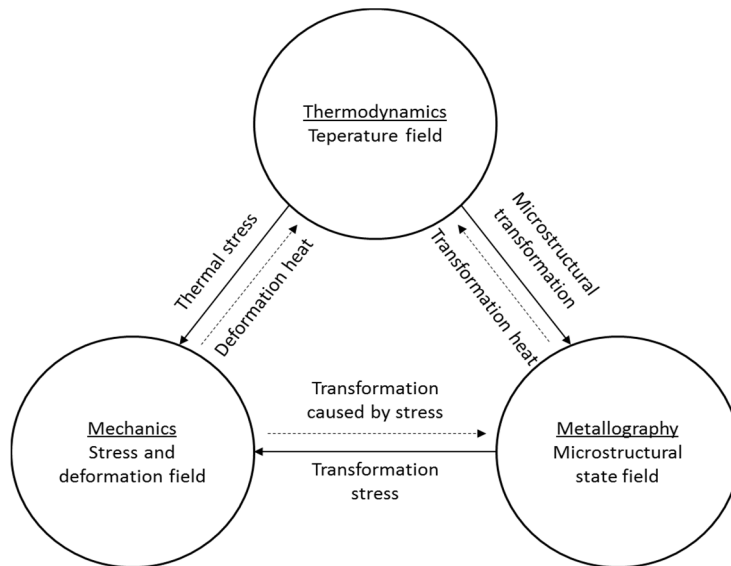


Figure 3.2 The major interactions, decoupling and mutual influencing of temperature field, stress, deformation and microstructural field after [100].

Volumetric strains due to thermal expansion and phase transformations, so-called thermal dilatation, are a dominant load in the stress analysis. To this comes that transformation plasticity particular in high strength steels has a major effect in reducing the residual stress level in welds, [100]. As the temperature changes from above the melting point to room temperature, stress-strain relationship changes from viscous over elasto-viscoplastic to rate independent elasto-plasticity. The resulting microstructure evolution influences the constitutive equations. Grain size, microstructure composition and phase changes influence the mechanical properties, discussed by [104], as well as the thermal properties and can be accounted for by incorporating mixture rules for the material properties in the model. The deformation of the structure changes the thermal boundary conditions and influences the microstructure evolution. Beyond this, the deformations are generally accompanied by a flow of heat due to variations of strain. This latter coupling, for example, is usually negligible but must be accounted for in cases where the thermos-elastic dissipation is of primary interest, [95]. In friction stir welding the coupling must necessarily be included, but in traditional welding processes it can be omitted. As a consequence of the various coupling effects and the earlier mentioned three-dimensional and transient nature of the welding process, a great deal of assumptions have to be made if reasonable computation times have to be achieved. Especially in connection with an industrial use of the method, the objective of keeping the CPU time as low as possible is desirable to have in mind when the model is developed. As with all modelling no matter the context, it is important to do only an adequate modelling of the process compared to the purpose of the analysis.

### 3.5 Residual Stresses

Residual stresses can be defined as internal forces which are in equilibrium with themselves. These stresses exist without an application of any intended or unintended loads<sup>3</sup>. These stresses are introduced to the pieces in the production and assembling processes, for instance welding, cutting, rolling, machining etc. there are several ways for reducing the amount of stress existing in the piece such as heat treatment. In some cases the stresses could be totally vanished by heat treatment or can be also changed from tensile to compressive stresses on the surface.

First kind ( $\sigma^I$ ), or macroscopic, residual stresses extend over macroscopic regions spanning several grains of material. These are the residual stresses that are of particular interest for engineering applications. Their origin and distribution is described using continuum mechanics. Second kind ( $\sigma^{II}$ ), or microscopic residual stresses act between the grains of the metallic structure (sizes between 1.0mm to 0.01mm). Figure 3.3 shows the discipline of first and second kind of stresses. The third kind of residual stresses ( $\sigma^{III}$ ) act between atomic regions in an individual grain in the sizes between 10.2 nm to 10.6 nm. An example of the latter kind is the residual stresses formed around a single dislocation in the crystalline structure. Figure 3.4 illustrates the three various types of residual stresses [100].

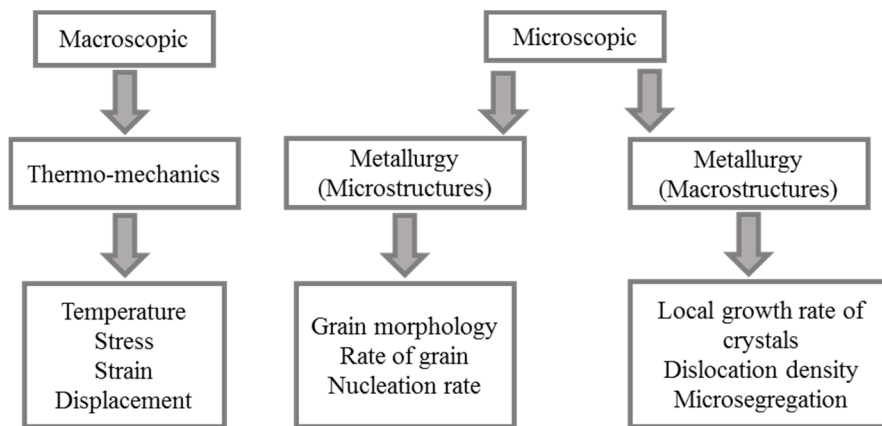


Figure 3.3: Stress level, discipline, dependent effects and variables.

\*\*\* Macroscopic residual stresses are those described by thermos-mechanics i.e. temperature, strain/Stress and displacement relations down to around 1mm. Microscopic stresses can be divided in two arising from metallurgical concerns.

<sup>3</sup> Residual stresses in this sense are also termed constraint stresses. Residual stresses as a result of external self-equilibrating support forces are termed reaction stresses and may superimpose the constraint stresses to give the total residual stresses. Finally, the stress state is determined by superimposing the total residual stresses to the external load stresses.

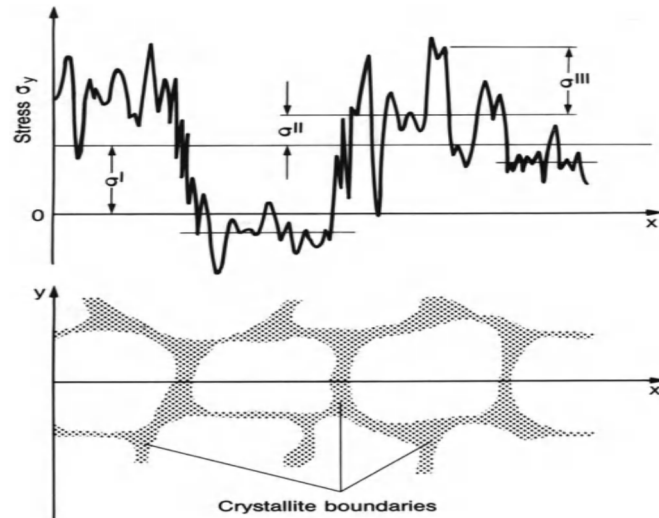


Figure 3.4: First, second and third order residual stresses ( $\sigma^I$ ,  $\sigma^{II}$ ,  $\sigma^{III}$ ) in crystallite, structure, acting in  $y$ -direction, plotted over coordinate  $x$ ,  $\sigma^{II}$  recorded as crystallite mean value; after [100].

### 3.5.1 Description of Welding Residual Stresses

Residual stresses induced by welding could be defined as follow; these stresses are developed due to non-uniform thermal expansion which is also due to locally heating the structure. The material yield stress is highly temperature dependent which means the stress value at any point in the metal is related to the local temperature. However, the stress magnitude could not exceed the initial yield stress, so the thermal expansion causes non-uniform plastic deformations in the structure where the actual yield strength is exceeded. During the welding process the metal pieces to be welded undergo a sharp heat compare to the surrounding area as plotted in Figure 3.5. As a consequence of application of heat the material expands which is restrained by the surrounding colder area which led to a rise in the thermal stresses. The thermal stresses exceed the yield limit which is lowered at elevated temperatures. On the other hand, in the weld area after cooling down tensile residual stresses grow and the surrounding area contains compressive residual stresses. Increase in the volume of the material is caused by phase transformation for instance ( $\gamma\alpha$ ). If this happens the pattern of residual stresses would change, compressive stresses would grow in the weld area and tensile stresses in the surrounding area. Figure 3.6 illustrates various zones affected by heat.

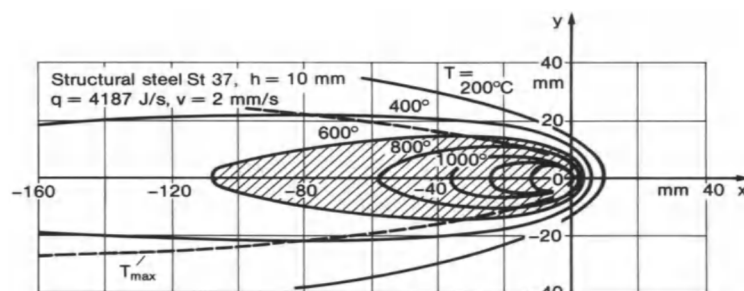


Figure 3.5: Temperature field iso-surfaces around welding heat source moving uniformly and linearly on a plate [100].

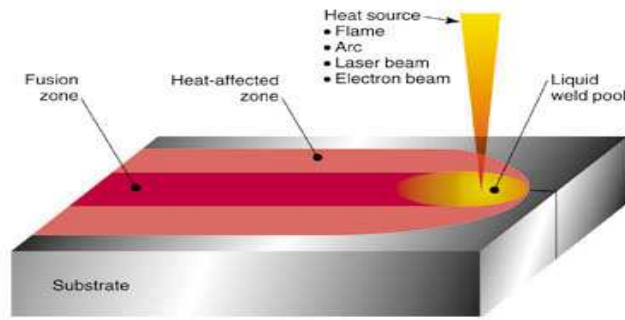


Figure 3.6: Illustration of a fusion zone [105].

According to [100] welding is joining technique by means of applying heat for creating a part from pieces of metal. There are various types of welding such as GMAW, GTAW, SMAW, etc. for arc welding, joining of metal pieces is done by melting and solidifying the parts in a desired path. The joining of metal parts could be with or without filler material. The application of heat has a high importance. The application of heat, requires heat source which differs as different heat sources are used for welding such as gas flame, electric arc, laser beam, etc. Figure 3.7 presents MAG welding which has been used for joining of the pieces and assembling of the T-joints.

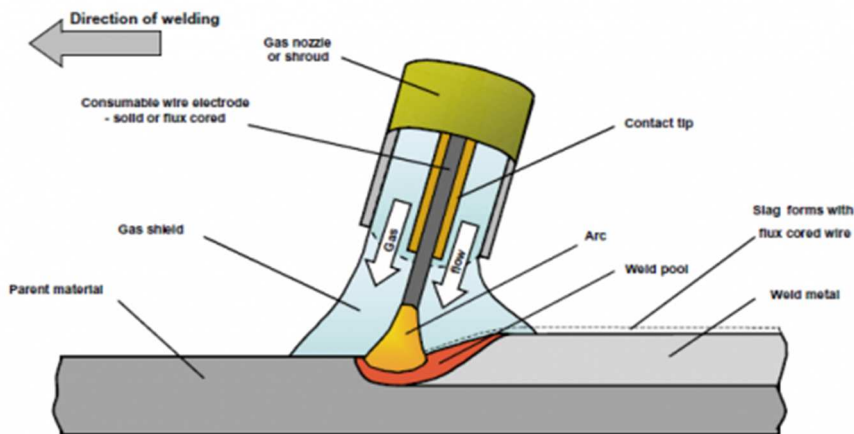


Figure 3.7: Metal-active gas welding (MAG) [106].

Welding induces deformations and stresses. The imperfection induced by welding reduce the load bearing capacity and also they might influence the fatigue resistance significantly. The mechanical effects are highly influenced by residual stresses. Furthermore, depending on the tensile/compressive stress state, the buckling strength can be reduced just as a tensile stress state can lead to stress corrosion cracking.

### 3.5.1.1 Longitudinal Stresses

As an Example related to this work, a plate has been welded. The stresses distributions have been studied and illustrated in the Figure 3.9 to Figure 3.12. The longitudinal and transverse stresses can be described as follow. By neglecting some parameters such as clamping and fixing of the pieces,

big part of tensile residual stresses are distributed in the heat affected zone. Welding time is 50 seconds and the resulted stress distribution is considered after 550 seconds of cooling. At the edge perpendicular to the longitudinal direction, the stresses will drop to zero due to the free edge boundary condition. At some parts of the piece of metal away from the fusion zone and HAZ the material does not receive so much heat which means, it keeps its strength. This part of the material which does not receive enough heat would act as restraints for the heated material in and near the weld from expanding which actually led to opposite stresses (i.e. compressive stresses) which grows in the area which is not affected by the heat away from the HAZ. Comparing the residual longitudinal stresses patterns when welding is finished and also after cooling time of 550 seconds, illustrates reverse sign in what the pieces experience. After welding of the plates before the cooling period starts, compressive stresses are observed close to the weld and after cooling time the residual tensile stresses take place. The results plotted in Figure 3.9 to Figure 3.12 are from a welding simulation analysis in Simufact.Welding. The heat source model used in this example is Goldak's double-ellipsoid heat source with welding and heat source parameters plotted in Table 3-1 and Table 3-2.

Table 3-1: Welding parameters.

<b>Welding parameters</b>	
<b>Velocity</b>	4 mm/s
<b>Current</b>	190 A
<b>Voltage</b>	25 V
<b>Efficiency</b>	0.85

Table 3-2: Heat source parameters.

<b>Heat source parameters</b>	
<b>Front length <math>a_1</math></b>	3 mm
<b>Rear length <math>a_2</math></b>	6 mm
<b>Width (b)</b>	3 mm
<b>Depth (c)</b>	5 mm

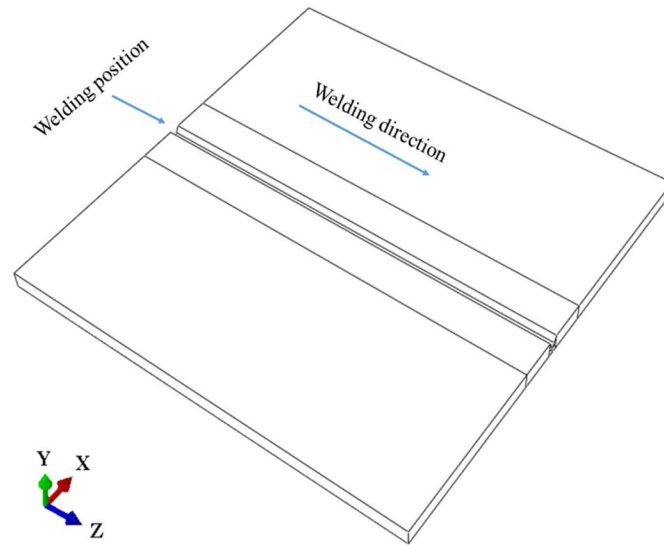


Figure 3.8: Location and position of an only one pass weld for welding two pieces of plates with the same geometry 200\*100\*8 millimeter.

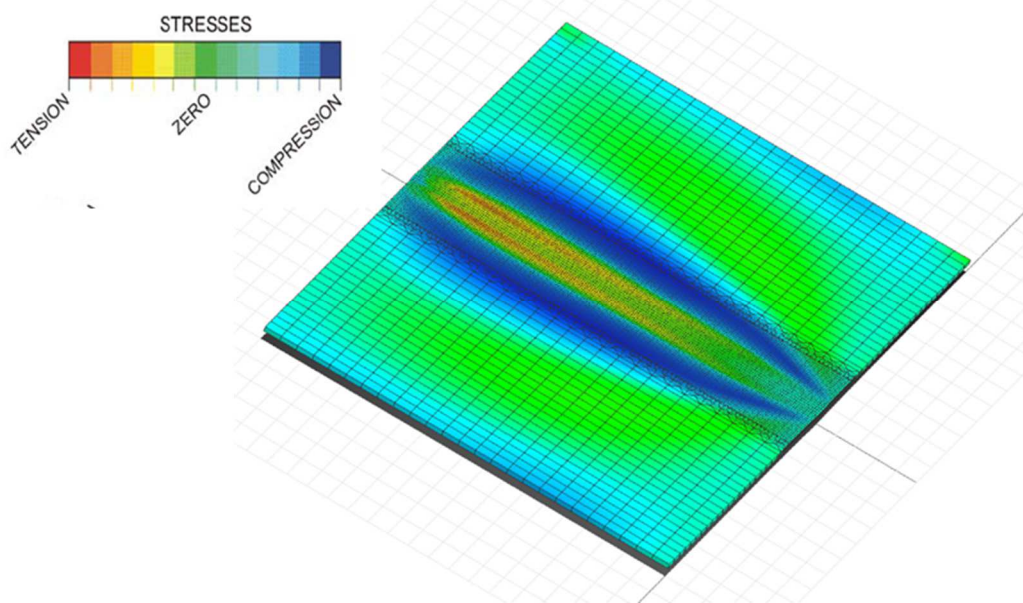


Figure 3.9: Residual longitudinal stress field at the end time of welding.



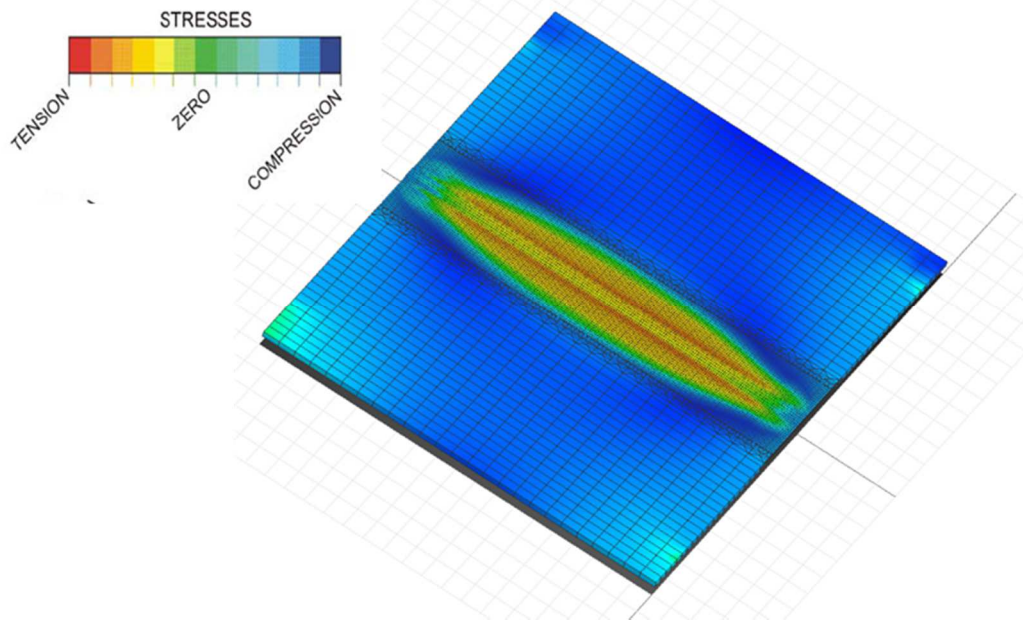


Figure 3.10: Residual longitudinal stress field after cooling time of 550 seconds.

### 3.5.1.2 Transverse Stresses

Figure 3.11 and Figure 3.12 show the distribution of residual transverse stresses. Welding has been done from one edge to another. According to the general understanding of start and end point, the last part to be cooled is the last part that was welded but the results of this example show that the middle part is the last part to be cooled which could be explained by thermal boundary conditions. The material on the edge will obtain its strength sooner than the one in the centre. Also, as usually film coefficient is defined by the surfaces defined to the simulation program, it makes sense that on the edge due to a bigger number of surfaces the pieces cool down faster. Residual stresses distribution is highly influenced by how the pieces are fixed in longitudinal and transverse directions. If the plates are free to expand towards the edges which is x-axis in this example, this would lead to compressive stresses in the near of the edges. On the other hand if they are fixed by clamps or fixers in the same axis, this would lead to residual tensile stresses close to the weld. Welding sequencing plays a very important role in how the member responds in terms of residual stresses which is clear even in this simple plate.

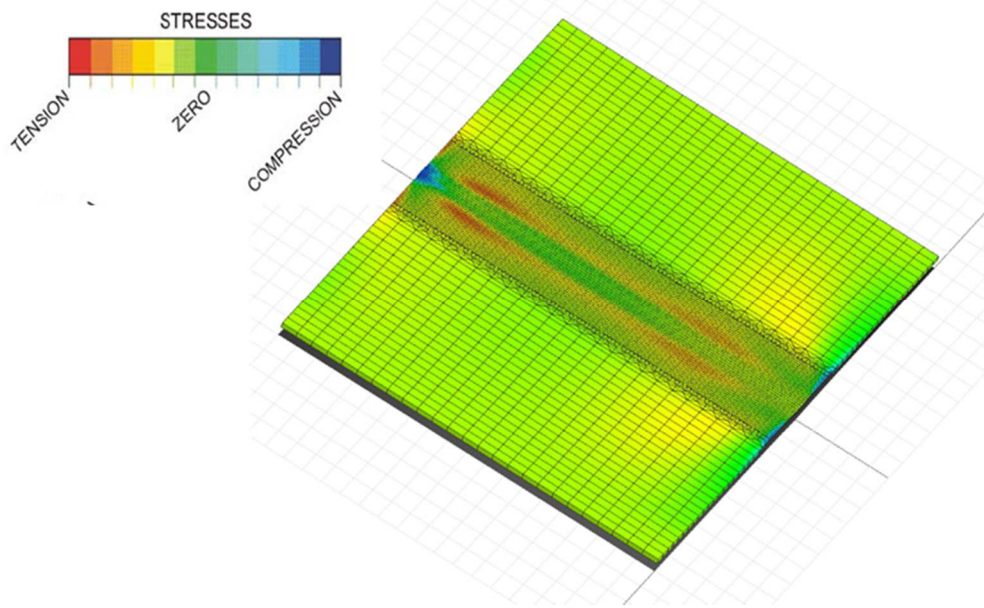


Figure 3.11: Residual transverse stress field at the end of welding.

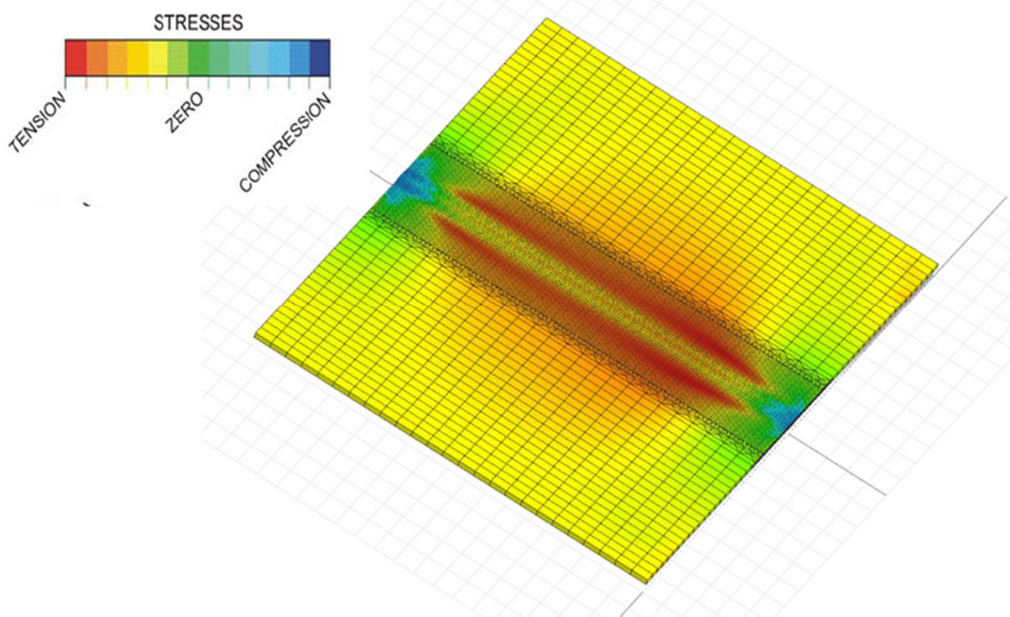


Figure 3.12: Residual transverse stress field after cooling time of 550 seconds.

### 3.6 Thermo-Mechanical Analysis of Welding

The procedure of thermo-mechanical analysis which has been also carried out in the present work could be explained as follows. In this analysis firstly the thermal analysis is done in order to calculate the time-temperature distribution in a non-linear heat transfer analysis. The heat required for welding the pieces is applied by a moving heat source with the same and constant shape.

In case of deep penetration fusion welds, a double ellipsoid model as illustrated in Figure 3.13 could be used, which has been also used in the present work. In this model the power from the welding

torch as well as the efficiency must be defined. This heat source model is one of the most respected heat source models existing and being used by simulators globally. This model offers a good estimation of the weld pool when experimental measurements do not exist. When experimental results do not exist, for validation of results the simulator needs a good background in simulating and parametric studies.

Figure 3.13 is a schematic representation of double ellipsoid.  $a_r$  and  $a_f$  are rear and front length respectively. Depth is presented by  $c$  and the width of the wing by  $b$ .

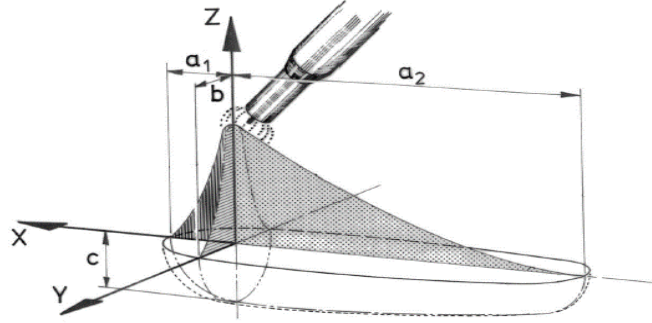


Figure 3.13: Moving double ellipsoid heat source model. Normal distribution of volumetric heat source density in front and rear of the weld [107].

The arrangement of two ellipsoids, approximately of the shape and the size of the weld pool allows for different gradients in the heat flux in the front and the rear of the source. The ellipsoids are described by the semi axes  $a_1, a_2, b$  and  $c$  and the following equations.

$$q_f(x, y, z, t) = \frac{6\sqrt{3}f_f Q}{a_1 b c \pi \sqrt{\pi}} e^{-\frac{3y^2}{b^2}} e^{-\frac{3z^2}{c^2}} e^{-\frac{3|x+v(\tau-t)|^2}{a_1^2}} \quad (3.1)$$

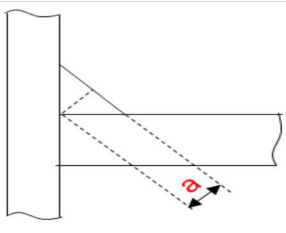
$$q_r(x, y, z, t) = \frac{6\sqrt{3}f_r Q}{a_2 b c \pi \sqrt{\pi}} e^{-\frac{3y^2}{b^2}} e^{-\frac{3z^2}{c^2}} e^{-\frac{3|x+v(\tau-t)|^2}{a_2^2}} \quad (3.2)$$

$$f_f + f_r = 2 \quad (3.3)$$

$$Q = \eta UI \quad (3.4)$$

Where,  $q_f, q_r$  are power density in front and rear ellipsoids.  $a_1, a_2$  are fractions of heat deposited in the front and the rear.  $v, t$  and  $\tau$  are welding speed, time and heat source x-position at  $t=0$ .  $Q$  is effective energy input rate and  $\eta, U$  and  $I$  are heat source efficiency, voltage and amperage. The heat source parameters differ depending on what code the user follows. For instance Table 3-3 presents the formulas which Simufact.Welding offers for the creation of the shape of Goldak's heat source model.

Table 3-3: Heat source parameters after [108].

<b>Front length <math>a_1</math></b>	$(a + 1.5 \text{ mm}) * 0.6$	
<b>Rear length <math>a_2</math></b>	$2.2 * (a + 1.5 \text{ mm})$	
<b>Width <math>b</math></b>	$a + 1 \text{ to } 2 \text{ mm}$	
<b>Depth <math>c</math></b>	$a + 2 \text{ to } 5 \text{ mm}$ (including a penetration depth for an acceptable root)	

If a construction plan is the basis for a first estimation, then the geometrical parameters can be estimated using the throat  $a$  as illustrated in Table 3-3.

### 3.7 Heat Source Modelling with ABAQUS

In the present work ABAQUS has been used as the finite element code beside SYSWELD. When deciding on a specific finite element procedure one has to make a fundamental choice of the basic behaviour of the method. In principle, an explicit integration scheme could be applied in the case of welded applications, but especially the time for cooling the structure is large and would lead to an excessive number of time steps and hence long analysis time. Those basic behaviours of the finite element formulation imply that the version of the finite element program used is ABAQUS/Standard. The same mesh is preferably used in the thermal as well as the mechanical model in ABAQUS/Standard though adequate accuracy of the thermal analysis can be achieved with coarser mesh compared to that needed for the structural analysis. The aim of the present work is to estimate the influence of sequencing on the patterns of residual stresses and also furthermore on the load bearing capacity of the T-node. Therefore, a sufficient modelling of the welding process in order to describe the temperature field in general, in the workpiece, is important for the subsequent mechanical/structural analysis. The residual stress field not only depends on the heat input from the welding process. Also the initial condition of the joint.

### 3.8 Geometrical Consideration in the Modelling of Welding

For the development of welding processes and for the metallurgy of welds, the temperature fields in the near weld zone region are most important and the far region can often be neglected. Size and shape of the weld pool are therefore of interest and hence the microstructure calculation. On the other hand, in many cases it has been mentioned that the distribution of the heat input into the weld and thereby the prediction of shape and size of the weld pool has only minor effects when calculating residual stresses globally in real structures. More important is the geometrical modelling and connectivity describing the constraints of the structure during welding. Most of the models need to be modelled three-dimensionally to adopt all deformations such as angular distortions, bends,

buckling etc. Taking into account the calculation time that normally can be expected with three-dimensional models.

### 3.9 The Moving Heat Source Principle in ABAQUS AWI (ABAQUS Welding Interface)

The moving heat source methodology is applied in a three-dimensional finite element model in ABAQUS. The weld preparation and filler material has been modelled with an adequately fine mesh specified in the total length of the weld. The elements serving as filler material initially are given a temperature above the melting temperature. Next, the filler elements are removed/deactivated and then reactivated successively step by step with the heat source moving along the weld seam. The principle can be seen in Figure 3.14.

Figure 3.14 and also Figure 3.15 are from the thermal analysis of two different models. Figure 3.15 illustrates how the temperature is distributed in the temperature application in the first of welding the members in ABAQUS AWI. By defining the path in AWI and the number of steps and chunks to be in the weld, ABAQUS begins the thermal analysis and later on after the thermal analysis is finished, thermo-mechanical analysis begins. Temperature application performs activation of elements step by step until the end of analysis.

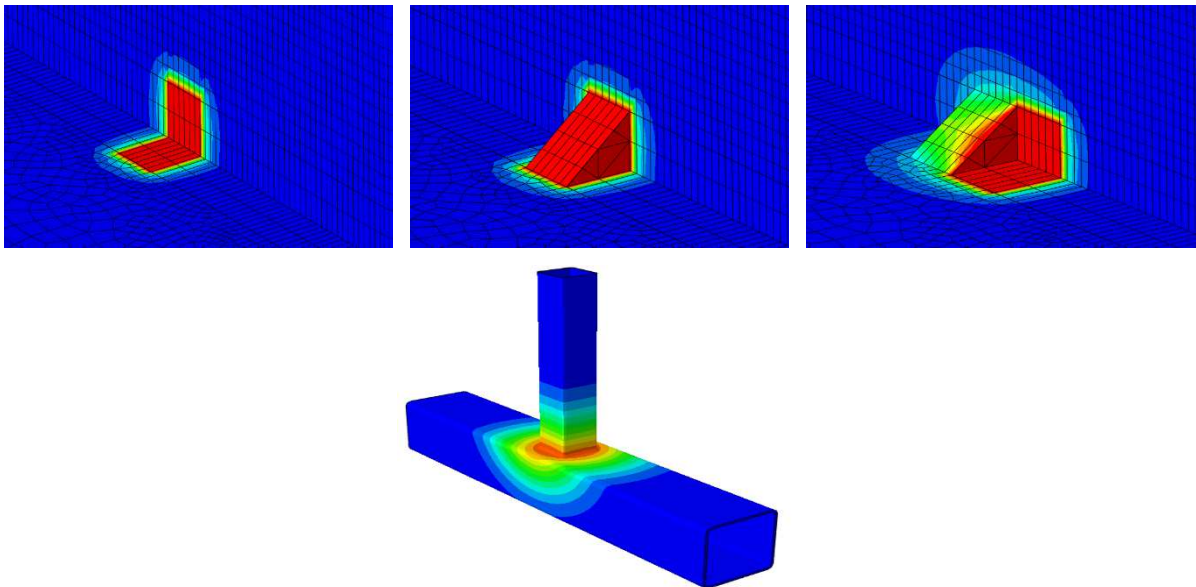


Figure 3.14: Principle of the moving heat source with successive activation of elements serving as filler material [109].



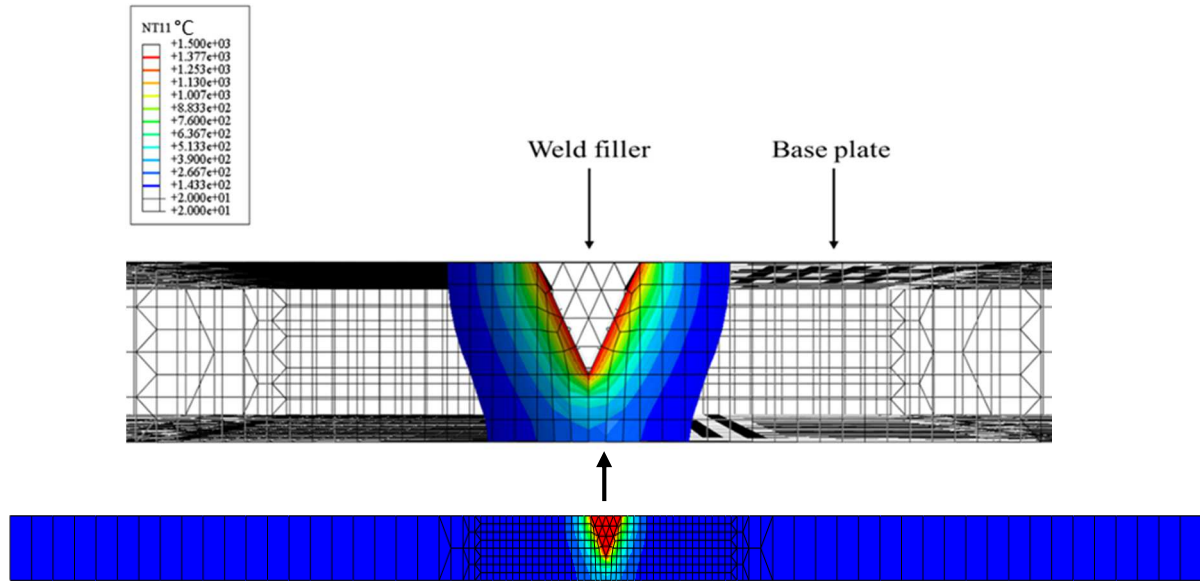


Figure 3.15: Cross section of mesh to model the weld preparation. Illustrating the temperature distribution [109].

### 3.9.1 Material Properties

In the material the mechanical properties are influenced and controlled by the chemical composition and the microstructure of the alloy. The influence of microstructure is considerably larger than chemical composition with respect to the carbon and alloy steels [110]. It is necessary to distinguish between austenite stabilizers (e.g. Mn, Ni, Cu) and ferrite stabilizers (e.g. Cr, Mo, Si) in order to mention some of the effects on for example pearlite growth [111]. During heating the microstructure change from ferrite + pearlite to austenite and during cooling from austenite to either ferrite + pearlite, bainite or martensite depending on the temperature cycle and cooling rates. The prediction of the formation of the microstructure during welding could be a determining factor in the material's cost of a structure and a great factor for the structure's performance. These days with existing welding simulation programs simulators could monitor what happens to the microstructure of the material during welding. One approach for modelling the microstructure dependence of the material properties in the heat affected zone as a function of the local temperature cycle, is to identify cooling rates in the heat affected zone and use these together with a maximum-temperature cooling-time diagram to estimate the microstructure of the material, after [112].

#### 3.9.1.1 Thermal Properties

To analyse the transient energy distribution in a material, conductivity and heat capacity of the material must be specified. If the material furthermore undergoes phase transformations this must be assessed to be captured adequately and especially if liquid-to-solid transformations occur, the solidification heat must be considered.

3.9.1.1.1 Thermal Conductivity

Heat transfer by conduction involves transfer of energy within a material without material flow as a whole. The rate of heat transfer depends upon the temperature gradient and the thermal conductivity of the material. The thermal conductivity is a function of temperature and microstructure. In Figure 3.16 the thermal conductivity as function of temperature is shown as it is applied in the present work. The conductivity for material representing the molten zone is increased over a rather wide temperature range to increase the computational efficiency. Large changes in material properties within a narrow temperature range combined with the large temperature gradients existing in the area of the weld calls for small time steps and a rather large number of equilibrium iterations in the numerical code. Such excessive non-linearities in the modelling of material behaviour should and can to a large extent be avoided in numerical modelling of welding, as is the case with the thermal conductivity.

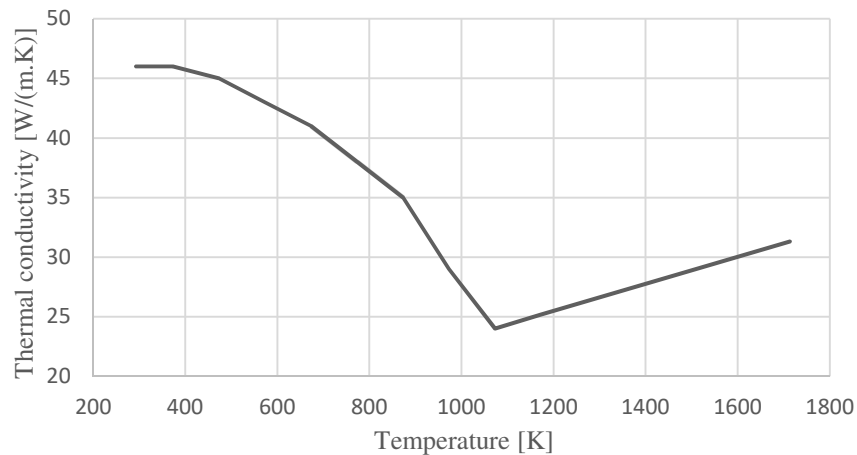


Figure 3.16: Thermal conductivity as a function of temperature [108].

3.9.1.1.2 Density

The density of a material must be specified in the thermal analysis to calculate the actual heat storage in the material. The property can as well be included directly in the specification of the heat capacity as a combined property  $\rho c_p$ , and in that way incorporated in the numerical code. When the density is specified at its own, it can usually be assumed temperature independent when considering typical steels. If temperature dependency is included, a linear decrease in the density at room temperature to that at melting temperature is often assumed [100]. A typical temperature dependence of the density is shown Figure 3.17 and conforms to the one adopted in the present models. Though the density of a material is a very “mechanical” quantity it is seldom used in the mechanical analysis unless the effect of gravity on the welded structure is taken into account.

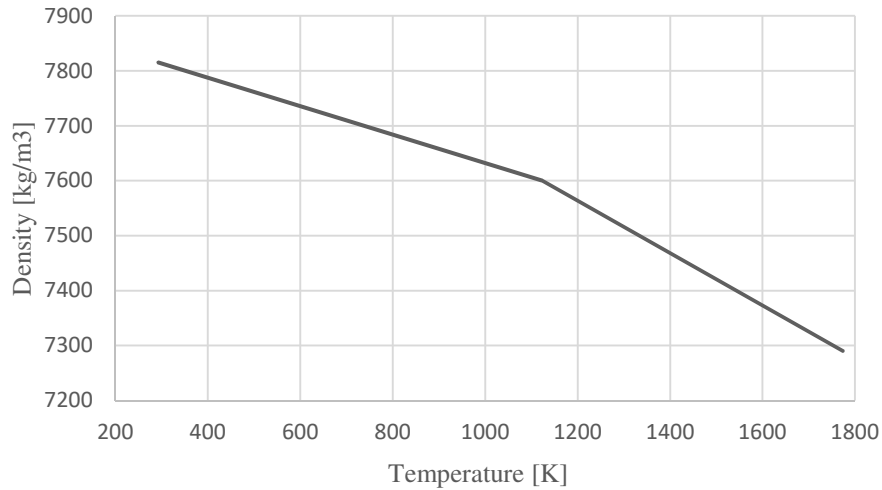


Figure 3.17: Density as a function of temperature [108].

### 3.9.1.1.3 Specific Heat

The heat capacity of a material is a measure of how well the material stashes heat. When heat is applied to the material, it would cause an increase in the material's temperature. The relationship between heat,  $Q$ , and a temperature change,  $T_1$  to  $T_2$ , can be expressed in terms of the state variable (enthalpy) which is actually defined as the sum of the internal energy plus the product of the pressure and volume. Specific heat is defined as;

$$C_p \equiv \left(\frac{dh}{dT}\right)_p \quad (3.5)$$

Where  $h$  is the specific enthalpy following  $dH = mdh$  ( $m$  is the mass), the change in the heat of the volume material  $V$ , with density,  $\rho$ , is given by;

$$Q_{12} = \Delta H = m \int_{T_1}^{T_2} C_p dT = V \int_{T_1}^{T_2} \rho \cdot C_p dT \quad (3.6)$$

With the density and the specific heat assumed constant, the energy related to the temperature change can be explained as follow;

$$Q_{12} = m \cdot C_p \cdot \Delta T \quad (3.7)$$

In the moving heat source models as in this presented work, filler material is added at a predefined temperature above the melting point temperature. With equation (3.2) the temperature which is given from the filler material to the base material could be calculated. The temperature dependence of the specific heat based on [108] is presented in Figure 3.18



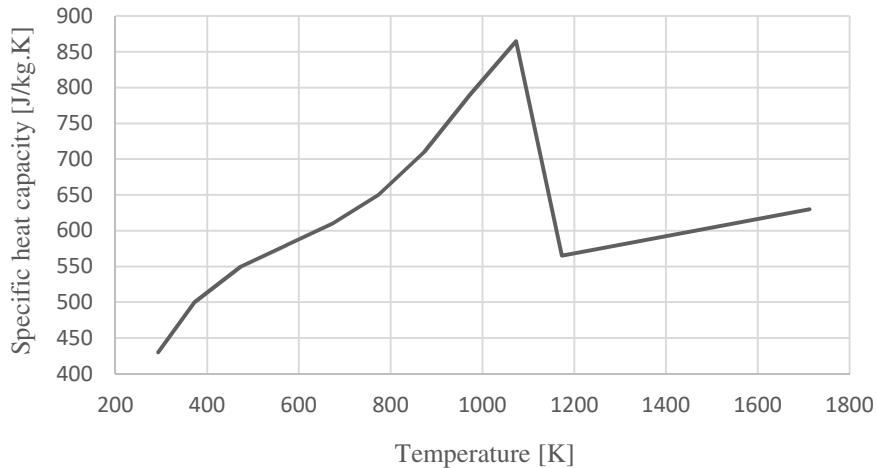


Figure 3.18: Specific heat as a function of temperature [108].

#### 3.9.1.1.4 Latent Heat

The latent heat of fusion,  $L$ , of a solid is the amount of energy that must be transferred to one kilogram of the solid at its melting point temperature, in order to melt it. This energy is called latent heat because there is no temperature change associated with this energy transfer, it is only associated to a change in phase. The energy originating from the liquid-solid phase changes is therefore expressed without including any temperature correlation.

$$Q_L = mL \quad (3.8)$$

For many cases it is reasonable to assume that the phase change occurs within a known temperature range. When materials as steel change phase during solidification, it takes place over a temperature range defined by the materials liquids temperature,  $T_L$ , and solidus temperature,  $T_S$ . The heat contribution related to the solidifying filler material given by equation (3.8) must be subtracted, together with the heat represented by equation (3.4), from the total net heat input, equation (3.9), representing the effective arc energy from the welding process.

$$Q = \eta UI \quad (3.9)$$

Where  $\eta$  is the arc efficiency coefficient,  $U$  is the voltage of the arc and  $I$  is the current.

#### 3.9.1.2 Mechanical Properties

The most essential factors when calculating residual stresses in welds induced by thermal strains are the effects of temperature and thermal history on the mechanical properties. The thermal history affects the mechanical properties through the microstructure, which not only depends on the current temperature but also on the past phase transformations and in that way the thermal history.

The three most important mechanical properties when doing analysis of welds are yield strength, elastic modulus and coefficient of thermal expansion. Besides these properties, Poisson's ratio must be included and if necessary the hardening modulus.

### 3.9.1.2.1 Yield Strength

The yield strength is an expression of the stress necessary to produce significant plastic deformation in a material under uniaxial tensile or compressive load. It can be defined as the stress at which a material exhibits a specified limiting deviation from proportionality of stress to strain. The level at which this so-called yielding happens is strongly temperature dependent. As the temperature increases and the material softens, the yield strength decreases. For typical carbon steels the yield strength is considerably reduced for temperatures around 800-1000°C and naturally vanishes at the melting temperature. Figure 3.19 shows the temperature dependence of the yield stress as considered for the material in the present work.

As it is the yield limit deciding whether the material reacts elastically or plastically and thus forms the stress distribution in the structure, a temperature dependent modelling of this material property is very important. But it also makes the zone, dividing the material in an elastic and a plastic region, temperature dependent and hence strongly non-linear and computational demanding, taking the temperature gradients in the vicinity of the weld into account. Therefore, a gentle slope as function of temperature should be intended in the modelling of the yield stress.

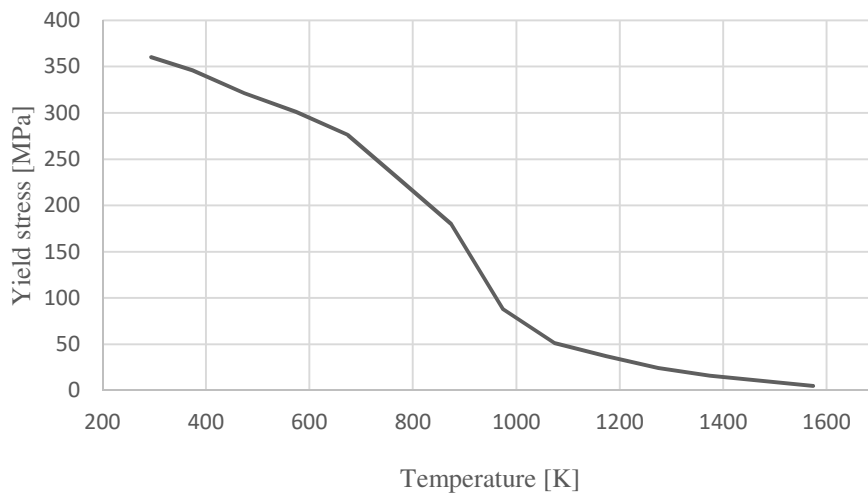


Figure 3.19: Yield stress as a function of temperature [113].

### 3.9.1.2.2 Young Modulus

According to Hooke's law, the strain is proportional to stress within the elastic region of the stress-strain curve, i.e. prior to yielding. The constant ratio of the two (for constant temperature) in a uniaxial test is Young's modulus and indicates the elasticity of the material. At temperatures above 400°C the stiffness of mild steel material diminishes in consequence of a strong reduction of Young's modulus to approximately 40 GPa at 700°C and to 10 GPa for temperatures above 1000°C. This last reduction is made on basis of a widely-held praxis more than a reflection of an actual physical reason, as questioned in the literature [114].

Figure 3.20 shows a fairly smooth approximation of Young's modulus still considering a certain drop in stiffness for temperatures above 673.15 K though starting to drop somewhat earlier. Often the stiffness is held around 200 GPa till well above 673.15 K. In [100] a more or less linear decrease of Young's modulus to approximately 150 GPa at the austenite transformation temperature (approx. 1023 K) is declared with a rapid drop hereafter. In [99] a similar description of Young's modulus is found though the very characteristic drop is 373.15 K earlier at 923.15 K. A sudden drop at 573.15 K is also seen for the representation of Young's modulus of mild steels as in e.g. [115]. This indicates the difficulties in measuring the temperature dependence of material properties for elevated temperatures.

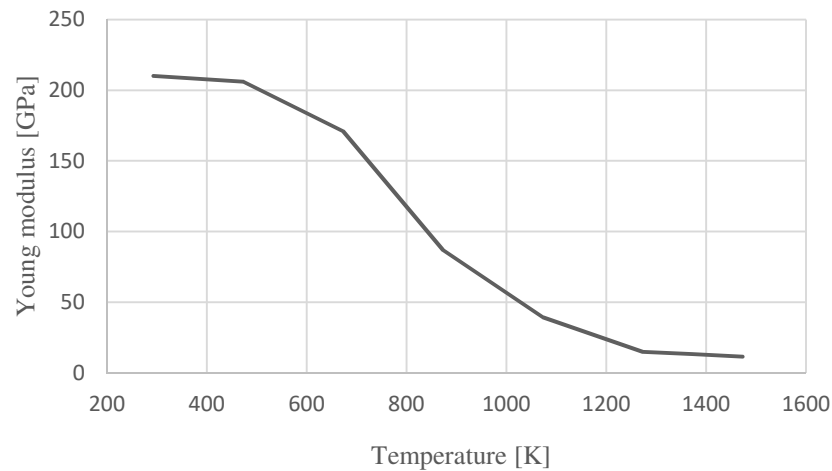


Figure 3.20: Young's modulus as function of temperature [108].

### 3.9.1.2.3 Poisson's Ratio

Steel materials elongating due to tension will diminish perpendicular to the direction of tension. This relative volumetric change in shape is expressed by Poisson's ratio and Young's modulus through the bulk modulus. Most steels have a Poisson's ratio in the range of 0.28 to 0.33 at room temperature. In the present material models Poisson's ratio is assumed to be constant value of 0.3.

### 3.9.1.2.4 Thermal Expansion

An unrestrained body subject to a temperature increase will normally expand with the increase in temperature, diminishing density, and shrink when temperature decreases. This behaviour is known as thermal dilatation and the proportionality factor between strain and temperature is the coefficient of thermal (cubic) expansion. For small strain theory the relation can be written as;

$$\frac{\Delta V}{V} \cong \varepsilon_{kk}^{th} = 3 \cdot \alpha \cdot \Delta T = \beta \cdot \Delta T \quad (3.10)$$

Where  $\alpha$  is the linear thermal expansion coefficient. In general, the thermal strain is given by;

$$\varepsilon_{kk}^{th} = \int_{T_1}^{T_2} \alpha(T) dT \quad (3.11)$$

It should be noted, that in this thesis the filler metal is assumed the same material as that of the base metal and therefore the influence of dissimilar metal welds is not considered further.

The thermal expansion coefficient increases with temperature, as shown in Figure 3.21, until the transformation point where the denser atom packing of the face-centred austenite compared to the body-centred ferrite gives an abrupt change just as for the specific heat.

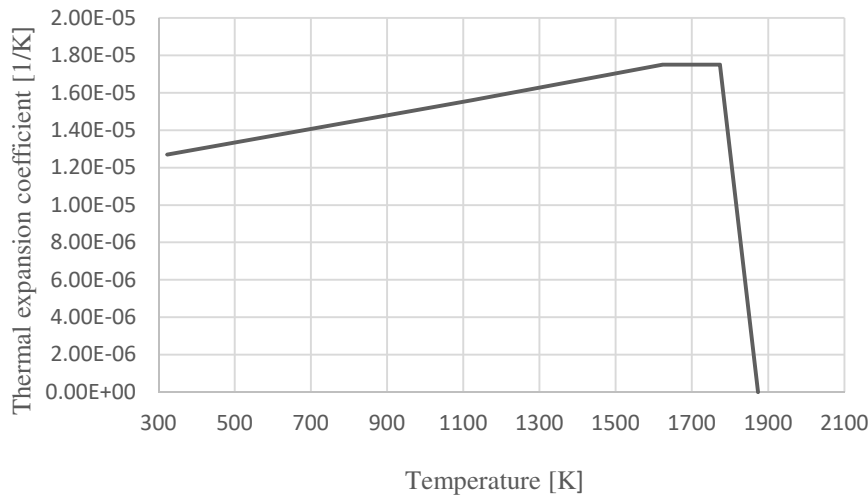


Figure 3.21: Thermal expansion coefficient as function of temperature [108].

If a material is non-hardening, the stress point at which the material starts to yield is always the same for a given temperature, that is, a constant yield locus (temperature dependent) at which the strains are indeterminate. The material is said to follow a perfect plasticity model. Few materials exhibit this ideal plastic behaviour. In reality, some hardening will probably occur and hence the assumption made with a perfect plasticity model is conservative; if the material hardens, the plastic strains will be less than those predicted by the simulation.

Strain hardening or work hardening is a process by which the material grows stronger as it is deformed. For a strain hardening material, the size and shape of the yield locus depends on the total history of deformation. If a material has reached the yield limit for a tension load in a certain direction, then a reversed loading can result in a lowering of the yield stress. This phenomenon happens because microscopic defects in the material in combination with different stress states in different grains (microscopic residual stress) interact making the straining of the material harder to achieve [116]. Such a reduction of the yield stress in one direction resulting from inelastic loading in the opposite direction is called the Bauschinger effect. This has to be considered in the case of a cyclic alternating loading condition as e.g. that of multi-pass welding. Two approaches to describe the way a material yields are isotropic hardening and kinematic (anisotropic) hardening,

Zienkiewicz and Taylor [117]. In isotropic hardening, Figure 3.23, the yield surface expands during plastic flow and this expansion is uniform (isotropic) in all directions about the origin in stress space, thus initial shape and orientation is maintained. In the isotropic hardening theory, the Bauschinger effect is neglected. The isotropic hardening principle is applied for in this present work is illustrated in Figure 3.23.

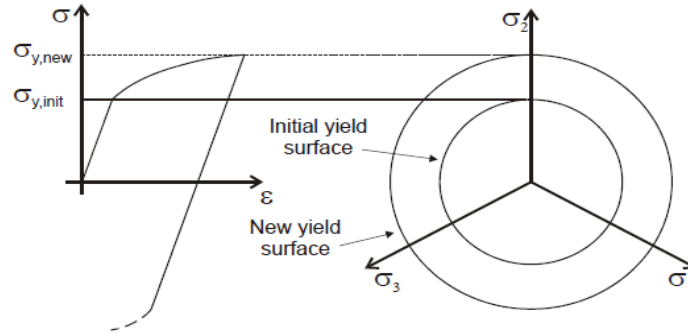


Figure 3.22: Schematic representation of isotropic hardening in principle stress space [117].

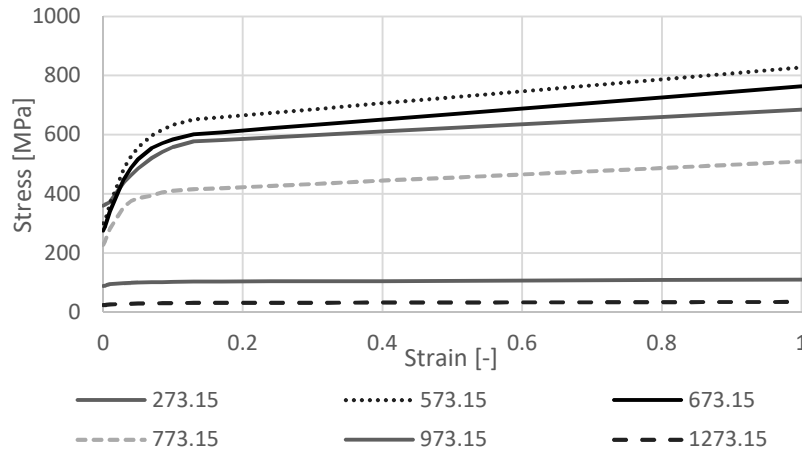


Figure 3.23: Isotropic hardening stress curves for selected temperatures in (K) [108].

## 3.10 Governing Equations

As mentioned before in the present work the welding simulation is done into two part first the thermal analysis and afterwards mechanical analysis. Here the equations used for both would be explained.

### 3.10.1 Thermal Analysis

Heat conduction is assumed governed by the Fourier law. Together with the source term from the process, the (transient) governing equation for temperatures becomes;

$$\rho c_p \frac{\partial T}{\partial t} = \frac{\partial}{\partial x} \left( k \frac{\partial T}{\partial x} \right) + \frac{\partial}{\partial y} \left( k \frac{\partial T}{\partial y} \right) + \frac{\partial}{\partial z} \left( k \frac{\partial T}{\partial z} \right) + Q_v \quad (3.12)$$

Where  $T$  is the temperature;  $\rho$  is the density of the material;  $C_p$  is the specific heat;  $k$  is the heat conductivity; and  $Q_V$  is the heat supplied externally into the body per unit volume from the welding process.

For the finite element formulation, the basic energy balance is expressed in the form of an integral over the volume of the body, by the “weak form” obtained from the principle of virtual temperatures, expressed as;

$$\int_V \bar{T}(\rho c_p) T' dV + \int_V \bar{T}' k T' dV = \int_S \bar{T}' q dS + \int_V \bar{T} r dV \quad (3.13)$$

Where  $V$  is the volume of solid material, with surface area  $S$ ;  $\bar{T}$  indicates that a virtual temperature distribution is being considered;  $q$  is the heat flux per unit area, flowing into the body; and  $r$  is the heat supplied externally into the body per unit volume.

### 3.10.2 Mechanical Analysis

The mechanical model is based on the solution of the three governing partial differential equations of force equilibrium. In tensor notation, these are written as;

$$\partial_{ij,i} + p_j = 0 \quad (3.14)$$

Where  $p_j$  is the body force at any point within the volume and  $\partial_{ij,i}$  is the stress tensor. As the basic equilibrium statement for the finite element formulation, the three equilibrium equations are replaced with an equivalent “weak form”, the principle of virtual work expressed as;

$$\int_V \sigma_{ij} \delta \bar{\varepsilon}_{ij} dV = \int_V p_i \delta \bar{u}_i dV + \int_S T_i \delta \bar{u}_i dS \quad (3.15)$$

Where  $\delta \bar{\varepsilon}$  is the virtual strain (corresponding to the virtual deformation),  $\delta \bar{u}$  is a virtual displacement field and  $T$  is the surface traction at any point on  $S$ .

The physical interpretation of the virtual work statement is that the work done by the external forces subjected to a virtual admissible displacement field is equal to the work done by the equilibrating stresses due to the same virtual displacement field.

### 3.10.3 Strain Decomposition

When solving the equilibrium equations, small strain theory can usually be applied in welding processes. The total strain is then assumed to be an additive decomposition of the strain in parts caused by elasticity (e), plasticity (p), transformation plasticity (tp), viscoplasticity (vp), creep (c), temperature (th) etc. This total strain can be expressed as;

$$\varepsilon_{ij}^{total} = \varepsilon_{ij}^e + \varepsilon_{ij}^p + \varepsilon_{ij}^{tp} + \varepsilon_{ij}^{vp} + \varepsilon_{ij}^c + \varepsilon_{ij}^{th} + \dots \quad (3.16)$$

In numerical analyses of welding, the thermal, elastic and some plastic part are always necessary in order to predict the residual stresses. Furthermore, see section 3.12 for different aspects of the role played by phase transformations in connection with the modelling of material properties and

behaviours. Thus, with these assumptions the total strain is composed of an elastic, plastic and thermal part as;

$$\varepsilon_{ij}^{total} = \varepsilon_{ij}^e + \varepsilon_{ij}^p + \varepsilon_{ij}^{tp} \quad (3.17)$$

The plastic deformation occurring as a result of the thermal cycle is responsible for the development of the residual stresses, i.e. the thermal expansion and contraction drive the stress changes through the plastic deformation but it is the elastic part of the strains that gives the stresses in terms of Hooke's law which is the fundamental way of relating strains to stresses. Experimental measurement methods, e.g. neutron diffraction and strain gauge measurements, also rely on this fact, i.e. they actually measure elastic strains and convert to stresses afterwards.

### 3.11 Boundary Conditions

In welding, the transient temperature distribution is the source driving the development of elastic and plastic strains leading to the final residual stress state in the structure. From the heated weld, the energy is transported by diffusion, i.e. conduction in the material, to the boundaries. The condition at these boundaries can be defined in different ways and is essential for a correct prediction of the transient temperature fields in the structure. Equally, the different restraints acting on the structure during welding and cooling of the material, have a decisive influence on the stress development. In the following, the boundary conditions are discussed with a distinction between those influencing the thermal analysis and those influencing the mechanical analysis.

#### 3.11.1 Thermal Boundary Conditions

Three thermal boundary conditions are considered in the following. The simplest thermal boundary condition is the prescribed temperature. It is mathematically very convenient, giving a strong condition (Dirichlet) since the solution is already known at the boundary. This means that there is no need for further iteration because of the boundary conditions. Although being mathematically well suitable, it is very seldom present in real problems. Even for a boundary to a cooling (or heating) medium, e.g. water at a constant temperature, a more appropriate boundary condition will be that of surface convection according to Newton's law. This is given by;

$$q_{con} = h_{con} \cdot (T - T_0) \quad (3.18)$$

Where  $h_{con}$  is the heat transfer or film coefficient and  $T_0$  is the sink temperature. Another surface effect is the heat loss due to radiation. According to Stefan- Boltzmann's law the radiative heat loss is given by;

$$q_{rad} = \varepsilon \cdot \sigma \cdot ((T - T_z)^4 - (T_0 - T_z)^4) \quad (3.19)$$

Where  $\varepsilon$  is the emissivity constant,  $\sigma$  is the Stefan-Boltzmann constant and  $T_z$  is the absolute zero on the actual temperature scale considered.

In addition to the heavy dependency on surface temperature, the radiation depends on the surface condition, e.g. how glossy the surface is and the colour of the heated surface. The lighter and glossier, the higher the emissivity constant  $\varepsilon$  and hence higher heat loss.

A convenient formulation of the boundary value problem of heat conduction involves the radiation loss being calculated by using an equivalent film coefficient<sup>4</sup> given by;

$$q_{rad} = h_{rad} \cdot (T - T_0) \quad (3.20)$$

Additional boundary conditions included in the thermal modelling are convection and radiation.

Convection and radiation are combined into the following heat transfer coefficient:

$$\bar{h} = \frac{\varepsilon_{em} \sigma_{bol} ((T - 273)^4 - (T_{amb} - 273)^4)}{T} + h_{con} \quad (3.21)$$

Where,  $\bar{h}$  is combined heat transfer coefficient.  $h_{con}$  is convective heat transfer coefficient.  $\varepsilon_{em}$  is the emissivity.  $\sigma_{bol}$  and  $T_{amb}$  are Stefan-Boltzmann constant and ambient temperature respectively.

### 3.11.2 Mechanical Boundary Conditions

If a metal piece is heated uniformly and has complete freedom to move in all directions, it will return to its original form if allowed to cool uniformly. These conditions do not exist during welding since the heating obviously is not uniform.

The heat is concentrated at the joint, with the arc temperature being much higher than that of the base metal. Uneven contraction between the weld material and the base metal will occur and lead to stresses generated across the welded joint. These stresses will be greatly influenced by factors as external restraint, material thickness, and joint geometry and fit-up.

As the amount of restraint increases, the internal stresses will increase and care should be taken to ensure that the material and the welded metal can accept the stress. Areas of stress concentration around the joint are more likely to initiate a crack at the toe and root of the weld. The degree of restraint acting on a joint will generally increase as welding progresses due to the increase in stiffness of the structure as the molten material solidifies. This is typically a greater concern in thicker metal structures. If no external restraint is applied during welding and cooling, the stresses will cause the structure to distort and will find a degree of relief. Internal constraints are composed of e.g. multidimensional nonlinear temperature fields. One can say that restraint is a measure of a structure's ability to develop residual stresses.

---

<sup>4</sup> This approach is used in the models presented in this thesis in order to save calculation time, though tests have shown that this has only little effect in ABAQUS with the kind of analyses investigated.



The mechanical boundary conditions that describe the external load condition on the free surface can be either kinematic or static. If the displacement is prescribed at the surface, the boundary condition is termed kinematic (or a Dirichlet condition), expressed by;

$$u_i = \bar{u}_i \quad (3.22)$$

This is the case when some part of the structure is encastred, i.e. fixed in space, and then;

$$u_i = 0.$$

Another part of the surface can be subjected to prescribed tractions as surface loads, i.e.

$$\sigma_{ij} \cdot n_j = \bar{t}_i \quad (3.23)$$

This is then termed a static boundary condition (or a Neumann condition). In the case of a welding application, this could be a clamping force on the work piece not large enough to ensure the fixation as the welding deformations develop. As usual the clamping force will be ample so the region of the structure that is clamped can be assumed fixed in space.

## 3.12 Microstructural Transformation

### 3.12.1 Welding Effects

When welding is performed, the based metal is highly heated and fused together with the filler material. The based metal in the fusion zone of the weld seam is subjected to short-time temperature cycles with a sharp rise over time up to almost melting temperature. The magnitude of temperature decrease away from the weld and fusion zone. As a consequence of melting and high temperatures, different microstructural layers are shaped and the weld region is commonly subdivided as shown in Figure 3.24 as well as Figure 3.25. Depending on the alloy of steel, a wide variety of thermally activated changes in the microstructure and properties may occur.

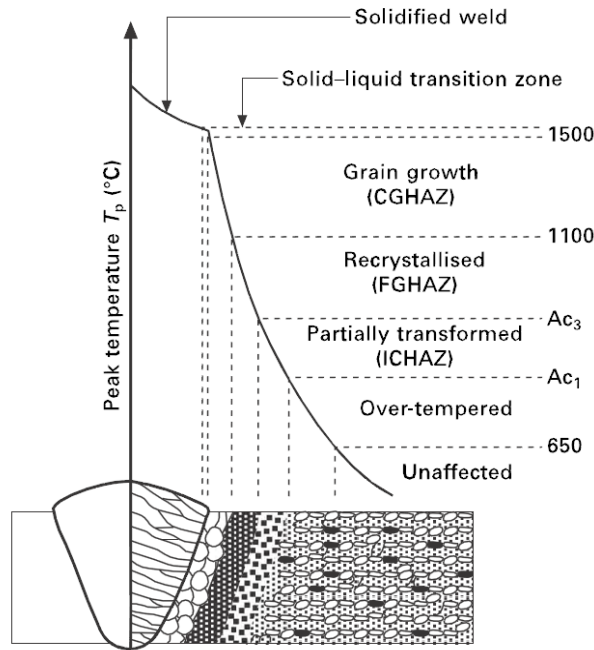


Figure 3.24: Metallurgical zones in a single-pass weld categorized by maximum temperature at each region [118].

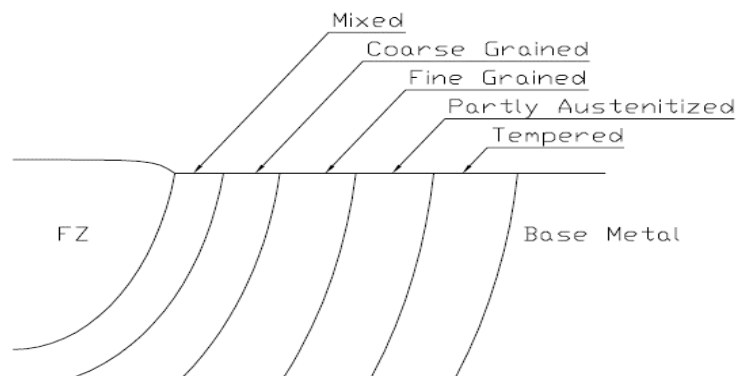


Figure 3.25: Zones of the HAZ [119].

The zones are categorized based on the severity of the thermal cycle they experience. The fusion zone (FZ) fully transforms into austenite during welding and after solidification the material undergoes solid-state transformation based on the cooling rate and CCT curve for that specific alloy. Heat Affected Zone (HAZ) is the region in the vicinity of FZ that is austenitized either partially (ICHAZ) or fully (FGHAZ and CGHAZ). Several subdivisions are observed in HAZ based on the extent of grain growth and austenitization they have experienced in the heating phase. These include coarse-grained zone (CGHAZ), fine grained zone (FGHAZ), inter critical zone (ICHAZ), and over-tempered parent metal. Obviously, phase-transformations do not occur at the last subdivision (over-tempered region) since it is not austenitized during the heating cycle.

During cooling, the regions transformed (fully or partially) to austenite will undergo a reverse transformation in temperature range  $Ar_3$  to  $Ar_1$  which are lower than  $Ac_3$  and  $Ac_1$ , respectively.

The reason why austenite decomposition is more sluggish than its formation being that diffusion speed of carbon atoms within the alloy in  $\alpha \rightarrow \gamma$  transformation and the reverse transformation are different. The kinetics of phase change can be illustrated by using continuous cooling transformation (CCT) diagrams, such as the diagrams shown in Figure 3.26. The diagrams are for steel grade S355 which is used in this work.

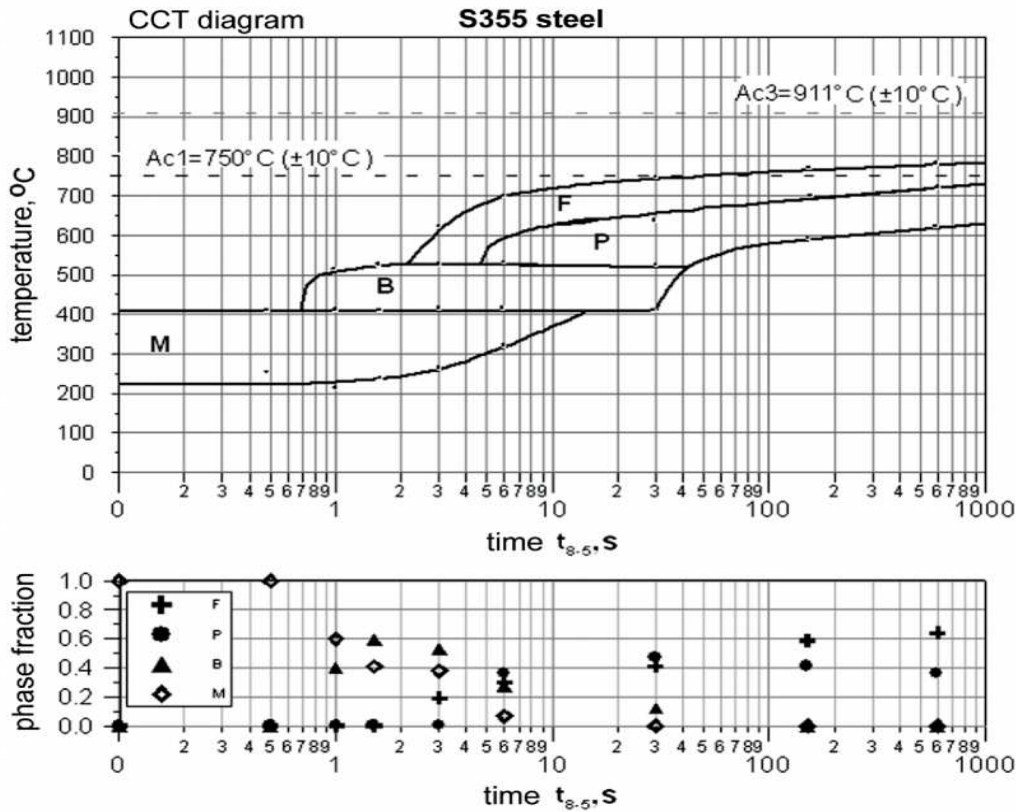


Figure 3.26: CCT diagram and phase composition of S355 steel [118].

A generally accepted index for representing thermal conditions in welding of low alloy steels, is the cooling time from  $800 \pm C$  to  $500 \pm C$  ( $t_{8/5}$ ) which is the range that austenite decomposition takes place [120]. As can be seen in CCT diagrams, very short cooling times (i.e. high cooling rates) lead to a microstructure that is exclusively martensitic. This corresponds to welds with low heat input. On the other hand, a high heat input welding will cool down slowly and the result will be a combination of bainite and ferrite/pearlite.

In addition to cooling rate, the phase transformation depends also on the grain size and carbon content of the transformed austenite [121]. That is why the peak temperature and hold time for the CCT curves should be similar to the welding process (usually between  $1350 \pm C$  to  $1400 \pm C$  in order to help grain growth). Heinze [122] investigated the effect of variation in austenite grain size on welding residual stresses of steel grade S355J2. Surprisingly, they observed no significant effect due to consideration of austenite grain size.

Various mathematical models for transformation kinetics are proposed by researchers. Two of the most known models are Leblond model for diffusive transformations ( [123]) and Koistinen-Marburger relation for martensitic transformation [124].

After a short survey between the all valuable sources mentioned in this chapter and introduction of various parameters to be defined in the welding process, GMA has been used for the welding simulation process taking into account the Goldak's double-ellipsoids model. Due to number of variables which are considered to be investigated, only a single phase material has been considered. However, some comparison regarding the differences between single phase and multi-phase material will be given in chapter nine.

## 4 EXPERIMENTS

### 4.1 Chapter Synopsis

The following chapter describes the welding process and the sequencing schemes. The major aim in this part is to examine the influence of different sequencing schemes on the load bearing capacity of the T-joints. For better understanding of the material, 8 tensile tests are performed and sufficient material properties are achieved which would be used in next step for numerical simulation. Metal active gas (MAG) is used for the welding process. A fillet weld of 5 mm is performed. Temperature distribution is measured at several points with thermos-couples for three different cases. In order to capture the joint behaviour due to welding in terms of deformation, Initial and after welding geometry are measured using the levelling camera. The specimens are tested under brace concentric loading using a 2000 kN testing machine. The load is applied using stroke control at a rate of 3mm/min up to failure. Several inductive displacement transducers are used in order to measure deformations at different point of the joint while the loading process. At the last step the outcome of all tests are compared and a conclusion is delivered.

### 4.2 Material Model

In numerical welding simulations not only input data of the geometry, the heat source, and the boundary conditions must be known but also the temperature dependent material behaviour. In order to model the welding process as realistically as possible, it is fundamental to use accurate values for the thermal and mechanical material model. The experiments in this work aimed to verify the temperature dependent reduction factors for the yield stress and the Young's modulus given in the Eurocode 3 [125]. The yield stress and Young's modulus are used to define an ideal elastic-plastic material model and they can be deduced from the stress-strain curve. In order to find the deformational behaviour and hence the stress-strain curves, a tensile testing is conducted. Therefore, specimens made of structural steel S355J2H, were tested at room temperature in a tensile test.

Usually, the tensile test is performed by universal testing machine as shown in Figure 4.1 or tensile testing machine. The material sample specimen is securely held by top and bottom grips in universal testing machine. Then tensile force is applied to the material and progressively increased up to the point of failure. While specimen is being forced, the applied force and displacement on sample specimens are recorded.



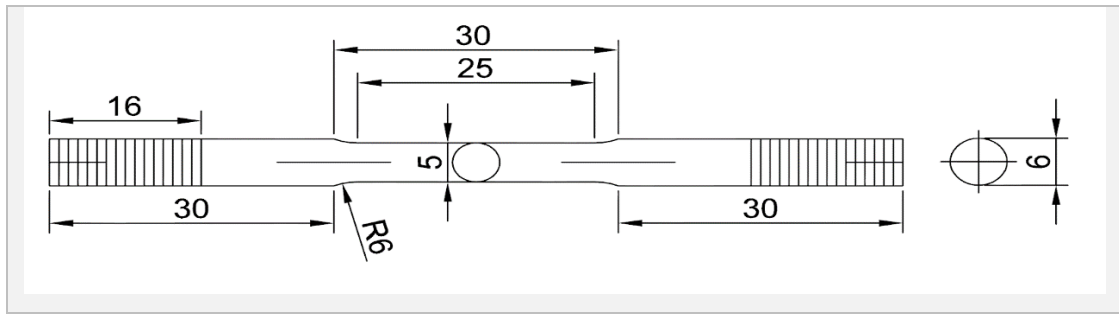
Figure 4.1: Universal testing machine UTM (left) and material testing specimen (right).

### 4.3 Specimen Geometry

The tests in this work were conducted with round specimens made of structural steel S355J2H from the hollow sections to be used later for assembling the T-joints, with the geometry shown in Table 4-1. The preparation of the round specimens has been done using a Tensile Mill CNC machine in FMPA (centre of experiments at Brandenburg University of Technology). Round form gives a uniform temperature distribution in case of testing under various temperatures. The outer part of the specimen is the so called shoulder, where the specimen is gripped by the machine. Due to the thickness of the profiles (6.3 mm), outer diameter of 6 mm was possible. For the material test, total eight steel specimens from the components consisting of the joint were tested under tensile loading. From the tensile test, engineering stress and strain for the steel were obtained. It provided true stress and strain of the steel, which was applied to numerical simulations.

Table 4-1: Detailed information on material specimens.

Square hollow section face and wall						
No.	Steel grade	Nominal value		Measured value		Gauge length (mm)
		Width (mm)	Thickness (mm)	Width (mm)	Thickness (mm)	
1	S355	25.20	5.08	36.55	2.36	25
2	S355	25.14	4.92	31.95	2.23	25
3	S355	25.00	5.05	33.70	2.39	25
4	S355	25.15	5.00	34.41	2.46	25
5	S355	25.14	4.99	33.78	2.24	25
6	S355	24.83	4.97	34.29	2.46	25
7	S355	25.11	5.02	32.77	2.33	25
8	S355	24.90	5.04	33.92	2.37	25



For tensile test, 4 steel sample specimens are prepared from the each component of the face and wall of the square hollow sections. The specimens were tested by universal testing machine (UTM) in Brandenburg University of Technology laboratory. The sequence of material sample test under tensile loading is showed in Figure 4.2.

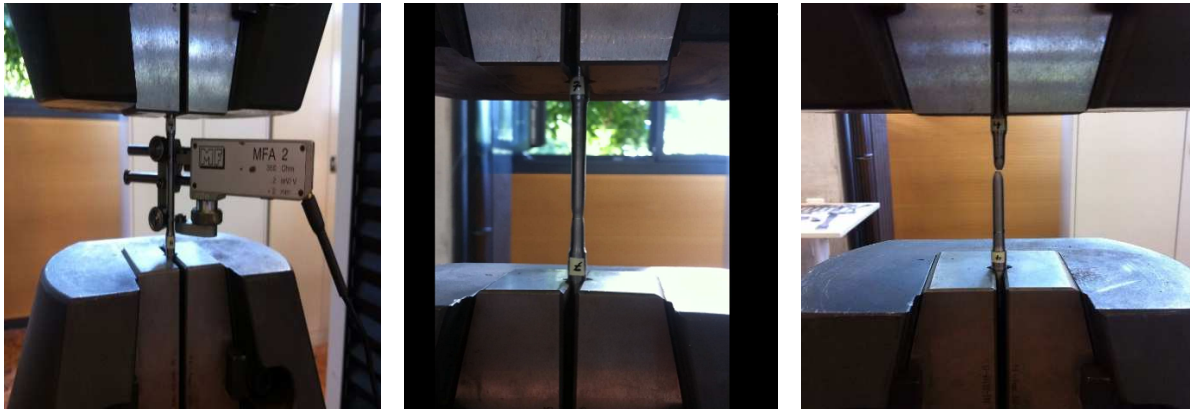


Figure 4.2: Yielding (left), necking (middle) and failure (right).

The specimens were tested to obtain the stress-strain curves. The true and engineering stress-strain curves for S355 are shown in Figure 4.3. The results from the test, which are measured yield stress, ultimate strength, elongation at fracture and elongation at maximum force, are summarized in Figure 4.2. The measured values from the experiment satisfy the minimum requirements from EN 10025-2:2004 [13]. Here it should be noted that testing of the first specimen was stopped (in elastic range) due to a failure in extensometer. However, after solving the problem and putting back the extensometer in place the test was carried on. So probably that could explain the difference in between the behaviour of stress-strain curve for the first test with others.

Table 4-2: Stress and elongation results for eight specimen made of S355.

Sample No.	$R_{eH} \left[ \frac{N}{mm^2} \right]$	$R_m \left[ \frac{N}{mm^2} \right]$	A [%]	$A_g$ [%]
1	324.62	436.43	20.26	32.97
2	378.95	492.52	19.01	33.53
3	389.19	502.20	20.02	34.39
4	348.91	460.65	19.63	31.49

5	376.31	500.39	19.55	33.35
6	405.15	507.34	19.40	34.77
7	376.38	500.19	19.79	31.01
8	384.91	504.40	19.95	33.05

$$R_m/R_{eH} = 1.30$$



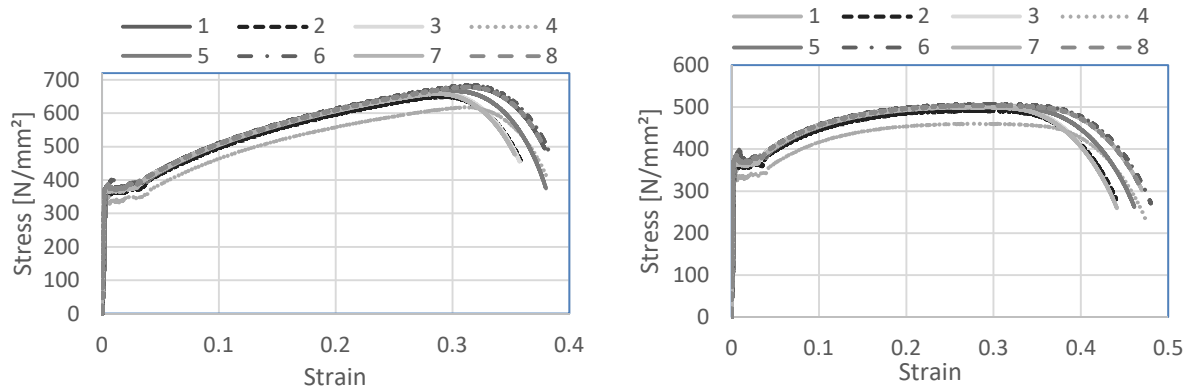


Figure 4.3: True stress-strain (left), engineering stress-strain (right).

## 4.4 Fabrication of Joints

### 4.4.1 Cutting of the Members

After a careful study on the mechanical properties of the material and gaining the stress-strain curves, for assembling of the joints the members have been cut in required lengths. For this aim a Metal Cutting Machine has been used which is existing in FMPA (centre of experiments at Brandenburg University of Technology). Joints made by hollow sections can have different lengths depending on the researcher's interest. In this work, the joints geometry have been chosen in a way which satisfy the requirements recommended by design guides. The joint, consists of two parts, a chord and a brace member. The chord which is the horizontal member has been cut in 1200 mm and the brace which is the vertical member in 600 mm. Figure 4.4 Shows the cutting machine which has been used in order to cut the members.





Figure 4.4: Horizontal Metal Cutting Band Saw Machine.

#### 4.4.2 Tack Welding

In this step the first thing has been to make sure that the surfaces are clean enough as dirty surfaces could cause contamination and create unstable arc. After cleaning the surfaces the middle lines for positioning the vertical member (brace) have been drawn on the chord. As big number tack welds causes initial stresses before welding so in total two tack welds have been done on each joint. Arc welding has been used for both phases of welding with Voltage of 22 and current of 230. Figure 4.5 shows the steps towards preparation of joints for welding.

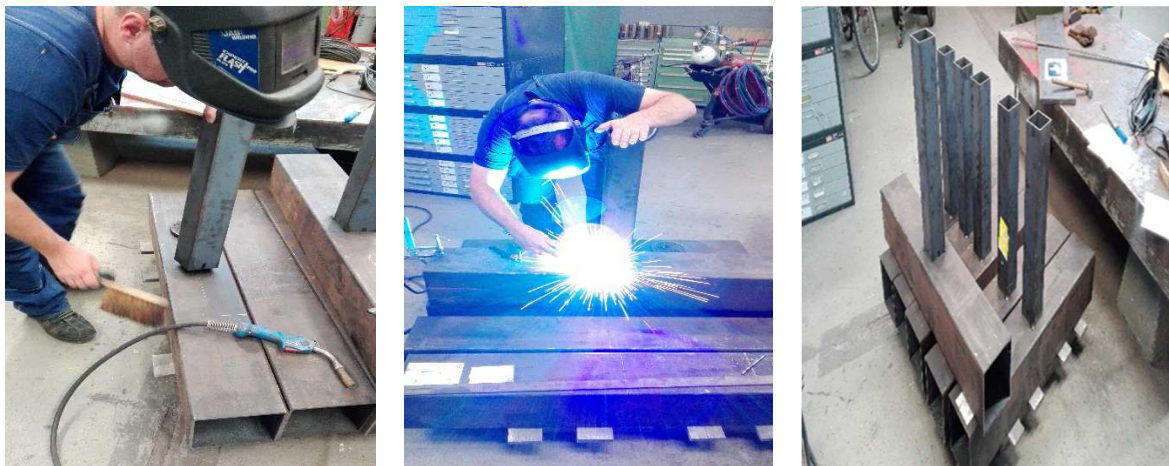


Figure 4.5: preparation of the members (left), tack welding (middle) and tack welded joint (right).

#### 4.4.3 Welding Procedure

Fabrication of joints started with tack welding of 100\*4 mm and 200\*6.3 mm members. In this joint the brace member 100\*4 mm forms the vertical member and the chord 200\*6.3 mm forms the horizontal member. Tack welding and welding were both done on a straight fixture. After tack welding the member was transferred to a welding centre for installation of thermocouples and welding. The welding of joints was done by hand. All joints were welded with the same machine

and same material and parameters. Figure 4.6 shows welding of the joints. The joints were restrained by tack welds to the base metal table used for welding until the end of the welding process.



Figure 4.6: Welding procedure and the welding machine.

#### 4.4.4 Welding Conditions

Welding was performed using one LORCH welding machine. The welding conditions applied for the case studies are listed in Table 4-3. Figure 4.7 shows the sequences of welding with start and end points.

Table 4-3: Welding conditions for the case studies.

Material	S355J2H	
Configuration	T-joint	
Wall thickness	Brace (vertical member)	Chord (horizontal member)
	4 mm	6.3 mm
Shielding gas	$\frac{\text{Ar}}{\text{CO}_2} = \frac{82}{18}$	
Welding speed	5.8 mm/s	
Voltage	22 V	
Current	230 A	
Efficiency	0.9	
Heat input	Gross	Net
	8724.14 J/cm	7851.72 J/cm
Welding time	70 sec	
Filler material	SG/Fe	
Filler thickness	1.2 mm	

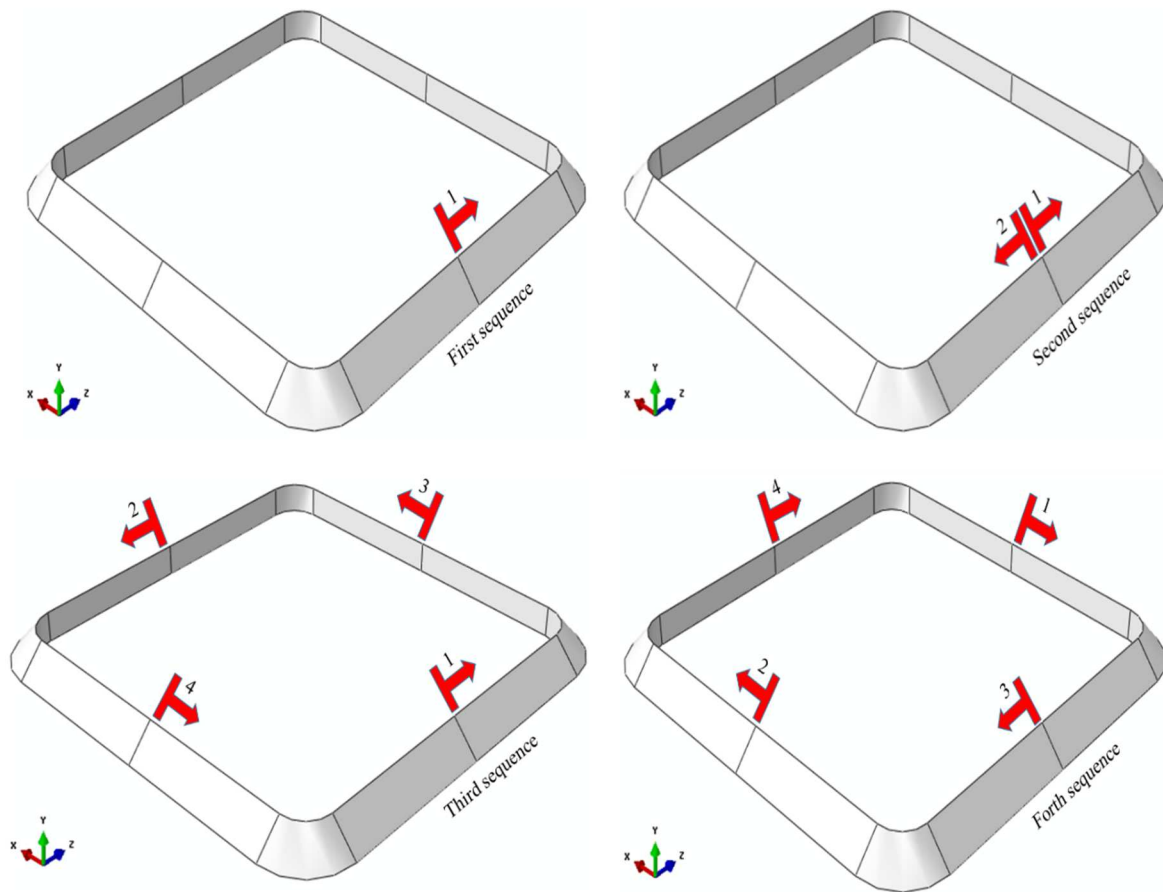


Figure 4.7: Sequences of welding, welding start and stop location

## 4.5 Temperature Measurement

Welding temperature history, and particularly cooling rate, is a crucial factor that affects HAZ microstructure. To ensure accuracy of the temperature field predicted by numerical welding simulation, validation against temperature measurements is needed. The main objective to register the weld-induced temperatures during fabrication was to acquire the data needed for validation of finite element models. Two series of thermocouples were carried out, one on the brace member and one on the chord. Figure 4.8 shows the locations of the installed thermocouples. In total the temperature was carried out at 11 points, 6 points on the chord and 5 on the brace respectively, ranging from 8 mm to 60 mm from the edge of the brace. The weld toe on the chord was not evident at the beginning of welding, the toe line and thickness was calculated ( $a=5$  mm) by considering the weld parameters and the wire to be used. The prediction showed satisfactory agreement with the finished weld geometry but with some changes in thickness as welding was not done by an automatic robot. Type K thermocouple wires were attached to the specimens. Temperatures were registered by one HBM instrument connected to a computer. In order to protect the wires against high heat caused by welding a protection layer was used (fireproof band tapes) as shown in Figure

4.9 However, the experiment showed that still the thermocouples close to the weld could fail as they receive a high magnitude of heat.

Figure 4.9 and Figure 4.10 show the temperature distribution for T-joint welded by progressive welding for the thermocouples installed on the chord and brace members respectively. Due to high heat application during welding the closest thermocouple installed on the chord failed. However, the rest of thermocouples could successfully complete the temperature-time curves. For all cases welding took around 1 min and 12 seconds ( $\pm 3$ -5 seconds due to hand welding). Roughly, 500 seconds was given to the specimens to cool down before disconnecting the thermocouples.

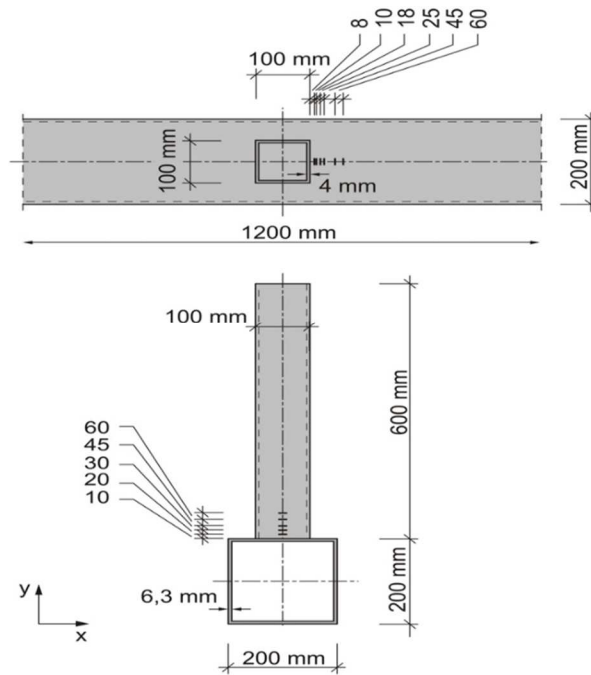


Figure 4.8: Location of thermocouples used for measurement of strain, distances in millimeter.

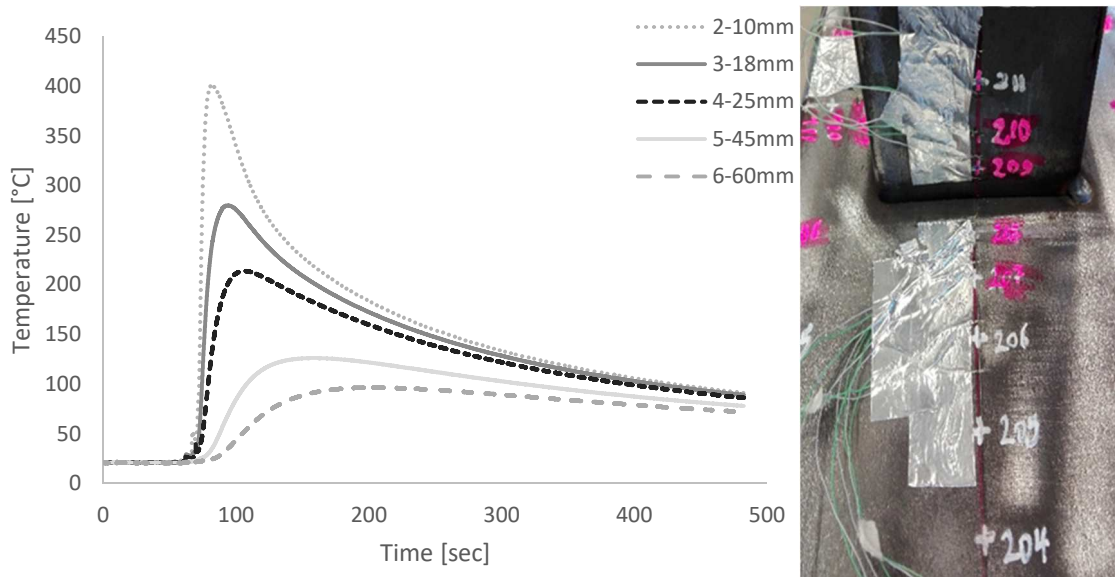


Figure 4.9: Progressive welding, thermocouples on SHS chord member.



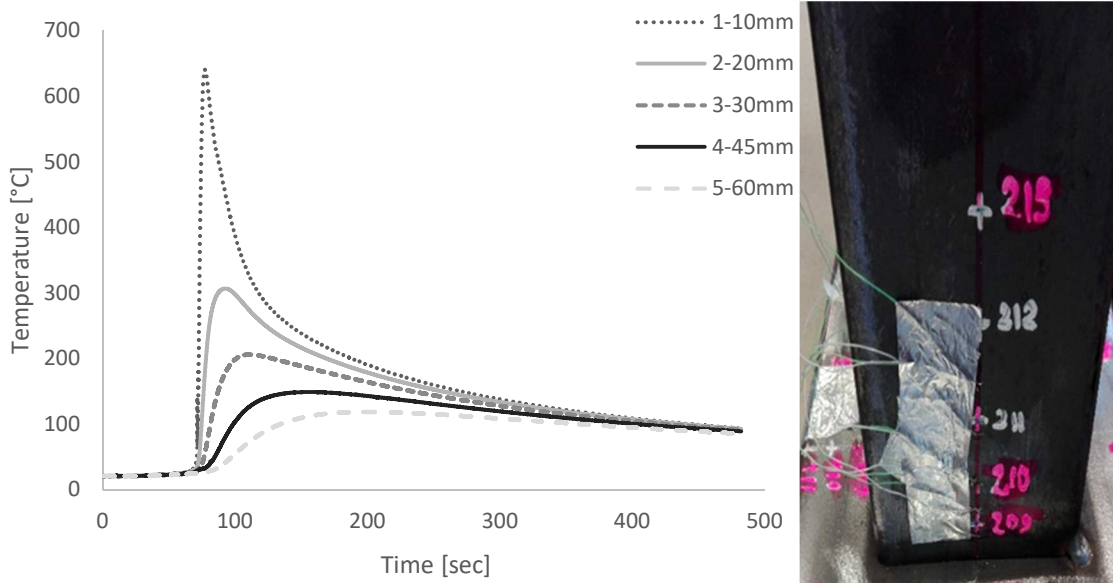


Figure 4.10: Progressive welding, thermocouples on SHS brace member.

From two phases progressive welding, one joint was prepared and welded. Temperature measurement was done with the same manner as in the first process. Comparison of data regarding temperature collected from the first welding process and the second one shows that both joints experience the same magnitude of energy. Figure 4.11 and Figure 4.12 show the data achieved from temperature measurement of T-joint welding in two phases of progressive welding. There is a good agreement in between the curves plotted compared to Figure 4.9 and Figure 4.10. The first thermocouple experienced the same failure as in the first process and burnt by high heat.

Measured temperatures for both chord and brace members for the specimen welded by skip welding are plotted in Figure 4.13 and Figure 4.14. It is clear that this specimen experiences peak temperature at different times due to the welding sequence scheme adopted. The closest thermocouple to the weld on the brace member was burnt by high heat. Depending on the start and end point of welding different temperatures are registered. The temperature data reported here are not further processed. The data would be used for later welding simulation.

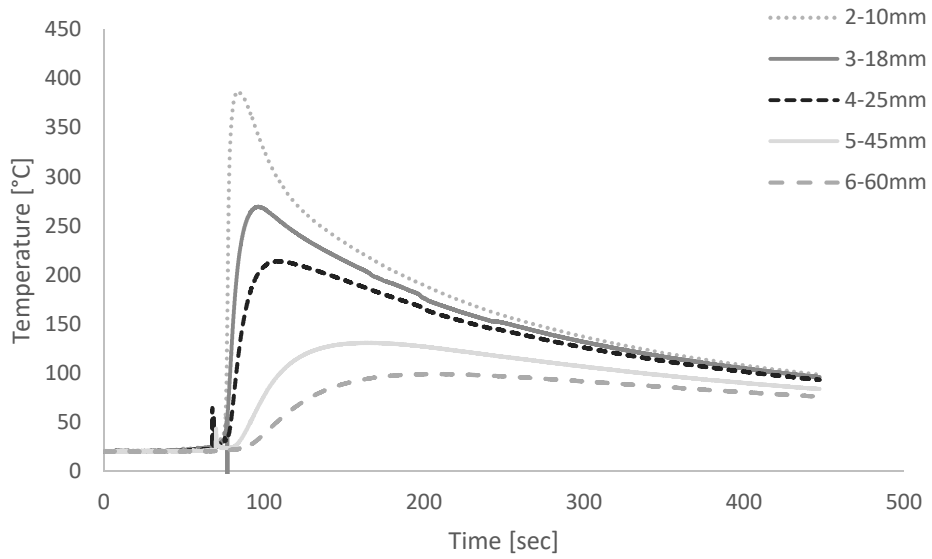


Figure 4.11: Double-phase progressive welding, thermocouples on SHS Chord member.

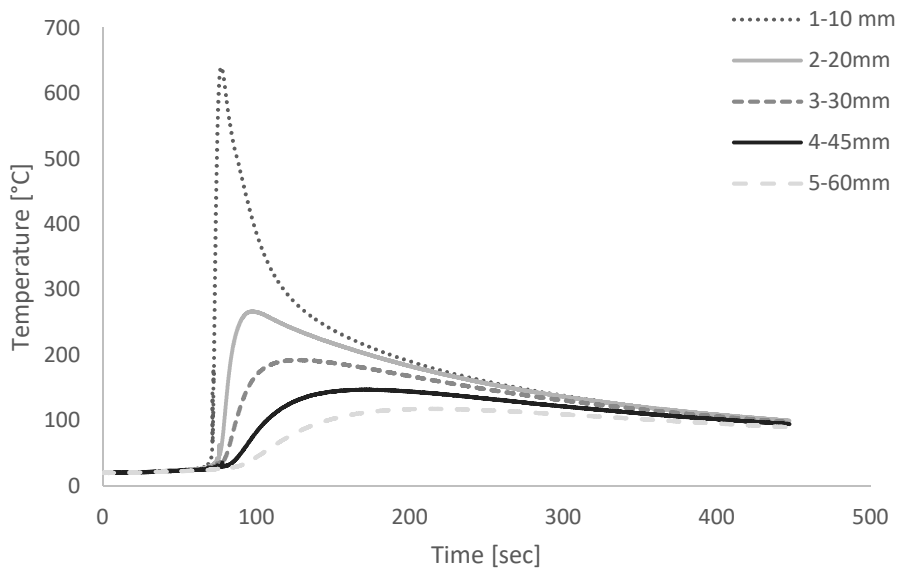


Figure 4.12: Double-phase progressive welding, thermocouples on SHS brace member.

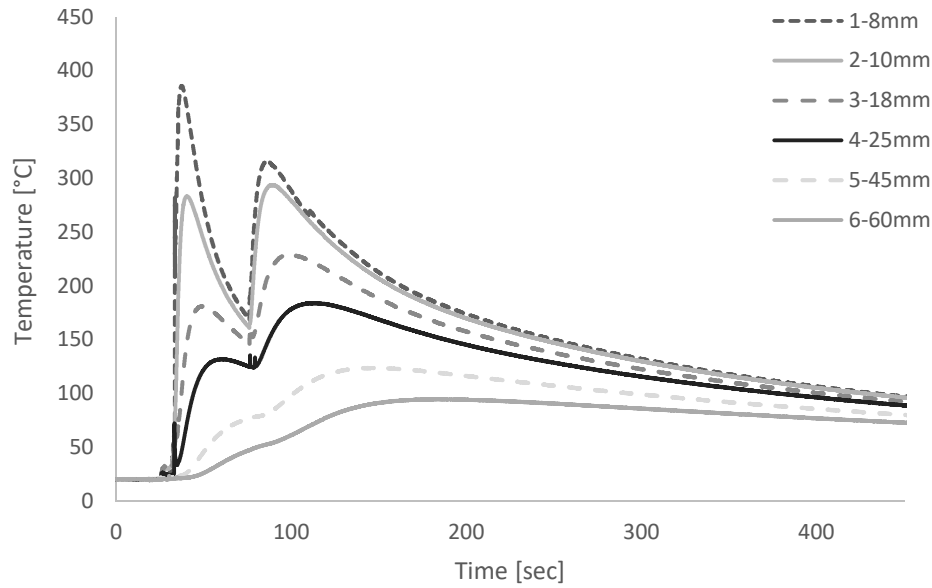


Figure 4.13: Skip welding, thermocouples on SHS chord member.

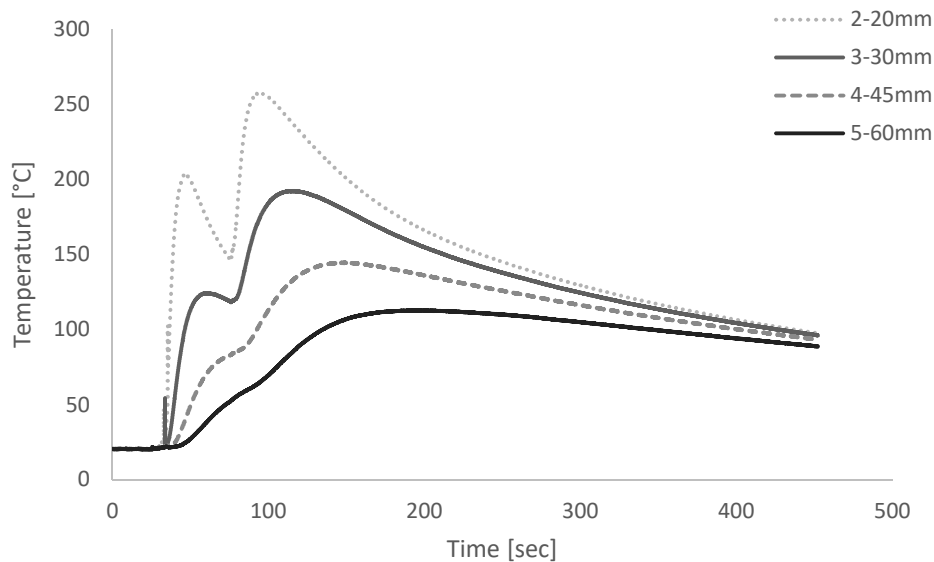


Figure 4.14: Skip welding, thermocouples on SHS brace member.

## 4.6 Test Set-up

In order to verify the validity and accuracy of the models which would be developed in numerical analysis for prediction of stress, deformation and load deflection behaviour, and several experimental tests were performed. The test samples are welded as previously described according to AWS specification. The testing machine which has been designed for the testing of the T-joints is shown in Figure 4.15 for the application of load a hydraulic actuator capable of applying both static and cyclic loading up to 2 MN was used.

A compression load with speed of 3 mm/min was applied in order to capture the ultimate load that the T-joint could bear. During the application of load strain was measured by strain gauges and deformation by inductive transducer sensors with lengths 50 to 100 mm. Measuring both load-

displacement and load-strain behaviours would enable a better observation in case of any changes between the various welding sequences adopted and also provides the possibility of choosing the best and clear way of comparing the joints. In order to be sure that the load is distributed uniformly on the top face of the vertical member a plate (150\*150\*4 mm) was placed between the sample and compression bar.

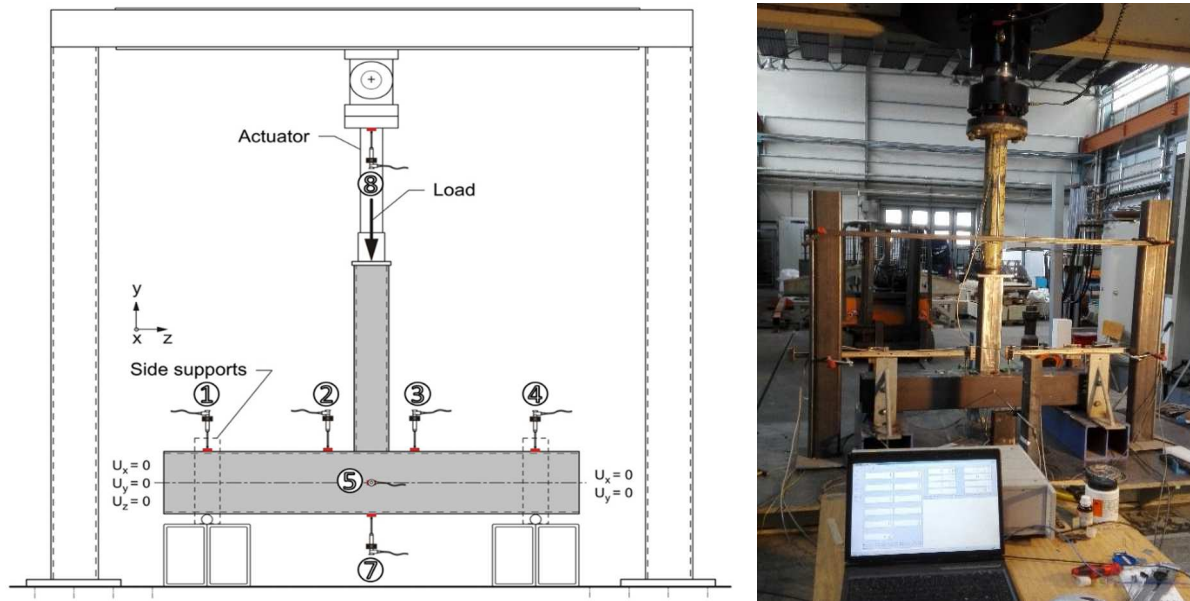


Figure 4.15: Load application machine and test set-up.

#### 4.6.1 Boundary Conditions

In order to apply the load as in practise and actual structure, an appropriate boundary condition should be introduced. In this work two types of supports are used. In the first type two rolled steel bars (nodal supports) with radius of 2 cm and made of S355 are used, at which the reaction forces are calculated. As shown in Figure 4.16, one bar is totally fixed in all directions and the other bar could move in in z-axis.

The other type of boundary condition which could be introduced as clamp is used in order to keep the T-joint in place while the load application as shown in Figure 4.16 on both sides of the chord member two plates which are bolted to two holders are used in order to prevent any movement during load application.



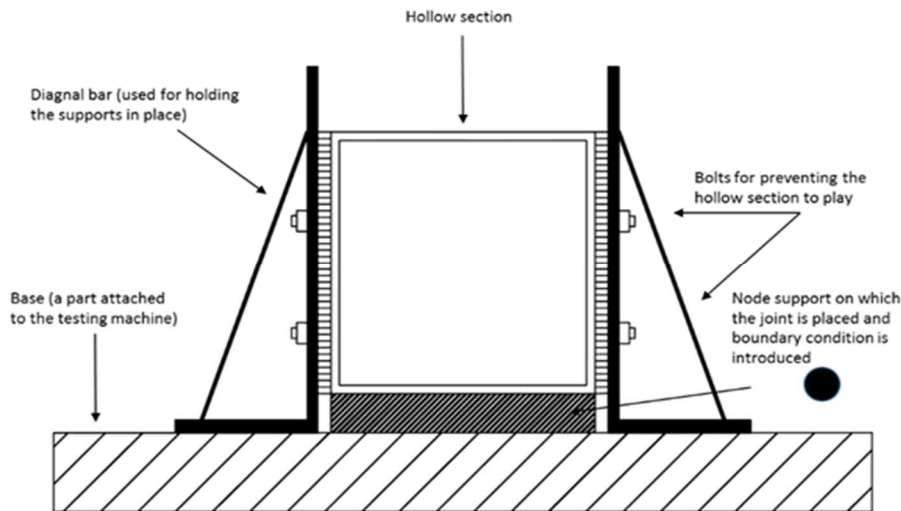
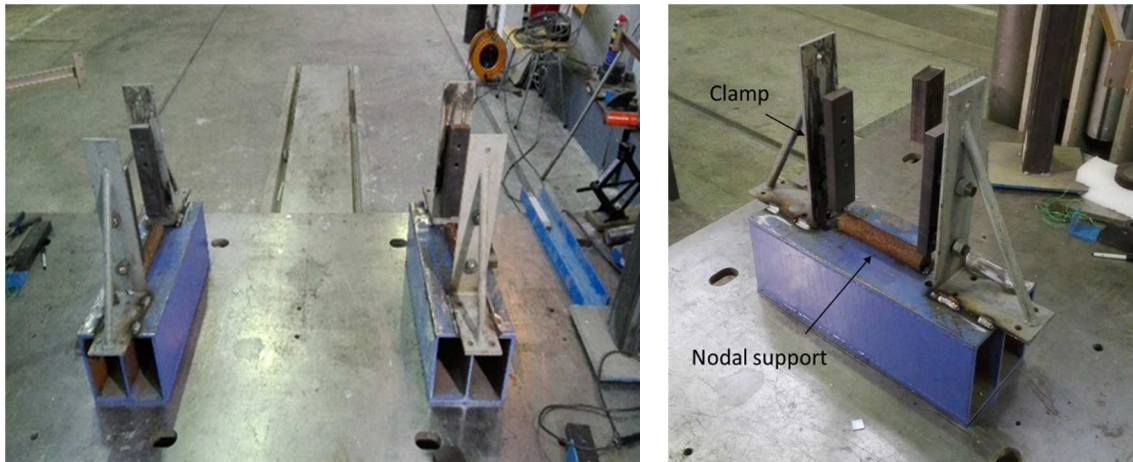


Figure 4.16: Boundary condition and clamping.

The same boundary condition was used for all the tests. The fixers were designed in a way that could be adopted to the hollow section easily. In order to make sure that the plates on the side fully meet the hollow section side walls, two bolts are installed on each side. It was expected when the load is applied the walls of the chord hollow section will start to buckle and later a force would be introduced to the side supports which tries to push them away. For that reason two diagonal bars are welded to the side supports which connect the vertical and horizontal members.

#### 4.6.2 Strain Gauges

For better understanding of the behaviour of the joints, in both brace and chord members, strain gauges type 1-LY11-6/350 were used. The strain gauges are installed in both x- and z- axis, with respect to the coordinate system shown in Chapter one. The aim on location sets for strain gauges, was to cover as many of start and end points of welding sequences as possible. Table 4-4 shows the strain gauges details used in the experiments.

Table 4-4: Strain gauge dimensions and resistance.

Type	Nominal resistance	Dimensions (mm)				Max. effective bridge excitation voltage
		a	b	c	d	V
Steel	W					
1-LY11-6/350	350	6	2.9	13	6	14

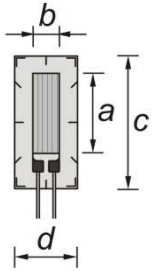
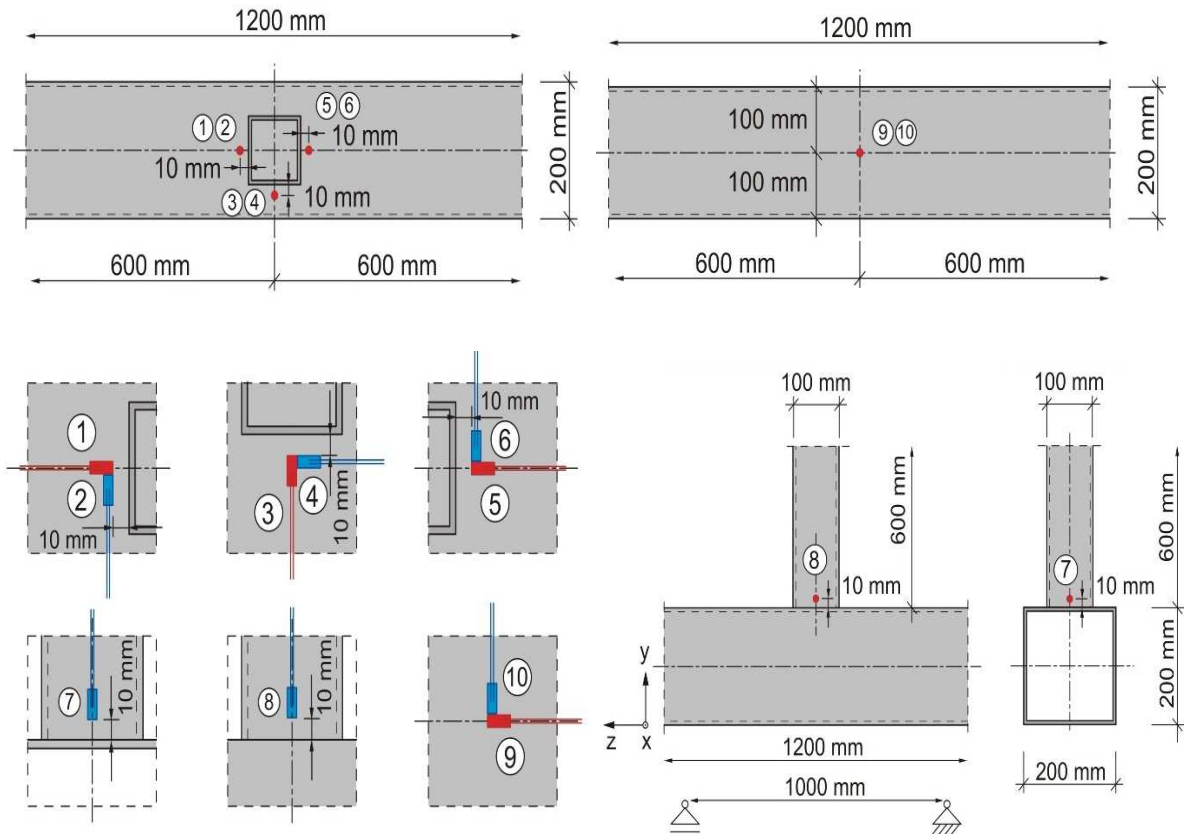


Figure 4.17 shows the positions of the strain gauges on both Chord and brace. In total 10 strain gauges were used for reading the strain while the load was applied. Before bonding the strain gauges to the surfaces at preferred points, the surface was totally cleaned. Usually when it comes to welding, strain gauges are mostly used perpendicular to the weld toe as parallel to the weld toe are assumed to be relatively small. But, in case of loading both must be checked. For the FE results which are presented in the next chapter, the results were read at the centre of the gauge location.



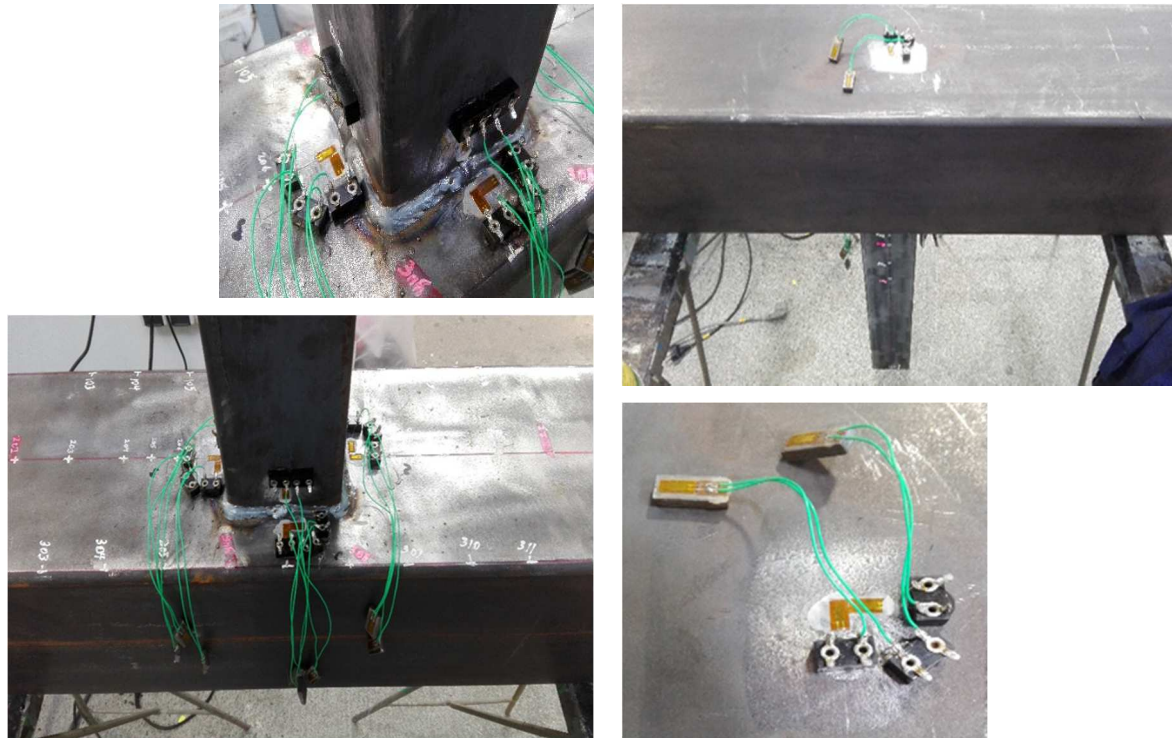


Figure 4.17: Strain gauges on chord and brace members.

### 4.6.3 Inductive Displacement Transducer

Apart from temperature and strain measurement, another parameter which can help validating the results from the numerical analysis is displacement. As previously explained, initial and after welding geometry were measured both with Leica camera. In order to study the behaviour of the T-joint in terms of displacement there are several methods which are being widely used around the world. For instance use of ARAMIS camera and the other common way is inductive displacement transducer. When displacement at a certain point is the interest, this transducer could perfectly satisfy the expectation.

As displacement varies at different points, two different transducers capable of measuring up to 50 mm and 100 mm linear displacement were used in order to prevent any failure. This transducer convert a linear displacement into a signal for recording. Figure 4.18 shows a typical inductive displacement transducer which was used in this work.



Figure 4.18: Inductive displacement transducer [126].

As only an axial compressive load is applied on the brace top face, so only one transducer is installed to measure the displacement vertically in order to see how much the brace member moves down and causes the chord to buckle. Chord wall and face failure was expected to happen according to Eurocode which are the most common failures in the T-joint made by square hollow sections. Due to that reason a special attention was paid to all faces on the chord member. In total 7 displacement transducers were used in order to capture the behaviour of the chord member in terms of deformation. Figure 4.19 shows the locations of a total number of 8 transducers on the T-joint.

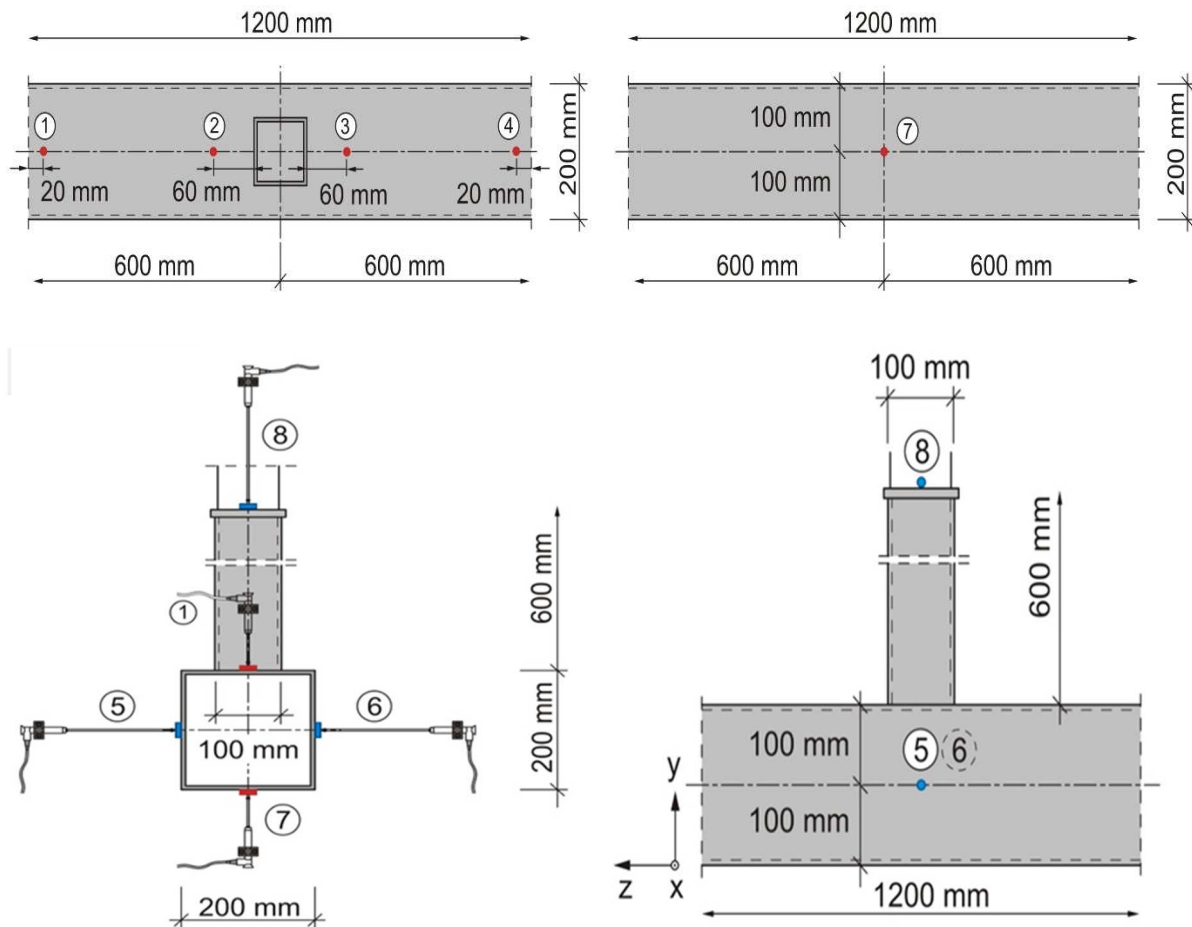


Figure 4.19: Inductive displacement transducer locations.

## 4.7 Load Application

The specimens were tested under brace concentric loading using a 2000 kN testing machine. The load was applied using stroke control at a rate of 3mm/min up to failure. The chord member was clamped at both ends using a special assembly as shown in Figure 4.20 the specimens were located on two rolled steel bars, apart from each other in order to provide a clear span of 1000 mm which is five times of the chord depth ( $h$ ) of 200 mm.





Figure 4.20: Test set-up arrangements.

This ( $L/h$ ) ratio of the chord was carefully selected as per recommendations in the literature. On one hand, the UK Department of Energy Offshore Technology report [127] and other researchers [128] suggested that ( $L/h$ ) ratio should not be less than four, in order to avoid effect of supports on the joint strength. On the other hand, others [129] indicated that ( $L/h$ ) ratio should not be excessive, otherwise chord failure may occur prior to joint failure as the plastic moment of the chord cross-section at the crown location is reached. In fact, some researchers [130] indicated a limit of 5.75 for ( $L/h$ ) to ensure joint failure in a simply supported chord. In this study ( $L/h$ ) ratio of 5 was used to avoid the influence of supports on joint strength. Some end fixities were provided by clamping to increase the load at which the yield and plastic moments occur, in order to focus on the joint strength.

#### 4.7.1 Load-Deflection Behaviour

Testing the specimens requires prediction of failure modes which was done according to Figure 7.2 EN 1993-1-8 [64]. Prediction of failure modes is important for later installation of inductive displacement transducers. Locating the transducers in the right place would lead to better understanding of joint's behaviour in terms of load-displacement and also better comparison with numerical results. Here in this section load-displacement behaviour of several points investigated experimentally are presented. Figure 4.21 shows the load-displacement behaviour of the brace member which was measured by installing a vertical displacement transducer to measure the inductive displacement linearly in an axis only.

Load bearing capacity of the welded T-joint with different welding sequencing schemes are presented in Figure 4.21 From the first welding sequence which is progressive welding three joints were tested in order to observe if the test set-up has any influence on the results. The load was applied using stroke control at a rate of 3mm/min up to failure. The first joint was stopped due to failure in two displacement transducers on the side walls of the chord as shown in Figure 4.22 Chord

face failure or buckling on the top face of the chord where the brace member is located led to chord side wall crippling. The side walls started to push out the displacement and further contact between two displacement transducers occurred and caused the failure. However, the data collected for the first test until the point it was stopped shows a good agreement with the second test and the third which were both from the same welding sequencing scheme. As no influence from the test set-up on the results was observed, the joints were tested one by one with the same condition. For each specimen the displacement at top of brace differed slightly at any given load, as a result of out-of-plane displacement of the chord sidewalls. This effect becomes more pronounced near the peak load. Generally, the load ascends almost linearly initially, followed by a non-linear behaviour of various degree of nonlinearity depending on the welding sequencing scheme of the welded joint, until a peak load is reached and a descending response can be observed. This behaviour is similar for all the joints. The same behaviour for all specimens was observed, except the peak load is higher for the joints welded by progressive welding.

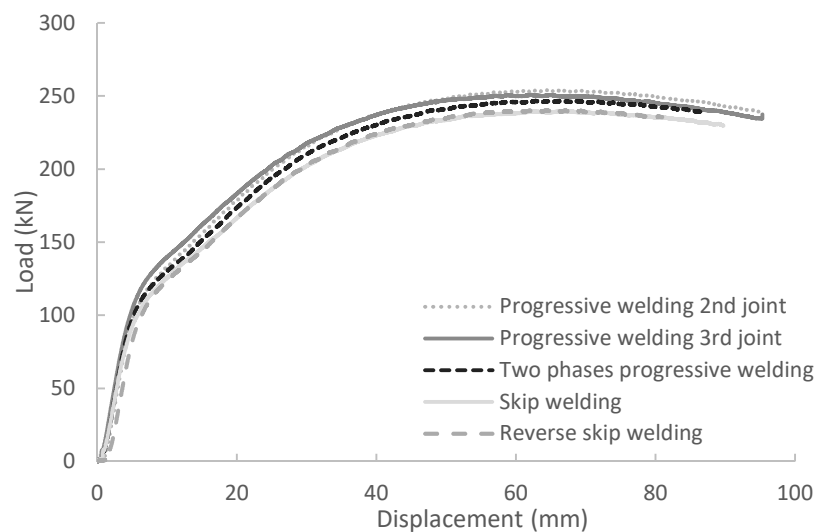


Figure 4.21: Load-displacement behaviour at top of the brace member, transducer 8.



Figure 4.22: First test, failure in the displacement transducers 5 and 8.

Figure 4.23 shows the load-displacement behaviour at top face of the chord. Transducers are located 60 mm away from the weld. Locating two transducer on both sides would allow checking the

tolerance and also if the load is applied 100 % straight downward. The maximum tolerance observed was 1 to 2 mm for the parts experiencing high. Figure 4.24 and Figure 4.25 show load-displacement for chord sidewalls and chord bottom face respectively. It was expected to observe a big deformation in chord side walls. The biggest displacement which was measured horizontally goes for progressive welding which was done in the first three tested joints with a displacement magnitude of 36 mm and the least goes to skip welding which was done in the last two tests with displacement magnitude of 27 mm. The same behaviour governs for the displacement at bottom face of the chord member. The bottom face deforms nearly 21mm and 14 mm for joints welded with progressive and skip welding schemes respectively.

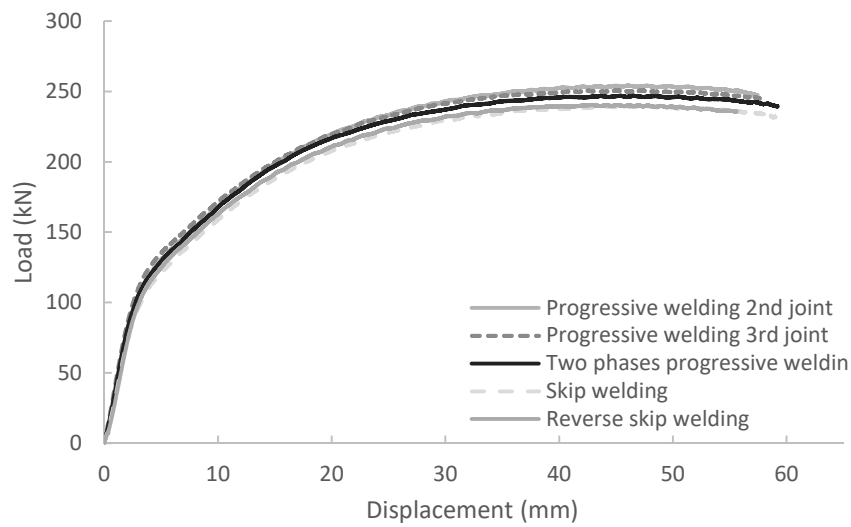


Figure 4.23: Load-displacement behaviour of chord top face, transducers 2 and 3.

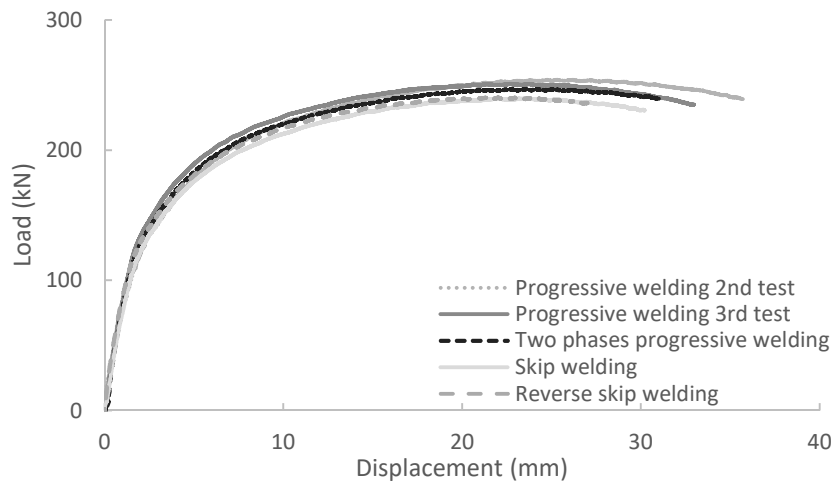


Figure 4.24: Load-displacement behaviour at chord side walls, transducers 5 and 6.

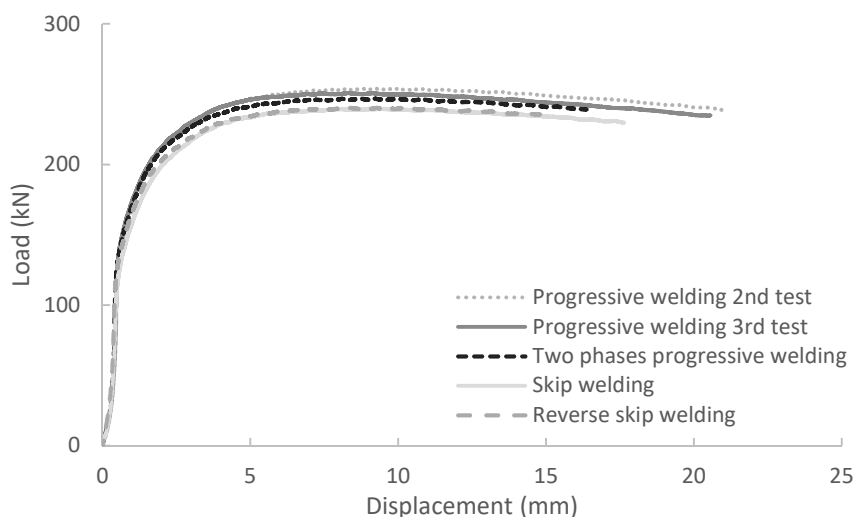


Figure 4.25: Load-displacement behaviour at chord bottom face, transducer 7.

Table 4-5 shows the ultimate load achieved for each T-joint investigated experimentally. Each single joint has been loaded under the same loading conditions. Due to an accident between two inductive displacement transducers the first test was stopped at an applied load of 200kN. Load-displacement results of the first three tests (joints welded by progressive welding) show the same behaviour until the stop points of loading. In the next step the joint welded by double phase progressive welding has been tested. T4 reflects a drop of 4% in strength compared to the joints welded by progressive welding (T1, T2 and T3). Joints welded by skip welding (T5) and reverse skip welding (T6) have been tested in the next step. Both present the same decrease in strength, nearly 7% compared to the joints welded by progressive welding. In total 6 joints have been tested with only one variable which has been the number of welds (start and end points). All joints reflect quite the same behaviour in the elastic region and later on the differences become clearer. As a small conclusion in this part, joints welded by progressive welding offer a better strength compared to other tested joints. The influencing parameters and how the strength drops by an increase in the number welds, will be discussed more in detail in the Chapter 6.

Table 4-5: Test matrix.

Specimen	Weld sequencing scheme	Maximum load (kN)	Gain in strength (%)
<b>T1</b>	Progressive welding	Stopped at 200	-
<b>T2</b>	Progressive welding	254	taken as 100
<b>T3</b>	Progressive welding	253	taken as 100
<b>T4</b>	Two phases progressive welding	245	-4
<b>T5</b>	Skip welding	239	-7
<b>T6</b>	Reverse skip welding	239	-7



### 4.7.2 Load-Strain Behaviour

The axial load is plotted versus axial and lateral strains of specimens in Figure 4.26 which presents load strain behaviour of strain gauges 1 and 2 for experimental tests 1 to 6. The following results are presented in order to assure the accuracy and equivalence of the loading process and further response of the material only in the experimental tests. All test specimens show the same behaviour in the elastic region. However, the plasticity occurs at different strain levels and hence the stability failure. For strain gauge number 1 the biggest difference could be seen in between specimens welded with progressive welding (T2 and T3) and two phases progressive welding T4. However, this difference in behaviour in terms of strain magnitude goes to the specimen welded with skip welding (T5). Both strain gauges 1 and 2 show that that yielding, failure and also plasticity limits happen in the same range of loading. Strain gauges 3 and 4 which are also on the chord surface where the chord face failure occurred are shown in Figure 4.27 as for strain gauges 1 and 2, here yielding happened before the peak load was reached and afterwards the stability failure. Strain gauge number 3 faced a failure as can be seen, presenting unreliable values for load-strain behaviour. Strain gauge number 4 behaves slightly the same as number 2 but obviously in reverse order. For strain gauges number 3 and 4, all the specimens show the same behaviour in elastic and plastic regions with minor differences.

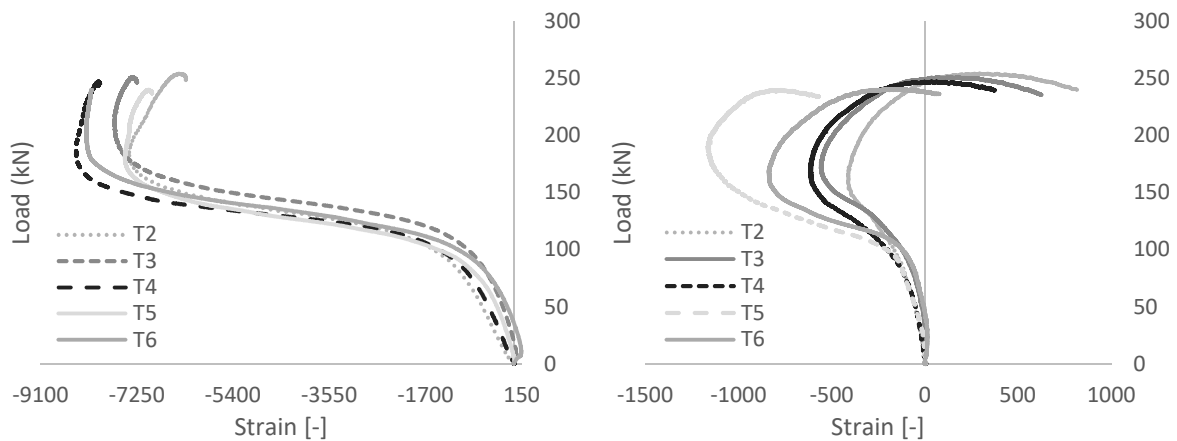


Figure 4.26: Strain gauge 1 (left) and stain gauge 2 (right).

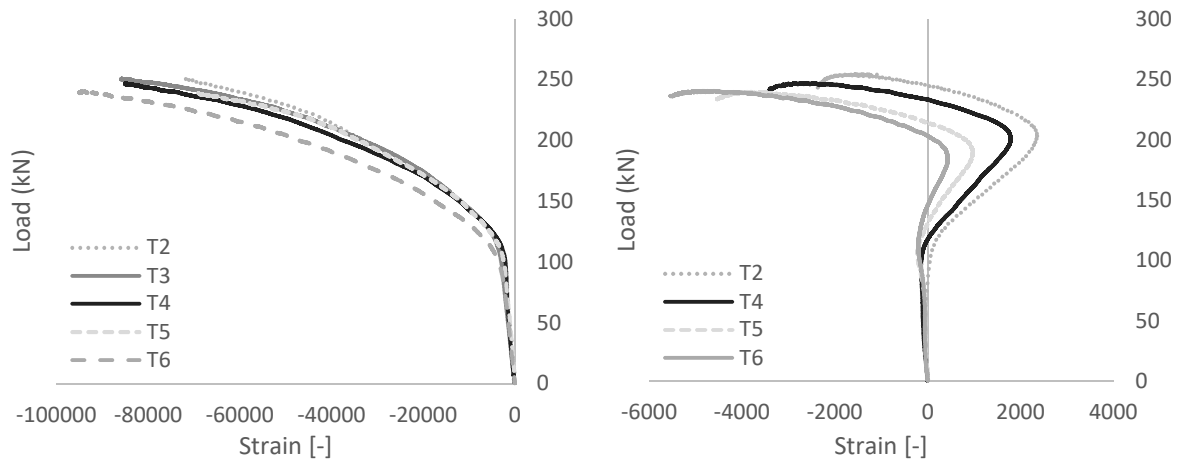


Figure 4.27: Strain gauge 3 (left) and stain gauge 4 (right).

Load-strain behaviour for strain gauges 5 and 6 are shown in Figure 4.28. Strain gauges 1 to 6 are all located on top face of the chord member. As can be seen in strain gauges 5 and 6 present the same behaviour as number 1 and 2 as these strain gauges were installed on the same axis but on various sides of brace. Data presented for strain gauge number 6 shows the difference between (T2, T3, and T4) and (T5, T6) clearer than in strain gauge number 2. Strains developed in strain gauges 7 and 8 are presented in Figure 4.29 these strain gauge were located on the webs of the brace. As it can be seen strain gauge number 8 which was installed close to the intersection part of brace and chord edge show extreme values which is due to high stiffness of this part.

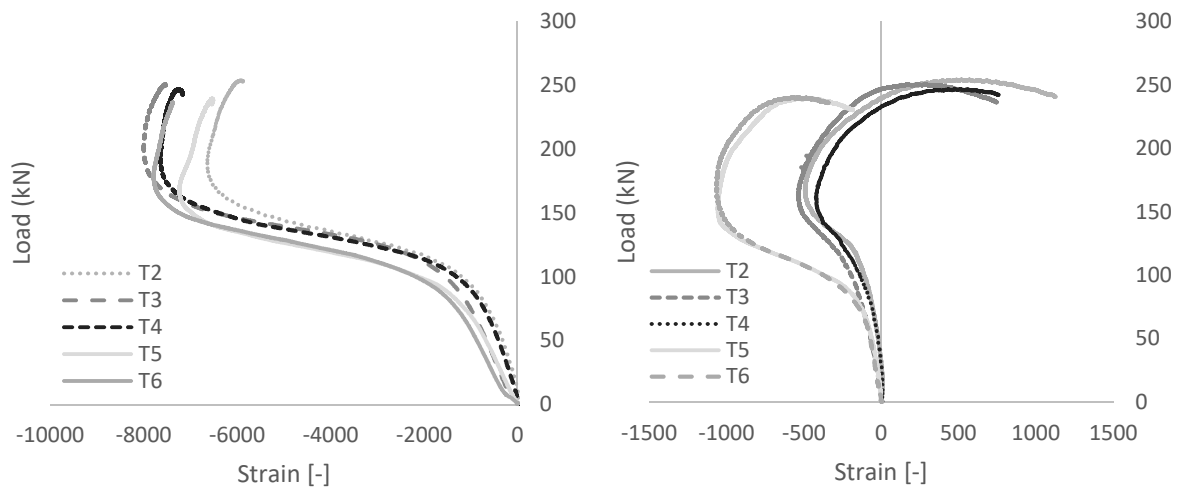


Figure 4.28: Strain gauge 5 (left) and stain gauge 6 (right).

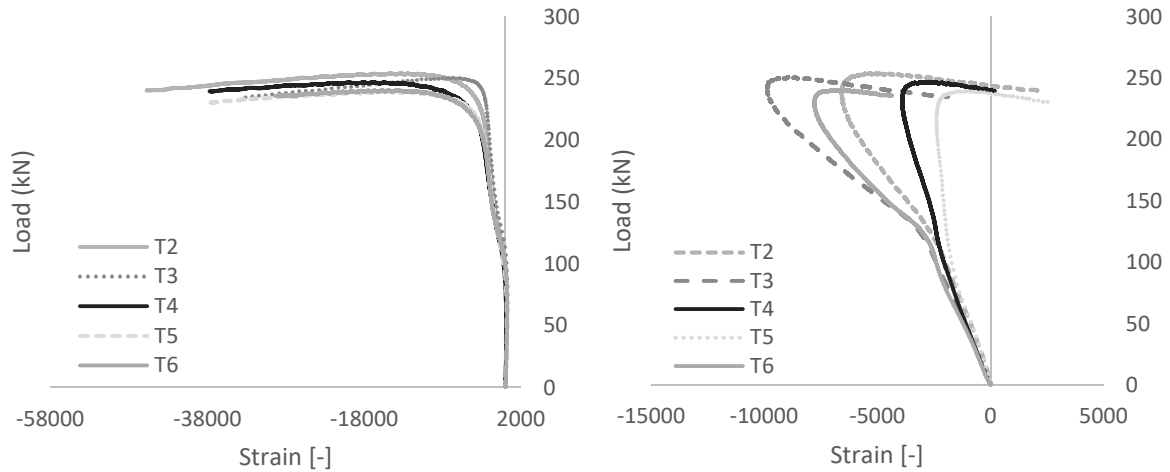


Figure 4.29: Strain gauge 7 (left) and stain gauge 8 (right).

Two strain gauges were also installed on chord bottom face in the centre, in order to observe the strains developing on this surfaces under loading which are both shown in Figure 4.30 as it can be seen both strain gauges present the same behaviour in elastic range reaching 220 kN, yielding and entering plastic range and afterwards stability failure. All specimens welded differently showed the same behaviour with very slight differences.

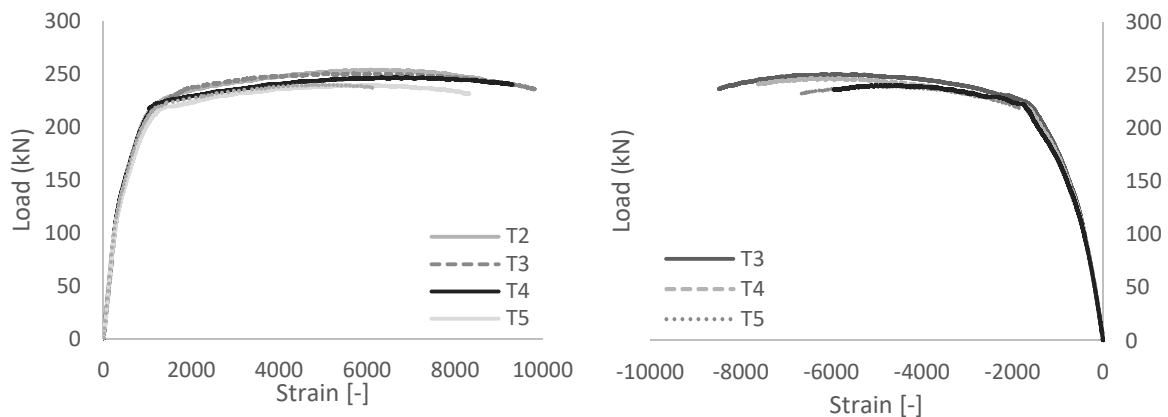


Figure 4.30: Strain gauge 9 (left) and stain gauge 10 (right).

An overview of all strain gauges points out the decrease in strength by increase in the number of welds to be used in welding of T-joint.

## 4.8 Failure Modes

Eurocode 3 [131] and CIDECT [132] have both covered the possible failure modes that could occur to T-joint made by SHS. The most common failure modes for T-joint made by SHS under axial compressive load are chord face failure and chord side sidewall failure (or chord web failure).

The experimental results show, all specimens 1 to 6 experience the same failure modes as stated above. The vertical member on which the compressive load was applied, first started moving down. High compressive load applied on the brace forces the chord face to deform and this deformation

on the chord face caused the symmetrical outward crippling of the chord side walls as shown in the Figure 4.31 As a result of the experimental test, it should be noted that various welding sequencing may influence load bearing capacity but it has no influence on the failure mode that T-joint experiences as the concept is the same.



Figure 4.31: Failure modes joint 1 to 6.

## 4.9 Conclusion

In this chapter 6 joints made of S355 welded by various welding sequences were experimentally investigated. The joints were welded under the same boundary conditions. The same welding machine and welding parameters were used for all the joints. The specimens were tested under brace concentric loading using a 2000 kN testing machine. The load is applied using stroke control at a rate of 3mm/min up to failure. By the comparison of the results the following conclusions can be made:

- Temperature distribution was successfully measured by using thermo-couples at different distances to the weld. However in 2 cases the elements were burnt due to the high heat close to the weld. The temperature was measured for three various welding sequences (progressive welding, double phase progressive welding and skip welding). The first two sequences present roughly the same distribution of temperature but the third case behaves totally different as the location of start and end points is different in this case.
- From the first welding sequence (progressive welding), three joints were welded and loaded which allowed a proper statistical investigation. When loading, the first joint was stopped as it reached the yielding point as some inductive displacement transducers failed due to their short length. The outcome of load vs displacement for the first three joints showed the same manner and magnitude. Around a maximum load of 255 kN was achieved for the joints with progressive welding.
- The results of experimental tests of load application (load vs displacement and load vs strain) show that increase in the number of welds could highly influence the gain in strength. The higher number of welds leads to less load bearing capacity of the joints. The outcome points out how important is the influence of stress concentration. Higher number of start and end points leave higher areas with concentrated stresses. A maximum load of 254 kN was achieved for the joint which was welded continuously with only one start and end point. For the second joint with 2 start and end points the gain in strength dropped by -4 %. The same applies to the joint (skip welding) with 4 start and end points by a reduction of -7 % in strength.
- Apart from the first test which was stopped, all the joints experienced the same common failure modes for T-joints made of RHS or SHS under compressive loading. At first, due to a high magnitude of compressive load the chord face failure occurred which caused the side walls crippling of the chord members.
- Various welding sequences have been investigated in order to study the influence of each single sequence on the overall behaviour of a T-joint. But it should be mentioned that continuous welding or so called progressive welding should be always considered when

## EXPERIMENTS

different welding sequences are being investigated as this sequence is widely and industrially adopted around the world with leaving only one start and end point.

# 5 NUMERICAL MODELLING

## 5.1 Chapter Synopsis

This chapter explains the Finite Element Modelling of welding and loading processes. Two software are used for this purpose (ABAQUS and SYSWELD). The FE-software SYSWELD v2014 is used for the thermo-mechanical simulation of the welding process and ABAQUS AWI is used for welding simulation in the meaning of temperature application. Investigations on the influence of welding sequencing patterns on the load bearing capacity of a S355 steel square hollow section (SHS) T-Joint are done. The type of welding process used is metal active gas (MAG) welding. A fillet weld with a throat thickness of 5 mm is performed. After the welding simulation, the results in terms of stresses and distortion are validated with the experimental data. Single phase material is used in both software and the influence of phase transformation is only included in the appendices. Due to the geometrical characteristics of this type of joint a compressive test is performed. A load is applied on the upper surface the vertical member (brace). The force-displacement behaviour is plotted and discussed. The differences and influencing parameters are identified. The modelling is done for all cases (listed in Table 5-1) involved in this work. For better evaluation of results two extra numerical simulations are performed in this chapter which help making a sufficient conclusion. Figure 5.1 shows the two extra cases adopted in this chapter.

Table 5-1: Cases investigated in the numerical simulation.

Cases	Welding sequence
N1	3 specimens welded by progressive welding
N2	Double-phase progressive welding
N3	Skip welding (4 welds)
N4	Reverse skip welding
N5	Back-step welding
N6	Skip welding (8 welds)

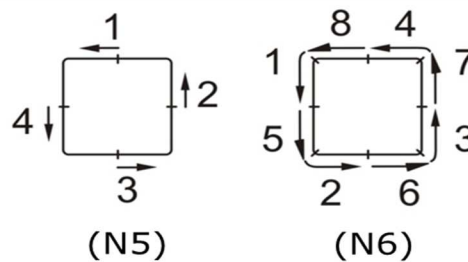


Figure 5.1: Extra adopted cases in the numerical analysis.



## 5.2 Finite Element Modelling

Finite element modelling is done in order to simulate what is happening in reality. To obtain results which are identical to those obtained from the experimental tests, FEM requires sufficient data such as the geometry itself, boundary conditions, loading and material properties. Sufficient data increases the accuracy of the results obtained and requires high attention and in some cases parametric studies. In the present work finite element method using ABAQUS [133] is used. The same model is built for all the cases listed in Table 5-1 as the only variable is the weld and its respective sequences. The geometry of the model with required partitions for mesh generation is shown in Figure 5.2. Finite element model solving is highly dependent on how the mesh is generated. Meshing has also a great influence on computation time. The basic problem in welding is the discretisation of a domain holding a localised region with large gradients in field variables. Thermal, microstructural and mechanical effects require the weld zone to be resolved down to a fabrication of millimetre while the far field region can be coarsely meshed. The mesh has been generated using ABAQUS and by element set definition, parts have been introduced in an input file to be used in SYSWELD.

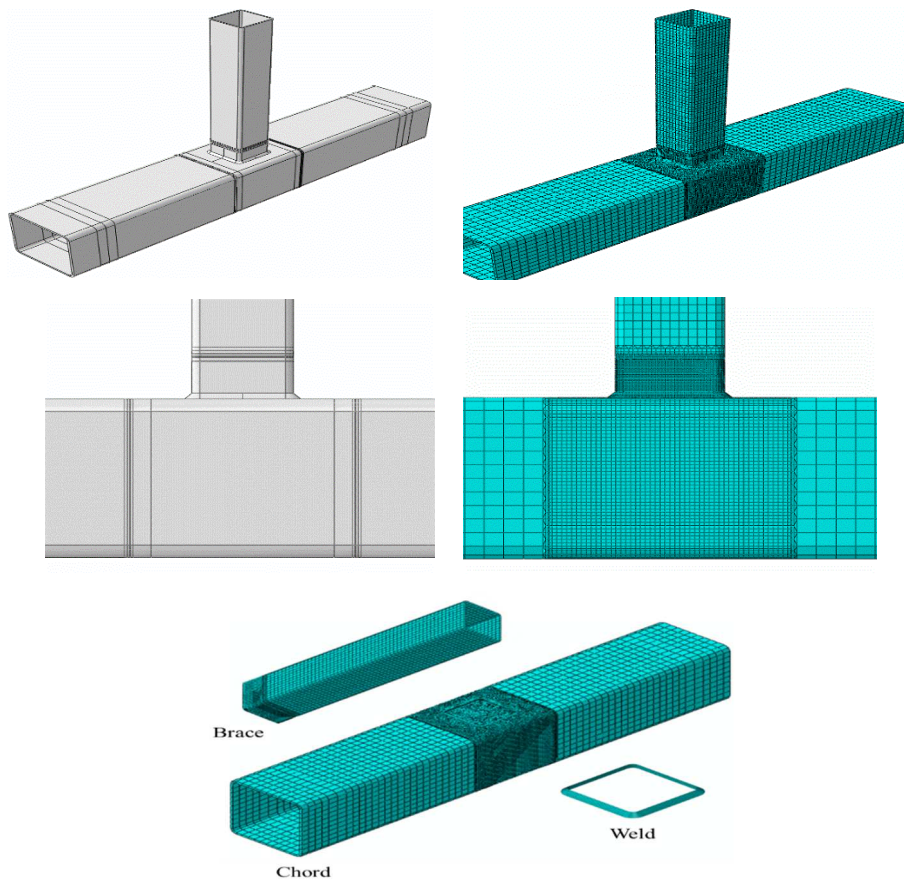


Figure 5.2: Geometry with the finite element mesh for the three-dimensional analysis.



The element types used for Thermal and Mechanical analyses in welding simulation are summarized in the Table 5-2.

Table 5-2: First order element types used for thermal and mechanical analyses.

<b>Heat-Transfer Element Types</b>	
<b>DC3D8</b>	An 8-node linear heat transfer brick
<b>DC3D6</b>	A 6-node linear heat transfer triangular prism
<b>DC3D4</b>	A 4-node linear heat transfer tetrahedron
<b>Stress Element Types</b>	
<b>C3D8</b>	An 8-node linear brick
<b>C3D6</b>	A 6-node linear triangular prism
<b>C3D4</b>	A 4-node linear tetrahedron

### 5.3 Boundary Conditions

Boundary conditions are important factors which can have direct effects on the outcome of numerical simulation. In the numerical simulation of welding and load application the same boundary conditions are applied as in the tests. Indeed, the boundary conditions during welding differ that the ones in loading.

As in test while welding the joint is fixed in x-, y- and z-directions at four points on the chord member. Regarding the boundary conditions for loading test, various methods can be adopted as in [40], [134] and [135] depending on the interests in outcomes. In this case, as the joint are comparably big so they require combination of boundary conditions to be applied.

Nodal supports are adopted below the chord member by taking into the consideration L/h as previously mentioned in load application in the experimental part. One node is welded to the base which makes the node totally restrained in all directions and the other node is only allowed to move in the z-direction. The sides are also supported and restrained in x-direction as in the tests. Figure 5.3 shows the boundary conditions adopted for welding simulation.

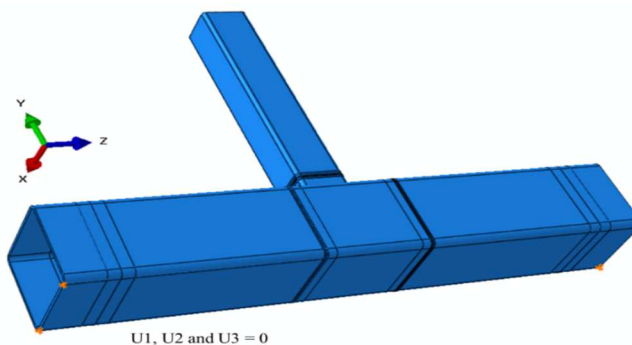


Figure 5.3: Adopted boundary conditions during welding.

As explained previously various boundary conditions have been adopted in the numerical analysis. The nodal supports and side supports are shown in Figure 5.4. The side supports are simply challenging. The nature of this support as used in test requires a parametric study in order to study the development of friction while loading between the plates used for avoiding the sides to deform in x-axis. The results have shown that consideration of friction with magnitude of 0.7 for dry steel on dry steel has no influence and the sides could be simply restrained in x-axis. The friction force can be expressed by the equation below, where  $F_f$  is the frictional force,  $\mu$  is the static or kinetic frictional coefficient and  $N$  is the normal force.

$$F_f = \mu N \tag{5.1}$$

The coefficient of friction between two materials in relative sliding may depend on contact pressure, surface roughness of the relative harder contact surface, temperature, sliding velocity and the type of lubricant whether the level of contamination. It's the reason that the data found in the many reference tables available may show a large variation [136].

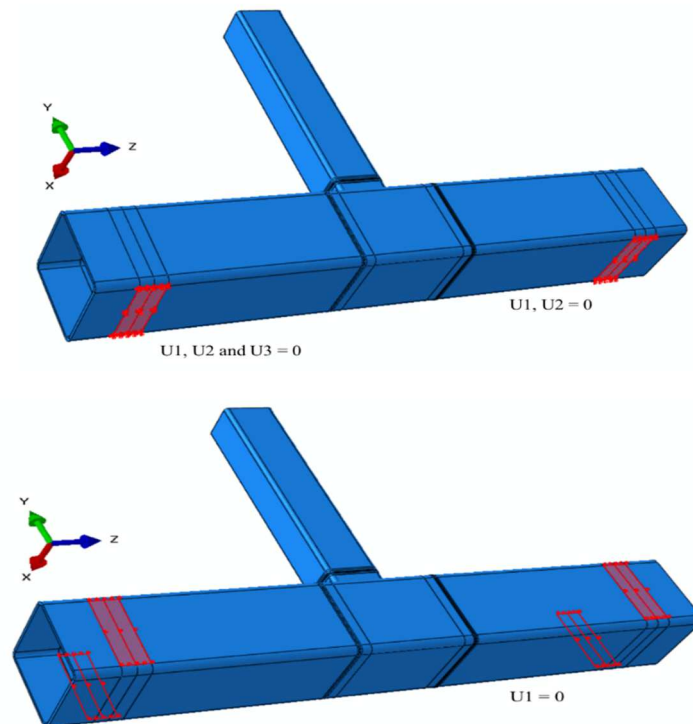


Figure 5.4: Nodal and side supports adopted for the loading analysis.

As in the experiment the load is applied on the top surface of the brace member (all surfaces are covered). The load is applied in the meaning of displacement with magnitude of -110 mm going downward vertically. Load application in the meaning of N or kN might cause tolerance and for avoiding that tolerance some introduce various boundary conditions. Therefore applying displacement has shown to be less problematic.

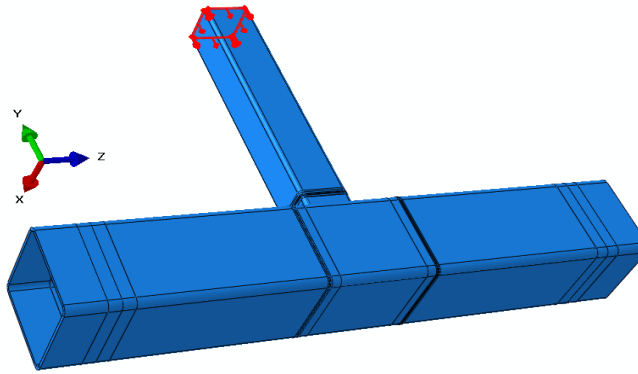


Figure 5.5: The geometry and applied load.

For studying the influence of welding imperfection on the load bearing capacity of the T-joint it is important to have the deformation caused by loading localised. Localised deformation (local deformation) in the intersection area where the weld exist would allow studying the sequencing affects better. Side supports play an important role in this case. These supports can perfectly shift the deformation to the intersection area where the members meet each other. On the other hand they let modelling and studying the behaviour of the joint as it is part of a truss.

## 5.4 Material Definition

Material definition of the joints in the numerical analysis has been done by using true stress-strain curves as shown in Figure 4.3. All thermal and mechanical properties of the material have been defined temperature dependent. As in this work the results of numerical analysis are compared between two different programs ABAQUS and SYSWELD, so it is very important to have the same material in both numerical simulation programs. ABAQUS does not cover users with material properties so it is important having access to a material library such as the ones from SYSWELD or SIMUFACT.

## 5.5 Models Validation

Residual stresses and deformation induced by welding have been only measured numerically. Calibration of the numerical models has been done based on the results from the tests. Deflection of the joint ( $U$ ) under the external load ( $F$ ) applied has been measured at several points as well as the temperature distribution for welding. After careful consideration of boundary conditions and material properties validation has been done by comparing the outcomes of numerical and experimental tests. The behaviour of joints with various welding sequencing and their respective  $F - U$  diagrams would be illustrated in this chapter by focusing on the welding imperfections.

### 5.6 Welding Simulation

ABAQUS AWI and SYSWELD have been used to create the heat transfer and stress analysis models. The joint segments being welded is 400 mm long. The weld metal properties are assumed to be the same as that of base material. For AWI an element face-based chunking option is used with 6 rows of elements per chuck, with each bead subdivided into 64 element-based chunks. A target torch temperature of 1500 °C is used as heat input from the welding source. A torch step time of 1.2 second was estimated for each chunk based on the welding speed in the experiments. AWI generates pre-defined temperature field required for stress analysis based on heat transfer analysis. In SYSWELD the welding parameters are given as in the experiment which are shown in the Table 4-3. In this part, it has been tried to compare both AWI and SYSWELD results and deliver an appropriate conclusion regarding the methods used in each program. As it has been mentioned previously, AWI is a temperature based welding simulation in which the heat source is missing, the tool tries simulating welding by activation and deactivation of elements introduced in the weld bead. However, SYSWELD offers a proper welding modelling with all required material properties and a great heat source model and relevant parameters.

In all the cases the T-joints were welded using MAG with a throat thickness of 5 mm. In the experiment the welding was done by hand so minor changes in the weld throat thickness was expected. However, this minor change in the throat thickness is neglected in the numerical simulation. Table 5-3 shows the welding and heat source parameters used for all various welding sequences. The welding parameters are set as the ones which have been given in the experimental analysis but the heat source parameters required for the welding simulation are achieved using the equations included in Table 5-3.

Table 5-3: Welding and heat source parameters.

Parameter	Value	Dimension	Equation	
Front length ( $a_1$ )	14.3	mm	$a_1 = (a + 1.5) * 0.6$	Heat source parameters
Rear length ( $a_2$ )	3.9	mm	$a_2 = (a + 1.5) * 2.2$	
Total length (L)	18.2	mm	$L = a_1 + a_2$	
Width (b)	8	mm	$b = a + 1 \text{ to } 2$	
Depth (c)	8	mm	$d = a + 2 \text{ to } 5$	
Heat input (Q)	872	J/mm	$(U.I/v) * 60/1000$	Welding parameters
Current (I)	230	A	-	
Voltage (V)	22	V	-	

### 5.7 Temperature Field

As explained in Chapter 4, measurements of temperature have been performed on both the chord and brace member at different distances to the weld bead with respect to the equation and the distances in Table 5-4. Temperature distribution is a key element which depends on so many parameters such heat source and welding parameters. Due to the importance of temperature distribution a careful comparison has been done for all cases involved in this study. So at the first step this key element is compared and validated. For the first two cases the thermos-element installed at the distance of 8 mm got defected by high heat input. The same occurred to the thermos-element installed at the distance of 10 mm on the brace member for skip welding.

Table 5-4: Points at which the temperature have been measured.

$T_{\max.LQ}(\delta y) = 0.242 \frac{qv^{-1}}{cp\delta y} + T_0$		
Chord	Brace	Dimension
8	10	mm
10	20	mm
18	30	mm
25	45	mm
45	60	mm
60	-	mm

Where  $q$  is the energy input and derived by the equation below;

$$q = \eta \cdot U \cdot I \tag{5.2}$$

Where  $\eta$  is the welding efficiency,  $U$  is voltage and  $I$  is ampere,  $v$  is the welding speed,  $T_0$  is the room temperature,  $p$  is the density and  $c$  is the specific heat.  $\delta$  value differs when considering each member shaping the joint with respect to the relation, full thickness of the member for which the temperature is measured plus half of the thickness of the intersecting member. As brace and chord members vary in the wall thickness so temperature distribution as well as fusion and heat affected zones vary too. Figure 5.6 shows the distribution of temperature in both members from SYSWELD. The heat source is fitted perfectly and apart from covering the weld with sufficient heat, it also reaches the members and an appropriate part of both members are melted when welding.

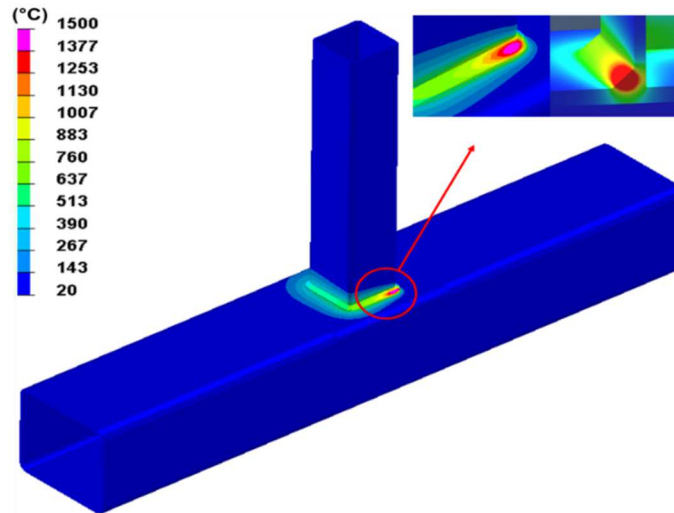


Figure 5.6: Temperature distribution, Fusion zone and heat affected areas (SYSWELD).

The temperature distribution for progressive welding performed numerically and experimentally are shown in Figure 5.7 and Figure 5.8 for both chord and brace member. As it can be seen the maximum temperatures reached are in a good agreement for the selected points at different distances. The peak temperature reached on the brace and chord member differ as the brace member is thinner. The curves follow the same trend with some small differences while cooling down. The joint was left to cool down for nearly 500 seconds and as it can be seen in both simulation and experiment it reached below 100°C. The temperature distribution for brace as for the chord was measured at different distances close to the weld and away. The closest thermos-element to the weld bead on the brace experienced the highest temperature with the magnitude of 640°C. However, the same point in welding simulation shows 625°C which reflects a very minor difference. The comparison of the results shows a good agreement and by getting away from the weld bead the difference gets smaller.

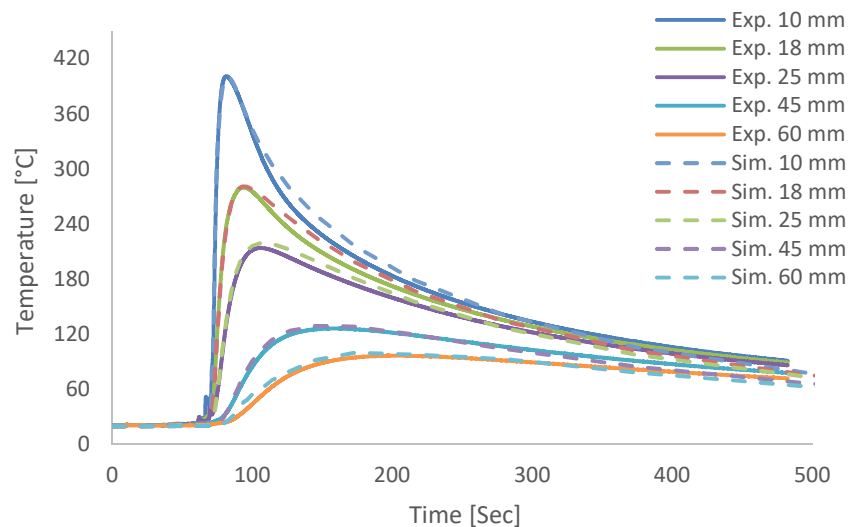


Figure 5.7: Temperature distribution on the chord – welding simulation vs experiment for progressive welding.

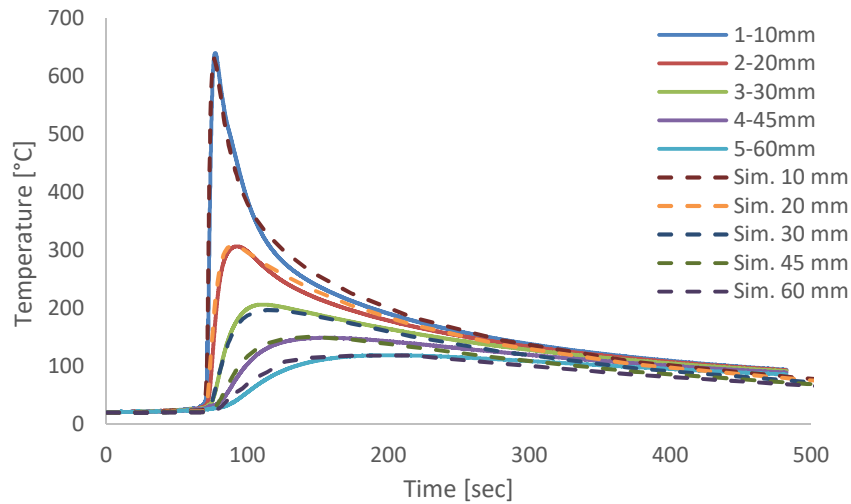


Figure 5.8: Temperature distribution on the brace – welding simulation vs experiment for progressive welding.

For the second case (double-phase progressive welding) the same temperature distributions have been captured as the points do not experience any differences compare to the first case. The results of temperature measurement for both chord and brace members are plotted in Figure 5.9 and Figure 5.10 for numerical simulation and from experiment of skip welding. As it can be seen the curves follow the same trend with very small discrepancies especially for the brace member which the data vary between the start and end points. The difference get bigger by getting away from the heat affected zone and by cooling down disappears. The location where the thermos-elements were set experience a start and end point. This is clearly shown in the related diagrams below in which two peak temperatures are observed.

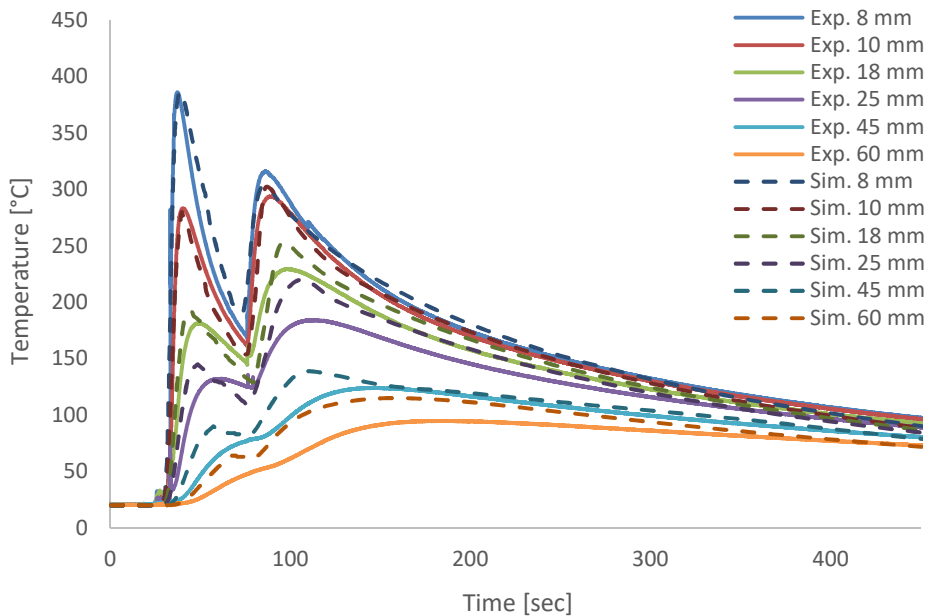


Figure 5.9: Temperature distribution on the chord – welding simulation of skip welding.

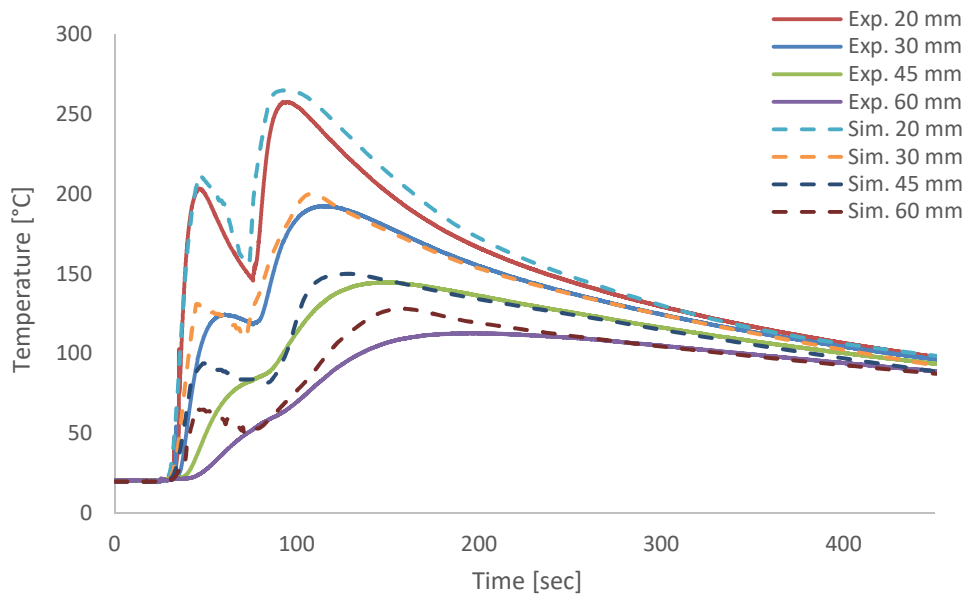


Figure 5.10: Temperature distribution on the brace – welding simulation of skip welding.

### 5.8 Numerical Load-Deflection Behaviour

The joints have been numerically tested under brace concentric loading using static general method. The corresponding behaviour of the joint is clearly shown in Figure 5.12. The structural imperfections have been introduced to the joint before the load application begins. The introduction has been done in the initial step. The load in the meaning of deformation with a magnitude of -110 mm was applied up to the failure. The boundary conditions were set as exactly in the experiment and briefly described in section 5.3. The (L/h) ratio of the chord was carefully selected as per recommendations in the literature. Due to the loading condition and concentrated force, in theoretical point of view considering geometrical imperfection might make sense but validation of results has pointed out that these imperfections have the least influence on the behaviour of the joints investigated in this work. As shown in Figure 5.11 the measured tolerance in the wall thickness falls below 0.2 mm on both sides of the chord member and hence the geometrical imperfection are neglected.

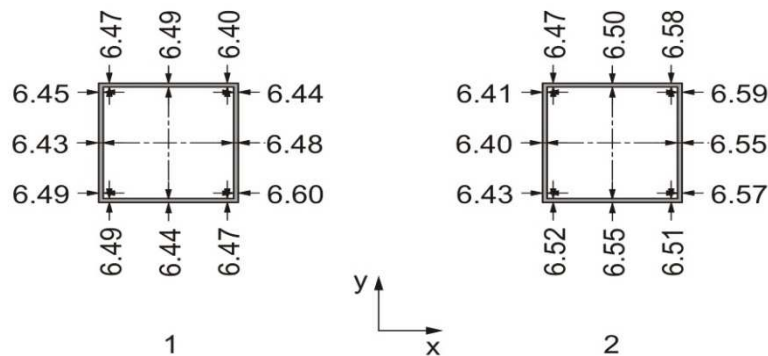


Figure 5.11: Measured tolerance in the wall thickness of the chord member in mm.



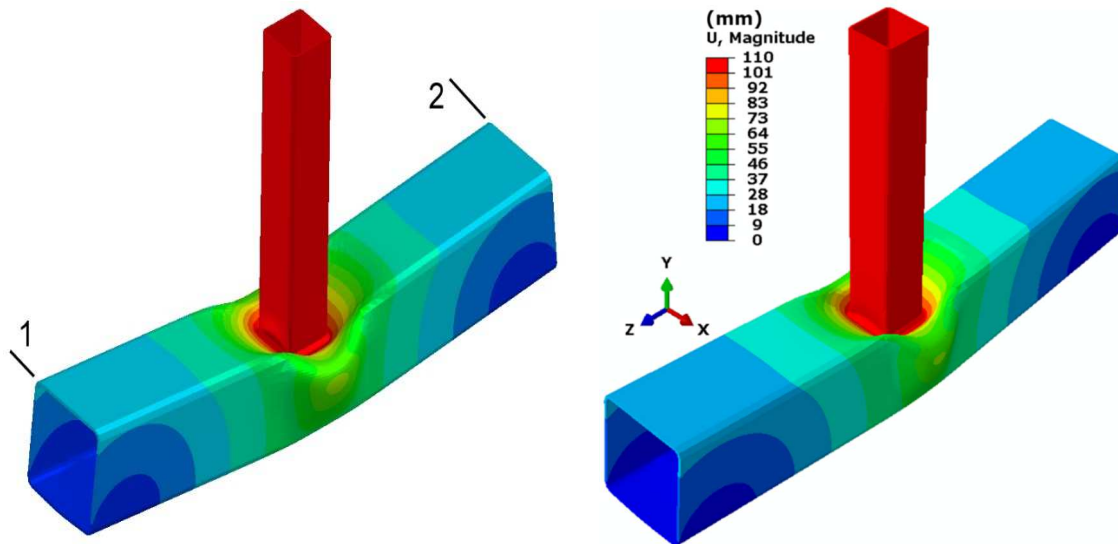


Figure 5.12: Progressive welding - load deflection behaviour of the T-joint, SYSWELD (left) and ABAQUS (right).

Apart from temperature/heat input validation, the overall behaviour of the joint under loading has been also investigated numerically and experimentally. Figure 5.13 shows the deformed joint after the loading process. The joint has experienced two possible chord side wall and face failure. As in the experiment, all the cases with various welding sequences have been loaded numerically. All the joints have experienced the two most common failure modes under axial loading which are chord face and side wall failure. The vertical member on which the compressive load was applied, first started moving down. High compressive load applied on the brace forces the chord face to deform and this deformation on the chord face caused the symmetrical outward crippling of the chord side walls as shown in Figure 5.13.

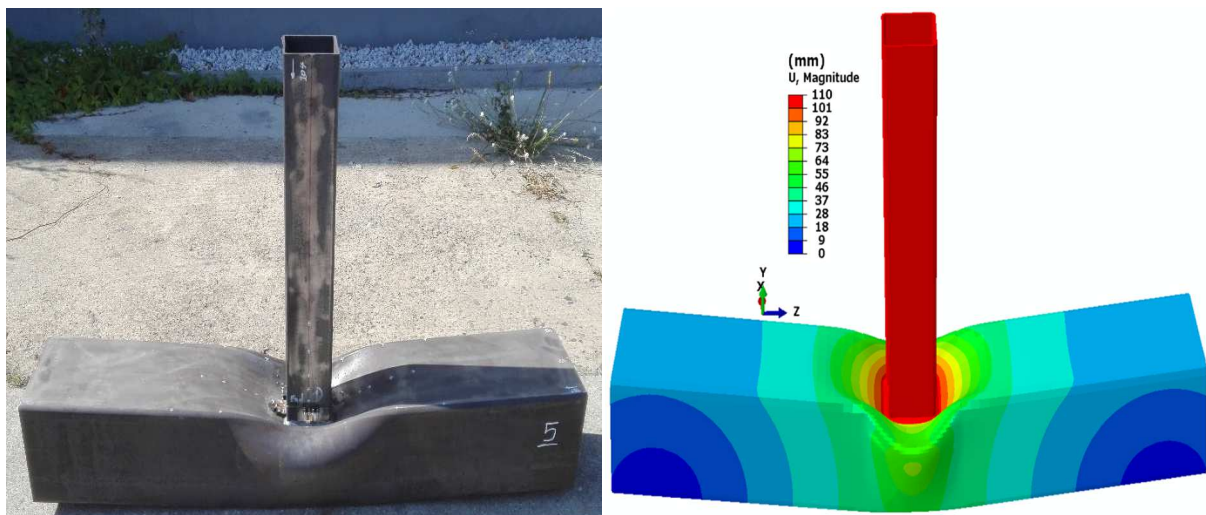


Figure 5.13: Deformed T-joint, test (left) and numerical simulation (right).

The load- displacement behaviour of the cases listed in Table 5-5 are illustrated in Figure 5.14. The results of numerical simulation from SYSWELD are compared with the tests results. The numerical and experimental investigated cases outcomes are in a good agreement. The material introduced to

the numerical cases more or less shows the same behaviour elastically and plastically as the load displacement curves offer minor disagreements. However, the maximum load reached differ slightly. For the joint which was welded by using progressive welding sequence, the maximum load reached in experiment has been 255 kN and 260 kN in numerical analysis. The joint which was welded using double-phase progressive welding behaves slightly different in terms of the maximum load reached. This joint has experienced a maximum load of 246 kN in the experiment and 255 kN in the numerical analysis. The third which was welded by using skip welding experienced a maximum load of 240 kN experimentally and 245 kN numerically.

As it can be noted the gain in strength drops when the number of welds increases. Compare to the first numerically and experimentally studied cases (V1 and N1), the second case (V2 and N2) experiences -4 % of gain in strength. The same applies for the third case (V3 and N3) by a magnitude -7 % gain in strength. The outcomes point out an important relationship. As the only variable in all cases investigated has been the welding sequences, so it could be clearly explained how stress concentration or so called the number of start and end points could highly influence the overall behaviour of the joints. In order to study the influence of stress concentration and also to observe what happens to the joint by increasing the number of start and end points a deep investigation on the overall stress distribution is required which is done in the following section.

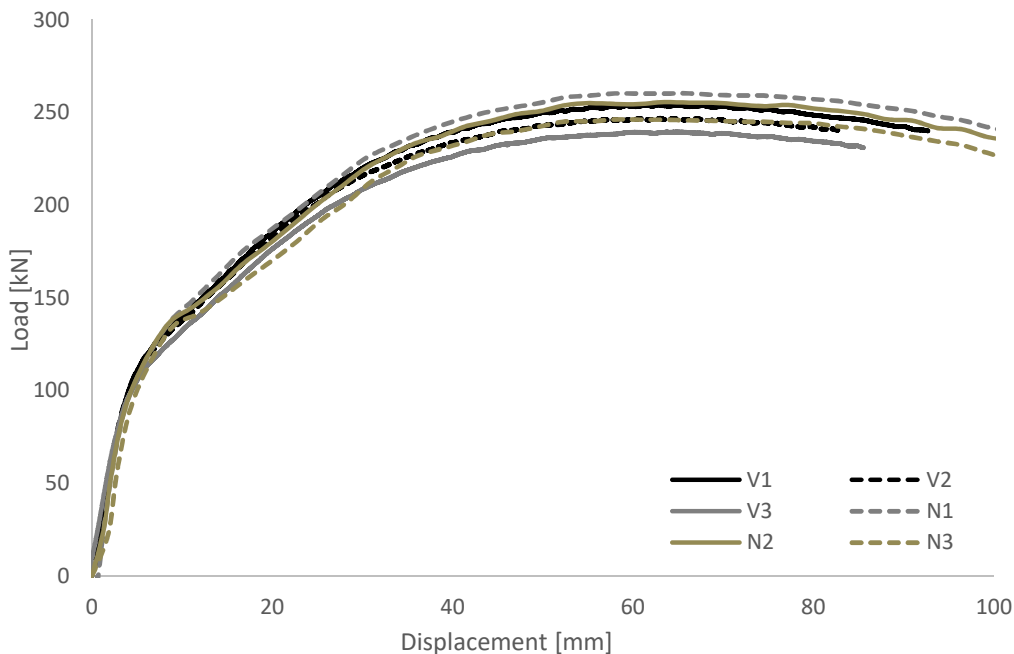


Figure 5.14: Numerical load vs displacement for all investigated cases.

Table 5-5: Maximum load reached for the investigated numerical and experimental cases.

Investigated cases	Investigation type	Welding sequence	Maximum load (kN)
V1	Experimental	Progressive welding	255
V2	Experimental	Double-phase progressive welding	246
V3	Experimental	Skip welding	240
N1	Numerical	Progressive welding	260
N2	Numerical	Double-phase progressive welding	255
N3	Numerical	Skip welding	245
N4	Numerical	Back-step welding	246
N5	Numerical	Skip welding (8 welds)	237

Figure 5.15 shows the load vs displacement from both software used. Both curves offer the same elasticity behaviour. However, ABAQUS tends to yield earlier. Compare to the experimental results shown in Figure 5.14, ABAQUS offers quite the same yielding behaviour than SYSWELD.

It should be mentioned that the disagreements are very small. Obviously, yielding earlier which happened in ABAQUS influences the plasticity and hence the maximum load reached differs slightly compare to SYSWELD. The maximum load reached in SYSWELD is 260 kN and in ABAQUS 258 kN. As both software offer more or less the same behaviour for further evaluation (load-displacement) the results from SYSWELD are only compared with the experimental outcomes.

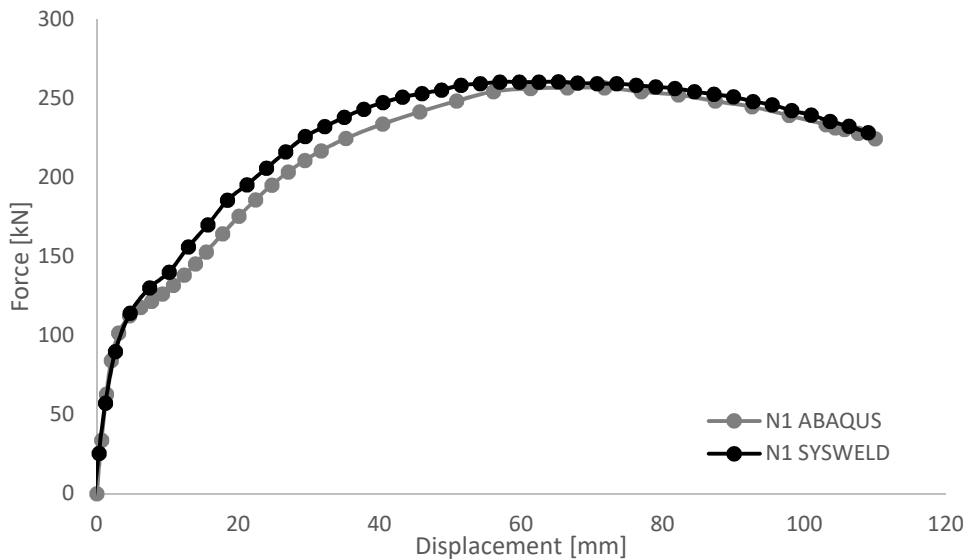


Figure 5.15: Load vs Displacement from ABAQUS and SYSWELD.

Apart from the brace member which is directly influenced by the concentrated force applied and shows the biggest deformation, the comparison of other points have been also done which helps a better validation of results. Figure 5.16 illustrates the load vs deflection behaviour of the points 3

and 4. Both points are located at 60 mm away from the weld beads on both sides. As it can be seen the curves follow the same trend with very minor differences.

Due to a high magnitude of load applied the chord face faces a high compressive load which leads to chord face failure. Close results of both sides also point out the zero or very small tolerance in the brace member while loading. Due to the nature of the closed section tested in this work and the kind of boundary conditions adopted, points 1 and 2 experience a maximum vertical displacement magnitude of -1.5 mm on both sides.

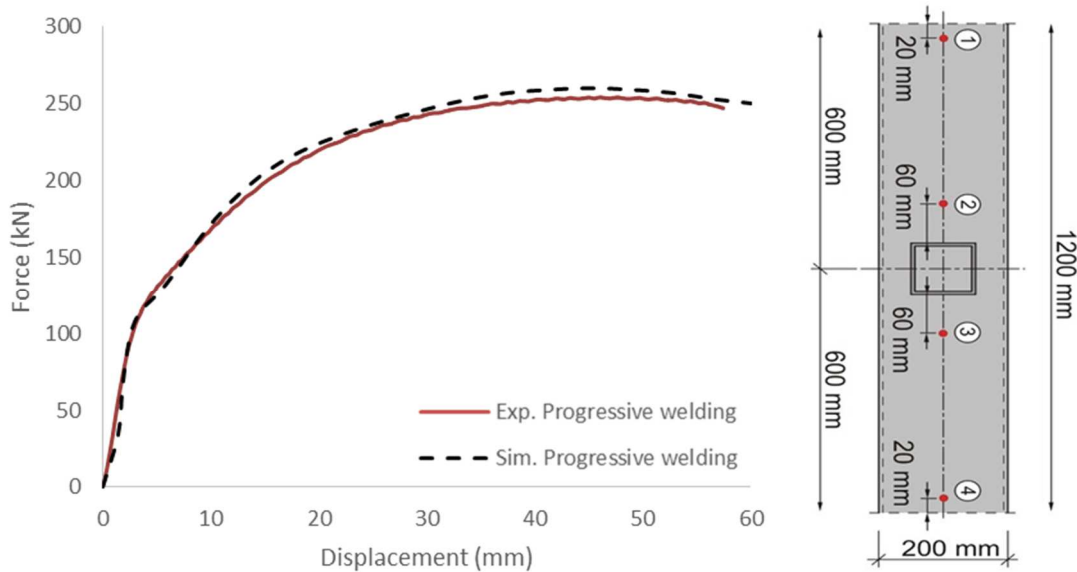


Figure 5.16: Load-deflection behaviour for points 3 and 4.

After the chord face experiences a high compressive load and moves towards inside, the chord side walls start crippling out. The magnitude of this crippling is shown in Figure 5.17 for points 5 and 6 which are located in the mid-surface on both sides of the chord member. A symmetrical deformation or so called crippling of side walls was expected as the centric loading allows for prediction. The results from experiment and simulation are in a good agreement with some minor differences in magnitude.

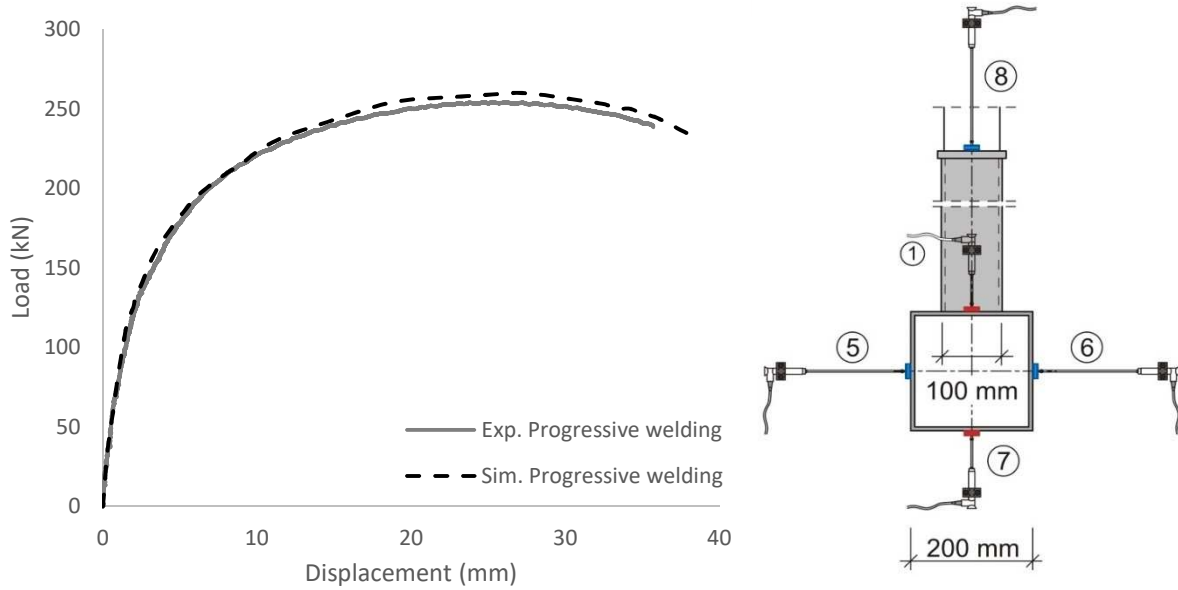


Figure 5.17: Load-deflection behaviour for points 5 and 6.

Figure 5.18 shows the load-displacement behaviour at point 7 which is located at the bottom surface and in the middle of the chord member. A maximum defamation of -23 mm has been captured after the loading process. Apart from some minor disagreements in the elastic and yielding parts, the results show a good and very close manners until the end of the loading process.

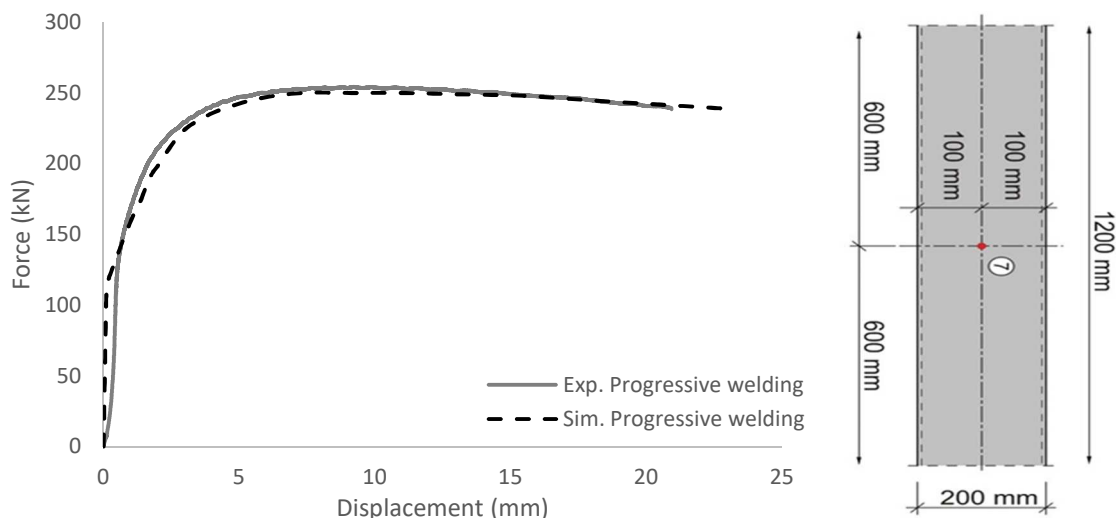


Figure 5.18: Load-deflection behaviour for point 7.

## 5.9 Distortions

This part shortly goes through the deformation induced by welding which was imported to the models before the load application as part of structural imperfections. The deformation distributions for both software are shown in Figure 5.19. The biggest deformation observed in both software happened at the top of the brace member as it could freely move and there was no boundary conditions set at this part. However the magnitude of maximum deformation observed reaches 1.14 mm but the overall deformation could highly influence the overall behaviour of the joint. Around

the weld bead and also in the chord member both software offer quite the same distribution. The difference in between the distribution of distortion is clearer at the top of the brace where a difference of nearly 0.5 mm could be captured.

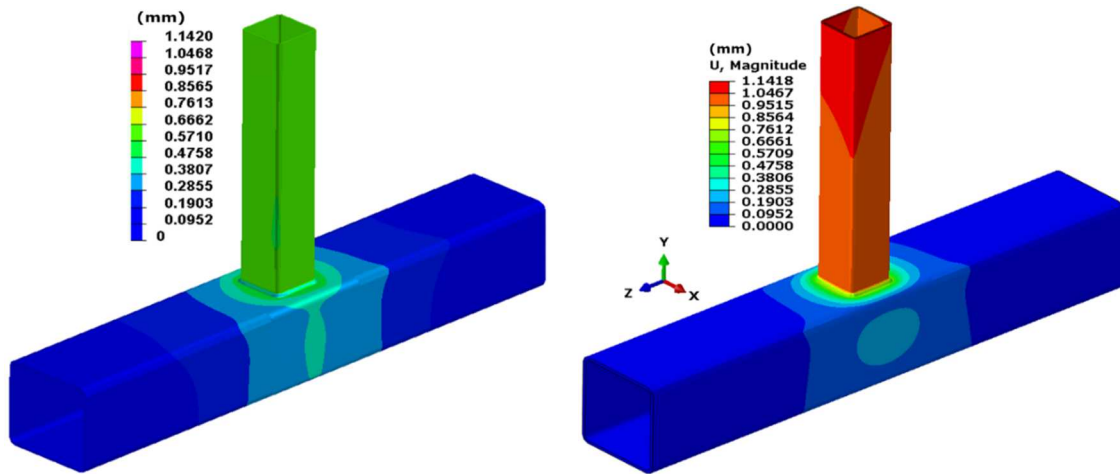


Figure 5.19: Welding induced deformation, SYSWELD (left) and ABAQUS (right).

## 5.10 Residual Stresses

Residual stresses have been always counted as important imperfections that welding leaves behind in the specimens to be welded and can influence the overall load-displacement behaviour until some extent depending on the joint. Figure 5.20 shows the influence of welding imperfections on the load bearing capacity of the T-joint determined with ABAQUS AWI. In this work, it has been tried to investigate the residual stress distribution numerically after a great validation of temperature fields. As residual stresses are only measured numerically, validation of results and studying the general behaviour of the welded joint requires both programs AWI and SYSWELD to be involved which delivers a better agreement regarding the overall distribution of imperfections and further behaviour of the joint under loading. Residual stresses in the longitudinal direction of the weld, in transverse direction and in the direction of plate thickness are considered as a results of similar mechanisms. The initial stresses induced by temperature application in ABAQUS AWI and a welding simulation of the T-joint by SYSWELD are shown in Figure 5.21. The distribution of Von Mises stresses offered by both programs are in a good agreement with some differences in the weld toe which is briefly explained by plotting the distribution of residual stresses in x, y and z directions in the next section of this work. The introduction of imperfection differ depending on the program used.

In ABAQUS the induced stresses from the temperature application are defined by setting predefined fields and also for induced deformation a .fil file has been created which also has been imported into the model before loading. However, the procedure in SYSWELD is less complicated and after the welding simulation and a given cooling period, the load application could be performed. Figure 5.22 shows the Von Mises stresses distribution for both programs after the load application.

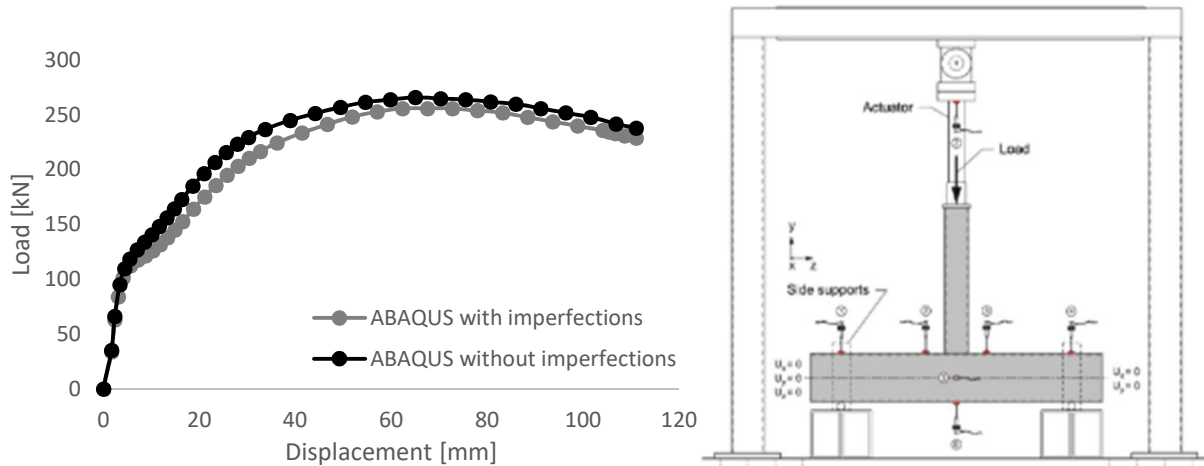


Figure 5.20: Influence of welding imperfections on the load bearing capacity of the T-joint.

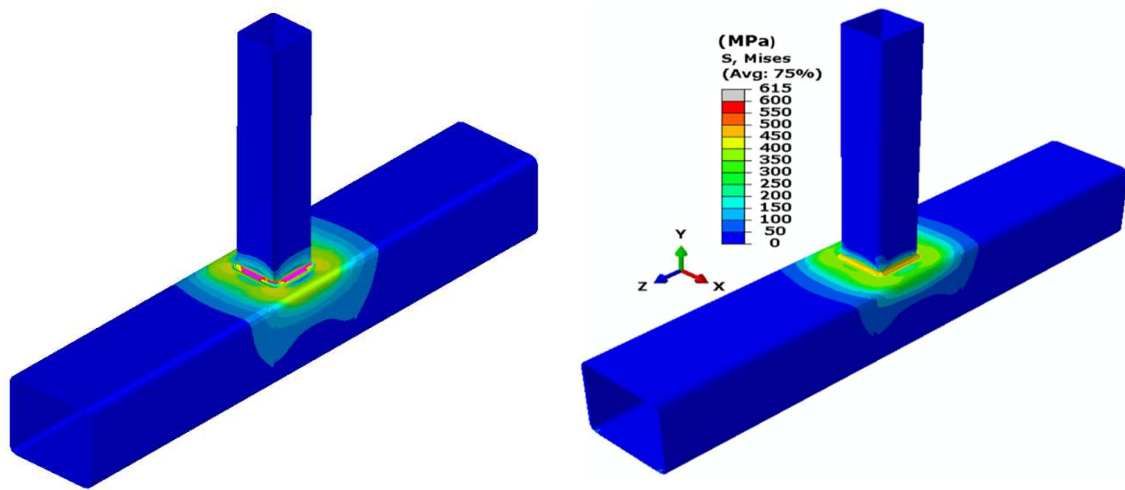


Figure 5.21: Von Mises stresses before the loading process, SYSWELD (left) and ABAQUS AWI (right).

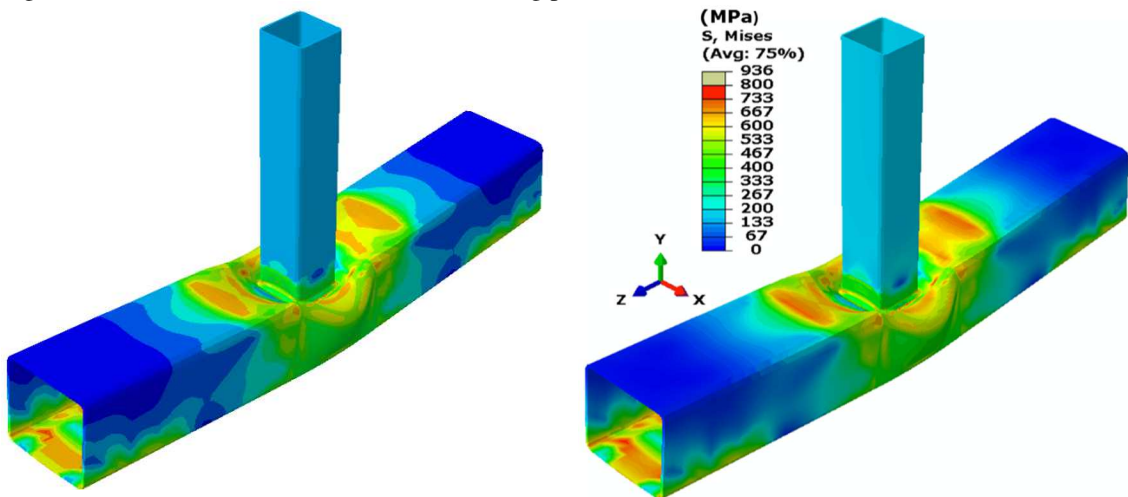


Figure 5.22: Von Mises stresses after the loading process, SYSWELD (left) and ABAQUS AWI (right).

For a better observation and also to compare the stress results, points on the midline of top surface of the chord member have been picked as shown in Figure 5.23. The aim behind selecting these nodes has been plotting the stress transition from the weld bead to the heat affected zone and then to unaffected areas (only surface nodes were considered).



The stresses are studied in two different phases. First phase goes through stress distribution after the joint cools down for a time period of 550 seconds and the second phase offers the residual stresses distribution induced by loading.

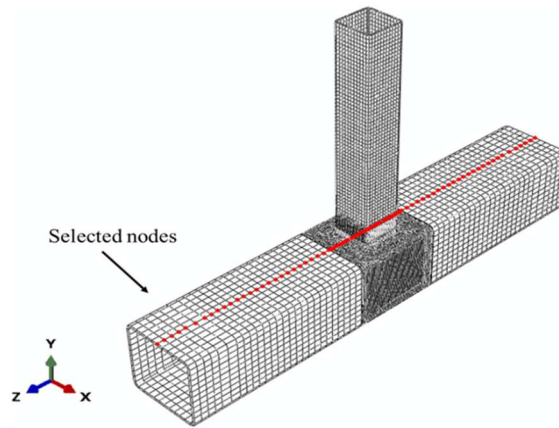


Figure 5.23: Line along which the stress is plotted.

### 5.10.1 Progressive Welding

#### 5.10.1.1 Longitudinal Stresses

##### Before the Loading Process

Figure 5.24 and Figure 5.25 show contour and line plots of the stress distribution in the x direction. Both ABAQUS and SYSWELD show quite similar distribution patterns. Compressive stresses are observed in the intersection area between the brace and the chord. By getting closer to the weld, the compressive stresses decrease to zero and then turn into tensile stress, which has a maximum magnitude of 500 MPa. The compressive stress reaches its highest value away from the weld (-250 MPa). Both curves display the same trend, with a small difference in the values in both compressive and tensile stresses. Point zero is the centre of the intersection area on the top surface of the chord and 50 mm from each side are the weld beads.

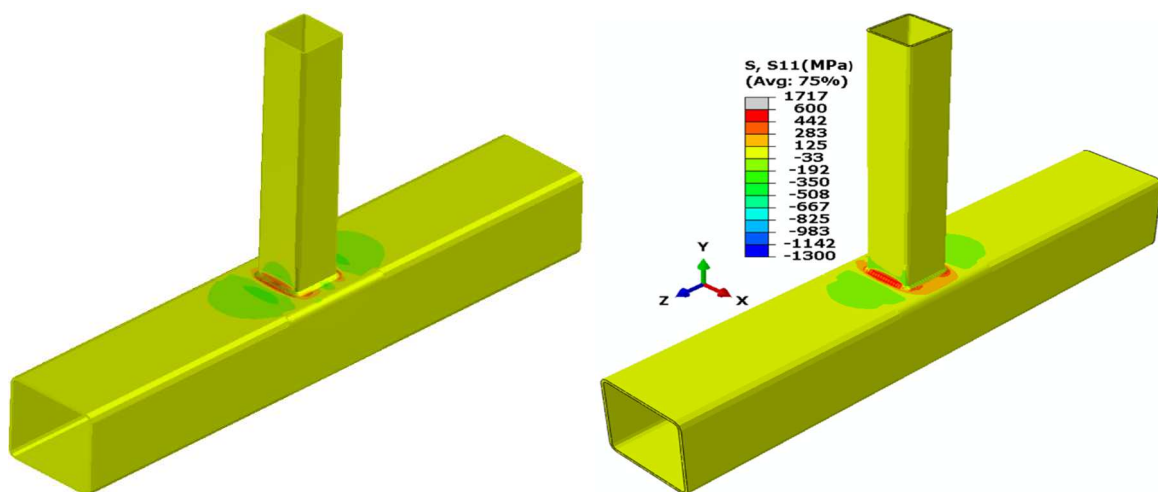


Figure 5.24: Progressive welding - stress distribution in x direction before the loading process, SYSWELD (left) and ABAQUS AWI (right).



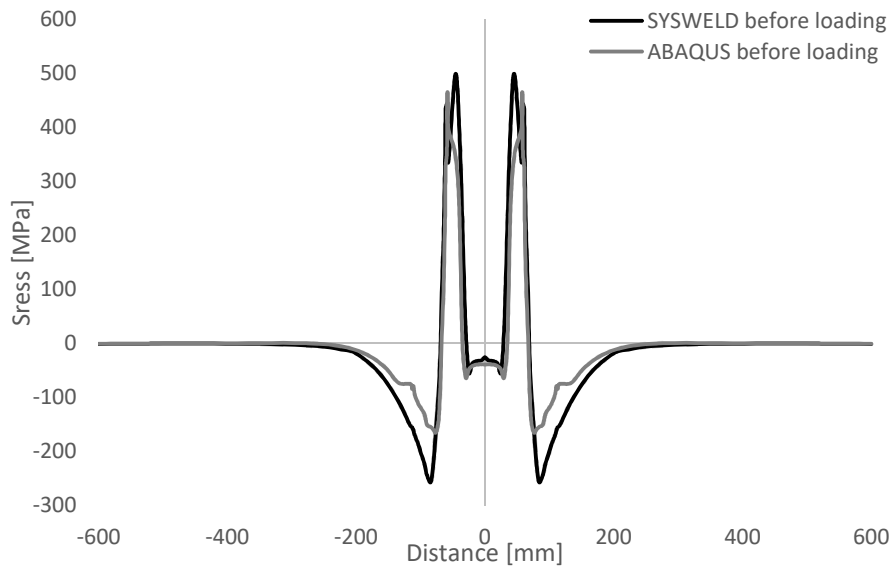


Figure 5.25: Progressive welding - stress distribution in x direction before the loading process.

After the Loading Process

In this section, induced longitudinal stresses due to loading are plotted. Loading has been modelled by applying displacement as in the experiment. Displacement with a magnitude of -110 mm has been applied on the top surface of the brace member as shown in Figure 5.5. The joint's behaviour after the load is applied with stress distribution in x direction are shown in Figure 5.26 and Figure 5.27. The behaviour of the two models shows minor differences in the intersection area and away. The maximum magnitude for tensile stresses at the centre of the intersection area is 420 MPa.

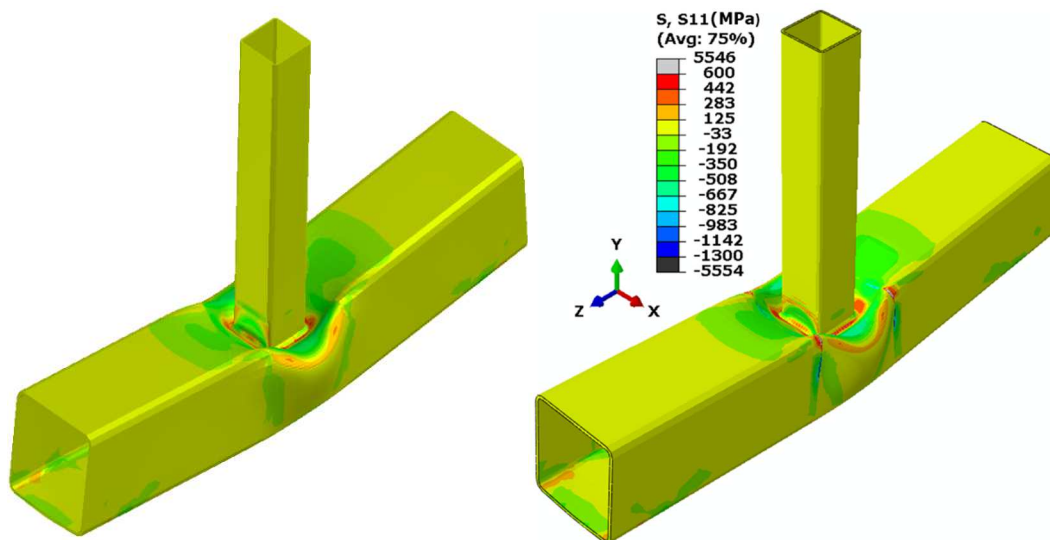


Figure 5.26: Progressive welding - stress distribution in x direction after the loading process, SYSWELD (left) and ABAQUS AWI (right).

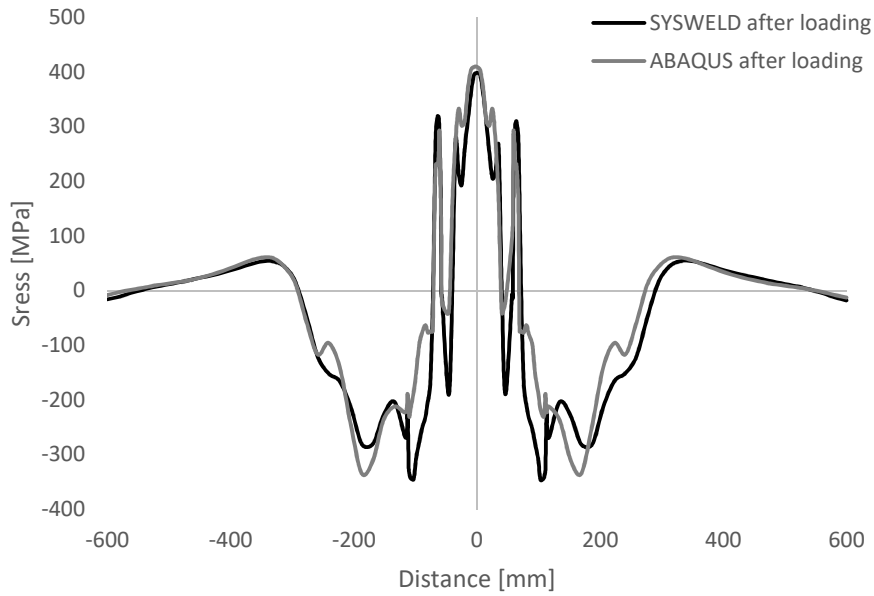


Figure 5.27: Progressive welding - stress distribution in x direction after the loading process.

5.10.1.2 Vertical Stresses

Before the Loading Process

Stresses in the y direction are plotted in Figure 5.28 and Figure 5.29. The comparison between the results from both software has shown that the behaviour of the joint does not differ significantly. The biggest difference observed is only 25MPa. As shown in the plots, the difference is small and can be neglected. The tensile stresses that appear here (26 MPa) rapidly turn into compressive stresses. The stress value doesn't face any further significant changes and reaches zero at the edge of the chord.

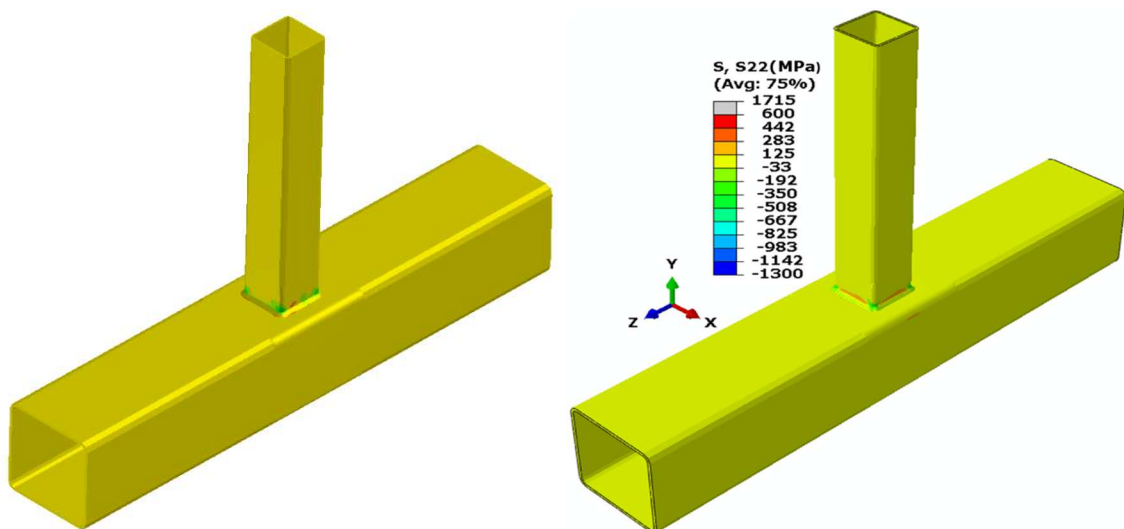


Figure 5.28: Stress distribution in y direction before the loading process, SYSWELD (left) and ABAQUS AWI (right).

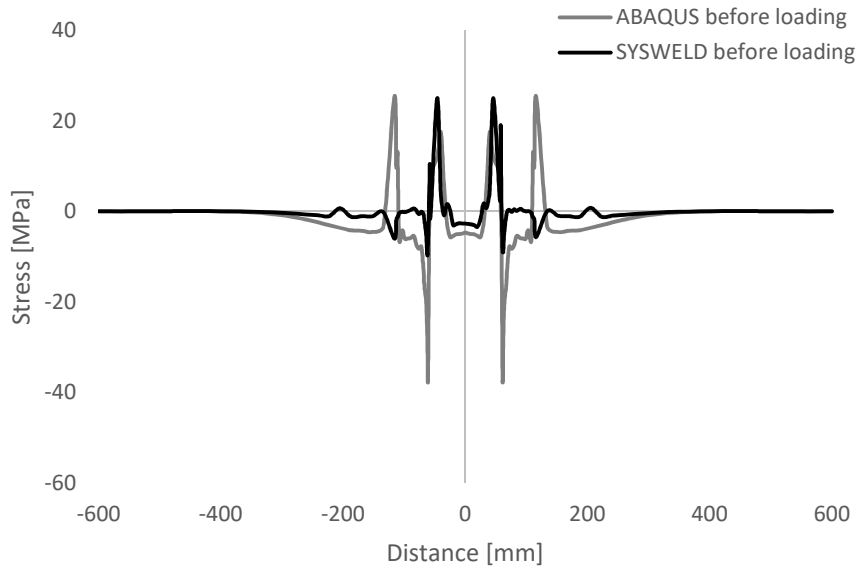


Figure 5.29: Stress distribution in y direction before the loading process.

After the Loading Process

The evolution of the stresses after the load is applied can be seen in Figure 5.30 and Figure 5.31. A stress concentration is identified in the lateral wall of the chord, where the tensile stress values reach around 700 MPa. Relatively high compressive stress values can be seen in the weld. This is in good accordance with the expected behaviour of the structure during compressive loading. However, similar to what has been analysed before the load was applied, local differences are seen between the results coming from ABAQUS and SYSWELD.

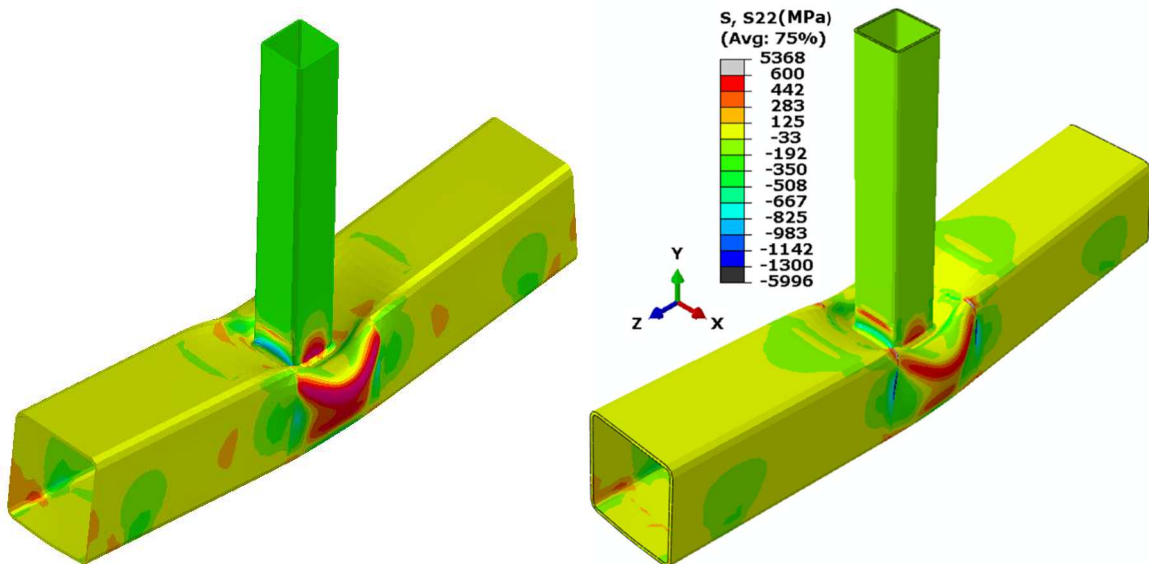


Figure 5.30: Stress distribution in y direction after the loading process, SYSWELD (left) and ABAQUS AWI (right).

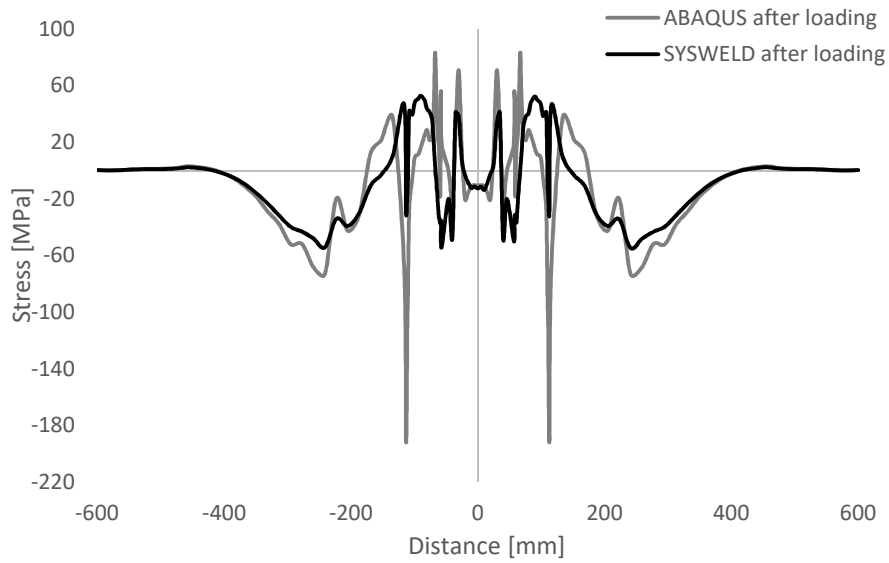


Figure 5.31: Stress distribution in y direction after the loading process.

### 5.10.1.3 Transverse Stresses

#### Before the Loading Process

Figure 5.32 and Figure 5.33 present the stress distribution after loading in the z direction for the midline. The stress patterns in both models are close. The maximum value achieved in ABAQUS for the stress in the z direction is 350 MPa whereas the maximum value in SYSWELD is 260 MPa. The behaviour at the intersection of the brace and chord differs, the values obtained by SYSWELD being slightly lower than those from ABAQUS.

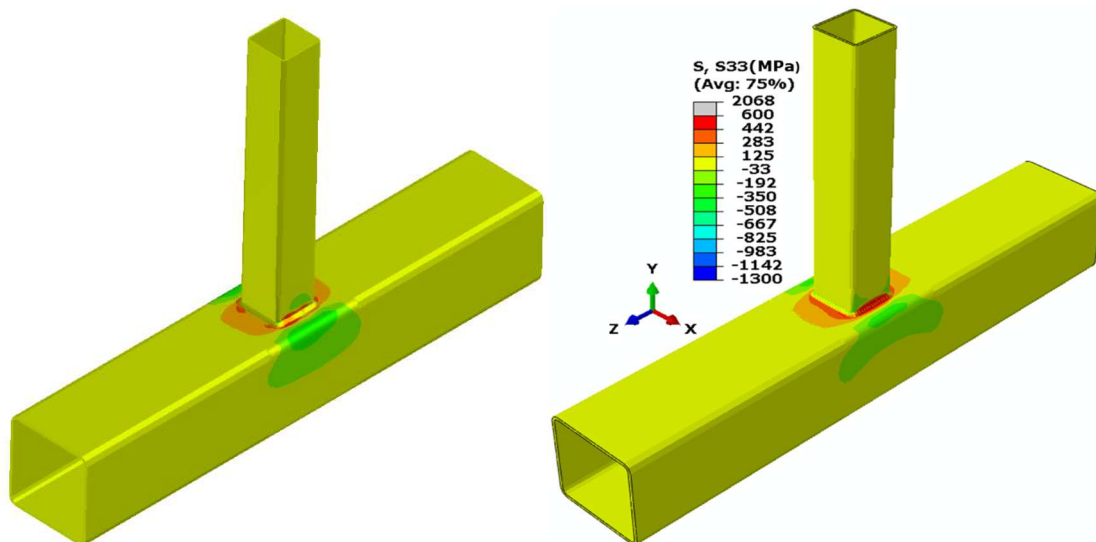


Figure 5.32: Stress distribution in z direction after the welding process, SYSWELD (left) and ABAQUS AWI (right).

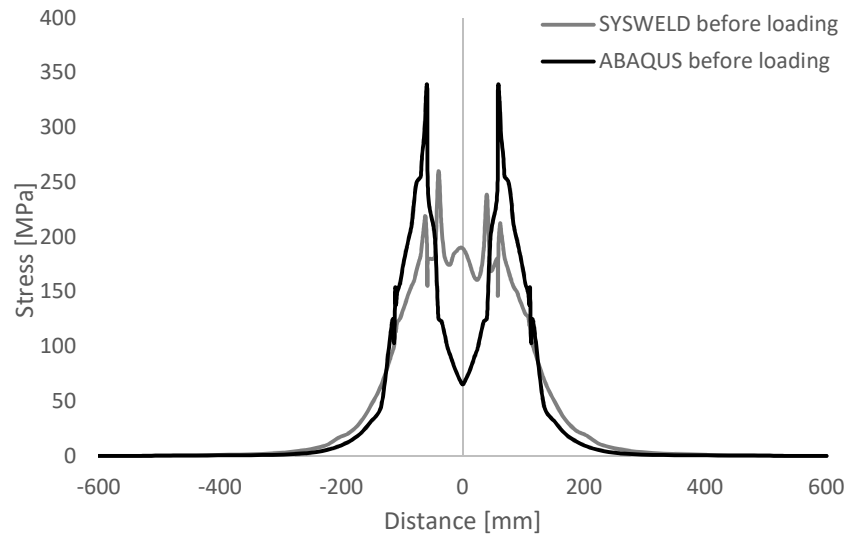


Figure 5.33: Stress distribution in z direction after the welding process.

After the Loading Process

Figure 5.34 and Figure 5.35 shows that there are no significant discrepancies between the stress distributions at the points located on the selected line in SYSWELD and ABAQUS. The results are in a good agreement with some minor differences in magnitude. High tensile stresses are reached especially at the intersection area with a magnitude of 500 MPa. High tensile stresses transform to compressive stresses with a maximum magnitude 540 MPa at weld toes. Shortly away from the weld toes high compressive stresses shift to tensile stresses and afterwards both curves from both programs tend to compressive stresses. Compressive stresses gradually reduce by entering the unaffected zone and reach zero at the chord top edges.

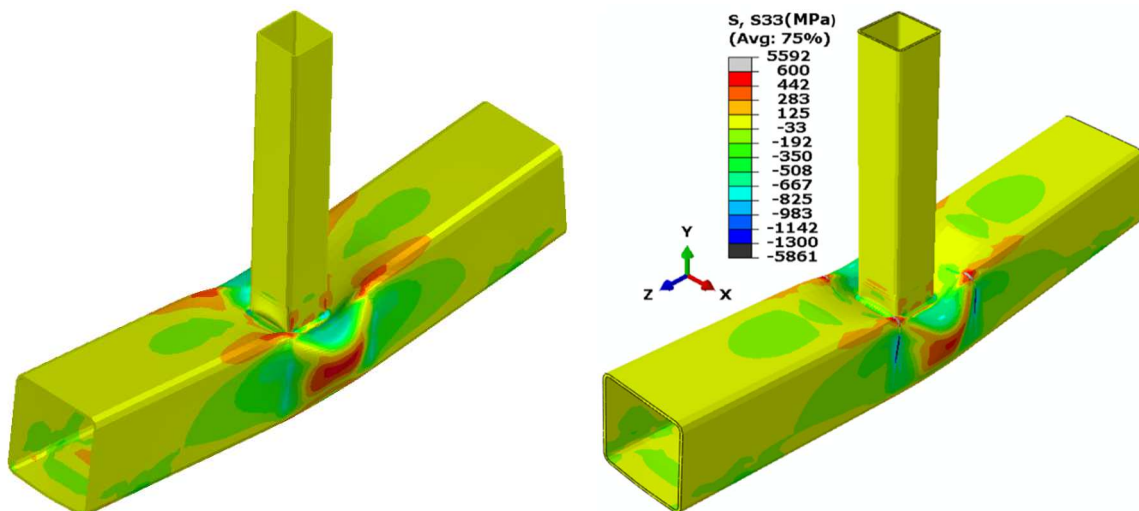


Figure 5.34: Stress distribution in z direction after the loading process, SYSWELD (left) and ABAQUS AWI (right).

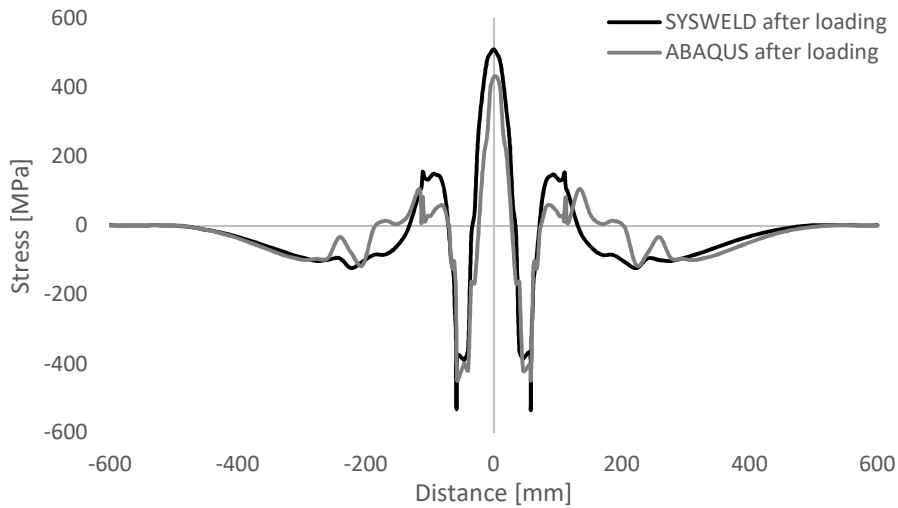


Figure 5.35: Stress distribution in z direction after the loading process.

### 5.10.2 Double-Phase Progressive Welding

#### 5.10.2.1 Longitudinal Stress

##### Before the Loading Process

Longitudinal stresses distribution for double-phase progressive welding for both ABAQUS AWI and SYSWELD are shown in Figure 5.36. Weld bead is located at the distance of 50 millimetres from each side. Both programs follow the same trend regarding the distribution of stresses after 550 seconds of cooling. High tensile stresses have shaped at the weld toe with a maximum magnitude of 550 MPa which shifts rapidly to compressive stresses with a maximum magnitude of -250 MPa. By getting away from the weld and also approaching the base material and the unaffected zone the compressive stresses reach zero.

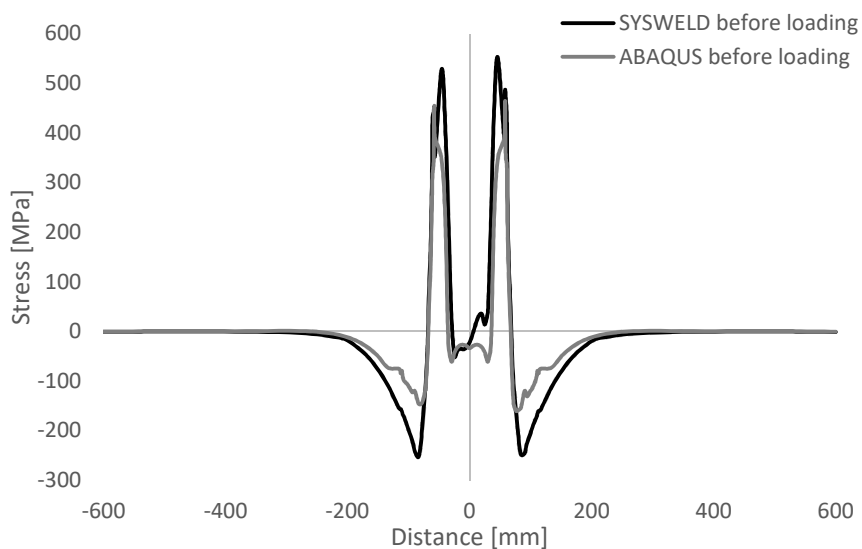


Figure 5.36: Double-phase progressive welding - stress distribution in x direction before the loading process.

After the Loading Process

As for the first case (progressive welding), the residual stresses are also investigated numerically for other remaining cases in order to clarify whether the magnitude or the distribution of initial stresses which are the structural imperfection induced welding will influence the overall behaviour of the joint in terms of load-deflection. The distribution of longitudinal stresses and the behaviour of the joint after loading is shown in Figure 5.37. Both programs are in a good agreement regarding the distribution of stresses with very minor differences in the magnitude. Apart from the weld toes, tensile stresses are also developed in the intersection area between the two weld toes with a maximum magnitude of 390 MPa which rapidly drops down and changes to compressive stresses.

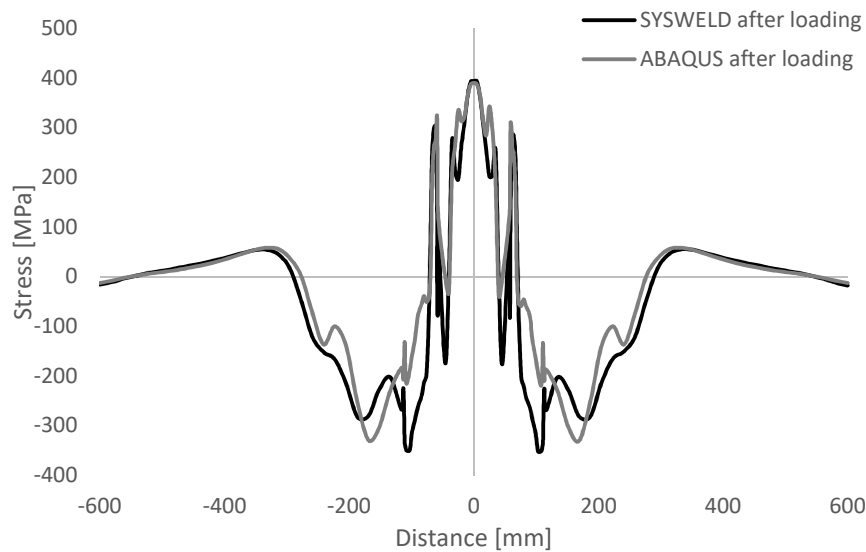


Figure 5.37: Double-phase progressive welding - stress distribution in x direction after the loading process.

5.10.2.2 Vertical Stresses

Before the Loading Process

Residual stresses in the y direction or so called vertical stresses are plotted in Figure 5.38. Compare to the longitudinal stresses, vertical stresses usually don not follow the same trend. The biggest transformation from compressive to tensile stresses are only observed at weld toes and also where the required partitions for meshing exist. Both programs offer rapid shifts from tensile to compressive stresses at the weld toes with different magnitude depending on how the mesh is adopted for the welding simulation. The maximum magnitude of tensile stresses at the weld toe observed in ABAQUS AWI reaches 37 MPa and for the same point 24 MPa by SYSWELD.

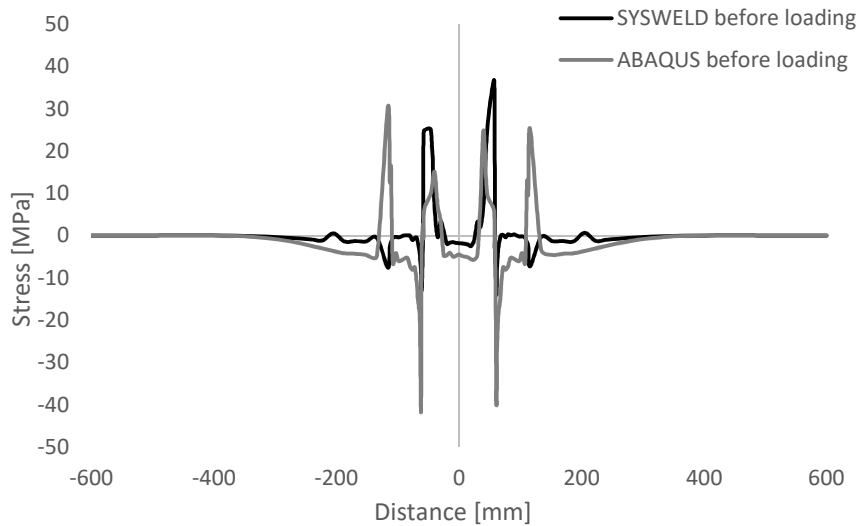


Figure 5.38: Double-phase progressive welding - stress distribution in y direction before the loading process.

After the Loading Process

Distribution of vertical stresses after the loading process as described for this case before loading does not offer a fixed equilibrium pattern as so many parameters could interoperate. Figure 5.39 show the distribution of vertical stresses after the loading process. Very minor differences are observed in the heat affected and fusion zones compare to the vertical stresses before loading. However, away from the welds compressive stresses are developed by reaching a maximum magnitude of -84 MPa in ABAQUS AWI and -54 MPa for the same point in SYSWELD. Due to the nature of vertical stresses, these kind of stresses are usually low. Disagreements regarding patterns and magnitudes of stresses are usually smaller by getting away from the heat affected areas.

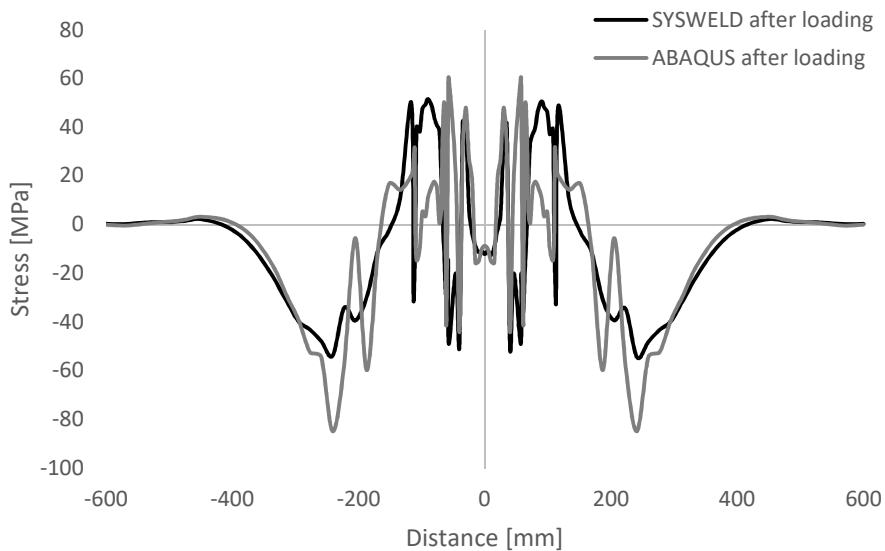


Figure 5.39: Double-phase progressive welding - stress distribution in y direction after the loading process.



5.10.2.3 Transverse Stresses

Before the Loading Process

The distribution of transverse stresses is shown in Figure 5.40. The maximum magnitude of tensile stresses are offered in both programs at the weld toes reaching around 290 MPa in ABAQUS AWI and 235 MPa in SYSWELD. Biggest disagreements are observed at and between the weld toes. This is actually where the biggest transformations are observed. High magnitude of tensile stresses changes to compressive stresses away from the weld toes and gradually decreases and approaches zero. Transformations offered by ABAQUS AWI are counted to be more sharp which reaches 100 MPa in this case which has occurred in the intersection area.

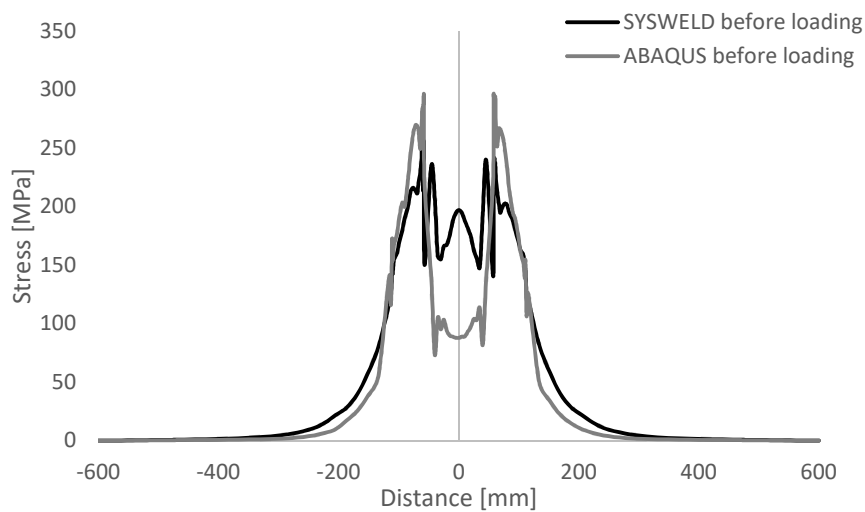


Figure 5.40: Double-phase progressive welding - stress distribution in y direction before the loading process.

After the Loading Process

The transverse stresses distribution after the load application is plotted in Figure 5.41. Compare to the transverse stresses before loading, stresses after loading expand and reach the supports on sides and bottom of the chord member. As for longitudinal stresses regarding the distribution and magnitude, transverse stresses offered by both programs are in a good agreement. In the intersection area the difference is maintained which has been observed before loading. Both programs follow the same trend with some disagreements only in magnitude. The highest magnitude of transverse residual stresses are observed in the intersection area and on the sides of the chord member where the plate crippling occurs with a maximum value of 600 MPa.

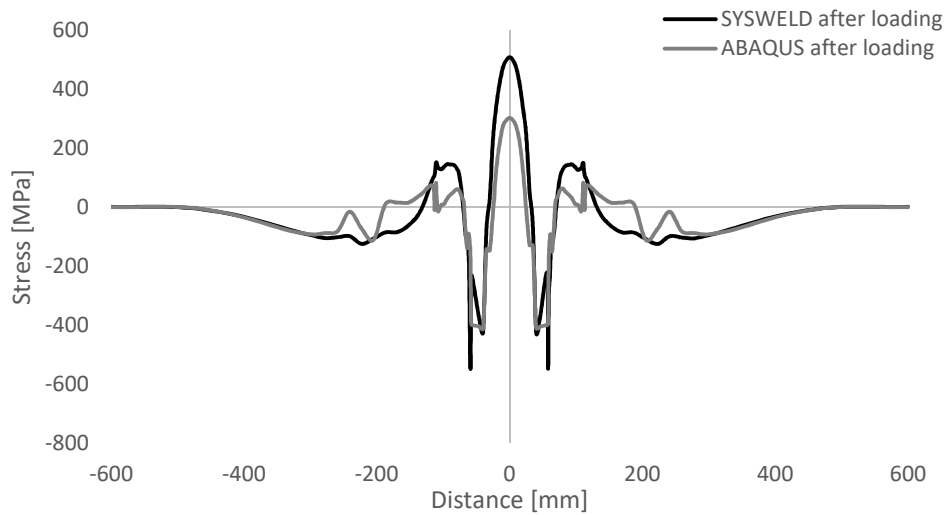


Figure 5.41: Double-phase progressive welding - stress distribution in y direction after the loading process.

### 5.10.3 Skip Welding

#### 5.10.3.1 Longitudinal Stresses

##### Before the Loading Process

The pattern distribution of longitudinal stresses in the joint welded by using the skip sequencing is shown in Figure 5.42. Both programs shown the same trend with some differences in the intersection area and weld toes. By entering the unaffected zone compressive stresses gradually reach zero.

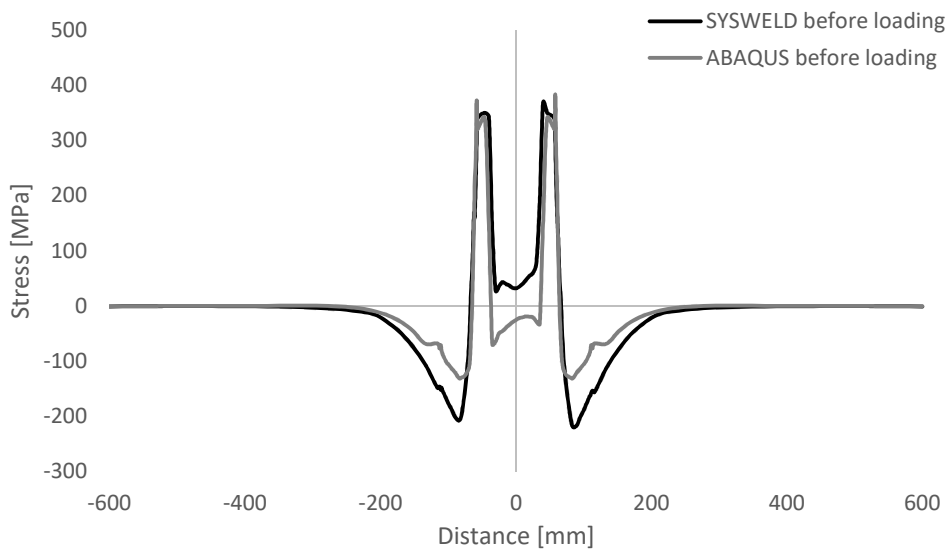


Figure 5.42: Skip welding - stress distribution in x direction before the loading process.

##### After the Loading Process

Figure 5.43 illustrates the stress distribution in x direction for the T-joint after the loading process. Compare to the results for the joint before loading, high tensile stresses have shaped at the weld toes with the magnitude of 320 MPa which rapidly changes to compressive stresses of a magnitude of 340 MPa and gradually approaching zero in the base material.

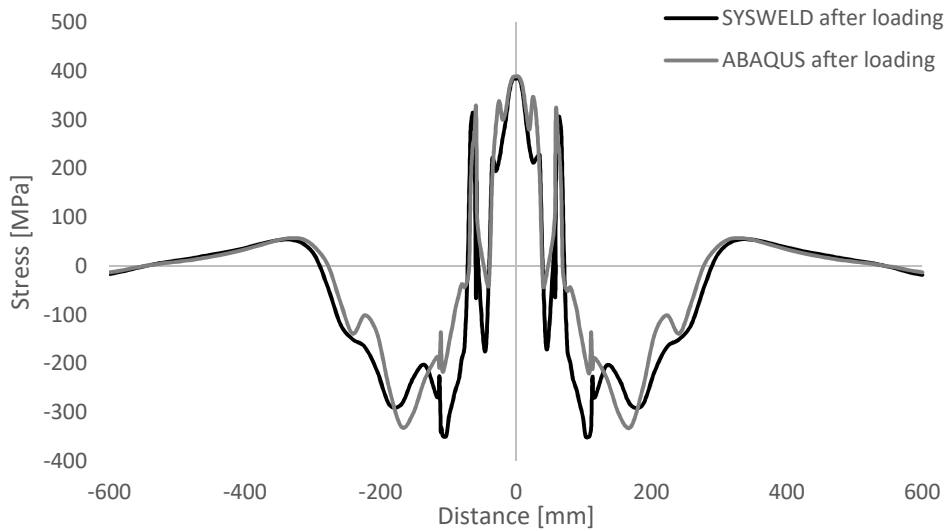


Figure 5.43: Skip welding - stress distribution in x direction after the loading process.

### 5.10.3.2 Vertical Stresses

#### Before the Loading Process

The distribution of vertical stresses before the loading process is shown in Figure 5.44. Both programs show the same distribution pattern especially in the unaffected areas. The highest tensile stresses are observed at the weld toes, especially by the results offered by SYSWELD. The high tensile stresses at the weld toes transform to compressive stresses away and with some minor changes approaches zero. However, as it can be seen the joint in ABAQUS AWI experiences another stage of transformation 50 mm away from the weld toes on both sides.

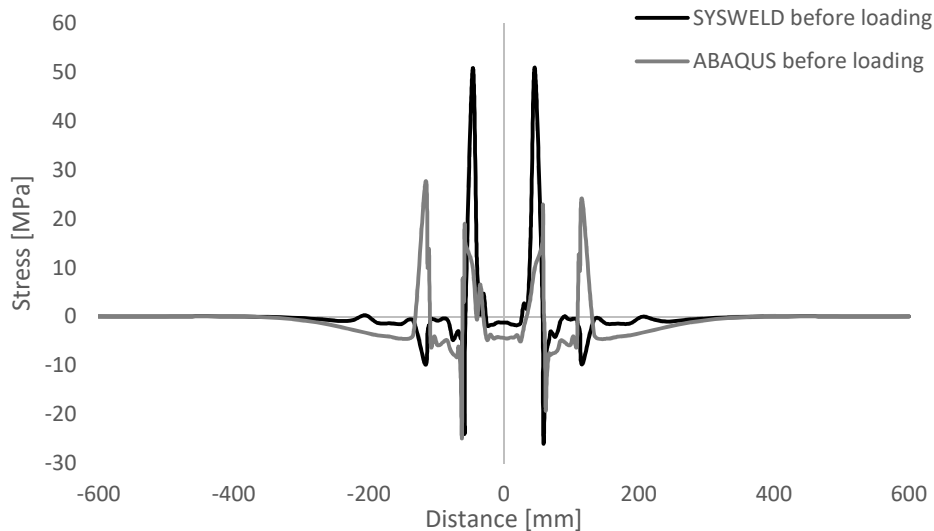


Figure 5.44: Skip welding - stress distribution in y direction before the loading process.

#### After the Loading Process

Figure 5.45 show the distribution of vertical stresses after the loading process. Very minor differences are observed in the heat affected areas compare to the vertical stresses before loading.

Away from the welds compressive stresses are developed by reaching a maximum magnitude of -84 MPa in ABAQUS AWI and -54 MPa for the same point in SYSWELD.

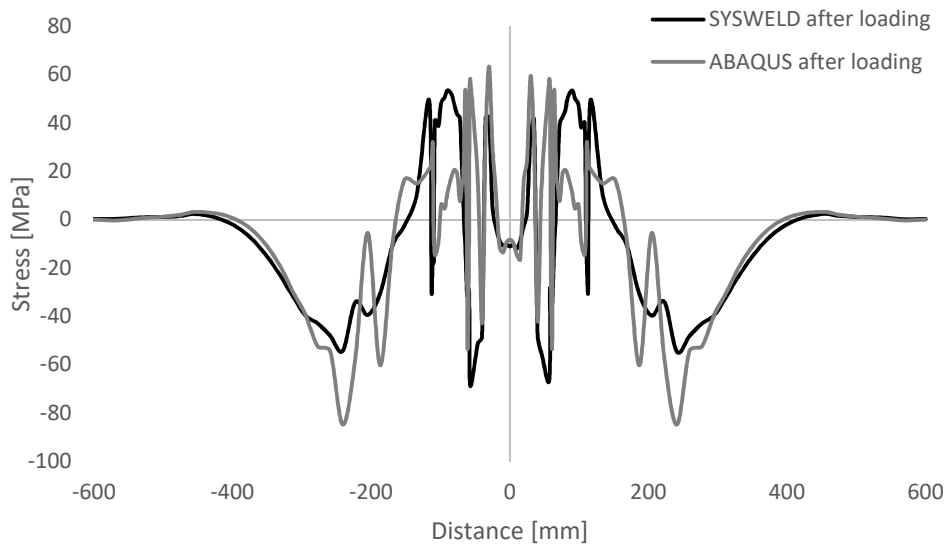


Figure 5.45: Skip welding - stress distribution in y direction after the loading process.

### 5.10.3.3 Transverse Stresses

#### Before the Loading Process

The distribution of transverse stresses is shown in Figure 5.46. The maximum magnitude of tensile stresses are offered in both programs at the weld toes reaching around 280 MPa in ABAQUS AWI and 220 MPa in SYSWELD. Biggest disagreements are observed at and between the weld toes. This is actually where the biggest transformations are observed. High magnitude of tensile stresses changes to compressive stresses away from the weld toes and gradually decreases and approaches zero.

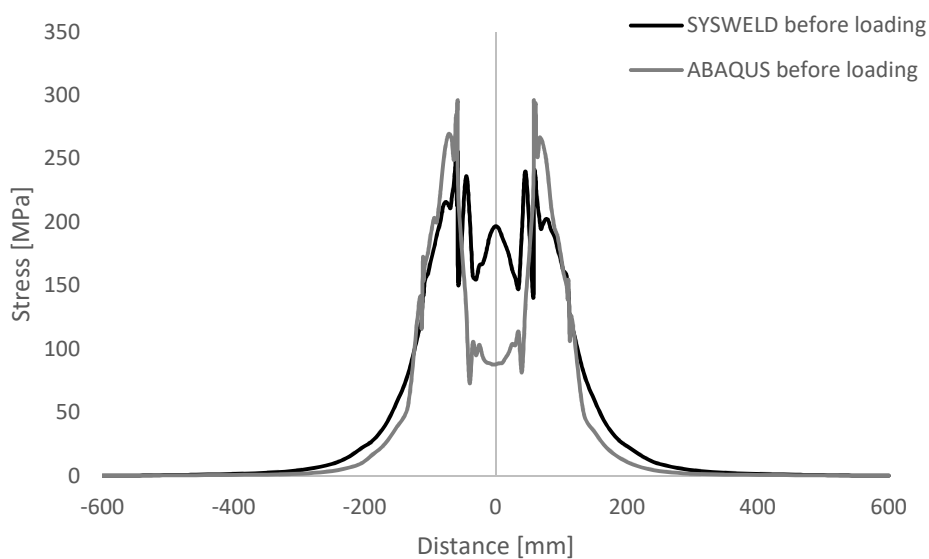


Figure 5.46: Skip welding - stress distribution in z direction before the loading process.

After the Loading Process

Figure 5.47 shows distribution of transverse stresses after loading. The results are in a good agreement with some minor differences in magnitude. High tensile stresses are reached especially at the intersection area. High tensile stresses transform to compressive stresses at weld toes. Shortly away from the weld toes high compressive stresses shift to tensile stresses and afterwards both curves from both programs tend to compressive stresses.

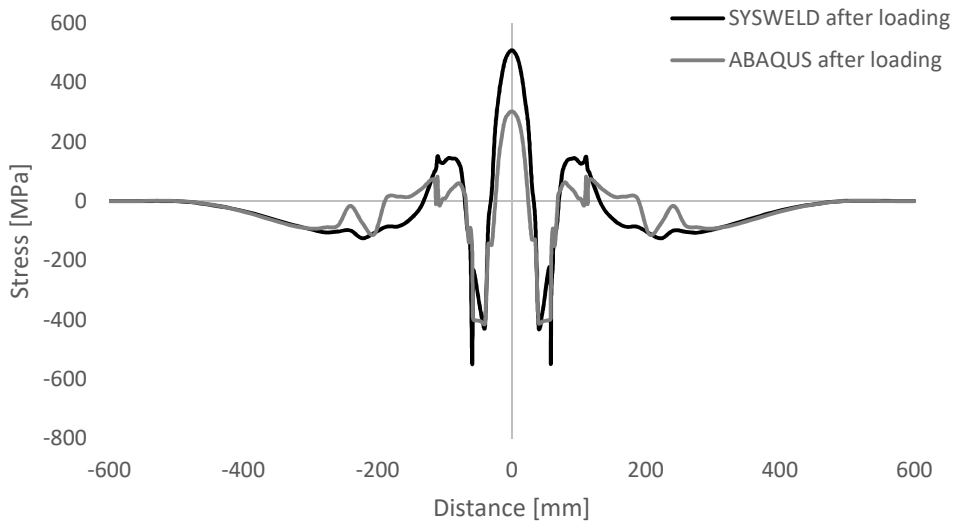


Figure 5.47: Skip welding - stress distribution in z direction after the loading process.

Figure 5.48 shows the longitudinal stress distribution with respect to the line selected along which the stress results were exported. As it can be seen both software are in a good agreement with some minor magnitude differences. The first case presents the highest tensile stresses at the weld bead as well as the second case.

However, a drop of 170 MPa is observed at the weld toe for the third case as the line meets start and end points at the weld toe. Reduction in tensile stresses for the third case has influenced the compressive stresses which shaped by getting away from the weld. Higher compressive stresses for the third case with a magnitude difference of 80 MPa are observed in both software.

It should be mentioned the difference between the stress distributions of all cases is only visible before the load application process. After the loading process all joints behave the same in terms of magnitude and the pattern.

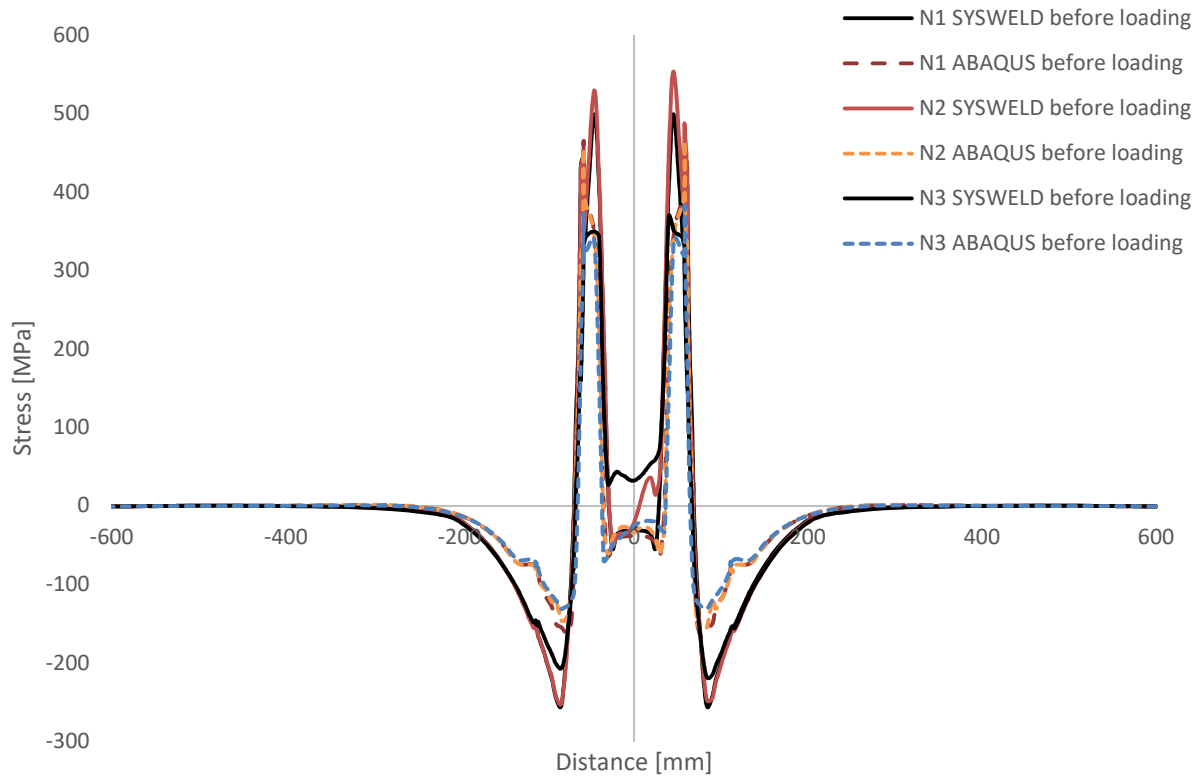


Figure 5.48: Stress distribution for both software in x direction before the loading process.

The transverse stress distribution for N1, N2 and N3 is illustrated in Figure 5.49. For these stresses the same differences are kept. However, as explained before the discrepancies between ABAQUS and SYSWELD are more visible in transverse stresses than in longitudinal stresses. All the curves obtained from the cases follow the same trends with some magnitude relevant disagreements. As for longitudinal stresses, the highest tensile stresses are observed for the progressive welding (N1) and by increasing the number of welds these stresses face reduction. The reduction of tensile stresses is more visible in the weld toes than other areas with a magnitude of 45 MPa.

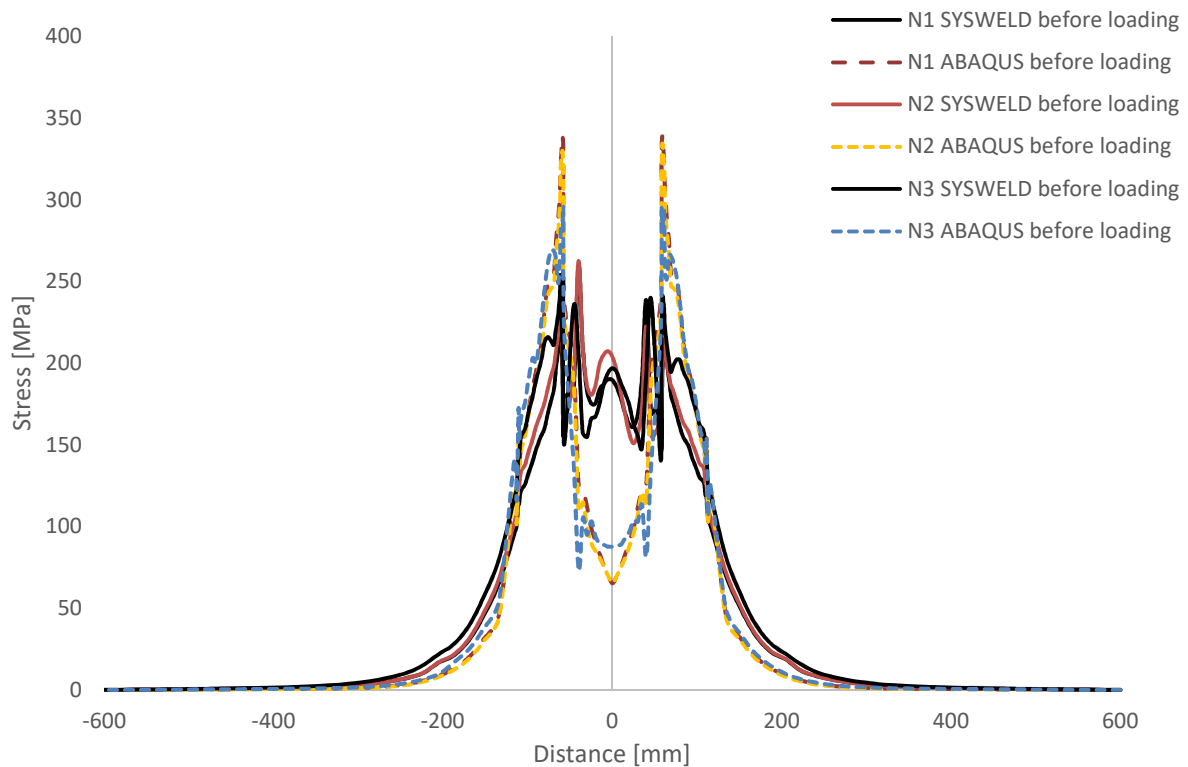


Figure 5.49: Stress distribution for both software in Z direction before the loading process.

#### 5.10.4 Back-Step and Skip Welding (8 welds)

After an observation of reduction in gain of strength in the joints for better underpadding of the influence of various welding sequences on the load bearing capacity two further cases have been performed numerically.

Back step welding as skip welding (4 weld) involves 4 start and end points in the simulation of welding. However, the last numerical case adopted in this work involves 8 start and end points. Further observation of residual stress distribution for the nodes along the selected line has not been possible as the start and end points lay on the same locations.

Figure 5.50 shows the load vs deflection for all numerically investigated cases. As it can be seen the first case (progressive welding) bears a higher load compare to other cases with 260 kN. The gain in strength drops by increase in the number of welds and reaches its minimum value in the last case (skip welding with 8 welds) with a magnitude of 237 kN. Compare to the first case, gain in strength drops by -10 %.

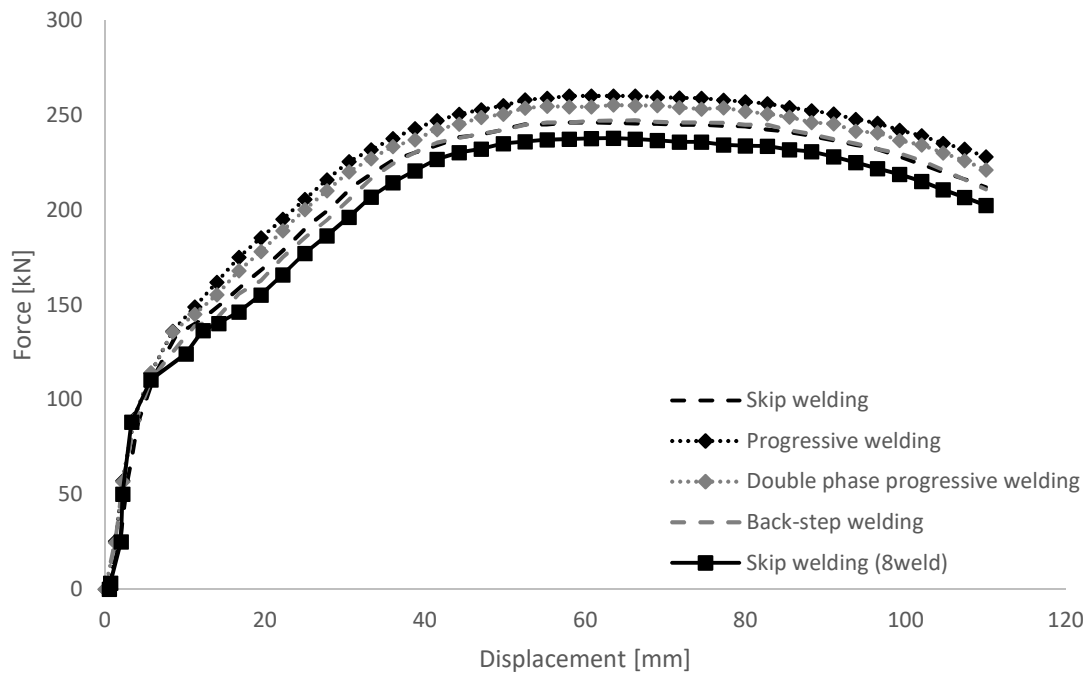


Figure 5.50: Load-deflection behaviour of the numerically investigated cases.

For a better evaluation of results and differences, the Mean stresses are plotted for all the numerical cases in Figure 5.51. As previously explained the stress distribution varies for different investigated cases. For progressive welding where only a continuous weld is involved the stress is distributed along the weld. N2 (b), clearly shows how two continuous welds could influence the stress distribution. Destructive stresses (tensile) occur in the area where start and end points of welding exist. The same governs for the third and fourth cases. The results of load bearing capacity also pointed out the similarities. (c) and (d) are respectively skip welding and back-step welding. In both cases 4 welds are involved. The last numerically investigated case has been (e) skip welding with 8 welds involved. Compare to other cases stresses more tend to expand in the surrounding areas. Bigger number of welds means welds with shorter length and the same heat input applied which has led to higher tensile stresses at and around the weld toes (start and end points). In all the cases compressive stresses are pretty the same distributed on the side wall edges of the chord member and the differences are only observed in/around the intersection area.



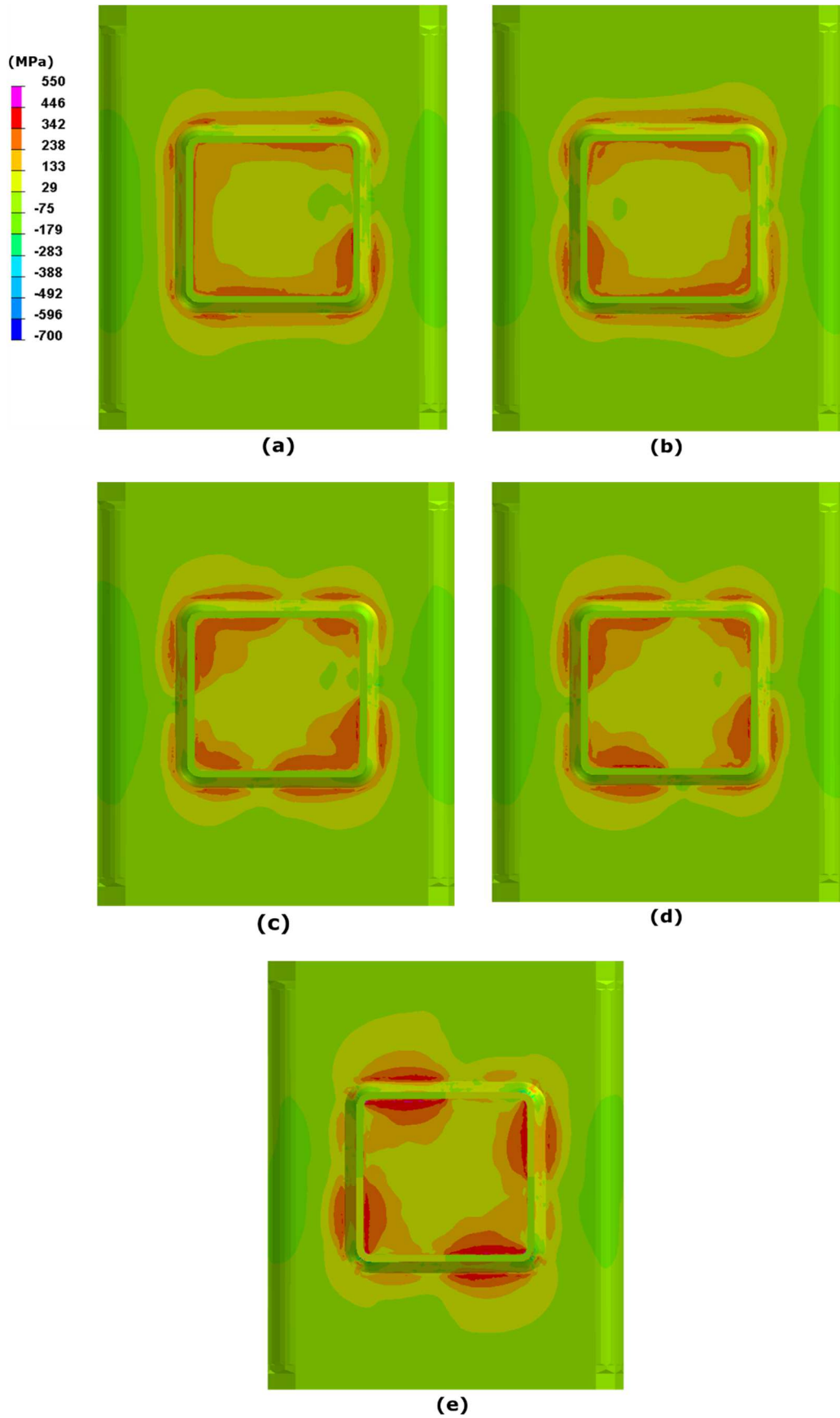


Figure 5.51: Mean stress distribution before the loading process (a=N1, b=N2, c=N3, d=N4 and e=N5).

## 5.11 Conclusion

From the numerical analysis of welding simulation and load bearing capacity by both software ABAQUS AWI and SYSWELD of the joints welded by using various welding sequencing the following conclusions can be made:

- As both programs adopt different techniques for heat application, the temperature distribution differs. The energy based approach with the Goldak's double ellipsoid body flux is widely used for welding simulation which is used also in this work by SYSWELD. ABAQUS AWI performs welding simulation based on temperature boundary conditions which is defined by setting required chunks. This technique in ABAQUS leave a high temperature concentration at high rate (1500 °C) and at lower temperature it gradually approached what SYSWELD offers. As the high temperature required at the chunks cannot be influenced so especial attention should be paid to the film coefficient adoption on all the surfaces involved in the welding simulation.

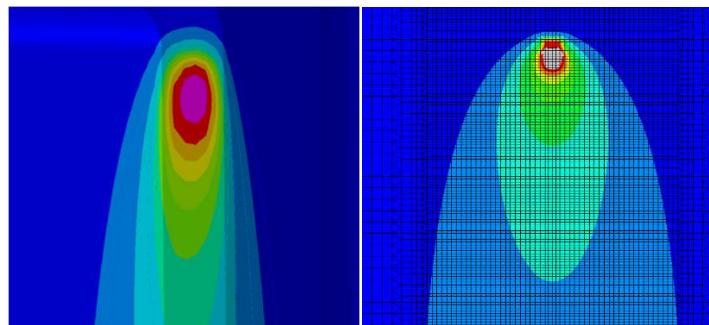


Figure 5.52: Temperature iso-surfaces, SYSWELD (left) and ABAQUS AWI (right).

- A high temperature concentration at the chunks or the weld toes leads to a higher magnitude of tensile stresses. ABAQUS AWI offers a higher magnitude of tensile stresses which is due to high temperature concentration. Away from the weld toe both software follow the same trend and pattern with so close magnitudes especially in less or not affected areas until approaching zero.
- Mesh consideration could influence results regarding stress distribution. When ABAQUS AWI is used for welding simulation the extension considers all model properties by reading the model tree. However, SYSWELD as other welding simulation software only considers the mesh. Comparison of results between ABAQUS and SYSWELD for stress distribution in x, y and z directions shows how consideration of required partitions for meshing in ABAQUS could influence the results by leaving high tensile stresses after the cooling period. These stresses transform to compressive stresses after loading or they keep the same magnitude after loading. Consideration of mesh and partitions does not allow a realistic prediction of stress distribution in ABAQUS AWI. Use of ABAQUS AWI requires a

parallel welding simulation by another software such as SYSWELD for validation of results.

It should be mentioned despite the differences the overall comparison of results from both software are in a good agreement. Residual stresses in all investigated directions in both programs follow the same trend with some minor differences in the magnitude.

- The results of numerical analysis of load application shows that increase in the number of welds could highly influence the gain in strength. The higher number of welds leads to less load bearing capacity of the joints. The outcome points out how important is the influence of stress concentration. Higher number of start and end points leave higher areas with concentrated stresses. A maximum load of 260 kN was achieved for the joint which was welded continuously with only one start and end point. For the second joint with 2 start and end points the gain in strength drops by -4 %. The same applies to the joint (skip welding) with 4 start and end points by a reduction of -7 % in strength.
- In order to investigate if other welding sequences such as back-step welding or a bigger number of welds could influence the overall load-deflection of the joint, these sequences were performed numerically. The outcome shown that back-step welding does not influence the results of stress distribution, distortion and load bearing capacity compare to the skip welding as there are the same number of start and end points. Skip welding with 8 start and end points faced a significant reduction of -10 %. It should be mentioned that the line along which the stresses were plotted could not present the results for skip welding with 8 start and end points as the same for skip welding and back-step welding only two start and end points lay on this line.

## 6 GENERAL CONCLUSIONS

The Objective of this work was to enable welding response prediction in a joint made by hollow sections. The main aim was to investigate the influence of various welding sequences on the overall behaviour of the joints and their respective load bearing capacity.

Overall 6 joints were tested, in which 4 various welding sequences were applied. In order to verify the validity and accuracy of the models which would be developed in numerical analysis for prediction of stresses, deformations and load-displacement behaviours several experimental tests were performed.

Three joints were welded by progressive welding in which only one continuous weld exist for further statistical investigation. The joints were all loaded under the same loading condition under brace concentric loading using a 2000 kN testing machine. The load was applied using stroke control at a rate of 3mm/min up to failure. The (L/h) ratio of the chord was carefully selected as per recommendations for nodal supports in the literature. Testing the specimens requires prediction of failure modes which was done according to EN 1993-1-8.

The experimental results show, all specimens 1 to 6 experience the same failure modes. The vertical member on which the compressive load was applied, first started moving down. High compressive load applied on the brace forces the chord face to deform and this deformation on the chord face caused the symmetrical outward crippling of the chord side walls. It should be noted that various welding sequencing may influence load bearing capacity but it has no influence on the failure mode that T-joint experiences as the concept is the same.

Numerical analysis of welding simulation and further load application was done for each single welding sequence separately. The mechanical properties of the material achieved from the coupon test were introduced to the models as well as the thermal properties from SYSWELD and SIMUFACT libraries. The Boundary conditions were set as in the experiment with a careful consideration of friction effects between the layers of dry steel on dry steel.

The thermo-mechanical welding simulation was successfully simulated for the steel SHS T-joints. The outcomes of both commercial software regarding temperature distribution, residual stresses, deformation, overall load-deflection behaviours and also the failure modes are in a good agreement. However, some differences especially in temperature and stress distributions have been observed by the results offered by both software. There are several factors to which these differences can be attributed. Their influence is different depending on the stage of the analysis. The effect could be different during the welding, after the cooling time and after applying the compressive load. Some recommendations for AWI users can be given based on the conclusions of the current work:

- a) The energy based approach with the Goldak's double ellipsoid body flux should be used in ABAQUS instead of temperature boundary condition (temperature application). Temperature iso-surfaces differ in both models. The reason for this is that in ABAQUS only temperature is applied, without any governing equations for heat source. In SYWELD the temperature iso-surfaces are obtained based on the Goldak's double ellipsoid heat source model for distribution of the heat. It should be noted that the results obtained from both software show that the shape of the heat source may have influence in the fusion and minor differences in the HAZ.
- b) The large number of elements means time-consuming computations and causes numerical convergence problems. Partitioning the geometry close to the weld beads and local mesh refinement is recommended in order to reduce the global number of elements.
- e) The model was created in ABAQUS and later transferred to SYSWELD. In SYSWELD, the partitions of the geometry are not recognized. However the AWI tool (ABAQUS welding interface) takes into account all the steps of model creation present the model tree. Significant differences in stress distribution patterns are due to the partitions used in the model. Partitioning causes stress concentration along the partition front separating the refined core and the outer areas of the chord. Special attention should be paid to the length and number of partitions in ABAQUS AWI.
- f) It is assumed that the deformation is applied only in vertical direction, which should lead to the same stress distribution on the brace and the chord in both models. By comparing the results, better results in terms of the symmetry-distributed stresses on both the chord and the brace is seen in SYSWELD. A parametric study which should study the influence of mesh generation and boundary conditions on the stress distribution is therefore required.

Results in terms of distortion shows a good agreement between both programs. Failure modes observed could be compared to failure modes (a) and (b) in Figure 7.2, EN 1993-1-8 which are the chord face failure and chord side failure respectively.

The numerical and experimental investigated cases outcomes are in a good agreement. The material introduced to the numerical cases more or less shows the same behaviour elastically and plastically as the load displacement curves offer minor disagreements. However, the maximum load reached differ slightly. The gain in strength drops when the number of welds increases. Compare to the first numerically and experimentally studied cases (V1 and N1, progressive welding), the second case (V2 and N2) experiences -4 % of gain in strength. The same applies for the third case (V3 and N3) by a magnitude -7 % gain in strength. The outcomes point out an important relationship. As the only variable in all cases investigated has been the welding sequences, so it could be clearly explained how stress concentration or so called the number of start and end points could highly influence the overall behaviour of the joints. Reduction in gain in strength is directly related to stress concentration which increases by the increase in the number of welds so progressive or double

## GENERAL CONCLUSIONS

progressive welding sequences are highly recommended for practise. These two sequences leave less number of start and end points which leads to less stress concentration.

## 7 FUTURE WORKS

Although an initial variation of the sequencing patterns for the joint being analysed has already been achieved, the influence of sequencing for multiple braces welded on the same chord is unknown. Due to the preponderance of such SHS joints in practical applications, more research should be done in this direction.

Welding sequencing and its influence on the load bearing capacity and overall behaviour of a T-joint should be investigated by various loading conditions. In the present work only a compressive load was applied. However the behaviour of the joint under tensile and moment loads is unknown. Apart from RHS and SHS, CHS also should be investigated in order to study if a change in shape would lead to different results. Large scale profiles enable including a bigger number of start and end points which should be considered. It should be mentioned that progressive welding should be always considered as this welding sequence is widely used and accepted. A consideration of progressive welding leads to a better understanding of the influence various welding sequences on the overall behaviour of the specimens to be tested.

As the increase in the number of start and end points has shown negative influence on the gain in strength, a special attention should be paid to stress concentration. Experimental measurement of residual stresses must be done which leads to a better understanding and validation of stress distribution.

Choice of software is very important, especially if only ABAQUS AWI is used. The users of ABAQUS AWI must implement the subroutines using the program FORTRAN which allows writing the codes for an application of heat flux.

In some cases such as the T-joint investigated in this work, it is not clear which part of welding imperfections can influence the load bearing capacity. So it is highly recommended for future numerical and experimental investigations that a good attention being paid to residual stresses and deformations separately.

Phase transformation is an important aspect which should be taken into account when applying load on a joint such as the one investigated in this work. Phase transformation can be critical especially when cracks occur when welding and developing by loading.

## 8 REFERENCES

- [1] L.-X. Li, G. Wang, C. Li, C.-q. Zhou and D.-f. FU, “Effect of welding sequence on residual stress in thin-walled octagonal pipe-plate structure,” *ScienceDirect*, vol. 24, pp. 657-664, 2013.
- [2] C. Tsai, S. Park and T. Cheng, “Welding Distortion of a thin-Plate Panel,” *Research Development*, pp. 156-165, 1999.
- [3] T. Schenk, *Modelling of welding distortion, the influence of clamping and sequencing (PhD)*, Delft, 2011.
- [4] I. Hernandez, *Welding sequence analysis (PhD)*, AGH , 2009.
- [5] P.-Y. Cheng, *Influence of Residual Stress and Heat Affected Zone on Fatigue Failure of Welded Piping Joints (PhD)*, Raleigh, North Carolina, 2009.
- [6] J. Chinaraju, M. Chitnis, A. Kulkarni, Y. Uke, M. Shubert and M. Pandheeradi, “Abaqus Welding Interface (AWI) - Isight integration for optimum weld-sequencing,” in *SIMULIA Community Conference*, 2014.
- [7] W. Jiang, L. Wang, P. Du and X. Li, “Determination of welding stress and distortion in discontinuous welding by means of numerical simulation and comparison with experimental measurement,” *Computational Materials Science* , vol. 49, pp. 535-543, 2012.
- [8] F. Jonassen, L. Meriam and E. Degarmo, “Effect of certain block and other special welding procedures on residual stresses,” *Weld Journal*, vol. 25(9), pp. 492s-6s, 1946.
- [9] E. Rybicki and P. McGuire, “The effects of induction heating conditions on controlling residual stresses in welded pipes,” *Trans ASME J Eng Mater Technol*, vol. 104, pp. 267-73, 1982.
- [10] R. Koch, E. Rybicki and R. Strttan, “A computational temperature analysis for induction heating of welded pipes,” *J Eng Mater Technol*, vol. 107, pp. 148-53, 1985.
- [11] B. Josefson, “Residual stresses and their redistribution during annealing of girth-butt welded thin-walled pipe,” *Trans ASME J Press Vessel Technol*, vol. 104, pp. 245-50, 1982.
- [12] B. Josefson, “Stresses redistribution during annealing of a multi-pass welded pipe,” *J Press Vessel Technol*, vol. 105, pp. 165-70, 1983.
- [13] F. Brust and E. Rybicki, “A computational model of backlay welding for controlling residual stresses in welded pipe,” *J Press Vessel Technol*, vol. 103, pp. 226-32, 1981.
- [14] Y. Ueda, K. Nakacho and L. Shimizu, “Improvement of residual stresses of circumferential joint of pipe by heat sink welding,” *J Press Vessel Technol*, vol. 108, pp. 14-23, 1986.



- [15] C. Chou and Y. Lin, "Reduction of residual stresses by parallel heat welding in small specimen of type 304 stainless steel," *Master Sci Technol*, vol. 8, pp. 179-83, 1992.
- [16] R. Weck, "Transverse contractions and residual stresses in butt welded mild steel plates," Admiralty Ship Welding Committee, 1947.
- [17] M. Watanabe, K. Satoh and K. Kimura, "Effect of welding methods and sequences on residual stress distribution of welded joints," *Japan Weld Society*, vol. 24(4), pp. 146-53, 1955.
- [18] H. Kihara and K. Masubuchi, "Studies on the shrinkage and residual welding stress of constrained fundamental joint," Transportation Technical Research Institute, 1956.
- [19] T. Schenk, *Modelling of Welding Distortion, The Influence of Clamping and Sequencing*, Delft, 2011.
- [20] N. Syahroni and I. Purbawanto Hidayat, *3D finite element simulation of T-Joint Fillet Weld: Effect of various welding sequences on the residual stresses and distortions*, INTECH, 2012.
- [21] Bette, "Fabrication, Applications Engineering," *The Welding Engineer's Current Knowledge*, vol. 12, no. EWE-3/4, pp. 8-11, 1999.
- [22] S. Company, "Simufact.Material," Berlin, 2016.
- [23] K. Jarmai and J. Farkas, *Mechanics and Design of Tubular Structures*, Wien: International Centre for Mechanical Sciences, 1998.
- [24] J. Wardenier, Y. Kurobane, J. Packer, G. Van der Vegte and X. Zhao, "CIRCULAR HOLLOW SECTION (CHS) JOINTS UNDER PREDOMINANTLY STATIC LOADING," in *DESIGN GUIDE*, CIDECT, 2008.
- [25] V. D. GmbH, *Preon box*, Düsseldorf: industry@vallourec.com, 2015.
- [26] J. Jubb and R. Redwood, "Design of joints to box sections," *The institution of structural Engineers conference on industrialised building and the structural engineer*, 1966.
- [27] L. Costa-Neves, L. Silva and P. Vellasco, "Experimental behaviour of end plate I-beam to concrete filled rectangular hollow section column joints," *International Journal of Applied Mechanics and Engineering*, vol. 9, pp. 63-80, 2004.
- [28] L. Lima, P. Vellasco, S. Andrade, J. Silva and L. Neves, *Structural response of K and T tubular joints under static loading*, Chicago: AISC, 2008.
- [29] G. Winkel, J. Wardenier and Y. Yu, "Deformation limit for the ultimate strength of hollow section joints," *International symposium on Tubular structures*, 1994.
- [30] R. Carol and F. Mirza, "Finite element analysis of RHS T-joint," *ASCE*, vol. 108(ST9), pp. 2081-2098, 1982.
- [31] D. Blockley and W. Eastwood, "Elastic Behaviour of Joint Between Structural Hollow Sections," *The Engineer*, pp. 22-25, 1968.

- [32] M. Mansour, *Theoretical Analysis of T-joints in Hollow Structural Sections*, Toronto: McMaster University, 1977.
- [33] M. El-Zanaty, *Vierendeel Trusses with Hollow Structural Sections*, Toronto: McMaster University, 1976.
- [34] F. Brady, *An Experimental Investigation of Unequal Width HSS Moment Connections for Vierendeel Trusses*, Toronto: McMaster University, 1974.
- [35] J. Mouty, *Theoretical Prediction of Welded Joint Strength*, Toronto: International Symposium on Hollow Structural Sections, 1977.
- [36] Eurocode 3, "Design of steel structures 1.8," in *Design of Joints*, Brussels, CEN- European Committee for Standardization, 2005.
- [37] J. Packer, "Moment Connections Between Rectangular Hollow Sections," *Journal of Constructional Steel*, vol. 121, no. 1402-1408, pp. 63-81, 1993.
- [38] J. Packer and J. Henderson, *Hollow structural section, connections and trusses.*, Ontario: Canadian Institute of Steel Structures, 2003.
- [39] X. Zhao, "Deformation limit strength of welded T-joints in cold-formed RHS sections.," *Journal of Constructional Steel Research*, vol. 53, pp. 149-165, 2000.
- [40] X. Zhao and G. Hancock, "Plastic mechanism analysis of T-joints in RHS subject to combined bending and concentrated force," in *6th International Symposium on Tubular Structures*, Nottingham, 1993.
- [41] J. Wardenier, R. Puthli and L. Lu, "Semi-rigid Connections Between Plates and Rectangular Hollow Section Column," in *6th International Symposium on Tubular Structures*, Nottingham, 1993.
- [42] G. Young, J. Packer and J. Cao, "Yield Line Analysis of RHS Connections with Axial Loads," *Journal of Constructional Engineering*, vol. 48, pp. 1-25, 1998.
- [43] J. Packer, N. Kostenski and J. Cao, "Design Guideline for Longitudinal Plate to HSS Connections," *Journal of Structural Engineering*, vol. 48, pp. 784-791, 1998.
- [44] J. Packer and N. Kostenski, "Welded Tee-to-HSS Connections," *Journal of Structural Engineering*, vol. 129, pp. 151-159, 2003.
- [45] J. Wardenier, G. Van der Vegte and R. Puthli, "FE Analysis for Welded Hollow Section Joints and Bolted Joints," in *Institution of Civil Engineers, Structures and Buildings*, 2010.
- [46] Z. Yang, C. Lee, S. Chiew and S. Lie, "Static strength of cracked square hollow section T- joints under axial loads," *ASCE Journal of Structural Engineering*, vol. 132, pp. 368-377, 2006.
- [47] L. Costa-Neves, *Monotonic and cyclic behaviour of minor axis and tubular joints in steel and steel concrete composite structures - PhD thesis*, University of Coimbra, Portugal, 2004.

- [48] (. International Organization for Standardization, Static Design Procedure for Welded Hollow-Section Joints Recommendations, Geneva, Switzerland: ISO 14346:2013, 2013.
- [49] L. Lima, L. Neves, J. Silva, P. Vellasco and S. Andrade, "Parametric analysis of RHS T joints under static loading," Edinburgh, 2007.
- [50] R. Matos, *Avaliação Paramétrica de Nós de Geometria "T" de Perfis Tubulares*, Coimbra, Portugal: University of Coimbra, 2008.
- [51] A. Czechowski, J. Kordjak and J. Brodka, "Flexibility formulae and modelling of joint behaviour in girders made of rectangular hollow sections," in *Proceedings of a State-of-the-art workshop on Connections and the Behaviour, Strength and Design of Steel Structures held at the ENS*, London, 1987.
- [52] J. Packer, J. Wardenier, X. Zhao and G. Van der Vegte, *Design guide for rectangular hollow section RHS joints under predominantly static loading*, CIDECT, 2009.
- [53] J. Szlendak, "Classification system for I-beam to RHS column connections. Tubular structures VII," in *Proceeding of the seventh international symposium*, Rotterdam, 1996.
- [54] K. Morita, Y. Harada and K. Fujita, "Evaluation of local rotational stiffness and strength of beam to column connection reinforced by increasing column thickness," in *Ninth international confernece on tubular structures*, Dusseldorf, 2001.
- [55] F. Gomes, *Etat limite ultime de la résistance de l'âme d'une colonne dans un assemblage semi-rigide d'axe faible*, Université de Liège, 1990.
- [56] J. Packer and N. Kostaski, "FEM Evaluation of Stiffened Longitudinal Branch Plate to RHS Member Connection," in *Ninth International Conference on Tubular Structures*, Dusseldorf, 2001.
- [57] W. Thornton, "A membrane method for transversely loaded column webs," in *Connection in Steel Structures IV, Behaviour Strength and Designm, Proceeding 4th international workshop Oct 2000*, Roanoke, Virginia, 2002.
- [58] J. Szlendak, "STRENGTH AND STIFFNESS OF RHS BEAM TO RHS CONCRETE FILLED COLUMN JOINTS," in *Connections in Steel Structures*, Amsterdam, June 3-4, 2004.
- [59] Y. Choo, B. Li, J. Liew, G. Van der Vegt and N. Zettlemoyer, "Static strength of T-joints reinforced with doubler or collar plates," in *Eighth International Symposium on Tubular Structures*, Singapore.
- [60] P. Llewelyn and K. Lee, "Offshore tubular T-joints reinforced with internal plane annular ring stiffeners," *ASCE*, vol. 130, no. 6, pp. 942-951, 2004.
- [61] T. Li, B. Shao and C. Zhang, "Study on the static strength of tubular joints reinforced with horizontal inner plate," *Steel Construct*, vol. 24, no. 123, pp. 25-29, 2009.

- [62] B. Shao, J. Zhang, Z. Qiu and J. Shang, "Strength analysis of large-scale multiplanar tubular joints with inner-plate reinforcement," *Space Struct*, vol. 24, no. 3, pp. 161-177, 2009.
- [63] J. Packer and J. Henderson, "Hollow Structural Section," in *Connections and Trusses*, Ontario, Canadian Institute of Steel Construction, 1997, pp. 124-125.
- [64] Eurocode 3, Design of Steel Structures, Brussels: European Committee for Standardisation, 2009.
- [65] X.-L. Zhao and G. Hancock, "Plastic Mechanism Analysis of T-joints in RHS Under Concentrated Force," *Steel Structures*, vol. 2, no. ISSN 0218-1746, pp. 31-43, 1991.
- [66] K. Johansen, "Bruchmomente der Kreuzweise bewehrten Platten," *Int. Ass. Bridge Struct. Eng*, vol. 3, pp. 277-296, 1932.
- [67] Y. Yu, *The static strength of uniplanar and multiplanar connections in rectangular hollow sections, PhD thesis*, Delft: Delft University Press, 1997.
- [68] J. Wardenier and T. Giddings, *The strength and behaviour of statically loaded welded connections in structural hollow sections, Monograph, No 6*, Corby: CIDECT, 1986.
- [69] J. Wardenier, *Hollow Section Joints*, Delft, The Netherlands: Delft University Press, 1982.
- [70] G. Marquis and T. Björk, "New Yield Line Theory Based Design Approach for Ultimate Capacity of Welded RHS X-joints," in *Design, Fabrication and Economy of Welded Structures*, Miskolc, Hungary, 2008.
- [71] M. Watanabe, K. Satoh, K. Kimura and R. Hoshi, "Effect of Welding Methods and Sequences on the Residual Stress Distribution of Welded Joints," *Japan Welding Society*, pp. 146-153, 1955.
- [72] C. Tsai, S. Park and W. Cheng, "Welding Distortion of a Thin-Plate Panel Structure," *The Welding Journal*, vol. 78(5), pp. 157-165, 1999.
- [73] M. Mochizuki, M. Hayashi and T. Hattori, "Residual Stress Distribution Depending on Welding sequence in Multi-Pass Welded Joints With X-Shaped Groove," *Journal of Pressure Vessel Technology*, pp. 27-32, 2000.
- [74] M. Kadivar, K. Jafarpur and H. Baradaran, "Optimization welding sequence with genetic algorithm," *Comp. Mech*, pp. 514-519, 2000.
- [75] T. Teng, P. Chang and W. Tseng, "Effect of welding sequences on residual stresses," *Computers and Structures*, pp. 273-286, 2003.
- [76] N. Prasad and M. Srinivasan, "Effect of boundary condition restraint and welding sequence on residual stresses in weldments," *Int. Journal for the Joining of Materials*, vol. 9, pp. 37-42, 1997.
- [77] N. Prasad and M. Srinivasan, "Effect of boundary restraint and welding sequence on residual stresses in weldments," *Journal for the Joining of Materials*, pp. 37-42, 1997.

- [78] L. Zhang, J. Zhang, H. Serizawa and H. Muakawa, "Parametric studies of welding distortion in fillet welded structure based on FEA using iterative substructure method," *Science and Technology of Joining and Welding*, pp. 703-707, 2007.
- [79] C. Schwenk, M. Rethmeier and K. Dilger, "Analysis of the transient deformation behaviour and numerical optimisation of an electron beam welded gearwheel," *Mathematical Modelling of Weld Phenomena* 8, 2007.
- [80] Y. Lin and C. Chou, "A new technique for reducing the residual stress induced by welding in type 304 stainless steel," *Materials Processing Technology*, pp. 693-623, 1995.
- [81] S. Fukuda and K. Yoshikawa, "Determination of welding sequence: a neural net approach," *Engineering Analysis with Boundary Elements*, pp. 78-82, 1990.
- [82] K. Kim, D. Kim and B. Nnaji, "Robot arc welding task sequencing using genetic algorithms," *IIE Transactions*, pp. 865-880, 2002.
- [83] M. Damsho and P. Ruhoff, "An evolutionary algorithm for welding task sequence ordering," *Lecture Notes in Computer Science*, 1998.
- [84] L. Xie and C. Hsieh, "Clamping and welding sequence optimization for minimizing cycle time and assembly deformation," *Materials & Product Technology*, pp. 389-399, 2002.
- [85] F. Guangming, I. L. Marcelo, D. Menglan and F. E. Segen, "Influence of welding sequence on residual stress and distortion of fillet welded structures," *Elsevier*, vol. 46, pp. 30-55, 2016.
- [86] F. Ding-fa, Z. Chang-qing, L. Can, W. Guan and L. Lou-xing, "Effect of welding sequence on residual stress in thin-walled octagonal pipe-plate structure," *Elsevier*, vol. 24, pp. 657-664, 2014.
- [87] K. Krekeler, K. Schmidt and H. Kauhausen, "Das Schweißen im Schiffbau," in *Unikum Verlag*, Bremen, 2011.
- [88] "Fabricating Metal Working," *The Business of Metal Manufacturing*, [Online]. Available: <http://www.fabricatingandmetalworking.com/>. [Accessed 06 07 2016].
- [89] H. B. Cary, *Modern Welding Technology*, Prentice-Hall, 1998.
- [90] A. Sarhadi, Numerical modeling of the conduction and radiation heating in precision glass, Lyngby: Proceedings of the 12th Euspen International Conference, 2012.
- [91] J. Hattel, *Fundamentals of Numerical Modelling of Casting Processes*, J. Hattel, Ed., Chicago: Nova Science Publisher Inc., 2012.
- [92] D. Rosenthal, *Mathematical Theory of Heat Distribution During Welding and Cutting*, *Welding Journal* 20, 1941.
- [93] N. Rykalin, *Berechnung der Wärmevergänge beim Schweißen*, Berlin: VEB Verlag Technik, 1957.

- [94] H. Jaeger and J. Carslaw, *Conduction of Heat in Solids*, Oxford: Oxford University, 1947.
- [95] B. Weiner and J. Boley, *Theory of Thermal Stresses*, New York: Dover publications, 1997.
- [96] B. Andersson, "Thermal Stresses in a Submerged-Arc Welded Joint Considering Phase Transformations," *Journal of Engineering Materials and Technology*, vol. 100, no. 4, pp. 355-360, 1978.
- [97] J. Goldak and M. Bibby, "Computational Thermal Analysis of Welds," *The Minerals, Metals & Materials Society*, pp. 154-164, 1988.
- [98] J. Goldak, M. Mocanita, V. Aldeak, J. Zhou, D. Downey and A. Zypchen, *Mathematical Modelling of Weld Phenomena*, The Insitute of Materials, 2001.
- [99] L. Karlsson, *Thermal Stresses in Welding*, 1986.
- [100] D. Radaj, *Heat Effects of Welding*, Berlin Heidelberg: Springer-Verlag, 1992.
- [101] J. Goldak, "Computational Weld Mechanics as a Coupled Problem," in *Conf. on Modelling of Casting, Welding and Advanced Solidification Processes*, 1991.
- [102] L. Lindgren, *Finite Element Modelling and Simulation of Welding*, Taylor & Francis, 2001.
- [103] T. Zacharia, J. Vitek, J. Goldak, T. Debroy and M. Rappaz, *Modelling of Fundamental Phenomena in Welds*, IOP Publishing Ltd, 1995.
- [104] H. K. Bhadeshia, *Models for Elementary Mechanical Properties of Steel Welds*, Institute of Materials , 1997.
- [105] S. & Technology, "Welding Science," Science & Technology, [Online]. Available: <https://str.lnl.gov/str/November01/Elmer.html>. [Accessed 18 Feb 2016].
- [106] Encyclopedia, "Steelconstruction.info," Encyclopedia, [Online]. Available: <http://www.steelconstruction.info/Welding>. [Accessed 17 Feb 2016].
- [107] P. Batista, P. Marcelo, Y. Prasad, J. Maria, V. Siqueira and R. Artur, "Determination of Residual stresses Numerically Obtained in ASTM AH36 Steel Welded by TIG Process," *Scientific Research*, 5th 4 2013. [Online]. Available: [http://images.google.de/imgres?imgurl=http%3A%2F%2Ffile.scirp.org%2FHtml%2F8-7701003%25255Ce62fc224-41e8-4404-a539-d4042dc35769.jpg&imgrefurl=http%3A%2F%2Ffile.scirp.org%2FHtml%2F8-7701003\\_30648.htm&h=315&w=640&tbnid=POXynga86D8h-M%3A&docid=mzNHhkqF3cpK-M](http://images.google.de/imgres?imgurl=http%3A%2F%2Ffile.scirp.org%2FHtml%2F8-7701003%25255Ce62fc224-41e8-4404-a539-d4042dc35769.jpg&imgrefurl=http%3A%2F%2Ffile.scirp.org%2FHtml%2F8-7701003_30648.htm&h=315&w=640&tbnid=POXynga86D8h-M%3A&docid=mzNHhkqF3cpK-M). [Accessed 27 March 2016].
- [108] Simufact.welding, *Heat Source*, Belrin: Simufact.welding, 2014.
- [109] M. Moradi, F. Simon, H. Pasternak, J. Hildebrand and M. Shubert, "Study on the load bearing capacity of a S355 SHS T-joint by taking into account the presence of welding imperfections," 2016.

- [110] S. Founders, *Mechanical properties of Cast Carbon and Low Alloy Steels*, Des, Plaines: Society of America .
- [111] D. Easterling and K. Porter, *Phase Transformation in Metals and Alloys*, 2nd ed., Routledge, 1992, pp. 338-339.
- [112] O. Voss, I. Decker and H. Wohlfahrt, *Consideration of Microstructural Transformations in the Calculation of Residual Stresses and Distortion of Laser Weldments*, The Institute of Materials, 1998.
- [113] M. Moradi, "Study on the load bearing capacity of a S355 SHS T-Joint by taking into account the presence of welding imperfections," *Journal of constructional steel research (to be published)*, 2016.
- [114] L. A. Bertram, *Some Consistency Requirements on Hardening-Recovery Evolution Equations for Welding*, Sandia National Laboratories Report, 1992.
- [115] P. DeBiccari and A. Michaleris, *Prediction of Welding Distortion*, Welding Journal Research Supplement, 1997.
- [116] J. L. Rhoads, *Basic Explanation of Creep Processes*, California : Department of Nuclear Energy University of California.
- [117] O. Taylor and R. Zienkiewicz, *The Finite Element Method*, Butterworth-Heinemann, 2000.
- [118] F. Zamiri, *Welding Simulation and Fatigue Assessment of Tubular K-Joints in High Strength Steel*, PhD thesis, ÉCOLE POLYTECHNIQUE FÉDÉRALE DE LAUSANNE, 2014.
- [119] L. Fuglsang Andersen, *Residual stresses and deformations in steel structures (PhD thesis)*, Technical University of Denmark, 2000.
- [120] V. O. Grong, *Metallurgical modelling of welding*, London: The Institute of Materials, 1994.
- [121] L. Erik Lindgren, *Computational Welding Mechanics*, Abington: WoodheadPublishing in Materials, 2007.
- [122] C. Heinze, *Dependency of martensite start temperature on prior austenite grain size and its influence on welding-induced residual stresses*, Amsterdam: Elsevier, 2013.
- [123] J. Leblond and J. Devaux, *A theoretical and numerical approach to the plastic behavior of steels during phase transformations*, Journal of the Mechanics and Physics of Solids, 1986.
- [124] D. Koistinen and R. Marburger, *A general equation prescribing extent of austenite–martensite transformation in pure Fe–C alloys and plain carbon steels*, Acta Metallurgica, 1959.
- [125] Eurocode 3, Normenausschuss Bauwesen (NABau) Deutsches Institut für Normung, Bemessung und Konstruktion von Stahlbauten - Teil 1-2, Tragwerksbemessung-Bemessung für den Brandfall, 2006.

- [126] HBM, [Online]. Available: <https://www.hbm.com/en/3058/wa-1-inductive-displacement-transducer-plunger/>. [Accessed 01 June 2016].
- [127] UK Department of Energy Offshore, “Background to new static strength guidance for tubular joints in steel offshore structures,” DoN, UK, 1990.
- [128] B. Krizelecji , A. Blachut and A. Moffat, “The effects of chord length and boundary conditions on the static strength of tubular T-joints under brace compression loading,” *Marine Structures*, vol. 9, pp. 935-947, 1996.
- [129] M. Lalani, “Developments in tubular joints technology for offshore structures,” in *Offshore and Polar Engineering Conference*, San Francisco, 1992.
- [130] M. Madros, N. Zettlemoyer and B. Healy, “Effect of chord can length on strength of T joints,” in *proceeding of the 27th annual Offshore Technology Conference*, Huston, 1995.
- [131] E. Standard, “Design of joints,” in *Eurocode* , Brussels, European Committee for Standardization , 2005, pp. 103-104.
- [132] J. Packer, J. Wardenier, X.-L. Zhao, G. van der Vegte and Y. Kurobane, “Design Guide for Rectangular Hollow Sections,” in *Construction with Hollow Steel Sections*, CIDECT, 2009, p. 31.
- [133] Abaqus, *user's manual*, version 6.14-5, 2014.
- [134] V. Kvocak and P. Beke, *Experimental Analysis of T-joints Composed of RHS, CHS and HEA Sections*, Technical University of Kosice, 2012.
- [135] J. Aguilera, *Strengthening T-joints of rectangular hollow steel sections using through-wall bolts and externally bonded FRP plates (MSc thesis)*, Ontario: Queen's University, 2012.
- [136] Tribology-abc, “Tribology-abc,” [Online]. Available: <http://www.tribology-abc.com/abc/cof.htm>. [Accessed 12 09 2016].
- [137] D. Radaj, *Eigenspannungen und Verzug beim Schweißen – Rechen- und Meßverfahren*, DVS-Verlag, 2002.
- [138] L. S. P. V. L.F. Costa-Neves, “Experimental behaviour of end plate I-beam to concrete filled rectangular hollow section column joints.,” *International Journal of Applied Mechanics and Engineering* , vol. 9, pp. 63-80, 2004.
- [139] J. Packer, *Theoretical behaviour and analysis of welded steel joints with RHS chord sections*, Nottingham, UK: University of Nottingham, 1978.
- [140] X. Zhao, *The behaviour of cold formed RHS beams under combined actions. PhD thesis*, Sydney: University of Sydney, 1992.
- [141] Academic Press Dictionary of Science and Technology, Morris, Christopher G. ed., Orlando: Elsevier Science & Technology, 1992.



- [142] T. C. E. Encyclopedia, "Encyclopedia Britannica," 16 Feb 2016. [Online]. Available: <http://www.britannica.com/technology/welding>.
- [143] Oxford, "Oxford Dictionary Online," 16 Feb 2016. [Online]. Available: <http://www.oed.com/>.
- [144] J. Packer and J. Wardenier, *Hollow Structural Section, Connections, Trusses*, Ontario, 2003.
- [145] F. Mashiri, X. Zhao and P. Grundy, "Fatigue behaviour of thin-walled tube-to-tube T-joints under in-plane bending," in *Tubular Structures IX*, Düsseldorf, 2001.
- [146] R. Porter Goff, J. Free and W. Tsiagbe, "Experimental Determination of Residual Stresses in Welded Tubular T-joint," *Fatigue of Offshore Structures*, pp. 285-295, 1988.
- [147] X. Zhao, P. Grundy, C. Münch and F. Mashiri, "T-joints, Fatigue crack initiation and propagation in thin SHS-to-SHS," in *Tubular Structures IX*, Düsseldorf, 2001.
- [148] G. Totten, M. Howes and T. Inoue, *Handbook of Residual Stress and Deformation of Steel*, USA: The Materials Information Society, 2002.
- [149] W. Piekarska, M. Kubiak and A. Bokota, "Numerical Simulation of Thermal Phenomena and Phase Transformation in Laser-Arc Hybrid Welded Joints," *Archives of Metallurgy and Materials*, vol. 56, no. 2, pp. 409-421, 2011.
- [150] F. Soul and N. Hamdy, *Numerical Simulation of Residual Stress and Strain Behavior After Temperature Modification*, INTECH, 2012.
- [151] J. T. Assis and V. Monin, "Nondestructive control of residual stress state of weld regions by x-ray diffraction methods," in *NDTISS'99*, Santa Maria, 1999.
- [152] Associação Brasileira de Normas Técnicas, *Design of steel and composite structures for buildings using hollow sections*, Sao Paulo: Associação Brasileira de Normas Técnicas, 2013.
- [153] N. Koteski and J. Packer, "Bracing Connections to Rectangular HSS Columns, Connections in Steel Structures IV- Behaviour Strength and Design," in *Fourth International Workshop*, Roanoke, Virginia, 2000.
- [154] N. Koteski, J. Packer and R. Puthlie, "A Finite Element Method Based Yield Load Determination Procedure for Hollow Structural Section Connections," *Journal of Constructional Engineering*, vol. 59, pp. 453-471, 2003.
- [155] M. Moradi Eshkafti, F. Simon, H. Pasternak and J. Hildebrand, "The influence of the welding sequence on the load bearing capacity and stress distribution of square hollow section steel joints," in *Simulationsforum 2016 Schweißen und Wärmebehandlung*, Weimar, 2016.

## 9 APPENDICES

### Initial Geometry

Welding causes imperfections and deformation is included. In order to study the influence of welding in terms of deformation on hollow sections, it has been necessary to measure the initial geometry. For this reason several techniques and ways exist. One way which has been also used in this work is the use of surveying camera. This camera is able to read the heights on a row of selected points accurately with accuracy of 0.3 mm/km. A total number of 60 points have been selected on the chord and brace member. The points are selected in manner that they could cover the important surfaces on which welding is done.

To read the heights from a surveying camera there is a need of a vertical element so called level which is widely used for levelling technique. Reading of height has been done with two different cameras and also two different levels as reaching some point close to the intersection area has been difficult. Figure 9.1 shows the selected points, camera and level used for measuring the initial geometry. The points have been selected on 5 different rows. Two rows on the brace member and three rows on the chord which can be seen in Figure.



Figure 9.1: Measuring the initial geometry by using surveying camera.

### First case (progressive welding)

Figure 9.3 shows the initial and after welding geometry for chord top surface for nodes selected at the middle line. As it can be noticed, welding has very small influence in terms of deformation on this closed section. By getting closer to the weld beads from both sides the difference between initial and after welding geometry even gets smaller. In the following the influence of welding in terms of deformation for various parts of the joint is shown. The numerical comparison has been neglected as the results from the experiment present very small deformation after the welding process.



Figure 9.2: Lines along which the initial and after welding geometry was measured.

It should be mentioned as the differences offered by the curves are significantly small. Due to the low values and also minor differences the cause could not be clarified and further validation by numerical analysis was neglected.

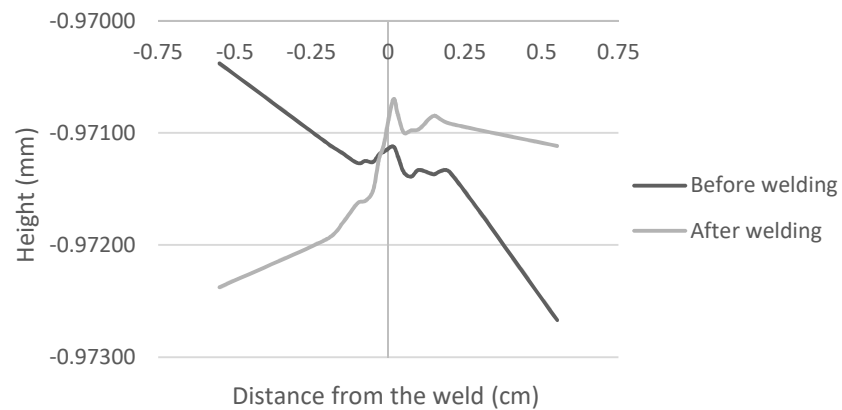


Figure 9.3: Initial and after welding geometry for chord top surface at middle line.

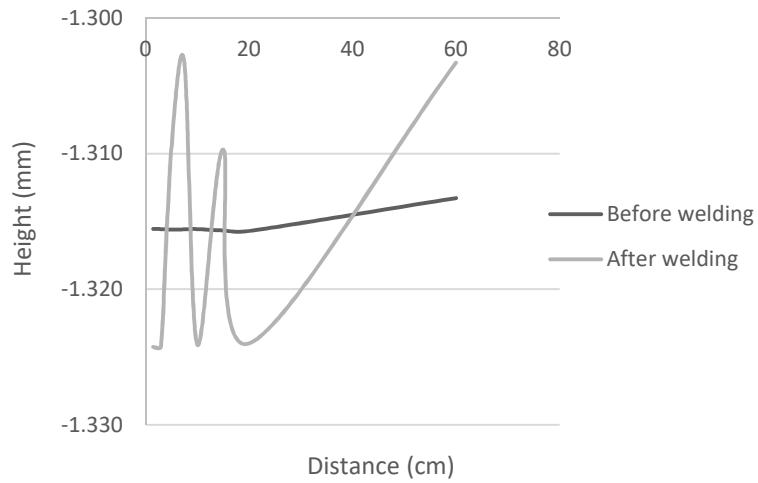


Figure 9.4: Initial and after welding geometry for the brace member midline in z direction.

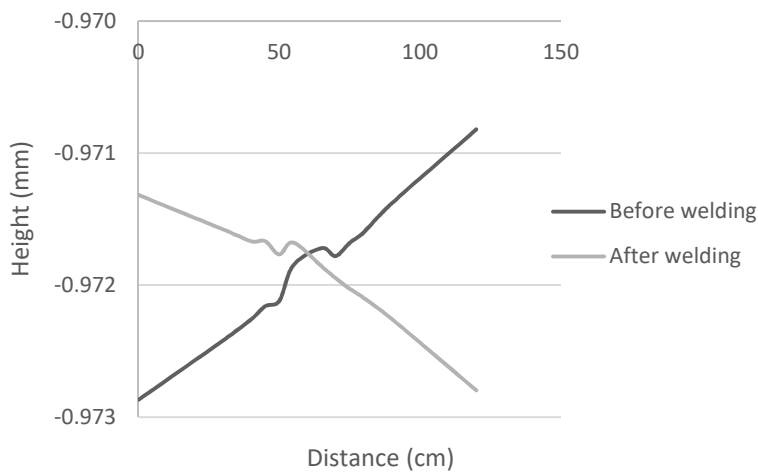


Figure 9.5: Initial and after welding geometry for the chord top surface edge.

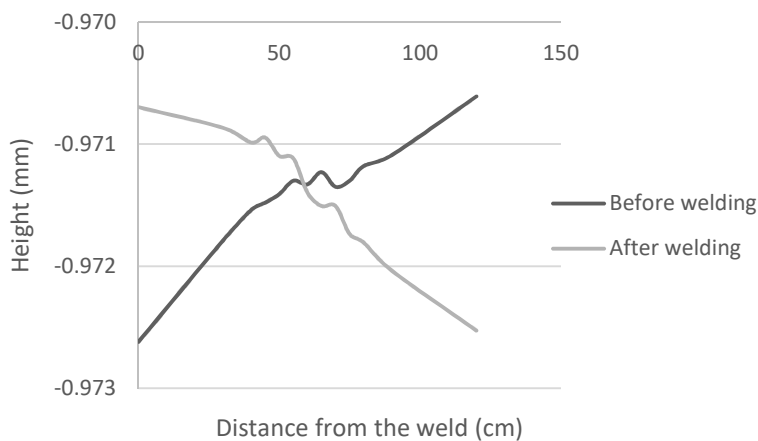


Figure 9.6: Initial and after welding geometry for the chord top surface edge in z direction.

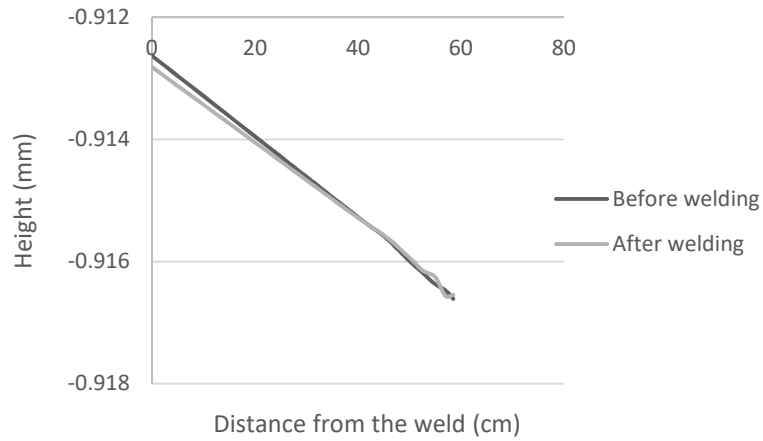


Figure 9.7: Initial and after welding geometry for the brace midline in x direction.

Second case (double-phase progressive welding)

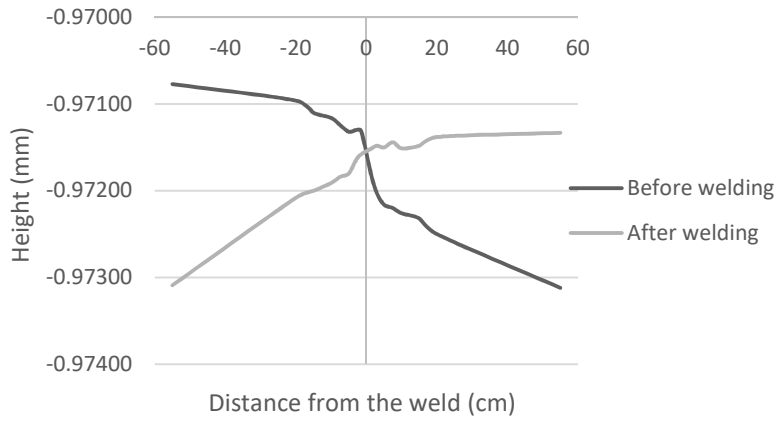


Figure 9.8: Initial and after welding geometry for chord top surface at middle line.

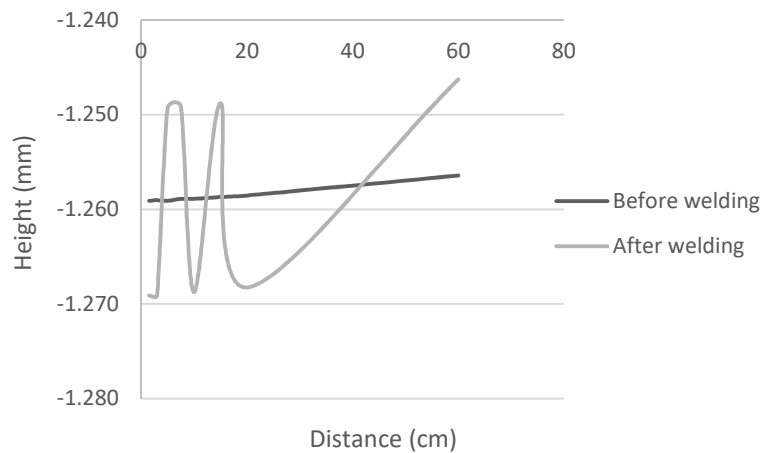


Figure 9.9: Initial and after welding geometry for the brace member midline in z direction.

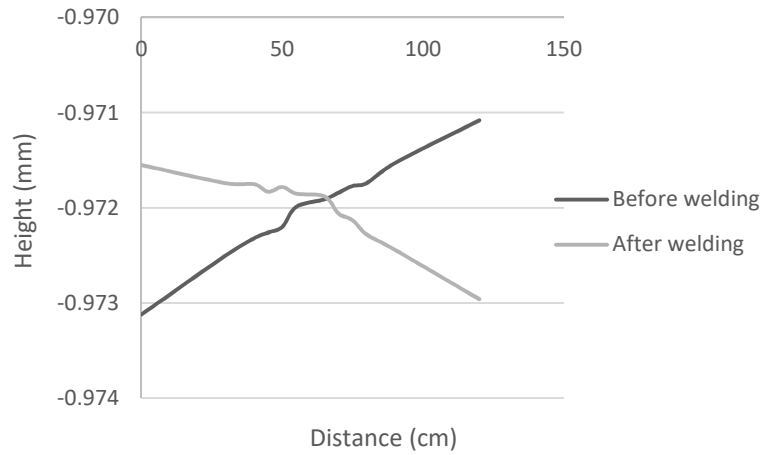


Figure 9.10: Initial and after welding geometry for the chord top surface edge.

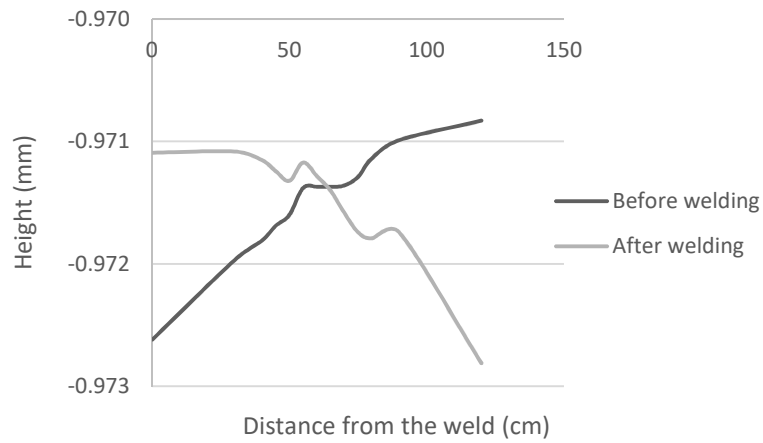


Figure 9.11: Initial and after welding geometry for the chord top surface edge in z direction.

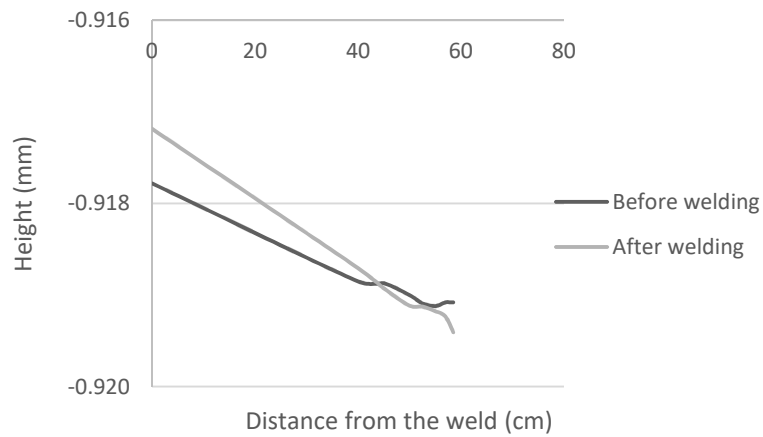


Figure 9.12: Initial and after welding geometry for the brace midline in x direction.

Third case (skip welding)

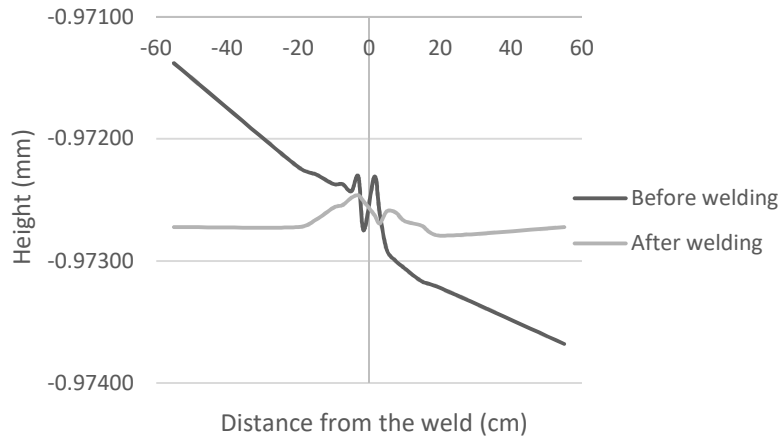


Figure 9.13: Initial and after welding geometry for chord top surface at middle line.

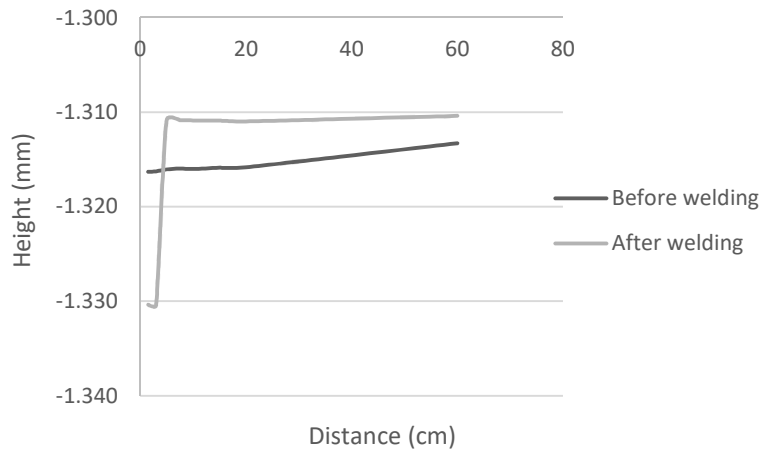


Figure 9.14: Initial and after welding geometry for the brace member midline in z direction.

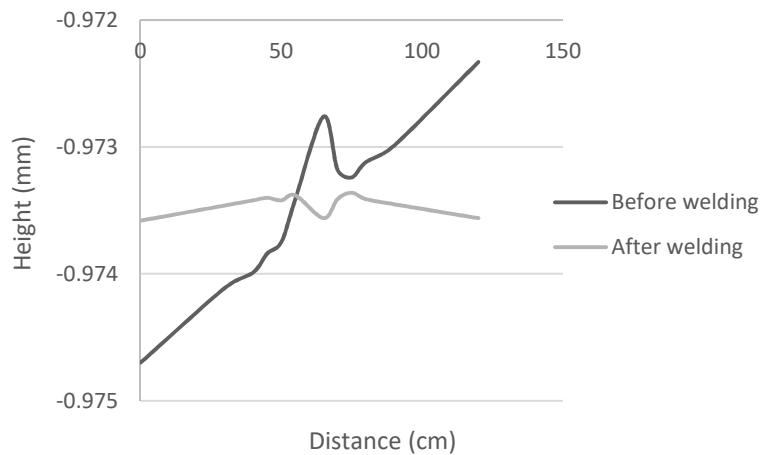


Figure 9.15: Initial and after welding geometry for the chord top surface edge.

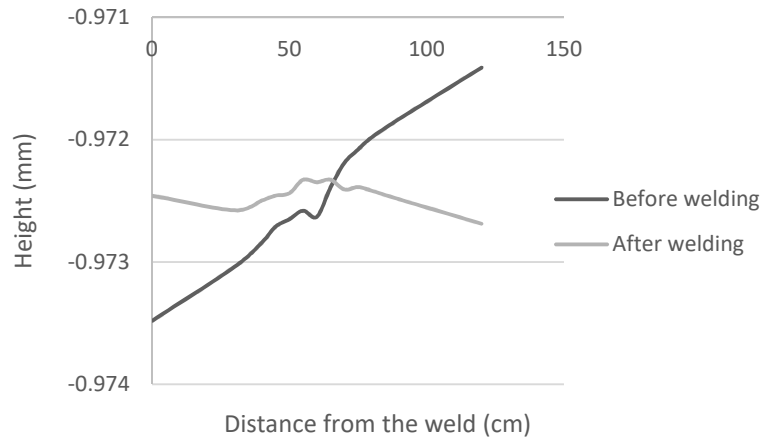


Figure 9.16: Initial and after welding geometry for the chord top surface edge in z direction

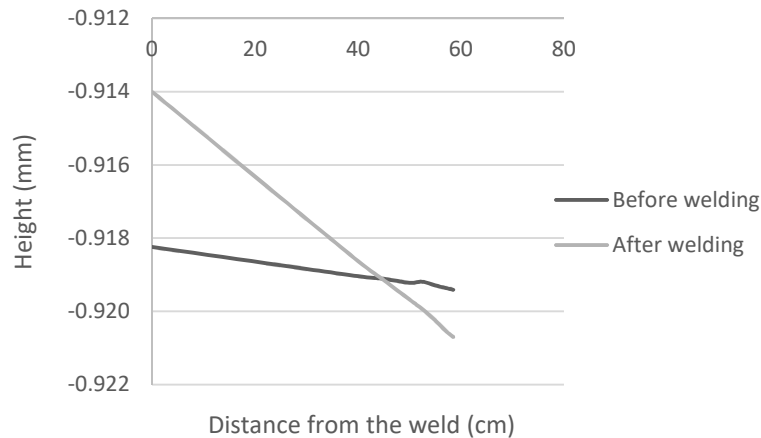


Figure 9.17: Initial and after welding geometry for the brace midline in x direction.

### Weld throat thickness examination

Before welding of the joints, welding of two plates was arranged. An equal plate thickness as the brace member which is the thinner member was selected. The same welding parameters were given to check the welding quality and also to make sure an appropriate portion of the plate would be melted and influenced by the heat. Afterwards the welded specimen was cut into 5 equal parts as shown in Figure 9.18 and the tolerance in the throat thickness was measured.



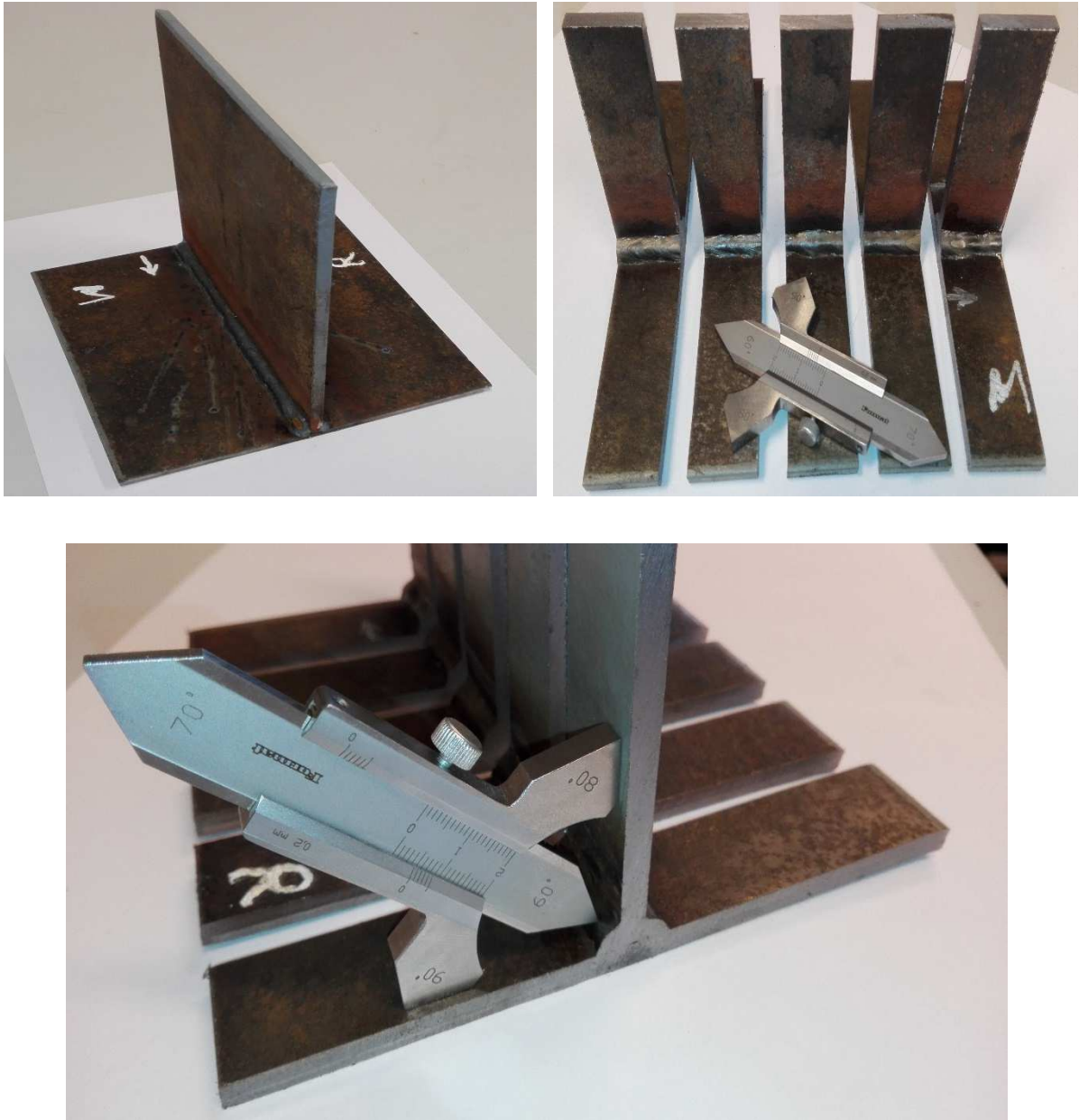


Figure 9.18: Weld throat thickness measurement.

### Temperature distribution for double-phase progressive welding

Figure 9.19 and Figure 9.20 respectively show the temperature distribution on the chord and brace members.

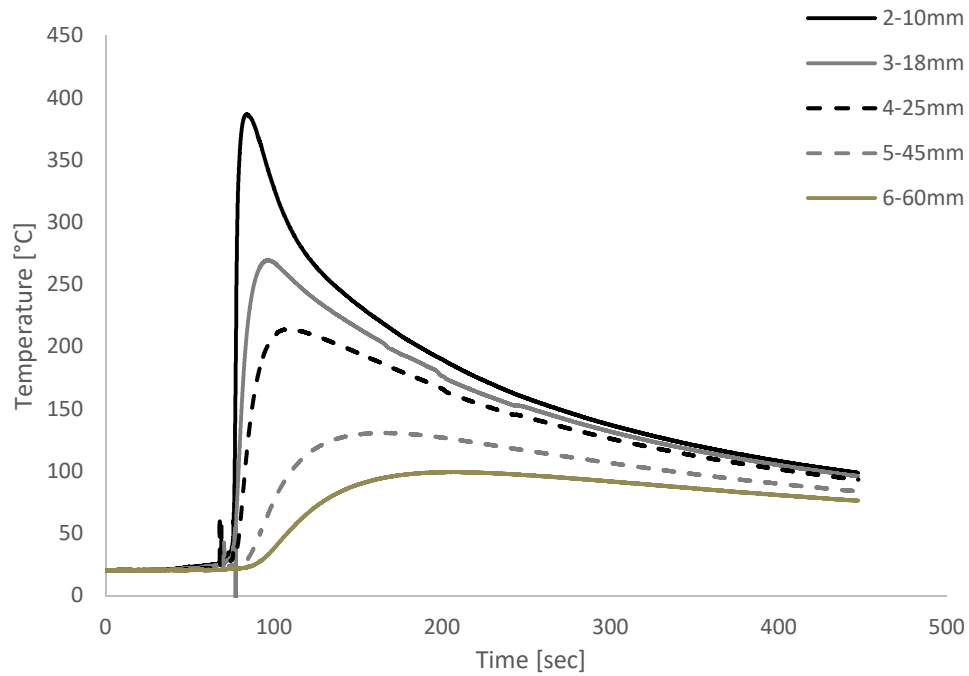


Figure 9.19: Temperature distribution from the thermo-couples on the chord member.

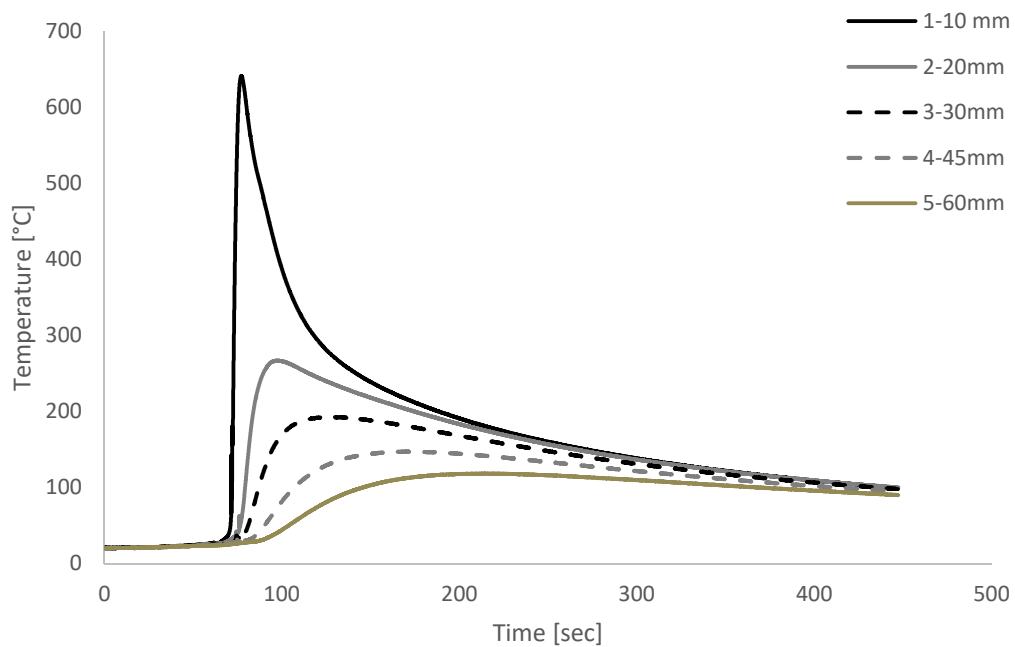


Figure 9.20: Temperature distribution from the thermo-couples on the brace member.

## Influence of phase transformation on the residual stresses distribution and distortions

Figure 9.21 and Figure 9.22 respectively show the stress distribution for single phase and multi-phase materials used. As it can be seen phase transformation has an influence on the magnitude of tensile stresses observed in the weld toes. The magnitude of tensile stresses experienced at the weld toe for the first case dropped by 35 MPa. The same reduction has been observed for the two-phase progressive welding. However not a big influence on the third case (skip welding is observed).

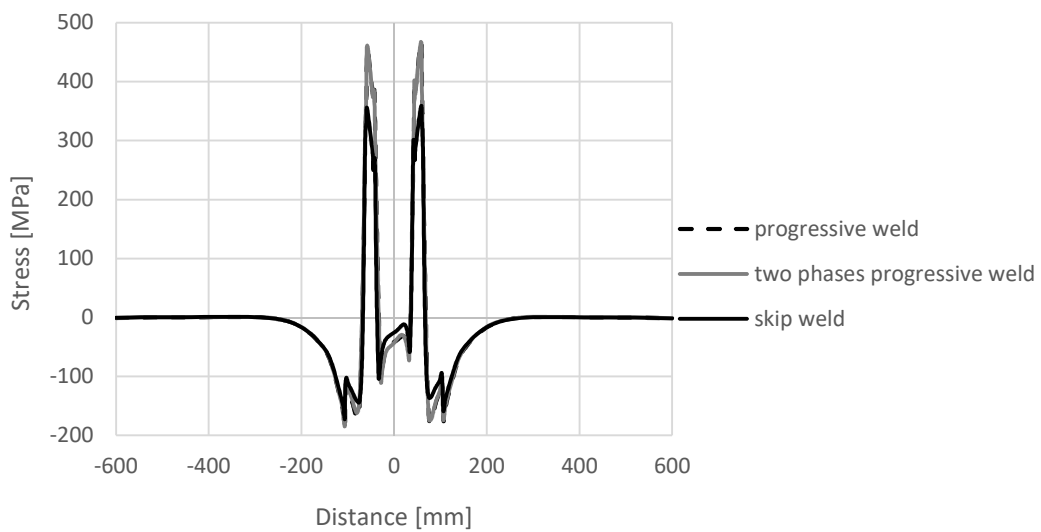


Figure 9.21: Longitudinal stress - single phase material.

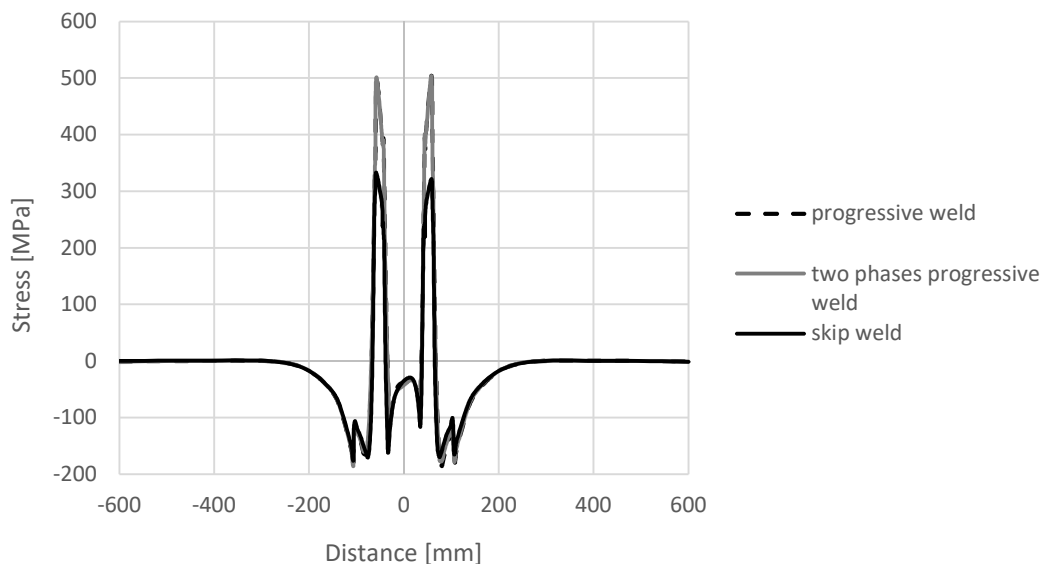


Figure 9.22: Longitudinal stress – multi-phase material.

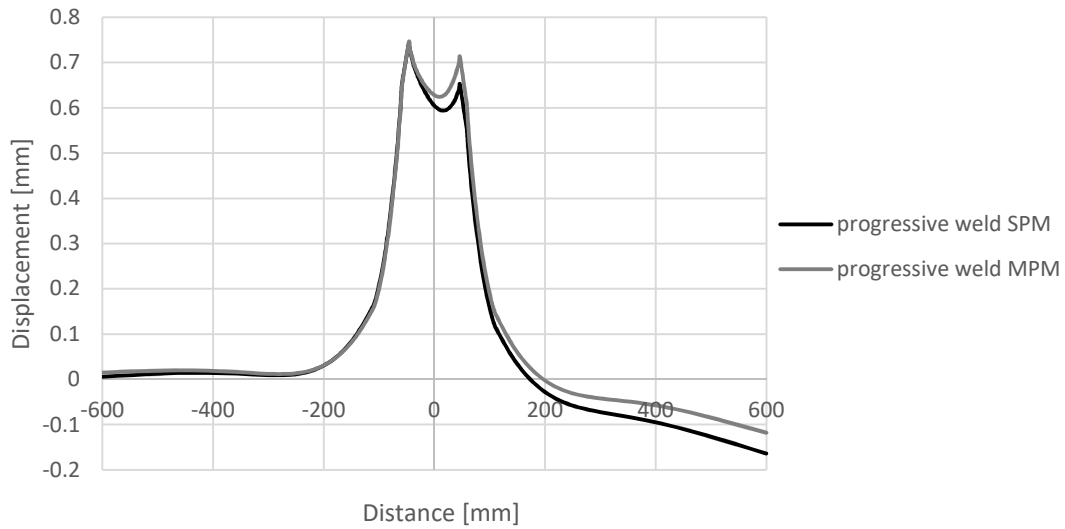


Figure 9.23: Welding induced distortion for the midline on the chord top surface- progressive welding.

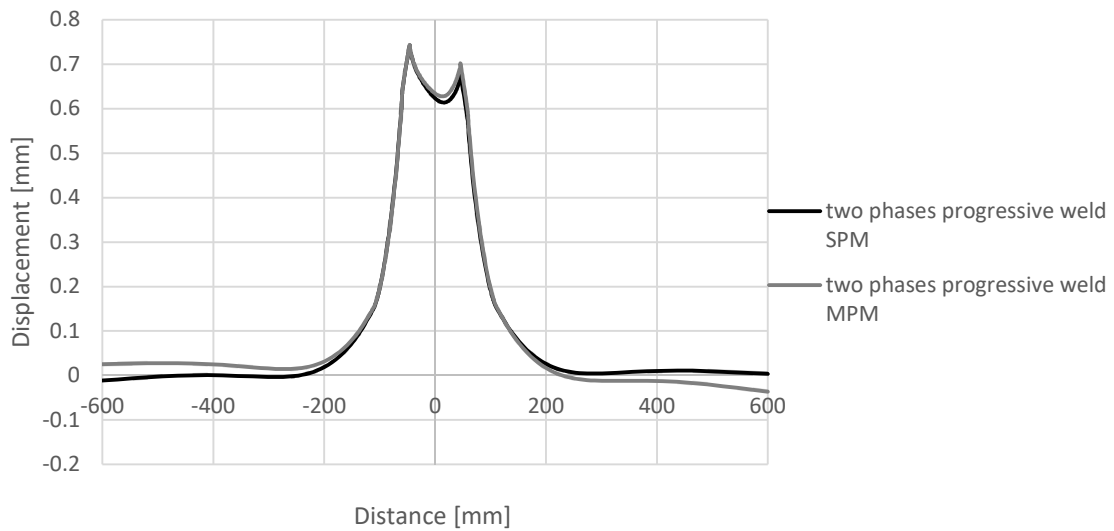


Figure 9.24: Welding induced distortion for the midline on the chord top surface- two phases progressive welding.

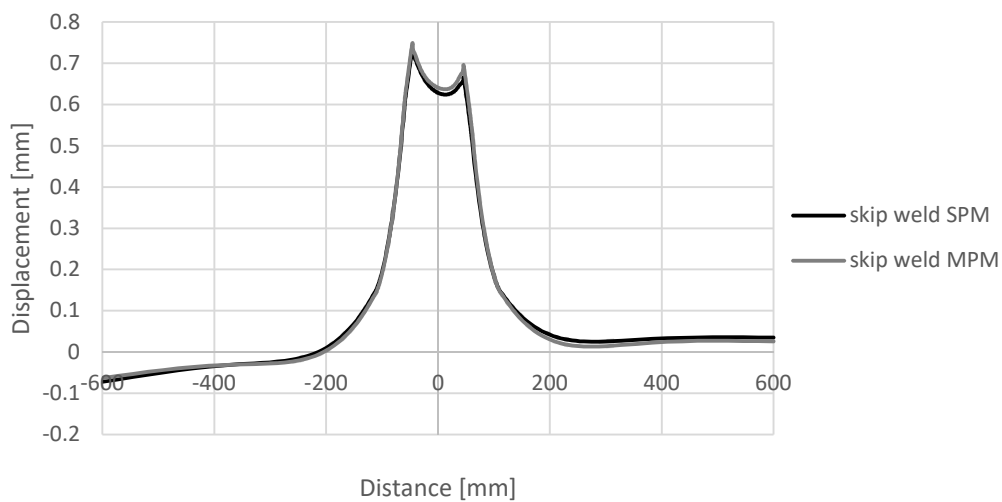


Figure 9.25: Welding induced distortion for the midline on the chord top surface- skip welding.

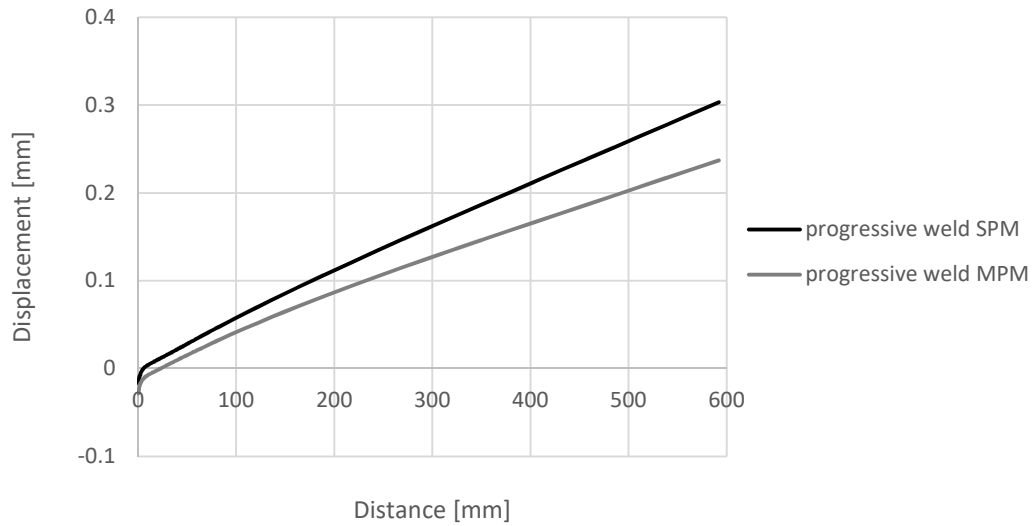


Figure 9.26: Welding induced distortion for the midline on the brace in x direction- progressive welding.

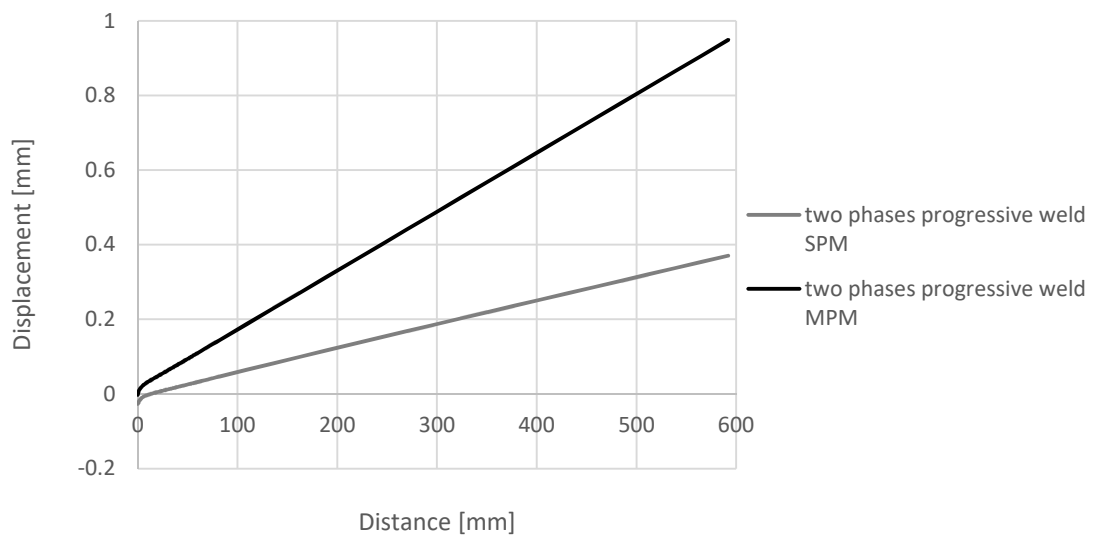


Figure 9.27: Welding induced distortion for the midline on the brace in x direction- two phases progressive welding.

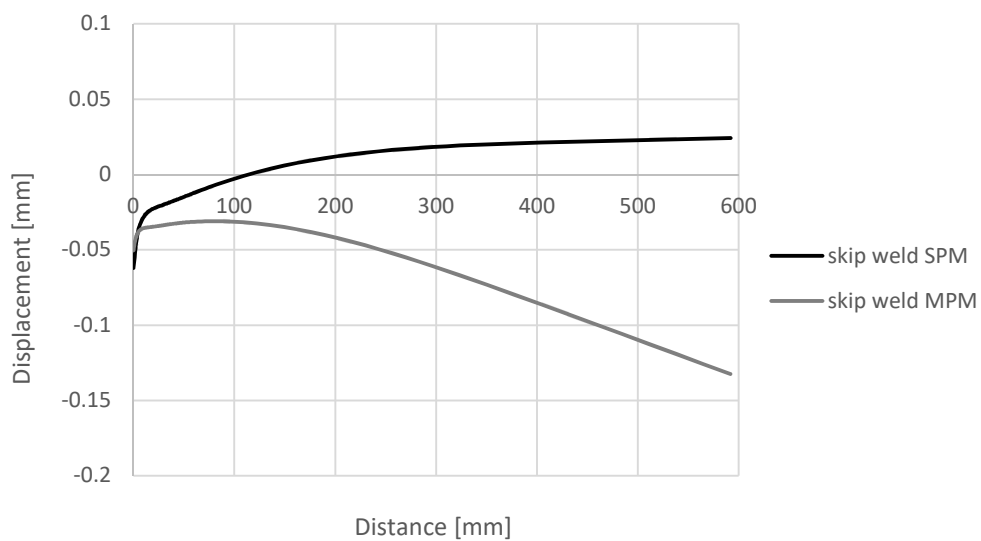


Figure 9.28: Welding induced distortion for the midline on the brace in x direction- skip welding.

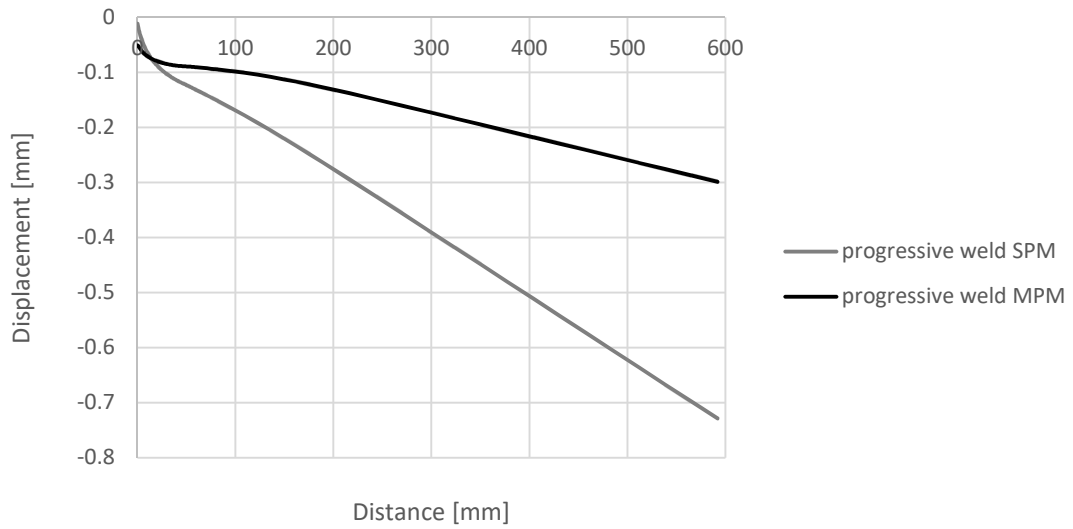


Figure 9.29: Welding induced distortion for the midline on the brace in z direction- progressive welding.

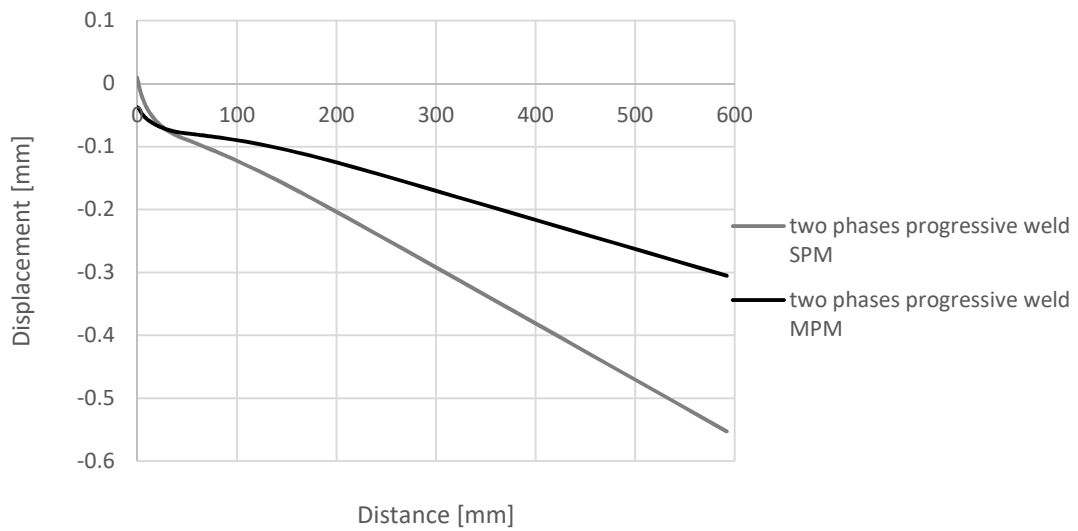


Figure 9.30: Welding induced distortion for the midline on the brace in z direction- two phases progressive welding.

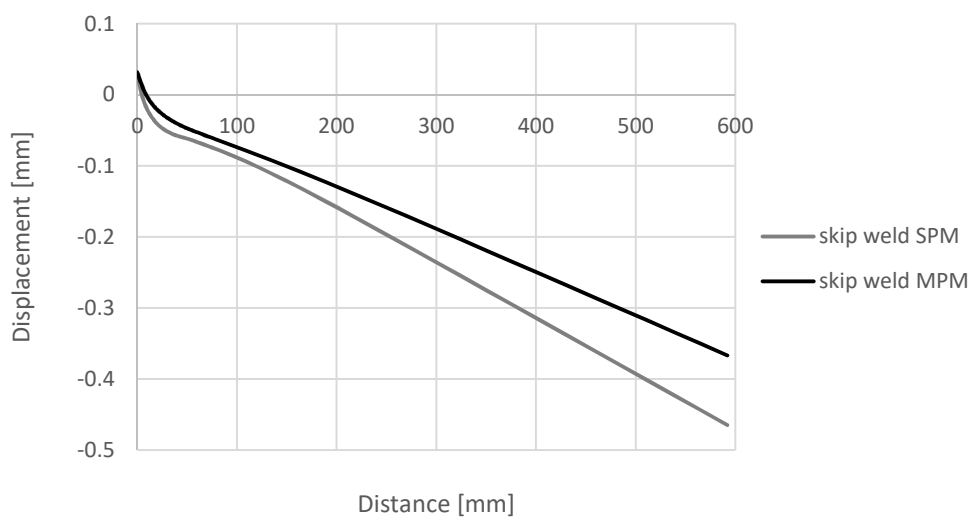


Figure 9.31: Welding induced distortion for the midline on the brace in z direction- skip welding.

### Distribution of residual stresses in thickness

Figure 9.32 shows how residual stresses develop in the thickness of the chord member. a parallel line to which on the surface was selected.

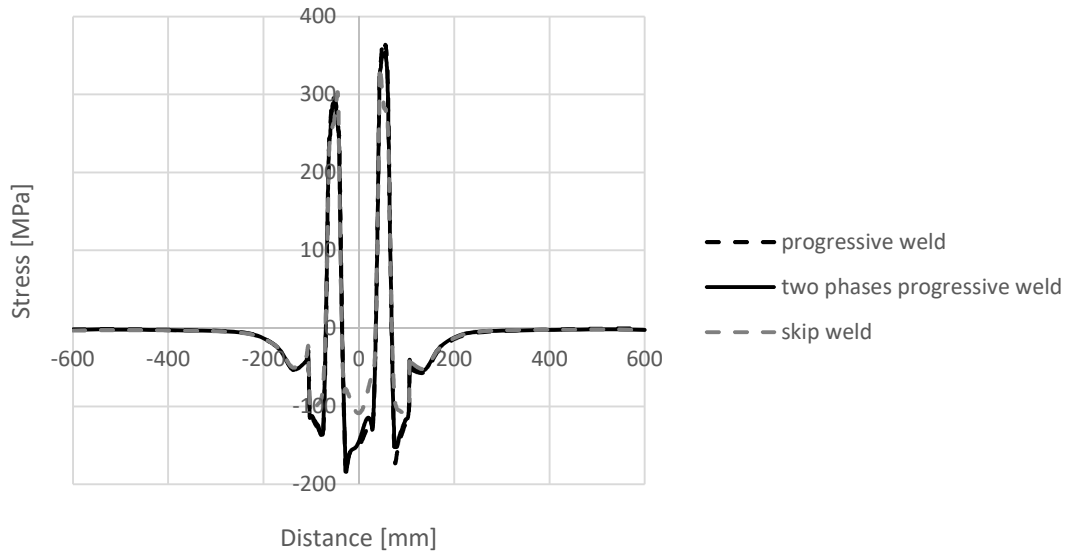


Figure 9.32: Distribution of longitudinal residual stresses in thickness of the chord member.

### Load-displacement behaviour

Figure 9.33 to Figure 9.35 illustrate the behaviour of the chord member in terms of displacement while the loading process. As overall behaviour of the joints for various welding sequences showed, difference between the curves here was expected. As it can be seen in all diagrams the first case shows a higher strength and then the second case with two welds with a reduction of -4 % and at last the third case with a reduction of -7 %.

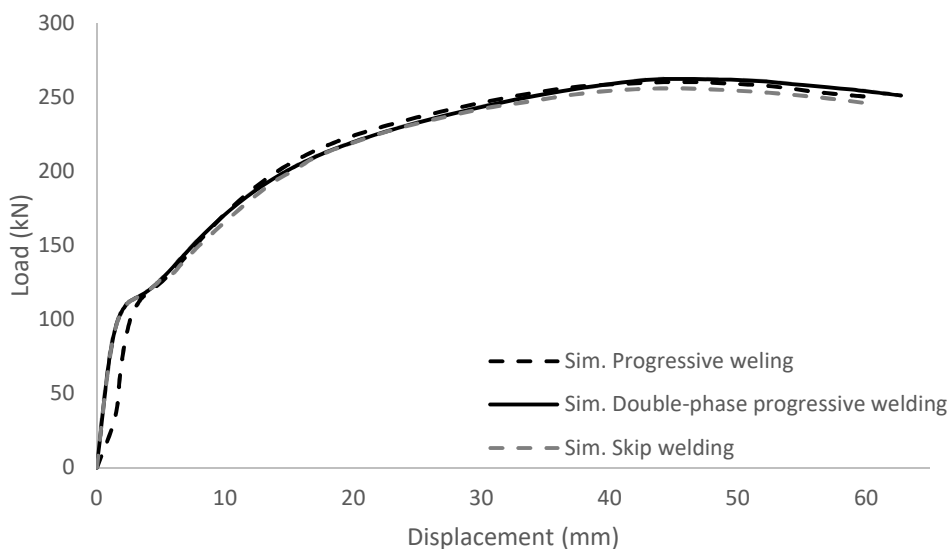


Figure 9.33: Load-displacement behaviour of points located 60 mm away from the brace on both sides on the chord

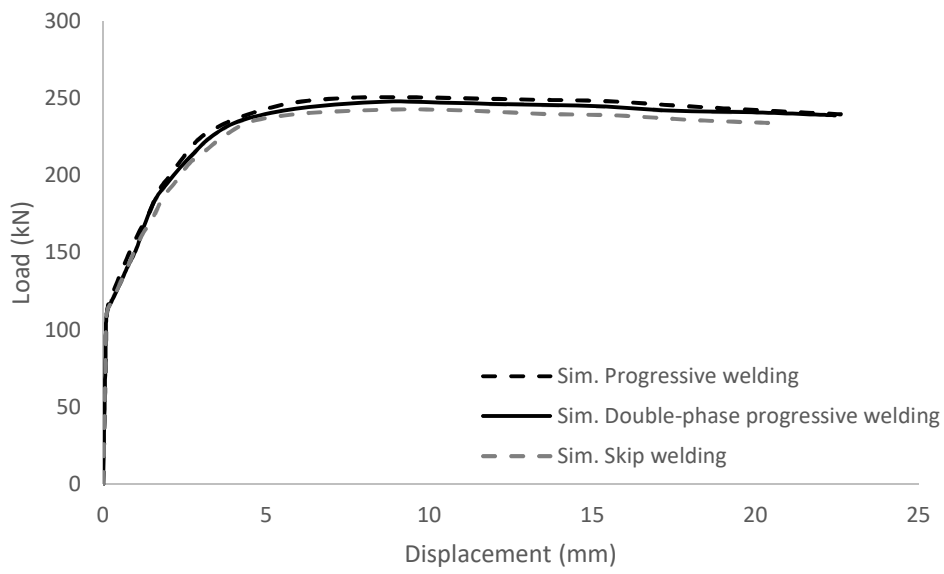


Figure 9.34: Load-displacement curves for the point on the bottom of the chord.

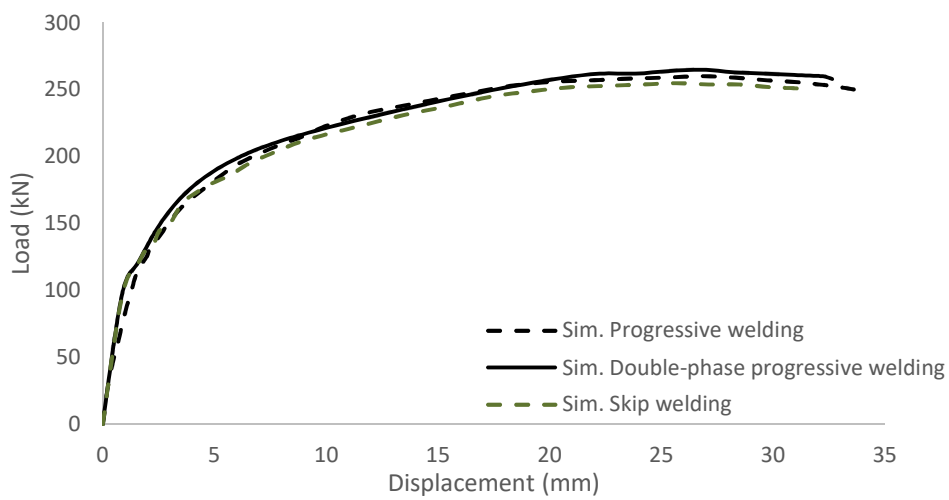


Figure 9.35: Load-displacement curves for the points on chord side walls.



## Plastic strain

Figure 9.36 shows the Von Mises plastic strain distribution in the T-joint. Crack development is an important issue which directly influences the strength of the joint and could appear at the weld toes around the brace corners where a high magnitude of plastic strain is observed. The crack development can appear at start and end points of welding and needs a high attention. Appearance of such a crack development in stress concentration areas as start and end points can lead to unexpected failures.

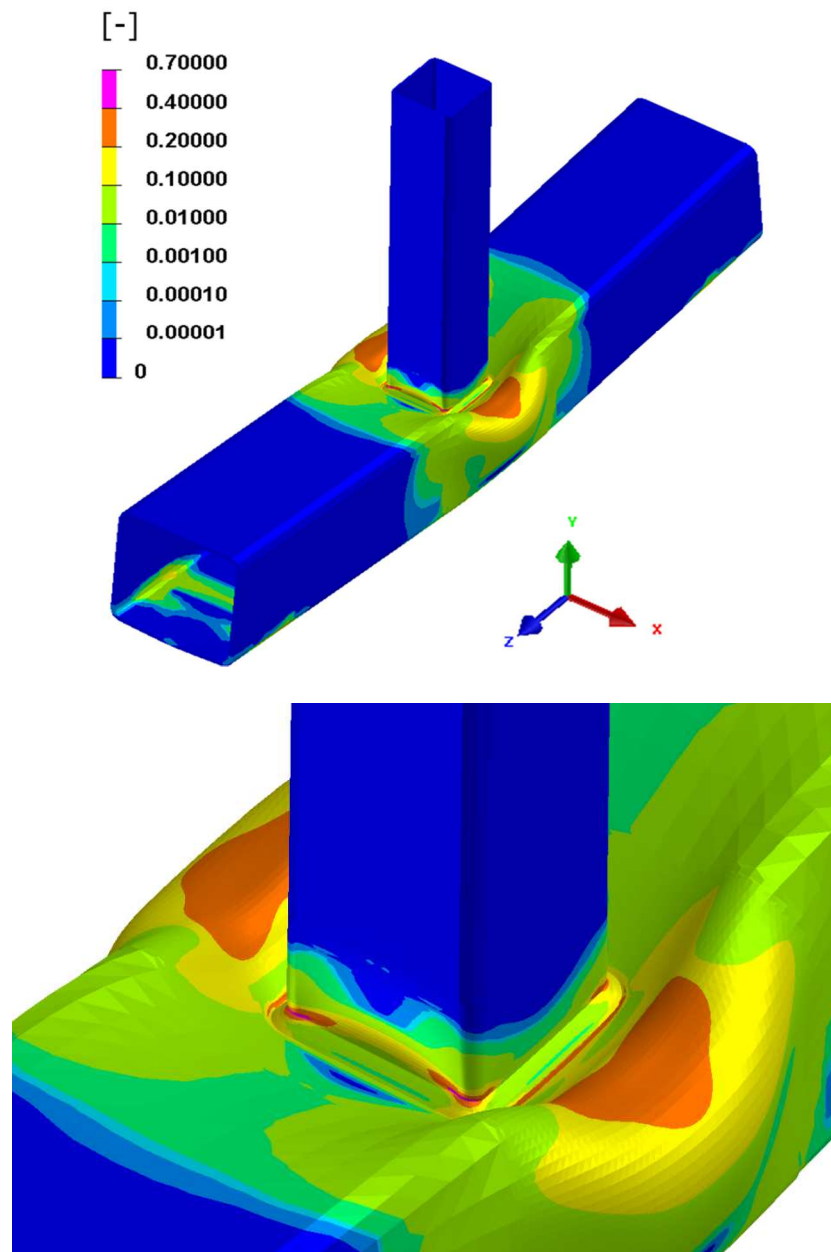


Figure 9.36: Plastic strain distribution.